Microoptical Multi Aperture Imaging Systems

Dissertation

zur Erlangung des akademischen Grades
doctor rerum naturalium (Dr. rer. nat.)

seit 1558

vorgelegt dem Rat der
Physikalisch-Astronomischen Fakultät
der Friedrich-Schiller-Universität Jena

von

Diplomphysiker Andreas Brückner
geboren am 09. August 1980 in Magdeburg

Contents

Die Menschheit existiert nicht um der Wissenschaft willen, sondern die Wissenschaft sollte betrieben werden, um die Bedingungen der Menschheit zu verbessern.

Mankind does not exist for science's sake, but science should be used to improve the conditions of mankind.

Jozef Maximilián Petzval (1807-1891)

1 Introduction

Vision is by far the most important sense of human beings. It enables the exact orientation in the 3D environment, reaches up to several kilometers in distance and has always been a transport medium of human's memories. The majority of man-made optical imaging systems follows the design principles of single aperture optics which is the basic architecture of all known mammalian eyes [1]. Single aperture refers to the fact that all light which is recorded in the image passes through a single clear aperture of the optical system. Even the ancestor of the photographic camera, the *'Camera obscura'* which had no lens at all, belongs to this type [2, 3]. In the second half of the 19th century, the manufacturing of optical glasses of constant quality, enabled the spread of matured optical systems such as telescopes, microscopes, and photographic objectives into scientific, medical, and consumer applications [4]. About one hundred years later, the fabrication of opto-electronic image sensors by photolithographic techniques known from micro-electronics engineering and the development of precise molding of plastic lenses using high grade optical polymers have paved the way for the miniaturization of imaging systems [5]. Shrinking pixel sizes enabled the increase of resolution in image space while reducing the image sensor size and the fabrication of highly precise aspherical lenses led to the development of compact and cheap optical imaging systems. Hence, digital cameras are now an integral part of various electronic products such as laptops, tablet PCs, and mobile phones but also automotive safety systems, video endoscopes, and point-of-care diagnostics to name only a few.

At present, miniaturized digital imaging systems are rarely smaller than $4\,\mathrm{mm}^2$ in footprint size with a thickness of 3 mm at 1.75 µm pixel pitch. A further downscaling yields pixel sizes below the diffraction limit, and thus a reduced spatial resolution as well as increased noise. Although this might be tolerable in consumer digital cameras, the effect on the performance of subsequent image processing and analysis is not acceptable in machine vision, industrial inspection, and medical imaging. Additionally, technological limits apply such as tight mechanical tolerances which severely increase the costs for a hybrid integration of small lenses. Lower f-numbers are hard to achieve, so that the diffraction limit cannot be shifted, leading to insufficient performance with standard fabrication techniques [6, 7].

For a further miniaturization of optical imaging systems, it is worth looking at some of the fascinating approaches which have been present in the tiniest creatures in nature for millions of years. The evolutionary solution of choice is found in the vision systems of invertebrates - the compound eyes. Here, a large number of extremely small vision systems (called ommatidia) on a curved base capture the visual information of a large field of view (FOV) in parallel at the sacrifice of spatial resolution. Each ommatidium itself has a small diameter and a low information capacity when compared to the single aperture eye. However, due to the large number of channels, a high information capacity of the overall multi aperture objective can be achieved.

Since the dawn of digital image sensors, several technical derivatives of compound eyes

have been realized in order to miniaturize man-made vision systems [8–14]. However, since the major challenge for a technical adoption of natural compound eyes is the required precision of fabrication and assembly, none of these attempts has led to a successful technology, since macroscopic fabrication methods were exploited for the manufacturing of microoptical structures. First examples of a realization by well adapted microoptical technologies provided the thinnest known optical sensors which were promising even though the achieved resolution was not yet appropriate for technical applications [15–20].

The aim of this thesis is the investigation of the prospects of multi aperture imaging optics (*MAOs*) in a combination of opto-electronics, optics, and image processing. Therefore, promising design rules of natural compound eyes are studied and adopted for technical solutions. In contrast to prior work, where the size advantage is often obtained at the sacrifice of resolution, here, the highest degree of miniaturization should be achieved while maintaining optical system parameters (such as resolution and field of view) which are relevant for industrial applications. General principles of insect vision such as (1) simplification of the design, (2) spatial segmentation of the field of view, (3) spectral segmentation, and (4) overlap of the FOVs of adjacent optical channels are applied to yield new approaches to miniaturized vision systems with high resolution which overcome the basic scaling limits of single aperture imaging optics. A classification is provided that distinguishes the different state-of-the-art and novel approaches with respect to their working principle and application potential. The scaling behavior as well as new and faster methods for the simulation and optimization of MAOs are examined. The discussion is focused on optical systems which can be fabricated in parallel by highly precise microoptics technology based on wafer-level techniques. The analysis includes new methods for the characterization in order to investigate the potential and differences of the various demonstrated approaches.

Chapter 2 starts out with an overview of applications of small single aperture digital imaging systems followed by an introduction of the basic properties of the optical and opto-electronic components as well as image processing. The fundamentals of spatial resolution including the effects of diffraction and aberrations are discussed as both have to be considered for optical elements of the proposed scale. The sensitivity is studied at the example of a single aperture camera lens. The geometric fill factor and the pixel pitch of the image sensor are introduced in order to understand their effect on the spatial frequency transfer. The chapter closes with a discussion of the scaling limits of single aperture imaging systems and the reason why the miniaturization is accompanied by a reduction of the information capacity.

Chapter 3 deals with the working principles of natural compound eyes and introduces the state-of-the-art artificial compound eyes. It is distinguished between the *apposition compound eye* (*APCO*) as well as the neural superposition compound eye as an evolutionary approach to improve sensitivity. The superposition compound eye and an uncommon type of eye are briefly discussed together with their technical counterparts [14,21]. Subsequently, a novel classification is introduced which compares three different kinds of multi aperture imaging systems according to their segmentation of the FOV. In addition to the well-

known *apposition type* [9,15], the electronic, and optical stitching of segments are of central interest. The electronic stitching creates a digital image by the post-processed fusion of images of FOV segments that have been captured in separate optical channels, whereas the optical stitching of segments achieves a regular image of the object in the image plane prior to capture. A fourth principle - the multi aperture *Super-Resolution* - is added for completeness. It differs from the others as it uses no segmentation of the field.

In a following section of Chapter 3, the methodology of optical design and simulation is proposed. The design steps starting from a paraxial model, over analytical relationships to numerical simulations and optimization are discussed whereas the focus is set on specific characteristics of multi aperture optics. The paraxial 3x3 matrix formalism is introduced which is later applied to systems of the optical stitching type. A novel semi-automated approach for the system optimization and the simulation of optical cross talk are examined.

Chapters 4 and 5 are dedicated to the demonstration systems of two kinds of multi aperture optical imaging systems. Chapter 4 deals with the simulation, fabrication, and characterization of two MAOs with electronic stitching of segments. First, the *artificial neural superposition eye* (*ANSE*) is discussed which states an enhancement of the *APCO* with increased information capacity enabling increased sensitivity or color imaging. A second type, the *electronic cluster eye* (*eCLEY*), uses an overlap of the FOVs of adjacent optical channels with a sub-pixel displacement in order to increase the sampling in the object plane. Its potential for a high resolution makes it a promising candidate for miniature camera applications. Different examples with respect to size and resolution are investigated whereas two demonstrators have been realized using microoptical fabrication on wafer level. The software stitching is discussed together with the correction of distortion by image processing. Finally, the prospects of *eCLEYs* with respect to megapixel resolution are examined.

The demonstration systems for the optical stitching of segments are presented in Chapter 5. A first example is the *optical cluster eye* (*oCLEY*) which uses an array of focused microtelescopes with tilted optical axes in order to acquire a large FOV on small lateral sensor format. The scaling and stitching performance of such a system is analyzed and a prototype is presented. A special type of such a system with unity magnification is created using parallel optical axes of the channels. The so-called *ultra-thin array microscope* promises a resolution in the range of a few microns and cost-efficient fabrication on large optical format sizes so that parallelized imaging with high spatial resolution over an extended field is feasible. Finally, a microoptical counterpart of the natural *superposition compound eye* is designed and demonstrated. The 3x3 matrix formalism is used to yield the scaling behavior and trade-off of sensitivity and resolution for the *microoptical Gabor Superlens* ($\mu oGSL$). The sensitivity increase is examined by experimental characterizations.

The final Chapter 6 provides a conclusion of the presented work and a discussion of future tasks for the examination and practical realization of multi aperture optical imaging systems.

2 Fundamentals

Imaging systems and cameras of various sizes can be found in a large number of products nowadays. The main reasons for their widely spread use, are the breakthrough of opto-electronic image sensors, the miniaturization and the resulting reduction of fabrication costs. This chapter starts out with application examples for digital imaging systems which have an aperture stop diameter of less than five millimeters. The basic properties of the components of a state of the art miniature vision system are discussed. Finally, the aspects and limits of miniaturization are concluded from the investigation of the scaling laws of single aperture imaging optics.

2.1 Applications of Miniaturized Imaging Systems

The fields of application of small imaging optics are so widely spread that it is beyond the scope of this thesis to list all possible examples. Instead, relevant fields are mentioned together with some example applications.

Consumer electronics
A prominent example for miniaturized imaging optics are glass or plastic molded lenses which are sold in millions of pieces annually in pickup heads for optical data storage on CDs, DVDs etc. [22,23]. Plastic molding is also used for the fabrication of imaging lenses of optical navigation sensors in PC mice and optical finger navigation devices [24]. The same technology is applied to the more sophisticated objectives of miniature digital cameras which are becoming an integral part of virtually all portable information and communication devices like tablet PCs, laptop computers and mobile phones [6].

Bio-/ Medical imaging
Endoscopy is a classical field of application for miniaturized imaging optics. Especially flexible endoscopes suffer from low resolution and high costs due to the fiber bundles used for image transmission. Rigid systems achieve a better resolution, but the image transfer via fibers or gradient-index lenses makes them fragile and expensive too. The current development of chip-on-the-tip digital video endoscopes is promising because the complete miniature camera is integrated in the head of the device, creating a very small, flexible endoscope and yielding better stability at lower costs [25]. These efforts reach as far as to the so-called 'pill cam' - an encapsulated miniature endoscope that may be swallowed by the patient as a whole for remote controlled endosurgery [26].

Automotive
Modern cars already carry several imaging systems for a variety of purposes such as autonomous cruise control, lane departure support, head light assistance and parking

aid [27, 28]. There is an increasing number of safety applications in the interior like out-of-position detection or occupant monitoring. Weight, energy consumption and occupied space are important issues driving the miniaturization of the future optical sensor solutions for driver assistance.

Machine vision and robotics

Small imaging optics is applied for inspection e.g. of the interior of small hollow parts with video endoscopes [29], quality control of textiles or print material using CIS modules [30] as well as for safety systems like optical switches and light curtains in industrial fabrication environment. Civil applications of autonomous robotics are a demanding field for small and lightweight imaging systems especially for airborne platforms such as micro air vehicles (*MAVs*) [31, 32]. At present, tiny optical sensors are used for semi-autonomous functions such as altitude or speed control as well as obstacle avoidance [33].

What's next? - Applications of the near future

There is a growing need for non-stationary treatment in our aging society pushing point-of-care diagnostics [34]. Mobile and thus smaller versions of the lab-borne medical technology have to be developed and the miniaturization of imaging optics plays an important role e.g. for skin and blood analysis or high-throughput screening using fluorescence imaging. The field of soft robotics attempts to bridge the gap between human and machine [35] so that light-weight vision systems are necessary to enable autonomous robots to interact with humans in daily life. The application of microoptics in 3D imaging and display is already within reach [36]. First products using the fundamentals of integral imaging have been presented for both image acquisition and display [37, 38]. 3D image acquisition using small stereo vision cameras just entered the consumer market whereas the *plenoptic camera* is a promising candidate for 3D imaging from a single device which applies a combination of conventional lenses and microoptics to capture a 4D light field [39, 40]. At present stage, first available versions are used to increase the depth of field in industrial inspection [41].

2.2   Introduction to Digital Vision Systems

A digital vision system is able to create and record a sequence of two-dimensional images of a part of the three-dimensional environment by detecting light over a limited spectral range of the continuum of optical radiation. The complete imaging system is made of several basic components such as optics, image sensor, electronics and housing as well as signal processing hard- and software. The present scope shall be limited to devices which have a lens aperture diameter of less than five millimeters, as vision systems exist in various scales. Figure 2.1 shows a schematic sketch of the components of a state of the art miniature camera with plastic molded lenses.

Figure 2.1: (a) Components of a state of the art miniature camera showing a number of plastic molded lenses which are integrated inside a barrel. This is screwed into the lens mount which is subsequently attached to the printed circuit board (PCB, laminate substrate) with bonded CMOS image sensor. An IR cut-off filter glass is included in the lens mount [42]. (b) Photograph of plastic lens barrel and mount [42].

2.2.1   Objective Lens

After more than 170 years of history of the photographic lens, the properties, trade-offs and mathematical ways of calculating single aperture objective lenses are well understood [3,43–49]. The dawn of the digital image sensor generated the new driving force of miniaturization of camera systems because the costs of a digital camera directly scale with the size of the image sensor chip. Shrinking pixel size and advances in optics fabrication technologies enabled the increase of resolution in image space and the widely spread use of aspherical lenses which lead to the development of more compact optical systems.

Injection molding became the dominating fabrication technology for the millimeter scale lens fabrication in high volume due to its high quality manufacturing at low cost. However, with the ongoing miniaturization, the subsequent assembly and packaging costs severely increase for miniature camera lenses with diameters below 4 mm. The hybrid manufacturing and packaging techniques, which are standard for plastic molded lenses of larger diameters, lead to insufficient performance when considering the mechanical tolerances with respect to the larger image resolution which is demanded by the shrinking pixel size [6, 7]. Element thickness and surface decenter tolerances are the most critical issues but also the sensitivity of small lenses to scratches and contamination have significant effects on the production yield. In the recent past, *wafer-level optics* (WLO) evolved as an alternative fabrication technique from microoptics technology and it has been established for the fabrication of low-end camera modules with lenses of less than 3 mm in diameter [50, 51]. A major advantage over injection molding is that the fabrication of lenses and the integration with spacers to objectives is carried out on wafer level for thousands of lenses in parallel. Additionally, these processes are operated in cleanroom environment so that contamination can be limited. However, the adoption of UV-molding techniques from the world of microoptics poses several challenges for the replication of mm-scale lenses with large sags.

The accuracy of mold wafer mastering, material shrinkage and tight z-height tolerances for the whole objective are issues which put a strong limitation on the performance and yield of WLO cameras. To date, commercially available WLO solutions hardly achieve a resolution higher than VGA (640x480 pixels). One example of a recent miniature objective lens design for wafer-level optics technology is shown in Fig. 2.2a.

<div align="center">(a)   (b)</div>
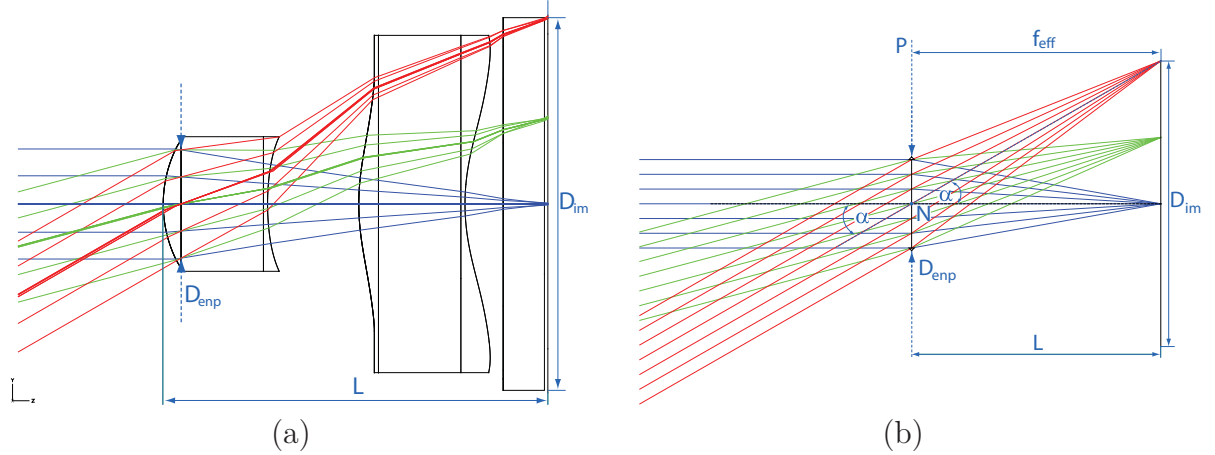
Figure 2.2: (a) Layout plot of a state of the art miniature lens design example which contains two convex-concave components with aspherical surfaces. The cover glass of the image sensor is placed in front of the image plane. Optical design courtesy of Dr. Frank C. Wippermann. (b) Thin lens or paraxial approximation of the lens from (a). Additional annotations show: the half angle of the full field of view α, the diameter of the entrance pupil D_{enp}, the total track length L of the lens, the effective focal length f_{eff} and the diameter of the image circle D_{im}. The major principal plane and the nodal point are denoted by P and N, respectively.

The effective focal length f_{eff} is the central parameter of an objective lens. With the aberration-free, thin lens approximation, it may be derived from Fig. 2.2b using the diagonal of the image sensor (D_{im}) and the half angle of the diagonal field of view (α, $n=1$ in object and image space):

$$f_{eff} = \frac{D_{im}}{2 \cdot \tan{(\alpha)}} \; . \tag{2.1}$$

The f-number in image space is calculated by [49]

$$F/\# = \frac{f_{eff}}{D_{enp}} \tag{2.2}$$

in the paraxial approximation and for an object at infinity. A list of the main geometric parameters of the example lens is given in Tab. 2.1.

In the following abstracts, the basic characteristics of an imaging lens will be summarized, in particular the resolution and sensitivity.

2.2.1.1   Resolution

A central figure of merit of an imaging system is the resolution or the ability to form distinguishable images of significantly close points in the lateral dimension of object space. The discussion is going to distinguish between *diffraction-limited* and *aberration-limited*

Table 2.1: Parameters of the single aperture imaging example system from Fig. 2.2a.

Property	Value
Sensor pixel pitch (p_{px}) [µm]	3.2
Image size [pixels]	640 x 480
Field of view (2α) (diagonal) [°]	60
F-number ($F/\#$)	3.0
Effective focal length (f_{eff}) [mm]	2.20
Total track length (L) [mm]	2.70
Diameter of entrance pupil (D_{enp}) [mm]	0.76
Diameter of image circle (D_{im}) [mm]	2.56

resolution. The term *diffraction-limited* means that, viewed from a ray-optical standpoint, the point image of a single in-focus object point is smaller than the diffraction blur which states the minimum physical spot size caused by diffraction at the finite aperture stop of the imaging system after a wave-optical model. In the *aberration-limited* case the image spot size of an in-focus object point is larger than the diffraction blur due to insufficiencies of the imaging optics. A general description of the resolution is provided by the *point spread function* of an imaging system.

Point spread function

The intensity distribution of a focused image E_{im} created by an imaging system with circular pupil under incoherent illumination can be described by a convolution of the geometric image E_{geo} and the intensity impulse response or *intensity point spread function (PSF)* $|h|^2$ of the optical system [52]. The geometric image is the object intensity distribution scaled with the magnification and *const* is a constant:

$$E_{im}(x,y) = const \cdot \int_{-\infty}^{\infty} \int_{-\infty}^{\infty} |h(x-u, y-v)|^2 \cdot E_{geo}(u,v) \ du \ dv \ . \qquad (2.3)$$

The coordinates $u = mh_x$ and $v = mh_y$ are coordinates in the object plane h_x, h_y scaled with the magnification m. In general, the PSF contains all considerable impulse response contributions such as diffraction and aberrations. If aberrations are neglectable, the size of an image point equals the *diffraction-limited PSF* which, for a lens with circular aperture, is given by [3, 52, 53]:

$$|h_{diff}(x,y)|^2 = \left[\frac{2 \cdot J_1\left(\frac{\pi}{\lambda \cdot F/\#} \cdot \sqrt{x^2 + y^2} \right)}{\frac{\pi}{\lambda \cdot F/\#} \cdot \sqrt{x^2 + y^2}} \right]^2 \ . \qquad (2.4)$$

Its shape is also known as the normalized *Airy diffraction pattern* or the squared modulus of the diffraction pattern of a circular aperture in Fraunhofer approximation for the wavelength of light λ (see Fig. 2.3a) [52]. The diameter of the center lobe is the *Airy diameter* which states the physical limit for the size of a single image point [3, 47, 49, 52]

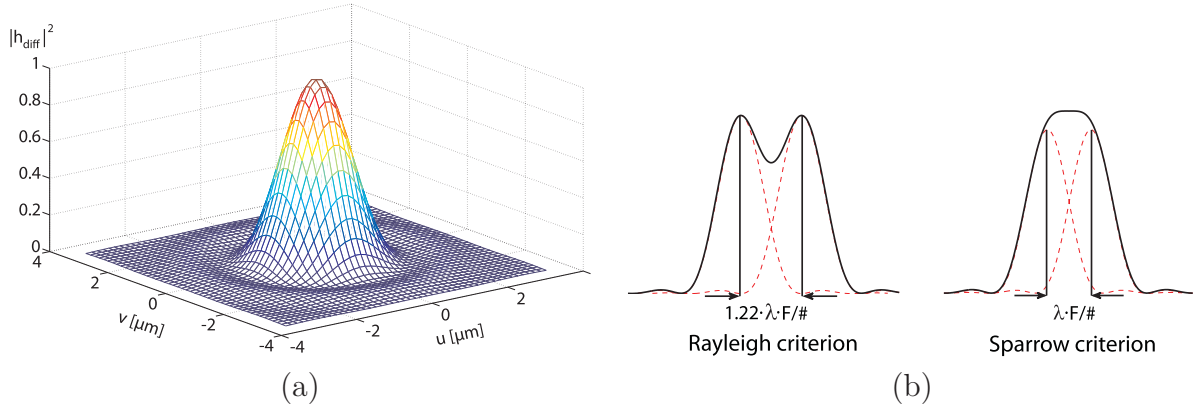$$d_{Airy} = 2.44 \cdot \lambda F/\# \ . \qquad (2.5)$$

Figure 2.3: (a) Normalized intensity distribution of the Airy diffraction pattern ($\lambda = 550$ nm, $F/\# = 3$). (b) The image intensity (black curve) of two adjacent incoherent point images (dashed curves) according to *Rayleigh* (left) and *Sparrow criterion* (right) for the resolution limit.

According to the *Sparrow criterion*, two image points have to be at least a distance of

$$\delta_{diff} = \lambda F/\# \tag{2.6}$$

apart to be resolved in a diffraction-limited imaging system (see Fig. 2.3b) [49]. The effective size of an image point A_p (sometimes referred to as 2D blur) may be approximated by the sum of the Gaussian moments of diffraction and transverse aberrations δ_a [54] which gives

$$A_p = (\delta_{diff})^2 + (\delta_a)^2 = (\lambda F/\#)^2 + (\delta_a)^2 \ . \tag{2.7}$$

Moreover, the smallest resolvable angle in object space $\Delta\delta$ results from the projection of Eq. (2.7) with the focal length:

$$\Delta\delta = \sqrt{\left(\frac{\lambda}{D}\right)^2 + \left(\frac{\delta_a}{f}\right)^2} \ . \tag{2.8}$$

The *space-bandwidth product (SBP)* which is defined as the number of resolvable image points over the image area A_I is an useful parameter for comparing imaging systems [54].

$$SBP = \frac{A_I}{(\lambda F/\#)^2 + (\delta_a)^2} \tag{2.9}$$

The SBP is also denoted as the spatial information capacity of an imaging system.

Optical Aberrations

In the practical case, imaging optics are rarely diffraction limited and the correction of aberrations plays a major role in the design and optimization process in order to achieve an adequate resolution and image quality. Specific aberrations can be studied in detail by applying a power series expansion to the wavefront as it propagates through an optical system. The optical path difference of the modeled wavefront with respect to a reference sphere gives the *wavefront aberrations* W (illustrated in Fig. 2.4). It can be expressed as a function of the radial field coordinate h, radial pupil coordinate r_n and the orientation angle in the pupil plane Θ in case of an optical system with rotational symmetry [53, 55].

For example, a series expansion up to the second order is used for a coordinate set that is invariant to rotation about the z-axis [55].

$$
\begin{aligned}
W\left(h^2; r_n^2; hr_n\cos(\Theta)\right) &\equiv W\left(h; r_n; \Theta\right) = \\
& a_{020}\cdot r_n^2 + a_{111}\cdot h\, r_n\cos(\Theta) + a_{040}\cdot r_n^4 + a_{131}\cdot h\, r_n^3\cos(\Theta) + \\
& a_{222}\cdot h^2 r_n^2\cos^2(\Theta) + a_{220}\cdot h^2 r_n^2 + a_{311}\cdot h^3 r_n\cos(\Theta) + W_{ho}
\end{aligned}
\tag{2.10}
$$

The aberration coefficients a_{ijk} are named according to their order i in h, j in r_n and k in $\cos(\Theta)$. By definition, the wavefront aberration W is zero in the center of the pupil so that the contributions for h^2, h^4 and constant terms have to vanish [55]. The term W_{ho} includes all non-zero wavefront aberrations of higher order.
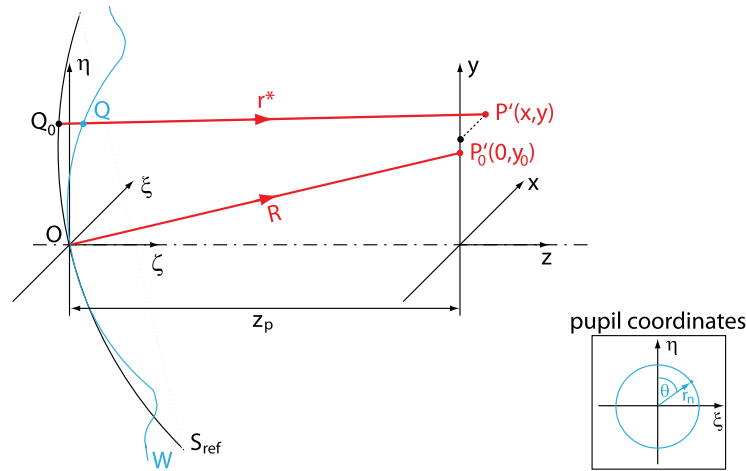

Figure 2.4: Visualization of wavefront and transverse ray aberrations. The coordinates ξ, η and x, y are defined in the (exit) pupil plane and image plane, respectively. The coordinates ζ and z are oriented towards the optical axis. The wavefront of the pencil from an object point P (not shown) is denoted by W and S_{ref} is the reference sphere centered in P_0' with a radius of curvature R. $\overline{OP_0'}$ is the chief ray from this object point. An arbitrary ray r^* from P meets the image plane at P' and its wavefront aberration is defined as the optical path difference $n\overline{Q_0Q}$ with n being the refractive index of the surrounding medium. The difference of W and S_{ref} for all points on the reference sphere gives the deformation of the wavefront from the ideal sphere or the wavefront aberrations $W(\xi, \eta)$ which can be expressed by cylindrical pupil coordinates (see inset on bottom right). The transverse ray aberrations are defined by the distance $\overline{P_0'P'}$ in the image plane. After [55].

A subsequent derivative of W yields the *transverse ray aberrations* [47,53,55]. Due to their impact, special attention is paid to the so-called *primary* or *Seidel aberrations* which result from the third order terms of the transverse ray aberrations in (hr_n).

Table A.1 in Appendix A demonstrates that all of the primary ray aberrations are of the structure:

$$
\delta_{primary} = const \cdot R \cdot h^i\, r_n^j \cos^k(\Theta)\;.
\tag{2.11}
$$

Here, R is the radius of curvature of the reference sphere. When using normalized coordinates for the field and pupil position Eq. (2.11) can be written as

$$
\delta_{primary} = const \cdot R \cdot h_{max}^i\, r_{ExP}^j\, \hat{h}^i\, \hat{r}_n^j \cos^k(\Theta)\;,
\tag{2.12}
$$

where $\hat{h}$ and $\hat{r}_n$ vary between 0 and 1 and h_{max} and r_{ExP} are the maximum field value and

radius of the exit pupil, respectively.

Distortion

Distortion is one of the serious aberrations for miniature imaging optics with wide field of view because it is often specified to a very low number (e.g. below 2 %). Additionally, it can drastically increase due to fabrication and assembly tolerances even if the theoretical distortion of the system is low [6]. The transverse ray aberration term of distortion is independent of the pupil coordinates (r_n, Θ) (see Tab. A.1 in Appendix A)

$$\delta_{distortion} = \frac{R}{n} \cdot a_{311} \cdot h^3 \ . \tag{2.13}$$

Hence, the effect of distortion is such that with growing field coordinate h, the position of the otherwise unaltered image point is increasingly displaced from its paraxial position. This could be described as a change of transverse magnification with field height. If $a_{311} < 0$ the distortion is of *barrel* type and if $a_{311} > 0$ of *pincushion* type [55]. Both are illustrated in Fig. 2.5.

barrel type   pincushion type
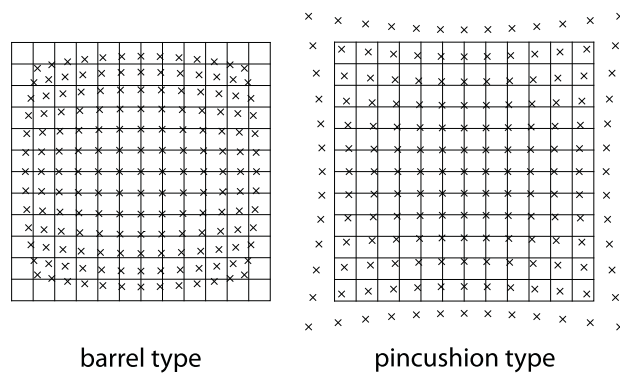
Figure 2.5: Real ray height (crosses) in comparison to the paraxial ray height (grid) in the image plane for barrel distortion (left) and pincushion distortion (right).

As the specific amount of an aberration reveals few about the resolution of an imaging system, another way of assessing the latter is introduced by analyzing the spatial frequency response of the system.

Modulation transfer function

The *modulation transfer function* (abbreviated *MTF*) is widely used for the characterization of the resolution of imaging optics because a complex optical setup can be summarized in a few diagrams of MTF curves, different systems can be compared by comparing their MTFs, and MTFs can be measured from images of test charts. The origin of the MTF as absolute value (or modulus) of the complex *optical transfer function* (*OTF*) of an imaging

system is derived from a normalized Fourier transform of the point spread function $|h|^2$ [52]

$$H(f_x, f_y) = \frac{\int\limits_{-\infty}^{\infty}\!\!\!\int |h(u,v)|^2 \exp\left[-2\pi\, i(f_x\, u + f_y\, v)\right] du\, dv}{\int\limits_{-\infty}^{\infty}\!\!\!\int |h(u,v)|^2 du\, dv} = \frac{F\left\{|h|^2\right\}}{F\left\{|h|^2\right\}\Big|_{f_x=f_y=0}} \quad. \tag{2.14}$$

The symbol $F\{\}$ denotes a 2D Fourier transform and the MTF is then given by

$$\widehat{H}(f_x, f_y) = |H(f_x, f_y)| \quad. \tag{2.15}$$

It describes the contrast in the image plane relative to the contrast in the object plane depending on the spatial frequency of the input modulation. Thus, it can be measured by determining the contrast K of a certain spatial frequency f_x from the minimum and maximum intensities E_{min} and E_{max} in the image

$$K(f_x) = \frac{E_{max}(f_x) - E_{min}(f_x)}{E_{max}(f_x) + E_{min}(f_x)} \quad, \tag{2.16}$$

and normalizing it to the contrast of the equivalent frequency component in the object plane [49]:

$$\widehat{H}(f_x) = \frac{K_{im}(f_x)}{K_{ob}(mf_x)} \quad. \tag{2.17}$$

For a given optical imaging system, the MTF generally varies with the position in the image plane (variation with field angle), with wavelength and also with orientation in the spatial frequency plane.

Optical Cut-off Frequency

The optical cut-off frequency ρ_0 indicates the spatial frequency at which the MTF vanishes and thus zero contrast is obtained in the image independent of the object contrast. The physical limit of the transfer of spatial frequencies by an optical imaging system is described by the diffraction-limited MTF. For a circular aperture it is defined by [49, 52]

$$\widehat{H}(\rho) = \frac{2}{\pi} \cdot \left[arccos\left(\frac{\rho}{\rho_0^{diff}}\right) - \frac{\rho}{\rho_0^{diff}} \cdot \sqrt{1 - \left(\frac{\rho}{\rho_0^{diff}}\right)^2} \right] \quad. \tag{2.18}$$

The spatial frequency ρ denotes a point in the frequency plane which is composed by the spatial frequencies f_x and f_y along the two dimensions

$$\rho = \sqrt{f_x^2 + f_y^2} \quad, \tag{2.19}$$

and the cut-off frequency ρ_0^{diff} of the diffraction limited system is linked to the physical properties of the lens such as the radius of the clear aperture $r_a = D_{enp}/2$, the wavelength of light λ and the axial position of image formation z_{im} which is equal to the focal length f in case of infinite object distance

$$\rho_0^{diff} = \frac{2 \cdot r_a}{\lambda \cdot z_{im}} \stackrel{z_{im}=f}{=} \frac{1}{\lambda \cdot F/\#} \quad. \tag{2.20}$$

In reality, imaging lenses hardly achieve a diffraction limited performance at full aperture

due to uncorrected aberrations, especially for larger angles of incidence, so that the MTF vanishes at a frequency considerably lower than ρ_0^{diff} (see Fig. 2.6a). The influence of certain aberrations on the MTF performance can be studied in [49, 52, 53]. Furthermore, different sources of noise in a digital imaging system cause a minimum detectable contrast level above zero, so that the image contrast vanishes even without a zero of the MTF at a certain frequency.

Depth of focus

The depth of focus is defined as the axial distance of defocus (δ_I) which is causing a blur diameter (b_I) under a certain tolerance threshold in the image space. It is closely related to the depth of field (δ_o) which is the axial distance in object space that is sharply imaged within this tolerance. With the transverse and longitudinal magnification denoted by m and $\widehat{m}$, respectively, it can be shown that [49]:

$$\delta_o = \frac{\delta_I}{\widehat{m}} = \frac{\delta_I}{m^2} \; . \tag{2.21}$$

The magnification can be determined for a given object distance s (negative) by

$$m = \frac{f}{s + f} \; . \tag{2.22}$$

For short focal lengths or large f-numbers the longitudinal diffraction blur is a good approximation for the depth of focus [49, 54, 56]:

$$\delta_I^{diff} = 4\lambda(F/\#)^2 \tag{2.23}$$

and with Eqs. (2.21) and (2.22) it follows for the depth of field caused by diffraction blur that

$$\delta_o^{diff} = \frac{4\lambda(F/\#)^2 \cdot (s+f)^2}{f^2} = 4\lambda(F/\#)^2 \cdot \left[\left(\frac{s}{f} \right)^2 + 2\frac{s}{f} + 1 \right] \; . \tag{2.24}$$

2.2.1.2   Sensitivity

The irradiance E_{im} that is received at an on-axis point of the image plane (image space in air) can be calculated from the radiance (radiant power per surface area element and steradian) B_{ob} emitted by the object surface by [45, 47, 56]

$$E_{im} = \pi\tau \cdot B_{ob} \cdot NA^2 \; . \tag{2.25}$$

It is assumed that the scene is created by extended light sources which can be described as Lambertian radiators and that the sources are in far distance with respect to the diameter of the entrance pupil. The *numerical aperture* is defined as $NA = n \cdot \sin(\beta)$ with the refractive index n of the space in consideration and the half cone angle β of light which enters the entrance pupil. For $NA < 0.174$ the f-number may be approximated well by [49]

$$F/\# \approx \frac{1}{2\,NA} \; . \tag{2.26}$$

Inserted into Eq. (2.25) this yields [15]

$$E_{im} = \pi\tau \cdot B_{ob} \cdot \frac{1}{4 \cdot (F/\#)^2} \quad . \tag{2.27}$$

The greatest degree of freedom for the manipulation of the sensitivity in Eq. (2.27) is given by the choice of an adequate f-number $(F/\#)$. Whereas τ - the transmission coefficient of the optical system - is mainly determined by the transmission and scattering properties of the lens material and additional coatings. On the other hand, the f-number is closely related to the resolution of a camera so that scaling sensitivity goes hand in hand with scaling resolution for a well corrected system.

The irradiance from a bundle of light that is captured on the image plane by an optical system depends also on the angle of incidence ϑ of that bundle in object space so that Eq. (2.27) has to be expanded to

$$E_{im}(\vartheta) = E_{im}(0) \cdot g(\vartheta) \quad , \tag{2.28}$$

whereas $E_{im}(0)$ is exactly given by Eq. (2.27). The so-called *relative illumination function* $g(\vartheta)$ describes the behavior with angle of incidence. In general, it is a rather complex function (see Fig. 2.6b) that depends mainly on the geometrical clipping of off-axis rays (vignetting). For a thin, aberration free lens the function can be described well by $g(\vartheta) = \cos^4 \vartheta$ [47, 49, 56].
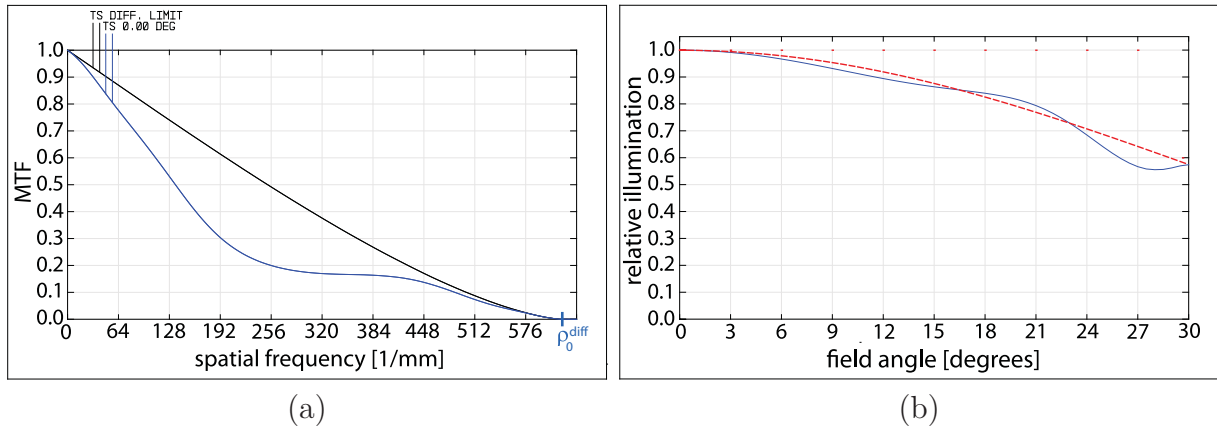
Figure 2.6: (a) A simulation of the monochromatic MTF of the lens from Fig. 2.2a for zero degree field angle (blue curve) in comparison to the diffraction limited performance (black curve). For both simulations a wavelength of $\lambda = 550$nm was used. (b) Simulated relative illumination in the image plane depending on the angle of incidence in object space of the example lens from Fig. 2.2a. The actual curve is shown as the solid blue line and a $g(\vartheta)$ that follows the $\cos^4$-law is shown as a dashed red line.

2.2.2 Image Sensor

The ongoing mainly cost-driven miniaturization of opto-electronic chips leads to a shrinkage of the light sensitive area of an image sensor and therefore a decrease of the sensor pixel size which in its smallest types is now approaching sub-micron scale.

Pixel Pitch, Resolution and Sampling

The name pixel is derived from "picture cell" and stands for the physical unit cell of an array of photodiodes which forms the light sensitive area of a CMOS or CCD image sensor (see Fig. 2.7a). Additionally, it is used to denote the virtual unit cell of a digital image. The pixel pitch p_{px} is the center distance of two adjacent pixels in the array. Usually, a squared distribution of pixels is used in a 2D image sensor. Especially for CMOS sensors, the pixel area $A_{px} = p_{px}^2$ is not necessarily equal to the size of the photosensitive area of the photodiode, $A_{ps} = d^2$, because additional read out electronics is integrated within each pixel. Hence, there is a certain pixel area which is insensitive to light [57]. The light sensitivity is proportional to the geometrical fill factor Φ_{IS}

$$\Phi_{IS} = \frac{A_{ps}}{A_{px}} \; . \tag{2.29}$$

In most CMOS sensors, a microlens array (*MLA*) is deployed in order to optically increase the fill factor. A microlens is formed directly on top of each individual pixel in one of the last fabrication steps so that incoming light is concentrated onto the photosensitive area of the pixel [58].

The finite pixel aperture size and the periodic sampling grid determine the spatial resolution of an image sensor. The spatial frequency response of a single photodiode gives the complex weighting factors for each spatial frequency component that can be recorded by the imager. Its modulus can be split in three components: (1) the so-called aperture MTF which is limited by the finite size and shape of the pixels, (2) the diffusion MTF which is caused by a diffusion of the photo-generated charge reducing its spatial confinement and, in CCDs, (3) a contribution which is due to the inefficient charge transfer in the shift register [57]. For large pixels, the dominant component is the aperture MTF. However, the diffusion component becomes considerable in case of small pixels, especially at longer wavelengths.

For simplicity, the case of a square pixel with an aperture width of d is assumed. The pixel aperture function can be described by

$$\widehat{P}_{px}(x, y) = \text{rect}\left(\frac{x}{d}\right) \cdot \text{rect}\left(\frac{y}{d}\right) \; . \tag{2.30}$$

The *rect-function* is defined as

$$\text{rect}(x) = \begin{cases} 1 & \text{if } |x| \leq 1/2 \\ 0 & \text{otherwise} \end{cases} \; . \tag{2.31}$$

The aperture MTF is the normalized modulus of the Fourier transform of $\widehat{P}_{px}$

$$\widehat{H}_{px}(f_x, f_y) = \frac{1}{d^2} \cdot \left|\frac{\sin(\pi d \cdot f_x)}{\pi f_x}\right| \cdot \left|\frac{\sin(\pi d \cdot f_y)}{\pi f_y}\right| \; , \tag{2.32}$$

which is a 2D sinc function [59]. An example section of the pixel aperture function and the related MTF are shown in Fig. 2.7b.
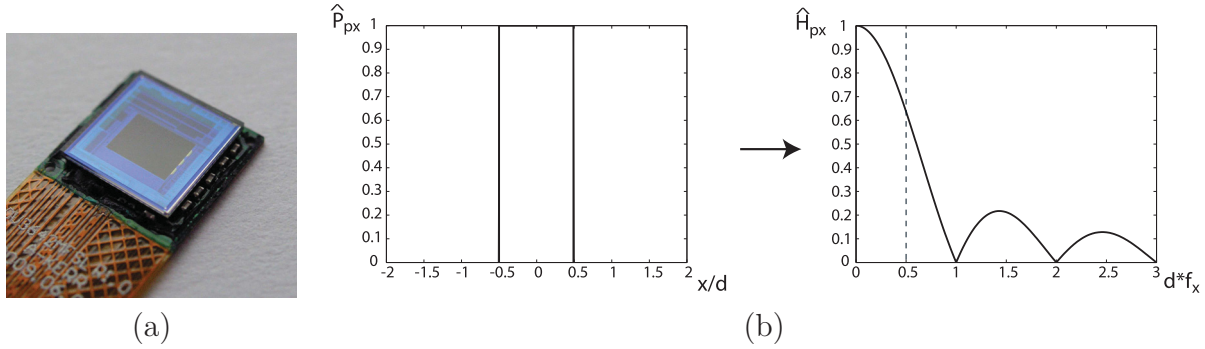
Figure 2.7: (a) Small CMOS image sensor (OmniVision OVT3642 3MP) with anti-reflection coated cover glass. The field of active pixels is visible as dark rectangle in the center. (b) Left: The rect-function as example for the pixel aperture function. Right: The related pixel aperture MTF. The dashed line indicates the Nyquist frequency (as defined below) for the case that the pixel aperture d matches the pixel pitch p_{px}.

Both the optics MTF $\widehat{H}_o$ and the pixel MTF $\widehat{H}_{px}$ have to be considered in order to calculate the total MTF of the image capturing process $\widehat{H}_{cap}$ by

$$\widehat{H}_{cap} = \widehat{H}_o \cdot \widehat{H}_{px} \; . \tag{2.33}$$

An example is shown in Fig. 2.8a. Other components such as filters can be added by multiplying the related MTFs with Eq. (2.33) [59].

The spatial distribution of pixels in the array with a pitch of p_{px} gives rise to a sampled digitization of the image that is created by the objective lens. Following the *Nyquist-Shannon sampling theorem*, a perfect reconstruction of the sampled image is possible only for frequency components that fulfill the condition [60]

$$f_{x,y} \leq \frac{f_{max}}{2} \; . \tag{2.34}$$

The upper frequency limit of that condition is called the *Nyquist frequency*. It is the half of the sampling frequency $f_{max} = 1/p_{px}$ of the image sensor in x and y direction :

$$\nu_{Ny} = \frac{f_{max}}{2} = \frac{1}{2p_{px}} \; . \tag{2.35}$$

The ideal theorem assumes a bandlimited signal which means that the signal frequency content should be perfectly zero for frequencies higher than the Nyquist frequency. The effect of *aliasing* occurs if this condition is not fulfilled [59]. Aliasing denotes the presence of false frequency content in a sampled image which has not originated from the signal and results in beat patterns with strong modulation at lower spatial frequencies. It is the result of the false reconstruction due to residual modulation beyond the Nyquist frequency (see Fig. 2.8b). The acquisition of bandlimited images is impossible in practice but aliasing can be mostly suppressed by e.g. a low pass filter, even though attenuation cannot be made perfect [59].
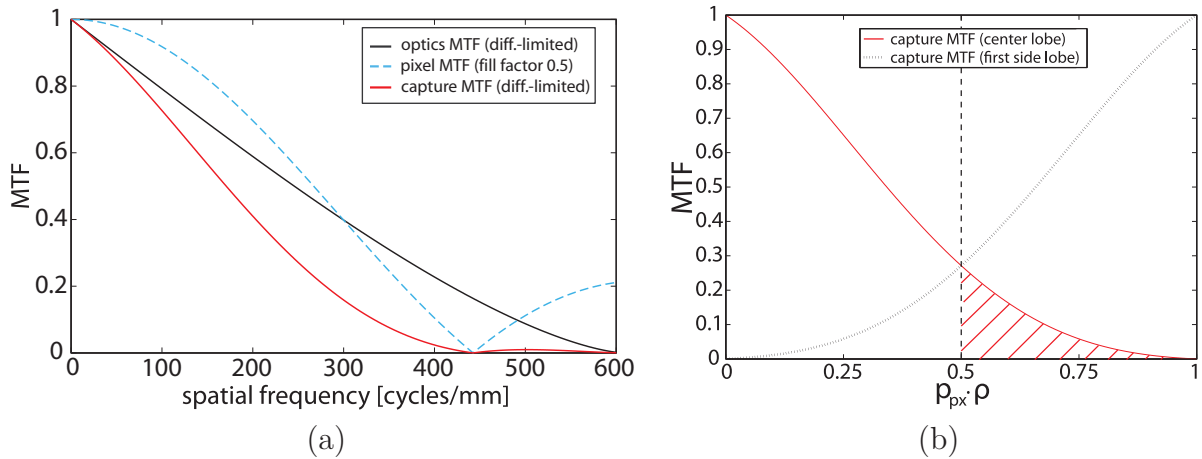
Figure 2.8: (a) Comparison of the MTF curves of the different system components. The capture MTF (red line) is formed by the multiplication of the optics MTF (black line) and the pixel aperture MTF (blue line). The diffraction-limited case is illustrated for the example system of Tab. 2.1. (b) The frequency components which contribute to aliasing during the sampling process are shown in the highlighted region where two sampling copies of the capture MTF overlap. The dashed line indicates the Nyquist frequency on the spatial frequency axis which is normalized to the sampling frequency $1/p_{px}$.

Color Imaging

For conventional digital color vision a spectrally, spatially or temporally split acquisition of the color signal has to be applied [58]. For example, a *color filter array (CFA)* which is integrated directly on the sensor pixels, the so-called Bayer mosaic [61], is most widely used (Fig. 2.9a).
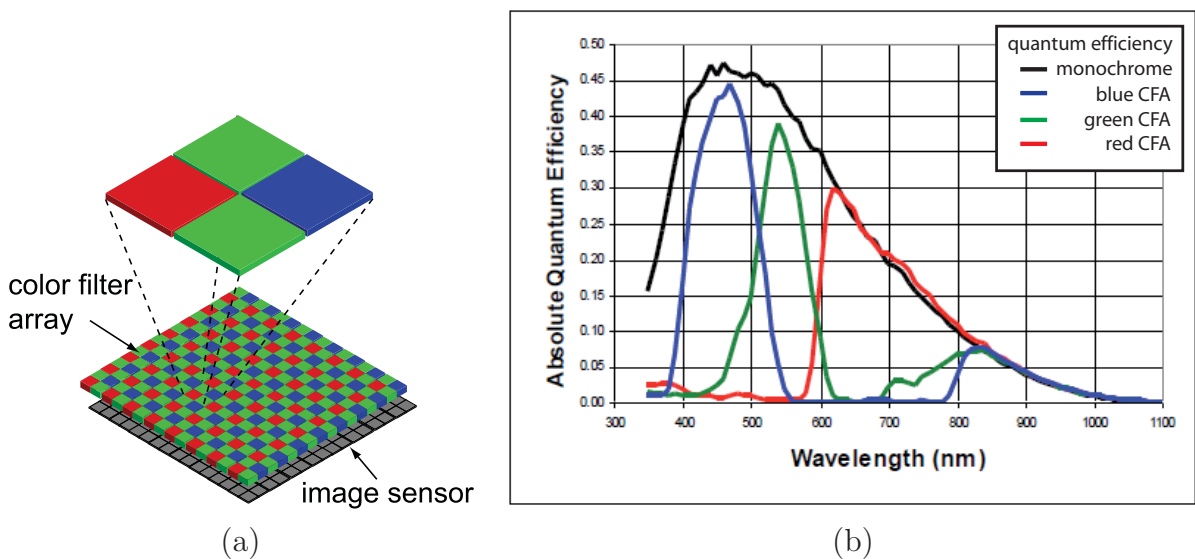
Figure 2.9: (a) Bayer color filter array on image sensor (adapted from [61]). (b) Absolute quantum efficiency as a function of wavelength for a CCD image sensor including the influence of fill factor enhancing microlenses and optional color filter array CFA (modified from [62]).

In order to reconstruct the highest possible resolution for the whole color image, sophisticated interpolation methods between the different single color images are used. Furthermore, color aliasing due to undersampling has to be suppressed at the expense of image sharpness [58,63]. These problems do not arise with a sensor which applies stacked photo-

diodes for the different spectral components in each pixel [64]. However, the complexity of such a pixel architecture increases the sensor costs and causes higher noise characteristics. Other methods like filter wheels, prisms and liquid crystal tunable filters will be excluded here because they are less suited for a miniaturized system due to size and costs.

Conversion Sensitivity and Noise

Besides the geometrical fill factor, other material and layer architectural parameters are important to determine the sensitivity of an imager. The spectral sensitivity (also called responsivity) R_λ is primarily specified by the quantum efficiency η_q or the number of generated electrons per incident photon [65, 66]:

$$R_\lambda = \frac{|e| \cdot \eta_q}{E_p} = \frac{|e| \cdot \eta_q \cdot \lambda}{h_P \cdot c} \ . \tag{2.36}$$

The other parameters are the fundamental charge e and the energy of an incident photon E_p. The Planck's constant and the speed of light are denoted by h_P and c, respectively. The spectral sensitivity (in [A/W]) links the photocurrent I_c which is generated in the collection region to the incident radiant power P_{in}

$$I_c = R_\lambda \cdot P_{in} \ . \tag{2.37}$$

In real detectors, η_q is a non-linear function of the wavelength due to several effects such as the wavelength dependancy of the photon absorption, the recombination of generated electrons after a limited lifetime and the absorption and reflection characteristics of any overlaying material such as color filters or passivation layers [65]. A typical quantum efficiency curve for a CCD sensor based on silicon is shown in Fig. 2.9b.

Together with the sensitivity, noise influences have to be considered in solid state image sensors. Noise sources can be categorized into temporal and spatial ones. In the temporal regime, CMOS image sensors are dominated by thermal noise (e.g. reset or kTC-noise, amplifier or read noise and dark current shot noise [67]) for low, and photon shot noise for high illumination conditions [68]. The latter states the ultimate limit to noise as it results from the statistic nature of the time delay between two photon hits on the photodiode. A shot noise of σ_{shot} is created for a mean number of generated electrons N_e during the time interval Δt according to a Poisson statistic [67]:

$$\sigma_{shot} = \sqrt{N_e} \quad \text{in [electrons]} \ . \tag{2.38}$$

In general, the different sources of thermal noise possess a nearly Gaussian probability distribution around the average signal [60].

In the spatial regime, pixels exhibit a non-uniform response to a homogeneously illuminated ('flat-field') scene (*fixed-pattern noise* or *FPN*). The reasons are twofold: Firstly, the difference in each pixel's sensitivity to light which causes an offset between the response curves of the individual pixels and secondly small differences of the gain factors [69]. This causes the *photoresponse non-uniformity (PRNU)* in case that a flat-field illumination is used and also a *dark signal non-uniformity (DSNU)* in total absence of a light stimulus

from the scene. The DSNU results from the local differences of the number of thermally excited electrons in each photodiode for a given temperature and integration time [67].

Signal-to-Noise Ratio and Frame Averaging
The output ($A_{i,k}$) of a single pixel with the indices i, k in the array can be described by a composition of the signal $S_{i,k}$, a temporal noise component $n_{i,k}$ (due to the thermal and shot noise) and a spatial noise component $o_{i,k}$ (due to the FPN):

$$A_{i,k} = S_{i,k} + n_{i,k} + o_{i,k} \; . \tag{2.39}$$

Here, $S_{i,k}$ is, for example, the photo current from Eq. (2.37). To simplify the problem, the assumption is made that $n_{i,k}$ and $o_{i,k}$ are independent of the signal and thus the photon shot noise is a small contribution to $n_{i,k}$ and may be neglected. The terms of Eq. (2.39) are fixed for a specific incident radiant power, gain and temperature, except the noise term ($n_{i,k}$) which is statistically Gaussian distributed. For the case of dominating thermal or dark current shot noise the value of $n_{i,k}$ is spread around its zero-mean according to the standard deviation σ. The *signal-to-noise ratio (SNR)* is then defined by

$$SNR = \frac{S}{\sigma} \; . \tag{2.40}$$

Gaussian distributed noise can be reduced by frame or signal averaging [60,67]. The average output pixel value is derived from the value of the pixel i, k from q different frames if the offset term $o_{i,k}$ is subtracted in each frame prior to averaging:

$$\widehat{A}_{i,k} = \frac{1}{q} \sum_{l=1}^{q} \left(S_{i,k}^{l} + n_{i,k}^{l} \right) \; . \tag{2.41}$$

The variance of the sum of all noise terms is equal to the sum of the individual variances [70] because the noise processes of the individual pixels are uncorrelated

$$\sigma^2 \left(\sum_{l=1}^{q} n_{i,k}^{l} \right) = \sum_{l=1}^{q} \sigma^2 \left(n_{i,k}^{l} \right) = q \cdot \sigma^2 \left(n_{i,k}^{1} \right) \; . \tag{2.42}$$

It is assumed that the variances of the individual pixels' noise processes are equal. It follows for the standard deviation of the sum of noise components σ_{tot} that

$$\sigma_{tot} = \sigma \left(\sum_{l=1}^{q} n_{i,k}^{l} \right) = \sqrt{q} \cdot \sigma \left(n_{i,k}^{1} \right) \; . \tag{2.43}$$

During summation the signal S increases proportional to q, whereas the standard deviation of noise σ_{tot} increases proportional to $\sqrt{q}$ which effectively leads to a SNR that is increased proportional to $\sqrt{q}$.

2.2.3   Image Processing

In contrast to former analog photography and video, digital imaging enables post-capture image processing by electronics or software which has gained an important role. The processing methods range from standards such as: interpolation between different color

planes of a captured raw image (*demosaicing*), application of color dependent gain curves for white balancing according to different lighting conditions or non-linear (e.g power-law) gray-level transformations in order to increase the apparent dynamic range (*gamma correction* [60]) to more elaborate ones like: the reduction of temporal noise, the application of a spatially dependent subtraction of reference data (FPN and shading correction) or spatial transformations and interpolations (correction of distortion and transverse chromatic aberrations [60]). For certain still photography applications even more complex algorithms are found, e.g. deblurring by deconvolution or extending the depth of focus by wavefront coding [60,71]. Especially in very small camera devices with low system complexity, extensive image processing can yield a largely improved image at low additional costs [7]. Basics about image interpolation as well as flat-field correction (FFC) are found in Appendix B.

2.3 Scaling Limits of Single Aperture Imaging Optics

The current section discusses the differences that result for conventional imaging optics of different scale. The effects of scaling on the properties of an imaging system that have been discussed in the previous sections will be studied. Therefore, two different ways of scaling are distinguished: (1) Scaling with constant f-number and (2) scaling with constant space-bandwidth product.

Scaling with constant f-number
The ratio between focal length and aperture stop diameter in Eq. (2.2) is kept constant in order to yield a constant f-number and constant FOV (2α) according to Eq. (2.1). The focal length, lens diameter and the image circle diameter are multiplied by the same factor M (Fig. 2.10b) which yields a linear scaling of the whole camera.

The primary ray aberrations scale linearly with the size of the optical imaging system in case of constant $F/\#$ which is derived in Appendix A. This conclusion is supported by numerical simulations which are shown in Fig. 2.11a.

With reduced size, the aberrations decrease, leading to a *diffraction-limited spot size* of Eq. (2.5) and a diffraction-limited MTF as shown in Fig. 2.12.

However, the Eqs. (2.20) and (2.5) indicate that scaling with constant f-number does neither influence the system's cut-off frequency nor the smallest possible spot size. Hence, the best possible image resolution is independent of scale [54]. In the diffraction-limited case, the number of resolvable image points (or the space-bandwidth product) decreases according to M^2 as the image diagonal is decreased. This can be interpreted as a reduction of the angular resolution and thus a scaling of the smallest resolvable angle according to $1/M$ [see $D \to MD$ and $\delta_a/f \to M\delta_a/Mf \to$ const. in Eq. (2.8)] because a larger patch of object space is imaged on the same image point.

According to Eq. (2.23), the depth of focus stays constant but it translates into a different depth of field, since δ_o^{diff} depends on $(s/f)^2$. The nominal object distance s is fixed by the
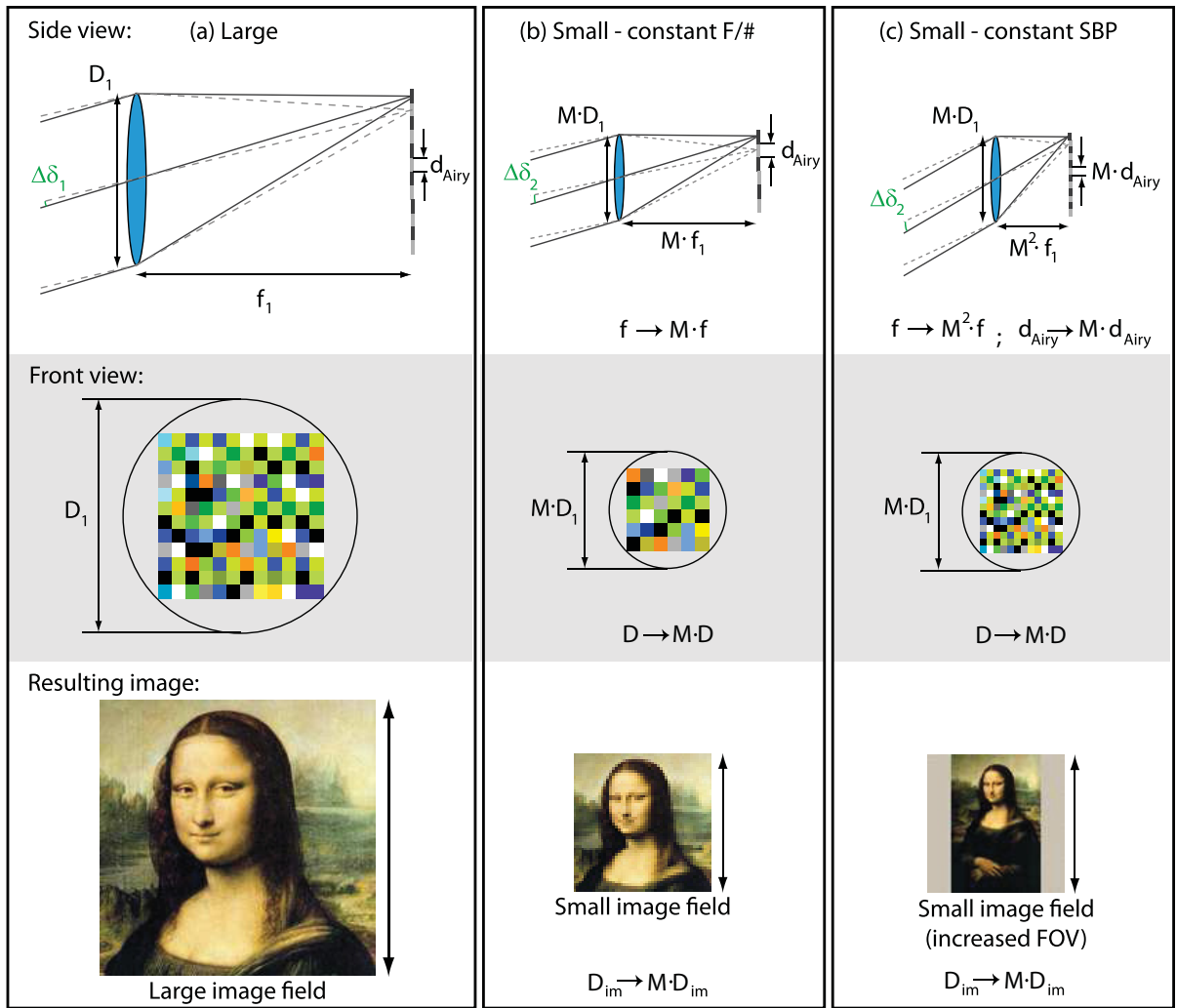
Figure 2.10: Scaling of a single aperture lens assuming diffraction-limited imaging. **(a) Large lens:** The size of one image point is proportional to $\lambda F/\#$. Due to the large focal length f_1, the angular projection of an image point into object space $\Delta\delta_1$ is small. The lens has a high angular resolution and a large space-bandwidth product (SBP) caused by the extension of the image circle and the small spot size d_{Airy}. **(b) Small lens with same F/#:** The size of one image point is the same as in (a). However, due to the shorter focal length, the angular projection of one spot $\Delta\delta_2$ is enlarged. Hence, the lens has a lower angular resolution and reduced SBP due to the smaller image circle. **(c) Small lens with same space-bandwidth product (SBP):** The spot size is decreased due to the reduction of the $F/\#$. The same angular resolution as in (b) results as the focal length is decreased with the size of one image point. Consequently, the information capacity in the image plane equals that of the large system but the information is gathered from a larger field of view with reduced angular resolution. (Adopted from [72].)

application which means that the depth of field grows indirect proportional to $(Mf)^2$ [Eq. (2.24)] even for small object distances (see Fig. 2.11b).
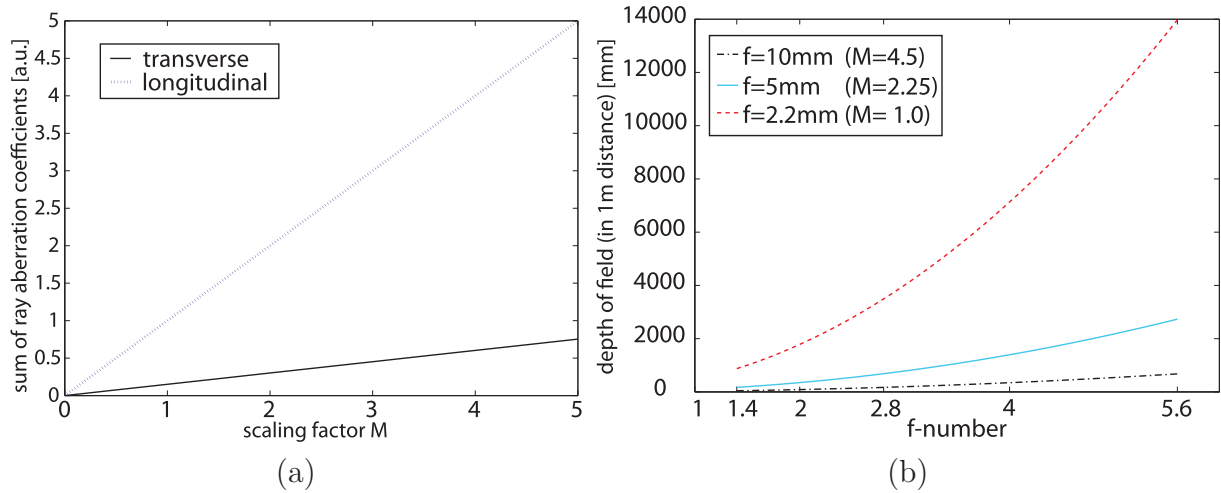
Figure 2.11: (a) The sum of transverse (black solid line) and longitudinal (blue dashed line) ray aberrations depending on the scaling factor M of an example objective with constant f-number. The sums include the following aberration coefficients: spherical aberration, tangential coma, astigmatism, field curvature, distortion, axial chromatic, lateral chromatic. (b) Scaling of the depth of field in one meter object distance for three different focal lengths depending on the f-number [according to Eq. (2.24)].
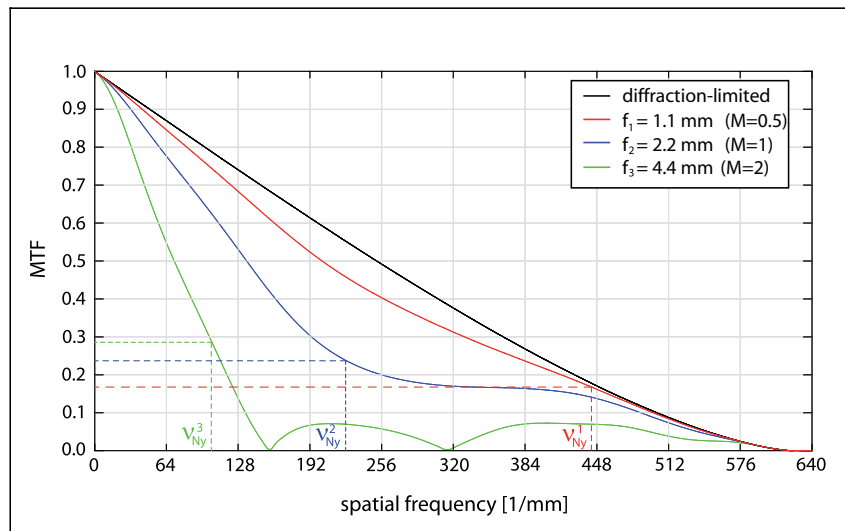
Figure 2.12: Monochromatic MTF ($\lambda = 550$ nm) in the image center simulated for three different scales of the objective lens of Fig. 2.2a with red curve $M_1 = 0.5$, blue curve $M_2 = 1$ and green curve $M_3 = 2$. The black curve shows the diffraction-limited MTF for $F/\# = 3.0$.

In case that the pixel size p_{px} is scaled together with the image circle diameter, the Nyquist frequency ν_{Ny} is shifted with respect to the diffraction-limited MTF which means that for smaller pixel size also the contrast at Nyquist frequency drops as shown in Fig. 2.12:

$$p_{px} \to M p_{px} \; ; \; \nu_{Ny} \to \nu_{Ny}/M \; . \tag{2.44}$$

For large values of M, the system is limited by undersampling and aliasing will occur. For small M, the optics MTF will vanish below the Nyquist frequency and the system is limited by optical blur. Thus, the information capacity of the image sensor pixel could not be exploited due to oversampling. Hence, downscaling by M does not strictly mean a scaling of the angular resolution by $1/M$ but the angular resolution will decrease additionally

according to the loss of contrast for the higher spatial frequencies that necessarily have to be transferred by the miniaturized system.

Influence of scaling on sensitivity

The sensitivity of the optical system can be maintained during scaling with constant f-number as long as the conditions for Eq. (2.27) are preserved. Even with an extremely decreased aperture stop diameter, the loss of angular resolution counterbalances that of sensitivity. Light that is imaged on a given image point is collected from a larger cone angle in object space [73].

The radiant power that is incident on one pixel in the image plane is calculated by multiplying Eq. (2.27) with the photosensitive area $A_{ps} = d^2$ of a squared pixel

$$P_{im} = \pi\tau \cdot B_{ob} \cdot \frac{d^2}{4 \cdot (F/\#)^2} \ .$$ (2.45)

If the pixel size is scaled by M, the number of photons and thus the radiant power in one pixel is scaled by M^2. The signal-to-noise ratio (SNR) of the image sensor decreases because noise and pixel crosstalk increase with shrinking pixel size [74]. Within certain assumptions, a minimum pixel size can be calculated from the specification of the SNR (see Appendix C). However, the smallest image sensor pixels migrate beyond this limit while noise is extensively treated by signal post processing.

Scaling with constant space-bandwidth product

In theory, there is another option which is the scaling of imaging systems with constant space-bandwidth product (SBP), illustrated in Fig. 2.10c. Here, the smallest resolvable image point A_P has to be scaled by M^2 in order to compensate for scaling down the image area A_I in Eq. (2.9). As the aberrations δ_a scale linearly with M, the f-number has to be changed by M which results in a scaling of the focal length f by M^2. Unfavorably, the scaling will alter the field of view ($\alpha \to \alpha/M$) due to the reduced focal length in Eq. (2.1). The miniaturized system could achieve the same space-bandwidth product as a large optical system, but it transfers a larger number of the same coarse object patches as in Fig. 2.10b. The angular resolution is also decreased in comparison to case (a) as a result of the scaling process. Furthermore, the maximization of the SBP by scaling up the FOV and decreasing the f-number is futile due to the dependancy on the aberrations (SBP $\propto 1/\delta_a^2$) which will increase with growing FOV and shrinking f-number according to Eq. (A.15) in Appendix A. Scaling down the f-number has several additional effects such as a reduced depth of focus, a shift of the diffraction-limited MTF and an increased sensitivity of the optical system. However, in reality, the fabrication of a small objective lens with low f-number and large FOV is a very challenging task as it asks for a series of very high precision surfaces with small radii of curvature, large sags and dramatically decreased tolerances. Thus, the application of scaling with constant SBP is very limited for current technological solutions.
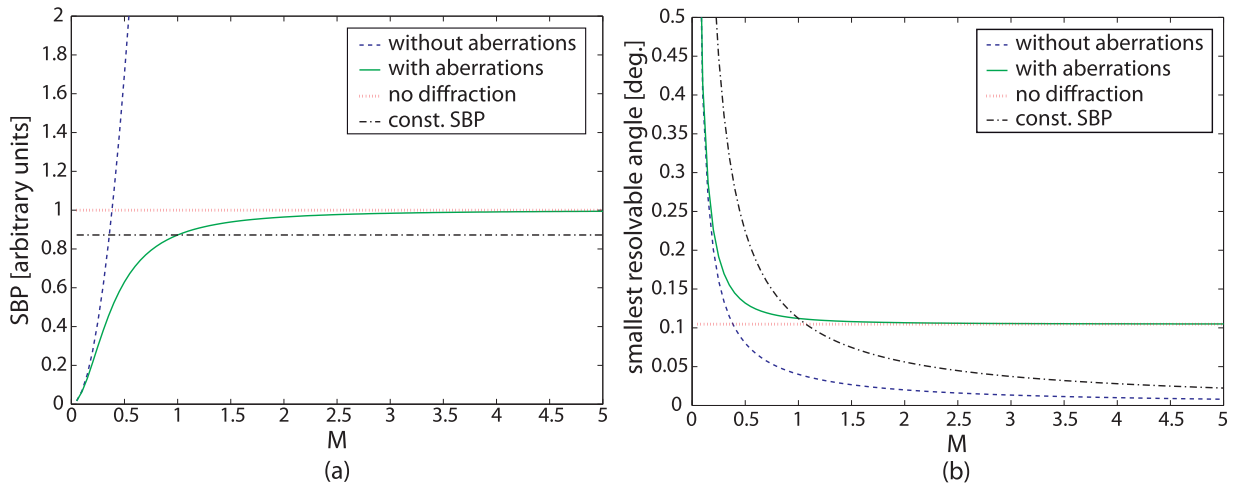
Figure 2.13: (a) Scaling behavior of space-bandwidth product SBP, according to Eq. (2.9), and (b) smallest resolvable angle, according to Eq. (2.8), with scaling factor M. Quantities are chosen according to Tab. 2.1. The blue, green and red dotted curves display scaling with constant f-number. The blue curves assume the absence of aberrations $\delta_a = 0$ (diffraction-limited). The green curves display the linear scaling of δ_a with M. These curves converge to the red dotted lines for large scaling factors M (scaling without diffraction). The black curves assume that both, the f-number and the aberrations, scale linearly with M so that the SBP is constant. Graph in (a) is modified from [54].

Summary of scaling of single aperture imaging optics

The graphs in Fig. 2.13a and (b) summarize the previous discussion by visualizing the qualitative behavior of the space-bandwidth product and angular resolution from Eqs. (2.9) and (2.8) with the scaling factor M. In conclusion, the miniaturization of a single aperture optical system has to be paid by a reduction of both the information capacity (or SBP) and the angular resolution when scaling with constant f-number and FOV. For a large optical imaging system ($M >> 1$), the SBP and the smallest resolvable angle approach constant values whereas the contribution of diffraction vanishes. The system is aberration-limited and any changes of the absolute values for the SBP and the angular resolution have to be achieved by increasing the system complexity (e.g. adding additional lens elements) in order to decrease the amount of aberrations. For the small scales ($M < 1$), the behavior of a diffraction-limited system is approached, with a decreasing SBP according to M^2 and a decreasing angular resolution according to $1/M$. Any point left of the blue curves (diffraction-limited case) in Fig. 2.13a and (b) is impossible to reach for the example system. The same applies for values larger than the red dotted line, in case of the SBP, and lower than the red dotted line, in case of the smallest resolvable angle. A scaling down with constant SBP requires a system with decreased f-number and larger FOV, which is impossible with respect to technological limits. A certain minimum system size is needed for both a high number of image details and a high angular resolution of a single aperture optical system [54].

3 Multi Aperture Imaging Systems

3.1 Natural Archetypes and State of the Art Technical Solutions

For the inspiration to the miniaturization of imaging systems, it is worth looking at some of the fascinating approaches which have been present in the tiniest creatures in nature for millions of years. The evolutionary solution of choice for the scaling problems of the preceding section is found in the vision systems of invertebrates - the compound eyes. Here, a large number of extremely small vision systems (called ommatidia) on a curved basis capture the visual information of a large field of view (FOV) in parallel. The use of multiple optical channels breaks the trade-off between focal length and the size of the FOV. Although each ommatidium exhibits a small FOV and thus a small information capacity, the sum of all ommatidia of the compound eye provides a large FOV and an information capacity that is large enough to enable accurate and fast navigation through the insect's habitat.

The multi aperture design suits to the fact that insects have an external skeleton but it is also well adapted to the weight and metabolic energy consumption of small invertebrates [1]. Compared to the single aperture eye, the arrangement of the ommatidia on a spherical shell is a major advantage which allows a very large field of view while the total volume of the eye remains small. Hence, the main volume of the head is still available for signal processing and other biological functions. Due to the very short focal length of each cornea lens, compound eyes have a large depth of focus and there is no need for a focusing mechanism. In nature, the lack of high angular resolution is often counterbalanced by high temporal sampling so that for instance the temporal sampling frequency of the vision system of a fly is about 250 Hz, nearly ten times faster than that of human vision [75]. In several species, zones of different resolution and additional functionalities, such as polarization sensitivity, hyperacuity or fast movement detection can be found [76–79].

Following the terminology found in literature, it will be distinguished between two major classes of compound eyes: (1) the apposition compound eyes and (2) the superposition compound eyes [1, 80, 81]. Additionally, a third uncommon class - the compound eyes of Strepsiptera - will be added to the discussion. Within the scope of this chapter a coarse overview of the different optical principles will be given and their main characteristics are going to be discussed.

3.1.1   Apposition Compound Eyes

The apposition compound eye evolved in day-active insects such as flies (Fig. 3.1a). It is one of the simplest forms of a compound eyes where a large number of microlenses are arranged on a curved basis with radius R_{EYE} (Fig. 3.1b) and each microlens is associated with a single photoreceptor in its focal plane [82]. One could find up to tens of thousands of these single microlens-receptor units which are commonly referred to as ommatidia. The intermediate space between adjacent ommatidia is filled with pigments that form opaque walls to prevent light from leaking out from one ommatidium into the next which would cause optical crosstalk [83].
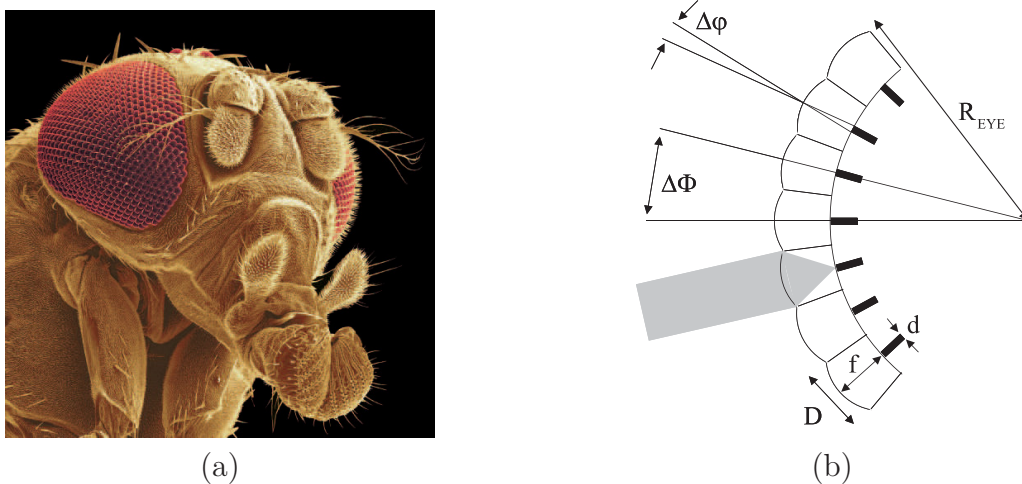

(a) (b)

Figure 3.1: Natural apposition compound eye. (a) Scanning electron microscope (SEM) image of the compound eye of a fruit fly (*Drosophila melanogaster*). Courtesy of Jürgen Berger, Max-Planck-Institut für Entwicklungsbiologie, Tübingen. (b) Working principle of a natural apposition compound eye [73].

Due to the curvature of the eye, the optical axis of each ommatidium points into a different direction so that nearly 360° of the visual surrounding is sampled by the interommatidial angle

$$\Delta\phi_{nat} \approx D/R_{EYE}. \tag{3.1}$$

Equation (3.1) gives the angular offset between the optical axes of two adjacent ommatidia with a microlens diameter D. The photoreceptor of each ommatidium accepts light from a finite angular interval centered on the corresponding optical axis [82,84]. The full width at half maximum ($FWHM$) of the angular sensitivity is the acceptance angle $\Delta\varphi_{nat}$. It can be considered as the most important parameter of a compound eye because it determines the trade-off between sensitivity and resolution. The acceptance angle has a geometrical contribution $\Delta\rho = d/f$ which is determined by the photoreceptor diameter d projected into the object space (via the focal length f). A second contribution λ/D originates from the diffraction at the microlens aperture for the wavelength λ. Provided that the photoreceptor diameter is approximately the same size as that of the diffraction spot of the cornea lens then their angular acceptances can each be described by a Gaussian function [82] and the

acceptance angle is [85, 86]:

$$\Delta\varphi_{nat} = \sqrt{\left(\frac{d}{f}\right)^2 + \left(\frac{\lambda}{D}\right)^2} \, . \tag{3.2}$$

A large $\Delta\varphi_{nat}$ means that each ommatidium collects light from a large angle. Therefore the sensitivity is high but the angular resolution is low and vice versa for a small acceptance angle. For that reason, the ommatidia must increase in both number and size in order to increase the total resolution [87]. This might be the reason why there are no large compound eyes found in nature [88].

Artificial apposition compound eyes

After opto-electronic image sensors became widely available, various technical approaches for compact vision systems exploited the principle of apposition compound eyes (APCO) [8–10, 31]. In contrast to the natural solution, most APCOs are planar configurations because the current image sensor technology is limited to planar substrates. The published solutions mainly suffered from inaccurate assembly because macroscopic fabrication technology was used and the individual arrays were composed bit by bit. The resulting resolutions were too low for any camera application. Later developments led to 3D microfabrication methods which yielded artificial compound eye optics on a spherical basis [18, 20, 89, 90]. However, the problem of recording the image from the curved image field remained unsolved in these approaches so far. The application of piezo-electric and thermal actuators were examined for the time-sequential increase of the sampling in object space [11, 91] or the expansion of the observed field size including a focus compensation [92]. Although, moving parts added a benefit to the system performance, the approaches lacked a considerable miniaturization due to the problem of integration with the optical components.

An example of a realized APCO which was manufactured with micro-technology consists of a planar microlens array (MLA) on a transparent substrate integrated on an opto-electronic sensor array [15, 16]. The thickness of the substrate is matched to the focal length of the individual microlenses f so that the detector pixels are located in the focal plane. A difference

$$\Delta p_K = p_L - p_K \tag{3.3}$$

between the pitch of the lenses p_L and the pixels p_K is used to achieve different viewing directions for the individual channels. Thus, each channel corresponds to one field angle in object space with the optical axis directed outwards (Fig. 3.2b), just like in the curved natural APCO.

Following the physiological definitions, the *interommatidial angle* is the angular offset between the optical axes of adjacent channels

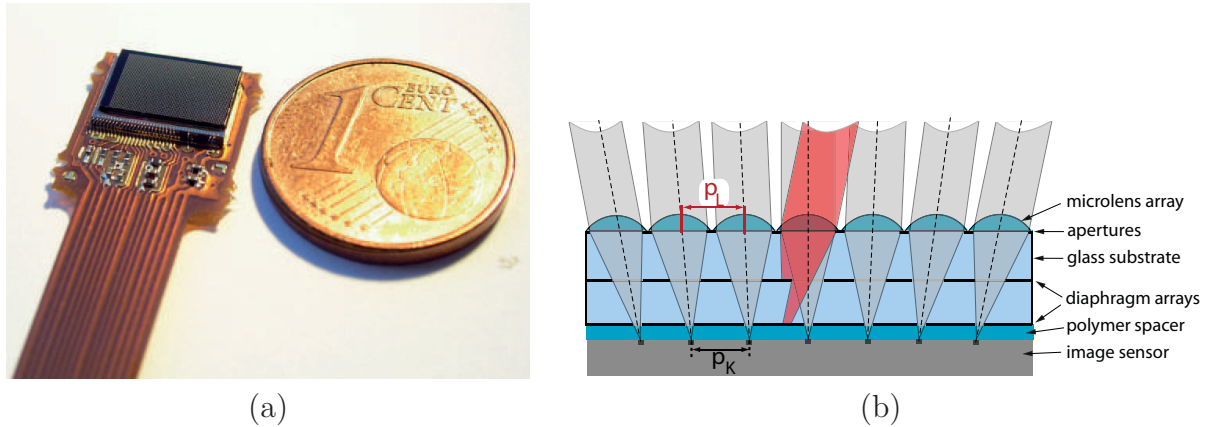$$\Delta\phi = \arctan\left(\frac{\Delta p_K}{f}\right) \, , \tag{3.4}$$

Figure 3.2: (a) Ultra-thin imaging sensor formed by an artificial apposition compound eye (APCO) attached to a customized CMOS image sensor on flexible printed circuit board [93]. (b) Schematic section of an APCO. The red colored ray bundle displays crosstalk that is suppressed by horizontal diaphragm arrays.

and the acceptance angle $\Delta\varphi$ can be approximated by Eq. (3.2) with d denoting the pixel diameter [73]. If required, the size of the sensor pixels can be narrowed down by a pinhole array on the substrate backside in order to increase the angular resolution $1/\Delta\varphi$ [15]. The angular position of contrast edges or point stimuli can be measured with an accuracy that is an order of magnitude higher than the coarse angular resolution which results for a short focal length [94,95]. Similar to hyperacuity in insect compound eyes [76,78], this is enabled by a controlled overlap between the acceptance angles of adjacent optical channels of an APCO.

Unlike the curved natural APCO, the planar microlens array suffers from aberrations under oblique angle of incidence which decreases the image resolution with increasing angle in the FOV. However, as each channel images only a small angular portion of the FOV, its lens parameters can be tuned according to the center viewing angle of the specific channel. Such a *chirped MLA* is formed by e.g. altering the radii of curvature in the main axes and the local pitch in order to correct for astigmatism, field curvature and distortion [96–98].

Another advantage of the APCO is the large depth of field. As a result of the short focal length of the microlenses and of the use of a single pixel per channel, the image remains sharp independently of the object distance [73].

A series of prototypes of microoptical APCOs was demonstrated based on the above principles [15, 16]. The latest system has been developed for an out-of-position detection in automotive applications is shown in Fig. 3.2a [93]. Its specifications are given in Table 3.1.

The pixel pitch p_{px} of the detector array has to be adapted to that of the microlenses p_L (typical 50...150 µm) while the photodiodes of each pixel should be small (2...10 µm) which is unusual for commercially available image sensors. For that reason, only a fraction of the whole number of pixels is illuminated and read out for standard image sensors of large size. Alternatively, a customized image sensor array can be used which additionally offers the possibility of implementing signal pre-processing within the periphery of each

Table 3.1: Selected parameters of the ultra-thin imaging sensor from Fig. 3.2a.

Parameter	Value
Number of channels	144 x 96
Total track length (L) [µm]	300
Field of view	85° x 51°
$F/\#$	4
Microlens diameter [µm]	50
Pixel size [µm]	3
Size of sensor head [mm^3]	10 x 10 x 1.2
2D fill factor [%]	0.34

pixel. In both cases, a large chip area is consumed by the APCO in order to achieve a certain image resolution. The low image resolution and the increased costs for the image sensor of adequate footprint size are the main problems of the APCO as far as commercial applications are concerned.

Neural superposition compound eye

In several species of flies, a special form of APCO can be found which has a set of photoreceptors in each ommatidium in contrast to a single one. Each object point is imaged by multiple photoreceptors from different ommatidia and the related signals are fused in the first synaptic layer of the eye (see Fig. 3.3a). The setup is known as the neural superposition type of an apposition compound eye [75]. This *redundant sampling* of the same part of the field of view enables an increased light sensitivity [99].
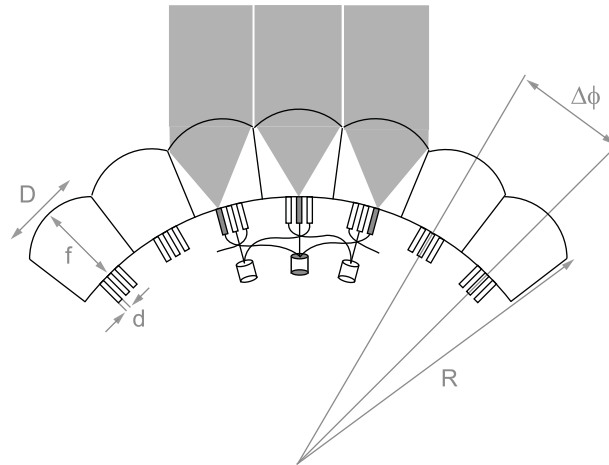
Figure 3.3: Working principle of the neural superposition eye of insects. The optical axes of different photoreceptors from adjacent ommatidia point on the same location of a distant object (inspired by [99]).

The main drawback of natural apposition compound eyes is a limited sensitivity which restricts the activity of those insects carrying them to daytime. Even though, the neural superposition type could expand activities into light conditions of dawn and dusk. Evolution came up with the second class of multi aperture vision systems – the superposition

compound eyes – which can be found in insects that are active at night or in low light habitats [1].

3.1.2   Superposition Compound Eyes

The superposition compound eye (Fig. 3.4) has primarily evolved in night-active insects and deep water crustaceans. Contrasting to the apposition type, the light that is focused by multiple neighboring lenses combines on the retina to form a single real image of the environment [1]. The decisive advantage of superposition compound eyes is that they are much more light sensitive because light bundles from one object point traveling through several adjacent ommatidia are deflected towards a common image point (Fig. 3.4b). In that way the effective light collecting aperture stop D_{eff} is increased to a size which is several times larger than the diameter of a single lenslet. This optical performance is not the result of a single microlens per ommatidium but of two axially aligned microlenses that form a micro-telescope setup [100]. Eyes with very low effective f-numbers ($F/\#$) can be found in nature. However, the resolution is below the diffraction limit due to the blur that is caused by the imperfect combination of light beams from several ommatidia [101, 102]. When comparing apposition with superposition eyes, it is evident that the clear zone that is needed for the fusion of light bundles leads to a larger volume in case of superposition compound eyes - a price that has to be paid for the higher sensitivity.

<center>(a)   (b)</center>
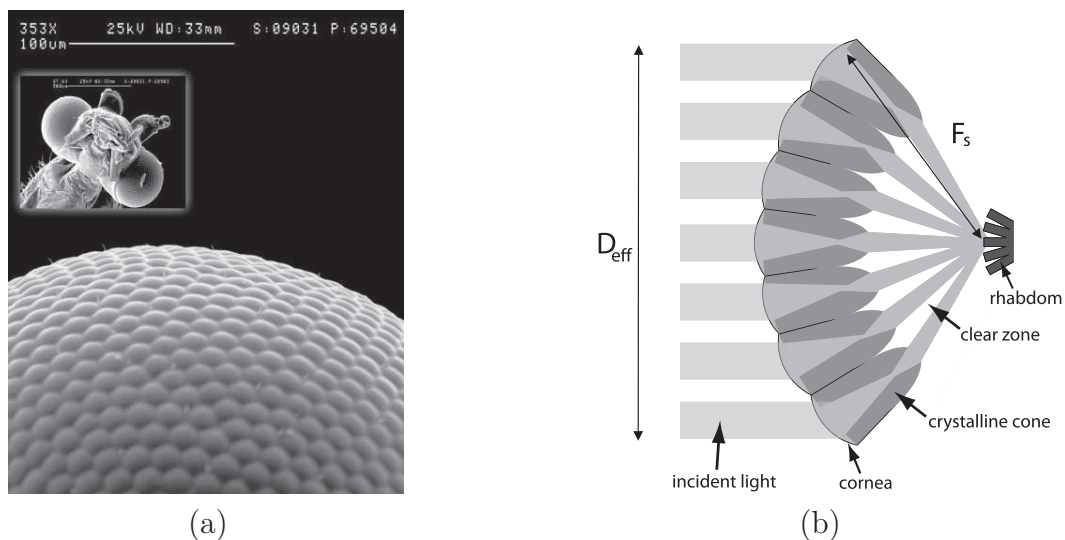
Figure 3.4: Natural superposition compound eye. (a) SEM image of the head and eye section of the moth *Ephestia kuehniella* (Courtesy of Tina Clausnitzer, [73]). (b) Schematic cross section of a natural superposition compound eye [19].

Artificial superposition compound eyes - Gabor Superlens

The basic scheme of an artificial superposition compound eye has been published by Dennis Gabor in 1940 [103]. A related patent claims a stack of two lens arrays with slightly different pitch axially separated by the sum of their focal lengths which would act like a conventional

lens of larger thickness (Fig. 3.5a). The difference between the pitch of the first lens array p_1 and the second p_2

$$\Delta p_{GSL} = p_1 - p_2 \tag{3.5}$$

leads to a back focal length F_s of the stack given by [21]:

$$F_s = \frac{f_2 \cdot p_1}{\Delta p_{GSL}} \; . \tag{3.6}$$

Even if the focal length of the second lens array f_2 is small, the focal length of a larger lens can be created by choosing the pitch difference Δp_{GSL} accordingly. Such a setup became known as the *'Gabor Superlens'* when it was experimentally demonstrated for the first time, more than fifty years after Gabor's patent [21, 104]. However, with a total track length of about 65 mm, a FOV of 10 degrees and a resolution of 2 line pairs/mm, this example was neither small nor suitable for an application, yet.
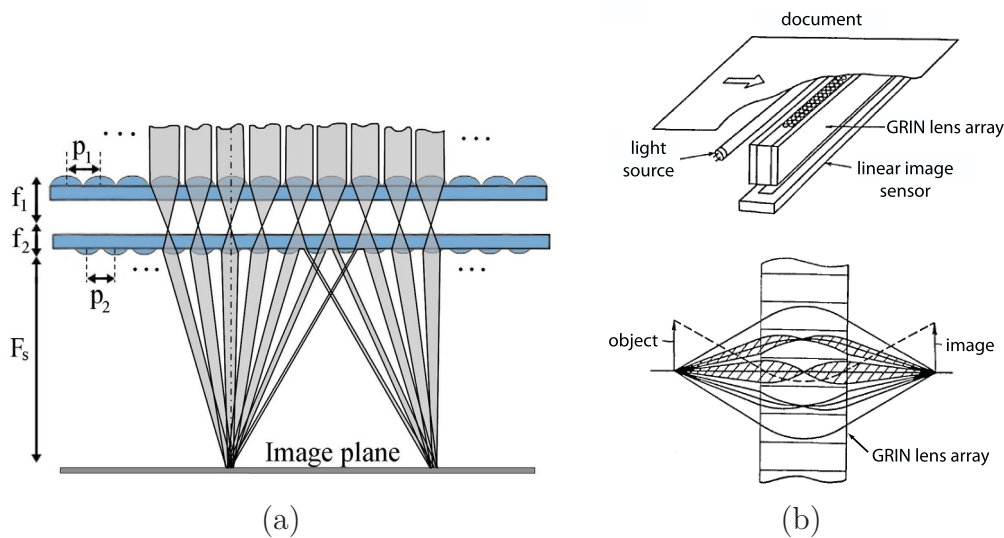

Figure 3.5: (a) Working principle of a Gabor Superlens (after [21]). (b) Top: Application of gradient-index (GRIN) lens arrays in facsimile [105]. Bottom: Image formation through a GRIN lens array [106].

Arrays of gradient-index (GRIN) lenses in a two or three row configuration such as found in photo-copying machines and flat-bed scanners can be regarded as a special case of an artificial superposition compound eye with unity magnification [106, 107]. Each lens forms an erect image, which superposes with the images of neighboring channels (Fig. 3.5b). This is achieved by a symmetric setup of lens arrays without pitch difference. The 2D image is generated by scanning the lines perpendicular to the orientation of the array. Similar optics is found in contact image sensor (CIS) modules that are widely used in industrial inspection [30]. Either the imaging system or the object has to be moved which causes a rather large setup with mechanically limited resolution. Also non-scanning, multi aperture optics with unity magnification have been reported [108] which principally overcome the scanning limitations by introducing 2D lens arrays for optical recording on photographic film [109] or with application in projection mask lithography [110, 111]. However, these have not yet been applied to obtain a compact digital imaging system.

3.1.3   Compound Eyes of Strepsiptera

Another type of compound eye is shown in Fig. 3.6a. It is the eye of a wasp parasite called *Xenos peckii* which belongs to the *Strepsiptera*. It has been reported that males of *Xenos peckii* have a particular kind of compound eye with only few but very large cornea lenses [112]. It reveals an extended retina at the image plane of each cornea lens and a photoreceptor bundle that is rotated by 180° on its way into the lamina due to the inverted image which is formed in each eyelet. Further anatomical features hint at a cross corre- lation between individual retina blocks of adjacent eyelets in order to improve its spatial resolution (see Fig. 3.6b). A similar structure has been found in the eyes of schizochroal trilobites [113]. Although other physiologists are still in doubt about whether the eye of *Xenos peckii* is an evolutionary optimum or an intermediate state [114], it offers some in- teresting features for technical counterparts.
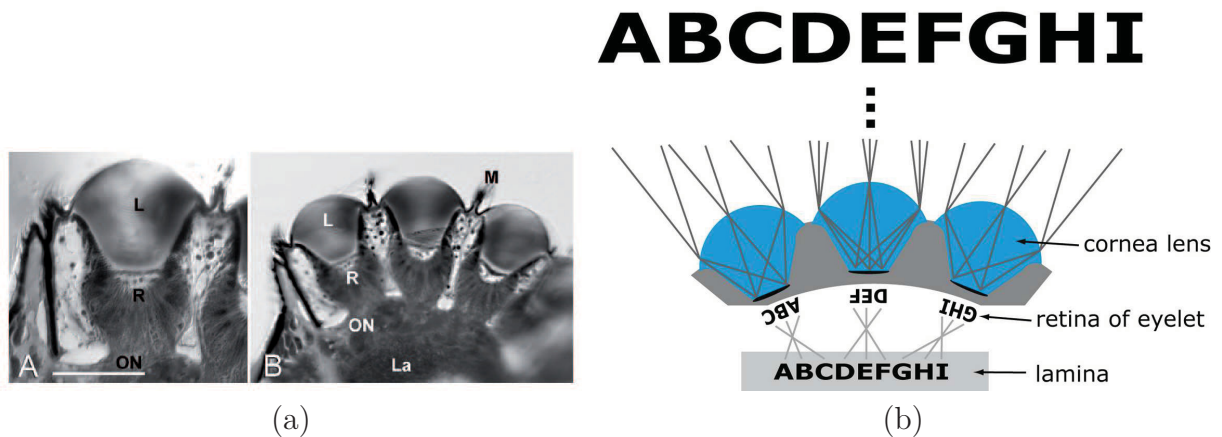

Figure 3.6: (a) Cross sections of one (A) and several (B) eyelets of *Xenos peckii*. Each consists of a large lens (L) and an extended retina (R) that has about 100 receptor cells. The lamina is denoted by (La). Scale bar is 50 µm [115]. (b) Schematic working principle of the compound eye of *Xenos peckii* (after [112]). Different extended parts of the object space (illustrated by letter sequence) are imaged onto the retina of each individual eyelet. The signals of each retina are rotated in the first neural layers. Finally, the partial images are linked up to a real image of the object space in the lamina.

Artificial compound eye of Xenos peckii type

Recently, an artificial compound eye has been published which follows the idea of the eye of *Xenos peckii* in a way that a part of the FOV is recorded in each individual channel and image processing is used to fuse the different partial images to an overall image of the whole FOV [14]. Its purpose is to create a compact imaging system for an application in the infrared spectral range. For the sake of a high optical fill factor and ghost light suppression, a stack of several microlenses was used (Fig. 3.7). Additionally, a prism array is applied for increasing the FOV to 30°. This compromises the compactness of the device (total track length is 24.8 mm) and its light sensitivity ($F/\# = 8$).
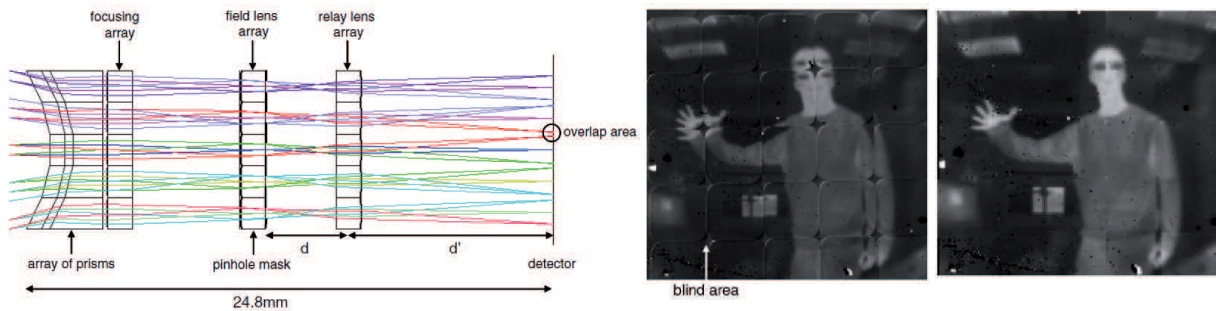
Figure 3.7: **Left:** Optical design layout of the infrared MULTICAM from [14]. **Middle:** Acquired images of 5x5 optical channels [14]. **Right:** Final image of the whole FOV after image processing [14].

It can be concluded that to date only few multi aperture imaging systems found a successful way into technical application. The reason is that most of the published examples are of mm-scale and have been fabricated with conventional macroscopic technologies so that assembly misalignments become critical when placing the optical channels beside each other. Additionally, most systems lack a considerable miniaturization. Microoptical technologies, instead, are promising for the fabrication of artificial compound eyes with a large number of channels. Fabrication and assembly technologies with high lateral precision in sub-micron range lead to compact imaging devices at applicable production costs because a large number of systems can be manufactured in parallel processes on wafer level. The prototype examples of Chap. 4 and 5 follow this approach.

3.2   Classification of Multi Aperture Imaging Systems

3.2.1   Basic Parameters of Multi Aperture Imaging Optics (MAO)

In order to formulate a general description of planar multi aperture optical imaging systems (MAO), it is noted that every parameter which applies for a whole single aperture optical imaging system (SAO) is applicable for each individual channel of the MAO. However, beyond the parameters of Sec. 2.2, there are additional ones that are special to multi aperture setups and will be explained in the following.

Basic geometric parameters
A multi aperture optical system is structured into a two-dimensional array of K_x times K_y individual optical channels. An optical channel is defined as the axial assemblage of at least one aperture stop together with at least one focusing element (e.g. a lens) and a spacer for the related propagation length to the image plane. Each channel is associated with a two-dimensional partial image of $n_x \times n_y$ pixels. In case of a square partial image, the number of pixels is $n_x = n_y = n_g$. The physical edge length of the square partial image is

$$I_p = n_g \cdot p_{px} \; . \tag{3.7}$$

The number of pixels in the final image is defined by N_x and N_y along the x- and y-direction. This corresponds directly to the number of object sampling intervals (see Fig. 3.8a). Thus, the number of optical channels (in x and y) is related to the ratio of the total pixel number and the number of pixels per partial image using

$$K_{x,y} = \frac{N_{x,y}}{n_{x,y}} \ . \tag{3.8}$$

For simplicity, it is assumed that the $K_x \times K_y$ partial images are arranged in a regular Cartesian array with equal pitch p_K along the x and y direction (see Fig. 3.8b). Hence, an 1D optical fill factor Γ in the image plane is defined as

$$\Gamma = \frac{I_p}{p_K} \ . \tag{3.9}$$

The 2D optical fill factor is given by Γ^2 in case of quadratic partial images in a square array lattice.
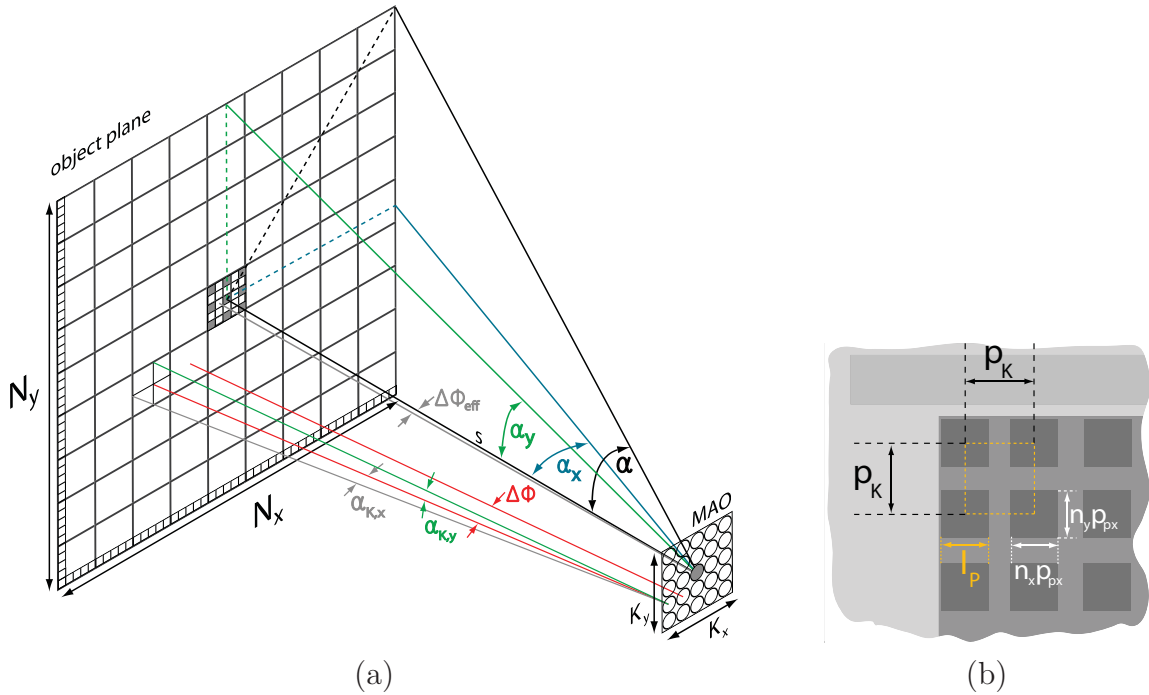
Figure 3.8: (a) Visualization of the basic parameters which characterize the FOV of multi aperture optics (MAO). (b) Schematic overview of basic parameters in the image plane of multi aperture optical systems.

Field of view

In most cases, the diagonal field of view (2α) is determined by the application. From rectangular triangles and trigonometric relations one relates α to the half cone angles of the FOV along the horizontal and vertical direction α_x and α_y:

$$\tan^2 \alpha = \tan^2 \alpha_x + \tan^2 \alpha_y \ , \tag{3.10}$$

and the ratio of the horizontal to the vertical edge length of the image is found using:

$$\frac{\tan \alpha_x}{\tan \alpha_y} = \frac{N_x}{N_y} \ . \tag{3.11}$$

The half angles of the horizontal and vertical FOV may be calculated using Eq. (3.10) and (3.11) according to:

$$\alpha_x = \arctan \left[\frac{\tan(\alpha)}{\sqrt{1 + \left(\frac{N_y}{N_x}\right)^2}} \right] ; \ \alpha_y = \arctan \left[\frac{\tan(\alpha)}{\sqrt{1 + \left(\frac{N_x}{N_y}\right)^2}} \right] \ . \tag{3.12}$$

The half angles of the field of view for a single optical channel in x,y are

$$\alpha_{K,x} = \arctan \left(\frac{n_x \cdot p_{px}}{2f} \right) ; \ \alpha_{K,y} = \arctan \left(\frac{n_y \cdot p_{px}}{2f} \right) , \tag{3.13}$$

which reduces to a symmetric FOV per channel in case of a square partial image.

Sampling angle

The interommatidial angle which is defined by Eq. (3.4) gives the offset between the central viewing directions of adjacent optical channels. Two different sampling angles are defined in addition to that: The interpixel angle $\Delta\phi_{px}$ which is the offset angle between two adjacent pixels of a single channel when projected in object space

$$\Delta\phi_{px} = \arctan \left(\frac{p_{px}}{f} \right) \ , \tag{3.14}$$

and the effective sampling angle

$$\Delta\phi_{eff} = \arctan \left(\frac{\Delta p_{eff}}{f} \right) \ , \tag{3.15}$$

which is the smallest angular sampling interval in object space. It could be created by the effect of a pair of different optical channels with an effective pitch difference of Δp_{eff} which is discussed in more detail in Sec. 3.2.2.2.

The total number of sampling points is limited by the number of pixels in the final image and the effective sampling angles in x and y can be alternatively calculated for an equidistant sampling of the FOV:

$$\Delta\phi_{eff,x} = \arctan \left(\frac{\tan \alpha_x}{N_x/2} \right) ; \ \Delta\phi_{eff,y} = \arctan \left(\frac{\tan \alpha_y}{N_y/2} \right) . \tag{3.16}$$

Interchannel distortion

When imaging a planar object onto a planar image surface, an equidistant sampling in angular space leads to a non-equidistant sampling on the object plane (see Fig. 3.9 left side) and thus a distorted image. However, the viewing direction of the individual channels in a multi aperture system can be chosen arbitrarily. Hence, they can be arranged in a way that a regular grid on a planar object surface is formed (see Fig. 3.9 right). This is achieved, if the viewing angle ϑ_r of the channel with indices $(i; j)$ along the horizontal and

vertical dimension in the array follows the equation [98]:

$$\vartheta_r = \arctan\left(\tan\left(\alpha\right) \cdot \frac{\sqrt{(i)^2 + (j)^2}}{\sqrt{\left(\frac{K_x - 1}{2}\right)^2 + \left(\frac{K_y - 1}{2}\right)^2}}\right) \tag{3.17}$$

or for a separate calculation along the x,y direction:

$$\begin{pmatrix} \tan\vartheta_x \\ \tan\vartheta_y \end{pmatrix} = \frac{\tan\left(\alpha\right)}{\sqrt{\left(\frac{K_x - 1}{2}\right)^2 + \left(\frac{K_y - 1}{2}\right)^2}} \cdot \begin{pmatrix} i \\ j \end{pmatrix}. \tag{3.18}$$

The numbers of channels K_x and K_y are assumed to be odd without loss of generality and $i, j \in [0; (K_{x,y} - 1)/2]$.
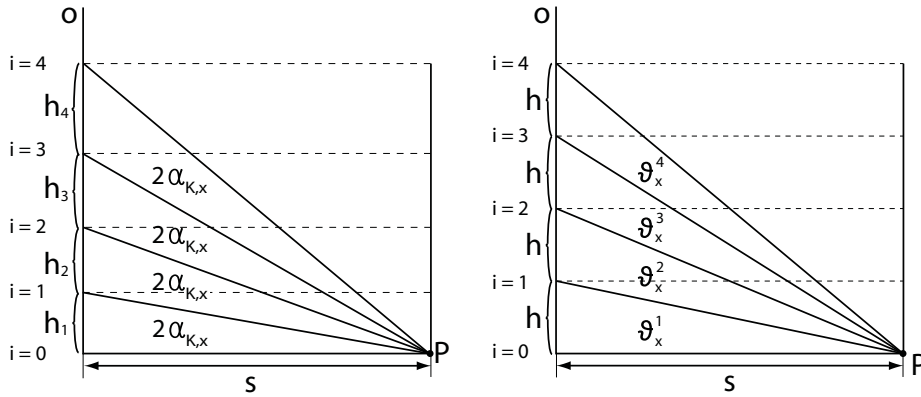
Figure 3.9: Sampling schemes with equidistant angle in FOV (left) and equidistant distance on object plane (right). The object plane is denoted by O. The optical system in P is placed in a distance s.

The easiest way to achieve such a correction of *interchannel distortion* is to adapt the local pitch difference according to the position of the channel in the array in Eq. (3.4). The result is an irregular or so-called *chirped* microlens array [96–98].

3.2.2   Concepts for Field of View Segmentation

The segmentation of the field of view by multiple optical channels can be carried out in several ways which lead to different basic architectures of the multi aperture optical systems (MAOs) that are shown in Fig. 3.10. For the first time, the following discussion provides a classification which allows to distinguish the various principles of the state of the art and the new approaches for multi aperture imaging systems.

Figure 3.10: Overview of the principles of single and different multi aperture optical imaging systems.

3.2.2.1   Apposition Type (APCO)

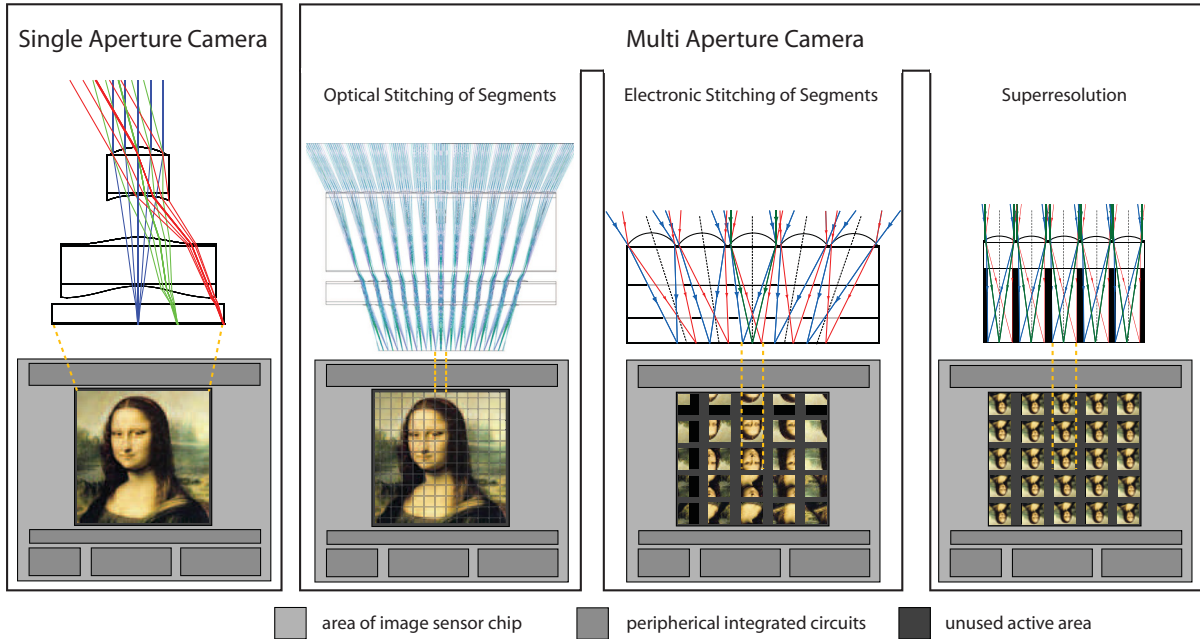The artificial apposition compound eye (APCO) uses only one pixel per optical channel, as illustrated in Fig. 3.2b. Thus $n_g = 1$ and the size of a partial image is that of a single pixel defined by either the pixel pitch p_{px} or the diameter of the photodiode d in case that both differ. Consequently, the number of pixels in the final image is directly given by the number of channels in Eq. (3.8) and the optical fill factor is $\Gamma = d/p_K$. If the size of the photodiode d is comparable to the size of the PSF, the full FOV per channel ($2\alpha_{K,x}$ and $2\alpha_{K,y}$) equals the acceptance angle $\Delta\varphi$. The effective sampling angle $\Delta\phi_{eff}$ equals the interommatidial angle $\Delta\phi$ of Eq. (3.4). If the condition

$$\Delta\phi_{eff} = \frac{\Delta\varphi}{2} \tag{3.19}$$

holds, the maximum transferable angular frequency in a single channel can be reconstructed in the final image [15]. The final image of the APCO can be made free of distortion by correcting the local pitch difference Δp_K in order to achieve a sampling according to Eq. (3.17) [96].

The APCO defines an extreme case which completely decouples the relationship between focal length, FOV and image size known from Eq. (2.1) because the overall image size of the APCO is determined by the moiré-magnification which is approximately [116, 117]:

$$m_{moire} = -\frac{p_K}{\Delta p_K} \ , \tag{3.20}$$

and thus independent of the focal length. It creates an image with a much larger magnification than that of each single optical channel and additionally it has a much shorter system length than a single aperture optical system with same magnification [15, 16].

3.2.2.2   Electronic Stitching of Segments

The second class of multi aperture optics uses multiple pixels per channel that are acquired in parallel within the separated partial images of each individual channel (see Fig. 3.10). Subsequently, the distributed image information is fused to a final image of the whole FOV via image processing (software or electronic image stitching).

This setup enables the highest degree of freedom and it will be distinguished between three different sampling schemes:

Redundant Sampling: Light that originates from each object point is sampled in multiple optical channels. This is achieved by choosing a pitch difference between adjacent optical channels Δp_K that is the m_0'th fraction of the pixel pitch p_{px} with m_0 being an integer value. Thus, starting from a channel with index l, there is another pixel which captures the same point of a distant object in the channels with indices $l + m_0$ and $l - m_0$ along one row of the MLA (see Fig. 3.11). The smallest sampling interval in image space is then given by $\Delta p_{eff} = p_{px}/m_0$. Redundant sampling can be used in order to acquire additional information about the object, like color, polarization and multispectral imaging or to increase the light sensitivity of artificial compound eyes. It is applied by the *artificial neural superposition eye* (*ANSE*) which reveals the inspiration from the neural superposition eye of insects.

Figure 3.11: Illustration of the redundant sampling scheme. On the right, each line O_i shows the sampling along a section in image space of the i'th channels for $m_0 = 3$. The last line O_{all} illustrates the final configuration in the post-processed image. The sampling interval of each pixel is indicated by a box-like function with the index of the channel.

Increased Sampling: The sampling is improved by overlapping FOVs of adjacent optical channels. The adjacent sampling grids need to be displaced by a sub-pixel amount Δp_{eff} i.e. the k'th fraction of the pixel pitch p_{px} whereas k must not be an integer divisor of the number of pixels per channel n_g (Fig. 3.12). The main purpose of this type is the decrease

of the total track length while maintaining the same image resolution compared to single aperture imaging systems with the same pixel size. The related device that achieves such an *increased sampling* is called *electronic cluster eye* (abbreviated to *eCLEY*). The eCLEY is inspired by the compound eyes of *Strepsiptera*.
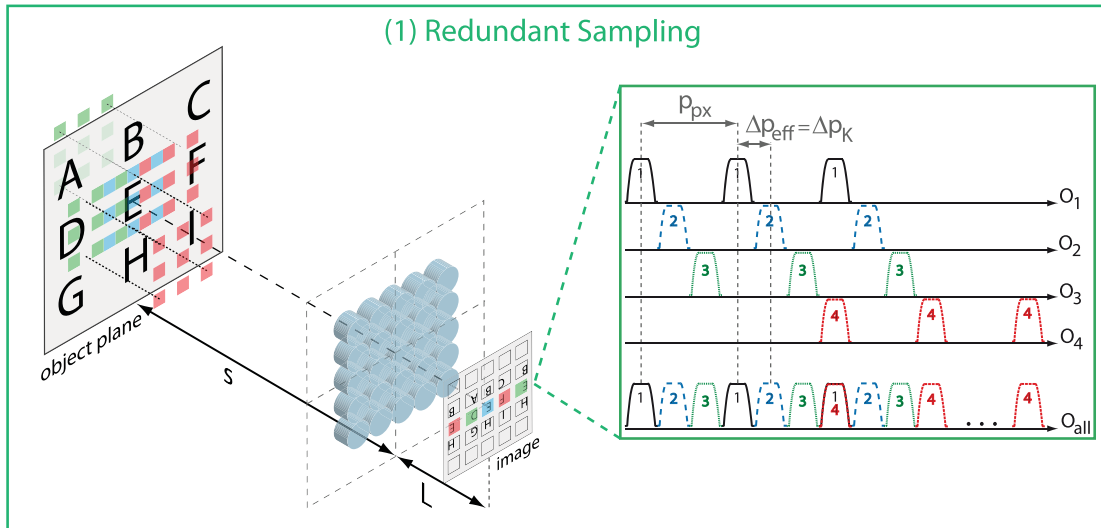

Figure 3.12: Illustration of the increased sampling scheme. On the right, each line O_i shows the sampling along a section in image space of the i'th channels for $k = 2$ and $n_g = 5$. The last line O_{all} illustrates the final configuration in the post-processed image. A pixel fill factor of about 50 % is assumed.

Simple Stitching: The channel pitch difference Δp_K equals the size of the partial images I_P and the individual fields of view of adjacent optical channels are seamlessly stitched by post-processing (see Fig. 3.13). The effective pitch difference Δp_{eff} is equal to the pixel pitch p_{px} in each channel. The application of this type can be compared to that of optical image stitching (to be discussed in the next section) with the difference that it offers the possibility to post-process the partial images prior to image stitching. There is no known natural archetype for the *simple stitching* scheme.
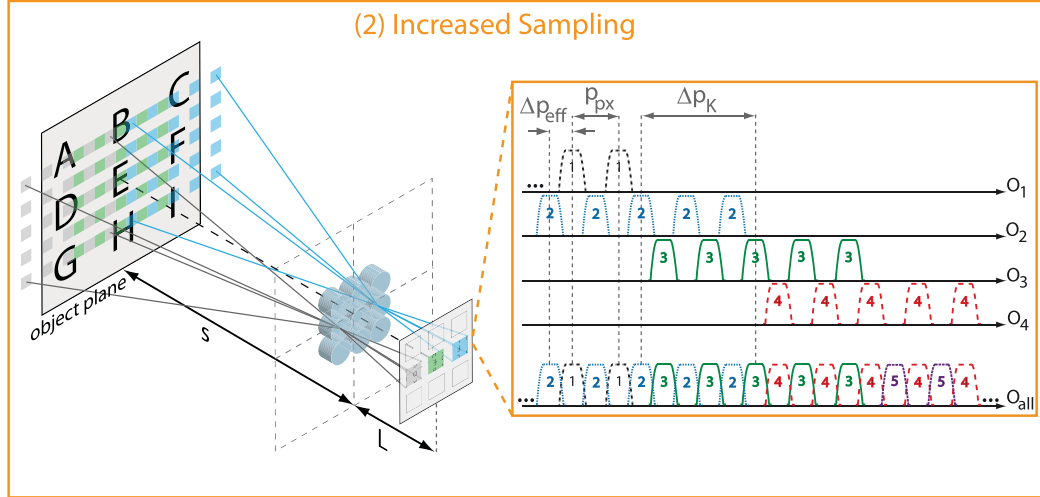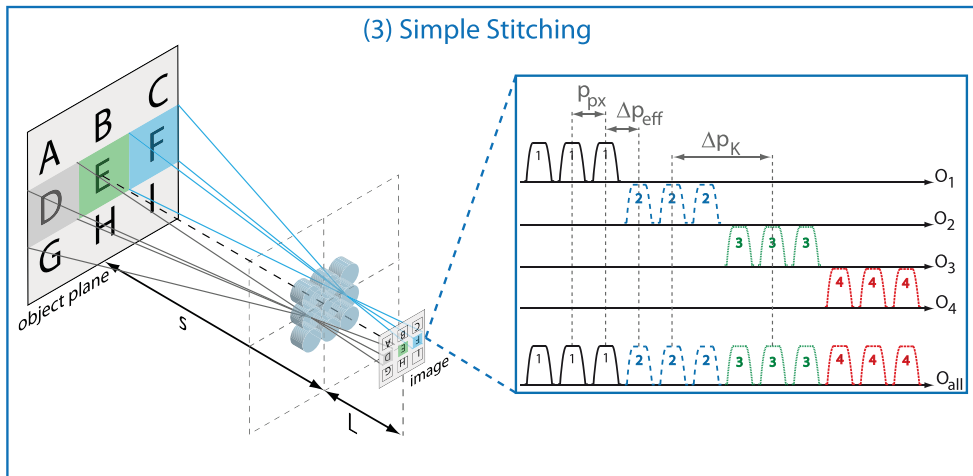

Figure 3.13: Illustration of the simple sampling scheme. On the right, each line O_i shows the sampling along a section in image space of the i'th channels for $n_g = 3$. The last line O_{all} illustrates the final configuration in the post-processed image.

Table 3.2: Summary of the different types of effective sampling for the multi aperture imaging systems using electronic stitching of segments from Fig. 3.11 - 3.13.

Parameter	(1)Redundant Sampling	(2)Increased Sampling	(3)Simple Stitching
Pitch difference	$\Delta p_K = p_{px}/m_0$ m_0 is integer > 1	$\Delta p_K = I_p/k$ k is not a divisor of n_g	$\Delta p_K = I_p$
Eff. sampling in image space	$\Delta p_{eff} = p_{px}/m_0$	$\Delta p_{eff} = p_{px}/k$	$\Delta p_{eff} = p_{px}$
Eff. sampling in object space	$\Delta \phi_{eff} = \Delta \phi \approx \Delta \phi_{px}/m_0$	$\Delta \phi_{eff} \approx \Delta \phi_{px}/k$	$\Delta \phi_{eff} = \Delta \phi_{px}$

The fraction of image sensor area that is used for the acquisition of partial images for the electronic stitching of segments is given by the 2D optical fill factor

$$\Gamma^2 = \frac{I_p^2}{p_K^2} \ . \tag{3.21}$$

There is a gap of $p_K - n_g \cdot p_{px}$ between adjacent partial images which cannot be used for active pixels so that $\Gamma^2 < 1$ (see Fig. 3.8b). Thus, the principle of electronic stitching of segments asks for a custom image sensor layout.

Whereas there is no state of the art for the redundant and increased sampling, the simple stitching is used by the *MULTICAM* which is introduced for infrared imaging in [14,118].

3.2.2.3   Optical Stitching of Segments

The optical stitching of segments denotes a multi aperture imaging system which achieves a seamless image of the total FOV by an optical recombination of all partial images (see Fig. 3.10 middle left). In this case, a conventional image sensor is applicable and the fill factor yields $\Gamma^2 = 1$. The lateral dimensions of such a multi aperture objective are comparable to that of single aperture systems. However, as the optical stitching is achieved by an imaging setup with at least one intermediate image, the number of optical elements per channel, the system complexity and overall thickness increase compared to the approach of electronic stitching of segments. Two main principles of the optical stitching can be distinguished:

Side-by-Side Stitching: Each optical channel transfers its related part of the FOV and adjacent partial images are optically stitched together in a way that the image details at the intersections between adjacent partial images are preserved (Fig. 3.14 left). Side-by-side stitching yields an artificial compound eye of high resolution that is especially compact in the lateral dimensions. The principle is used by the *optical cluster eye* (*oCLEY*) and the *ultra-thin array microscope.*

Overlapping Partial Images: Each optical channel images a larger portion of the full FOV and the individual partial images overlap in the image plane (right side of Fig. 3.14). Hence, the sensitivity of the artificial compound eyes can be considerably increased. This is the working principle of the microoptical Gabor Superlens ($\mu oGSL$).
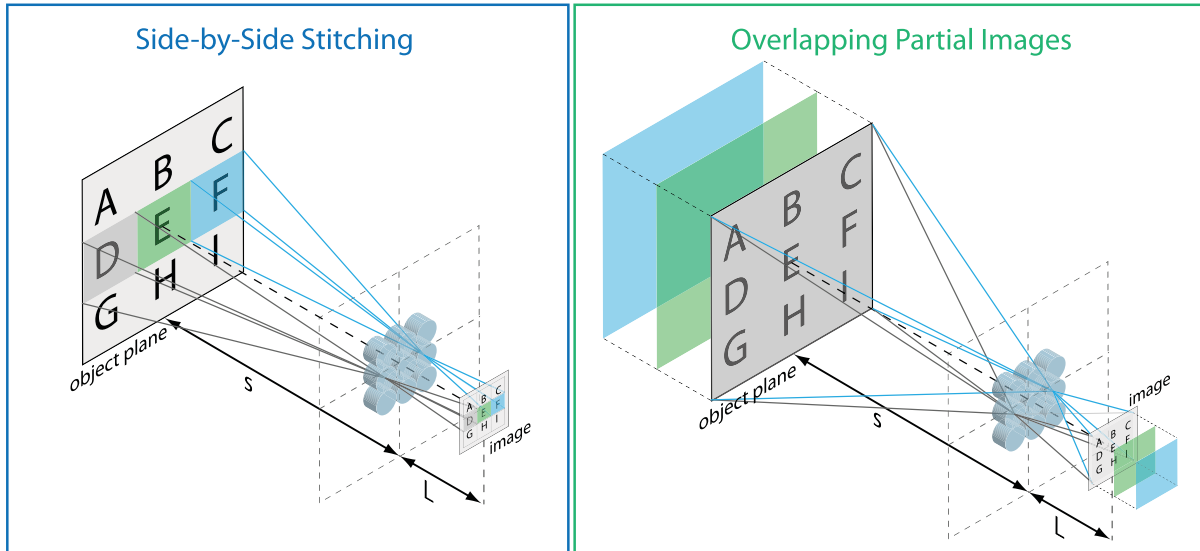

Figure 3.14: Overview of different object sampling solutions for the optical stitching of segments. Blue/left: The side-by-side stitching as used by the optical cluster eye ($oCLEY$). Green/right: Individual partial images are superimposed in the image plane. This scheme is found in the microoptical Gabor Superlens ($\mu oGSL$). The object distance and the thickness of the optical system are denoted by s and L, respectively.

Due to the working principle, there is no possibility to increase the sampling in object space beyond that given by the pixel pitch in Eq. (3.14).

3.2.3   Multi Aperture Super-Resolution

The fourth approach to multi aperture imaging systems (Fig. 3.10 outer right) has no known archetype in nature but it uses ideas of video image processing. The term *Super-Resolution* stands for the processing of a number of undersampled images with low resolution, e.g. out of a video stream, in order to create a single image with high resolution [119]. Instead of capturing multiple images over time, they could be captured at the same time in multiple optical channels. Correspondingly, a low-resolution image of the full FOV is captured in each channel and an image registration and fusion algorithm is used to create the final, high-resolution image from all sub-images. It has been proposed that this approach is promising as a thin and inexpensive substitute for imaging optics in the infrared spectral range [13]. A Japanese research group first published the so-called *TOMBO* system [12] which used diffractive lenslet arrays, GRIN lenses or conventional refractive microlens arrays for constructing a thin camera device based on Super-Resolution in the visible spectral range [12, 120]. It has been demonstrated that this device is suitable for color image acquisition and multispectral imaging by using RGB or several narrow-band

interference filters [121, 122]. Additionally, it has been shown that 3D imaging of objects in a distance of less than one meter is feasible [123].

However, multi aperture Super-Resolution is accompanied by several limitations. First, the FOV of the published examples is below 22° due to the limited usable image field per channel which is determined by the diameter of the related lens and the technological limits for the numerical aperture of the microoptics [12, 124]. Additionally, the approach is sensitive to object distance due to a change of parallax and thus sub-pixel disparity between images of neighboring optical channels. Only small object distances between a few centimeters up to about two meters are described in literature. The sub-pixel disparity is also altered across the field by distortion of each optical channel. The condition for fine-grained sub-pixel shifts between the different low-resolution images states the most crucial limitation: In contrast to a conventional image acquisition process, Super-Resolution requires aliasing of the low-resolution images within each optical channel. This can be expressed by a condition for the number of nonredundant channels K_{ch} [125]

$$K_{ch} = \nu_{px}/\nu_{Ny} = 2/\sqrt{\Phi_{IS}} \; . \tag{3.22}$$

Where ν_{px} and ν_{Ny} are the first zero of the pixel aperture MTF in Fig. 2.7b and the Nyquist frequency of Eq. (2.35). The pixel fill factor Φ_{IS} was defined in Eq. (2.29). This means that the optical MTF and thus the resolution of the lens system has to be high enough in order to transfer sufficient frequency content above the Nyquist frequency up to $\nu_{px} = 1/d$. However, this becomes difficult to achieve in practice when considering the tolerances of fabrication and alignment during assembly, especially for miniature cameras with small pixel pitch and thus high Nyquist frequency. Furthermore, the computational load and processing speed is still challenging for a real-time image acquisition [126, 127].

3.2.4 Reasons for a Thickness Reduction in MAO

There are a few fundamental amenities that summarize the advantages of multi aperture imaging optics in terms of the miniaturization of imaging systems:

Spatial Segmentation of the FOV: Each part of the total FOV that is transferred by an individual optical channel originates from a different position in object space. Thus, the properties of each optical channel can be adapted in order to create a best possible image of the particular segment. A smaller range of field values has to be imaged by each individual channel so that the correction of aberrations becomes much easier because, according to Eq. (2.10), most aberrations strongly depend on field coordinate h (see also Tab. A.1 in Appendix A). The resulting advantages with respect to single aperture optics are: a simple optical setup with few elements within each channel, a relatively small diameter and height for each of the microlenses and the feasibility of a large total FOV.

Spectral Segmentation: The information that is transferred by the individual opti-

cal channels differs in its spectral composition. Each channel transfers a part of the full spectral range of the multi aperture imaging system. This feature eases the correction of chromatic aberrations for the limited spectral range of the individual channel which yields a simplier optical setup with fewer elements within each channel in comparison to single aperture imaging optics.

Overlap of the FOVs of Different Optical Channels: The fields of view of different optical channels overlap to a desired extend which allows for features that are impossible for single aperture imaging optics. Examples are: the decrease of the total track length of the optical module due to increased sampling, the increase of sensitivity and information capacity (color, multispectral, polarization imaging) as well as three-dimensional imaging. The schematic Figure D.1 in Appendix D lists the assignment of the basic features of multi aperture imaging optics to the specific types.

Thickness Reduction due to Increased Sampling

When shrinking the size of the optical system, the interpixel angle ($\Delta\phi_{px}$) in a single aperture system increases with decreasing focal length according to Eq. (3.14). However, the viewing direction in the FOV can be chosen freely by applying the pitch difference (Δp_k) in case of multi aperture imaging optics with electronic stitching of segments. Hence, the angular sampling of the object space is not limited by the pixel pitch and the focal length of a single channel, but by the effective pitch difference Δp_{eff} (see Fig. 3.12). This yields:

$$\frac{\tan\left(\Delta\phi_{eff}\right)}{\tan\left(\Delta\phi_{px}\right)} = \frac{f_{sao}}{k \cdot f_{mao}} \tag{3.23}$$

when dividing Eq. (3.15) by Eq. (3.14) and replacing the effective pitch difference by the fraction of the pixel pitch $\Delta p_{eff} = p_{px}/k$ from Tab. 3.2. The focal length of the single aperture imaging optics is denoted by f_{sao} and that of a single channel of the multi aperture imaging optics by f_{mao}. The variable k is an integer number according to Tab 3.2. The same angular sampling has to be achieved for the multi aperture system compared to the single aperture system as this is desired for the application. Hence, the condition yields

$$\frac{f_{sao}}{k \cdot f_{mao}} \overset{!}{=} 1 \quad \rightarrow \quad f_{mao} = \frac{f_{sao}}{k} \ . \tag{3.24}$$

In conclusion, the effective focal length of the multi aperture optical system can be shortened by $1/k$ while the angular sampling and the pixel size are constant. The integer $k \geq 1$ is called *braiding factor*.

3.3 Methodology for the Optical Design and Simulation of MAO

The optical design and simulation of multi aperture imaging systems is structured into several subtasks which build up a complete working chain shown in Fig. 3.15.
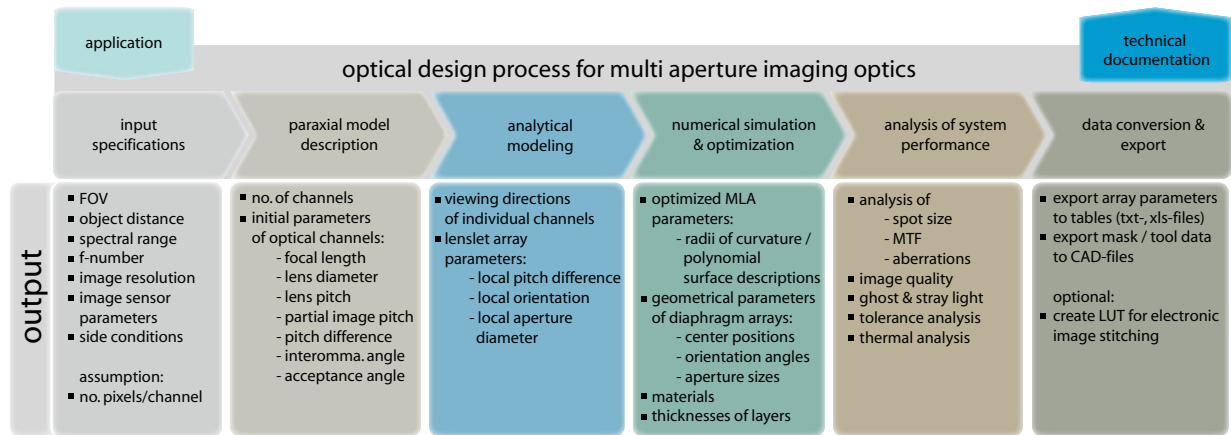
Figure 3.15: Overview of the basic steps of the optical design process for multi aperture imaging optics.

The design process starts with an input of system specifications which result from the application. These specifications such as FOV size or image sensor parameters are used to create a first approximate model with thin lens (paraxial) equations. In general, the paraxial model acts as starting point for the numerical simulation which is carried out by ray-tracing techniques. Depending on the complexity of the single channel setup, some basic parameters of the lenslets and diaphragm arrays (e.g. central viewing direction of each channel, center positions) are derived from analytical relationships in an intermediate step. During the numerical simulation, the single channel starting system is converted into a numerical description of the full multi aperture structure with optimized parameters. After optimization, the performance of the resulting system is analyzed by using simulations of spot size, MTF and test images. Additionally, ghost light suppression is checked and mechanical tolerances are analyzed. Finally, the design data of one multi aperture objective is exported for the creation of a lithography mask set and mold tools for the different layers.

Differences to the optical design of single aperture imaging optics (SAO)

The simulation of multi aperture optical imaging systems (MAO) features special characteristics when compared to that of single aperture systems. The aperture stop is divided in a number of sub-apertures according to the number of optical channels $K_x \times K_y$. Each optical channel is regarded as an independent single aperture optical system so that the design and simulation effort is multiplied by the total number of channels. However, depending on the complexity of the system, it is sufficient to use characteristic sections through the array or one unit cell for simulation due to lateral symmetry in the array. This drastically decreases the effort. Nevertheless, a semi-automated optical design method is recommended for the numerical simulation of systems which use chirped arrays as this requires the optimization of a large number of different optical channels. Another difference is that there are side conditions which define the relationship between different channels that have to be considered during the optimization. This relates to interactions such as the braided sampling in object space or the superposition of partial images in image space.

A significant difference is found in the origin and analysis of ghost and stray light. There is only few sources of stray light possible in a MAO compared to a SAO because there are no lens or housing side faces for the majority of channels (except those at the edges of an array) which are a common source of stray light. Furthermore, direct ghosts and lens flares are uncommon as there are only few air-glass interfaces in each channel. On the other hand, attention has to be paid to ghost images which, in contrast to SAO, are caused by light which entered the sub-aperture of one channel and travels to the partial image plane of another channel in an unintended way. The suppression of *optical crosstalk* by the optimization of the position and size of barriers and diaphragm apertures is a task that is unique to MAO.

Several side conditions and restrictions for the optical design result due to the scale and the fabrication by microtechnology. Examples of these are: the implementation of glass substrates as mechanical carriers for microoptical elements, the limitation to specific lens surface profiles and the limited numerical aperture of microlenses.

3.3.1   Paraxial Model

The paraxial approximation allows to calculate system parameters independent of the detailed layer structure or materials of the specific optical design. Equations of first-order (Gaussian) optics are applied and aberrations are neglected. It is used as a starting point for the numerical design of a single on-axis channel and further detailed simulations. Table 3.3 lists a typical set of input specifications from the application and the main on-axis parameters that can be derived from that set. An initial value for the microlens pitch is

Table 3.3: Overview of input and output parameter sets for the paraxial model.

Input	Output	Equation
Spectral range (λ_i)	focal length (f)	(3.15)
Number of image pixels ($N_{x,y}$)	microlens diameter (D)	(2.2)
Pixel pitch (p_{px})	acceptance angle ($\Delta\varphi$)	(3.2)
Size of FOV (diagonal, 2α)	number of channels ($K_{x,y}$)	(3.8)
F-number ($F/\#$)	horizontal and vertical FOV ($2\alpha_{x,y}$)	(3.12)
	effective sampling angles ($\Delta\phi_{eff,x,y}$)	(3.16)
	FOV of individual channel ($2\alpha_{K,x,y}$)	(3.13)
	pitch of partial images (Δp_K)	(3.3)

given by the sum of the microlens diameter D and a minimum spacing between adjacent lenslets Δs_L which yields

$$p_L = D + \Delta s_L \tag{3.25}$$

The value of Δs_L is a few microns due to restrictions of the MLA fabrication technology. The effective sampling angle and the acceptance angle should approximately fulfill Eq. (3.19) in order to follow the sampling theorem. The effective pitch difference Δp_{eff} and the pitch difference Δp_K of adjacent partial images result from the designer's choice of the

sampling scheme, e.g. from Tab. 3.2. Once the effective pitch difference is known, the Nyquist frequency of the system can be calculated analog to Eq. (2.35) by

$$\nu_{Ny} = \frac{1}{2\Delta p_{eff}} \ .$$

(3.26)

3.3.2 Paraxial Matrix Formalism

Matrix formalisms are advantageous in dealing with the numerous degrees of freedom of a more complex optical system made of several lenses [49, 128]. The well-known ABCD-matrix formalism is limited to the first-order (paraxial) optics description of rotationally symmetric single aperture systems. However, it can be extended using 3x3 matrices in order to describe optics that are decentered from the optical axis and tilted [129]. The resulting 3x3 matrix formalism was successfully applied for the simulation of optical systems containing MLAs [17, 73, 130, 131]. Each ray is described by a set of two coordinates which denote the lateral distance h to the optical axis and the angle α under which it subtends the optical axis. The transfer matrix $\widetilde{M}$ is used to map the input ray $(h_{in}; \alpha_{in})$ to the output ray $(h_{out}; \alpha_{out})$:

$$\begin{pmatrix} h_{out} \\ \alpha_{out} \\ 1 \end{pmatrix} = \widetilde{M} \cdot \begin{pmatrix} h_{in} \\ \alpha_{in} \\ 1 \end{pmatrix}, \quad \widetilde{M} = \begin{pmatrix} M_{11} & M_{12} & \Delta h \\ M_{21} & M_{22} & \Delta \alpha \\ 0 & 0 & 1 \end{pmatrix} .$$

(3.27)

The transfer matrix of the system $\widetilde{M}$ includes the well-known ABCD-matrix in the elements M_{ij} and the general decentration $M_{13} = \Delta h$ as well as tilt $M_{23} = \Delta \alpha$ [131]. The influence of each component on the propagation of the observed ray is described by a specific matrix. Typical matrices which are needed to model the paraxial ray propagation in MAOs, are the propagation matrix M_P through an homogeneous medium of the refractive index n_i with a thickness of d_i, the refraction at a thin lens M_L with focal length f and the decentration M_D by a distance Δh perpendicular to the optical axis:

$$M_P = \begin{pmatrix} 1 & \frac{d_i}{n_i} & 0 \\ 0 & 1 & 0 \\ 0 & 0 & 1 \end{pmatrix}, \ M_L = \begin{pmatrix} 1 & 0 & 0 \\ -\frac{1}{f} & 1 & 0 \\ 0 & 0 & 1 \end{pmatrix}, \ M_D = \begin{pmatrix} 1 & 0 & \Delta h \\ 0 & 1 & 0 \\ 0 & 0 & 1 \end{pmatrix} .$$

(3.28)

The system transfer matrix $\widetilde{M}$ is built up by the matrix multiplication of the specific matrices of all system components. Depending on the number of optical elements, the system matrix may have an intricate structure which contains the k_1 parameters of the paraxial system. Assuming that the total number of input parameters is k_2, at least $(k_1 - k_2)$ different ray sets $(h_{in}, \alpha_{in}; h_{out}, \alpha_{out})$ have to be known in order to solve the equation system in Eq. (3.27) for the unknown system parameters. Each of such a ray set is created by a side condition that has to be fulfilled by the system.

The paraxial matrix approach will be applied to find starting parameters for the different artificial compound eyes in Chapter 5.

3.3.3   Analytical Modeling

Due to the complexity and involved degrees of freedom of a MAO, it is futile to struggle for a complete analytical model for the description of image formation. However, finding an analytical relationship for certain parts of the system helps to accelerate the optical design process.

For example, the relationship between the channel pitch difference Δp_K and the chief ray angle (CRA) ϑ_r of the central viewing direction in each optical channels of artificial compound eyes that use electronic image stitching is examined. Geometrical optics is used to derive the relationship $\Delta p_K = f(\vartheta_r)$ with the help of Eq. (3.17).
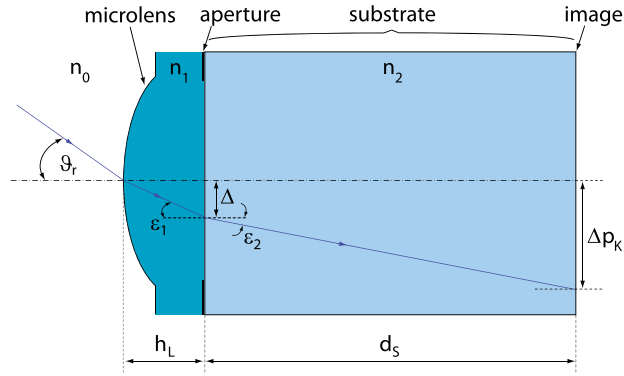

Figure 3.16: Illustration of the basic parameters in order to derive the relationship between the channel pitch difference Δp_K and the central chief ray angle ϑ_r.

For a single lens with the entrance pupil directly in the tangential plane of the lens apex (Fig. 3.16), it follows from Snell's law that:

$$n_0 \sin(\vartheta_r) = n_1 \sin(\epsilon_1) \ , \tag{3.29}$$

$$\tan(\epsilon_1) = \frac{\Delta}{h_L} \ , \tag{3.30}$$

$$n_1 \sin(\epsilon_1) = n_2 \sin(\epsilon_2) \ , \tag{3.31}$$

$$\tan(\epsilon_2) = \frac{\Delta p_K - \Delta}{d_S} \ . \tag{3.32}$$

Once the materials and thus the refractive indices for the individual layers are chosen, the sag of the lens h_L and the thickness d_S of the substrate are known from the paraxial model. The refractive index of the lens material is n_1 and that of the substrate is n_2, both at the center wavelength λ. The refractive index in object space is denoted by n_0. The relationship for the pitch difference results from Eqs. (3.29)-(3.32):

$$\Delta p_K = d_S \cdot \tan \left(\arcsin \left[\frac{n_0}{n_2} \sin(\vartheta_r) \right] \right) + h_L \cdot \tan \left(\arcsin \left[\frac{n_0}{n_1} \sin(\vartheta_r) \right] \right) \ . \tag{3.33}$$

In general, the system might contain a stack of several layers with different refractive indices so that a cascading sequence of the two equations

$$n_j \sin(\epsilon_j) = n_i \sin(\epsilon_i) \ ; \ \Delta_j = d_j \tan(\epsilon_j) \ , \tag{3.34}$$

is used to describe the transition from each layer i to the next layer j (starting with $d_0 = 0$ and $\epsilon_0 = \vartheta_r$). The change of the lateral distance to the optical axis due to the propagation through the j'th layer is denoted by Δ_j and the axial thickness of that layer by d_j. The pitch difference is then calculated by

$$\Delta p_K = \sum_j \Delta_j \ . \tag{3.35}$$

The relationship becomes intricate when a more complex optical setup is present for the individual channel. After axially separating the aperture stop from the microlens, the pitch difference cannot be explicitly calculated unless the decentration between aperture stop and the lens as well as the radius of curvature of the lens are known. A semi-analytical approach is used from this point onwards. At first, the pitch difference is calculated with the radius of curvature which has been derived in the paraxial model and the decentration is assumed to be zero. This is the starting point for a numerical optimization of e.g the radii of curvature. The calculation is then iterated with the new value for the radius of curvature, giving a new value for the pitch difference which is again entered into the numerical model. This loop is repeated until the numbers converge. Most of the setups which are proposed in Chapter 4 require a semi-analytical treatment mixing analytical relationships with numerical calculation which is described in the next section.

Ellipsoidal Microlenses

The segmentation of the field of view by different optical channels enables the optimization of the lens profiles in each optical channel according to its central viewing direction and size of the FOV segment. However, rotationally symmetric spherical or aspherical lenses cannot provide sufficient correction of off-axis aberrations under oblique angle of incidence as long as only few lenses are used in each channel. The special case of an ellipsoidal microlens provides the correction of astigmatism for a specific angle of incidence by tuning the tangential and sagittal radii of curvature according to the Gullstrand's equations [132]. Additionally, field curvature can be corrected for the central viewing angle of each lenslet across a microlens array when the tangential and sagittal image planes meet at the axial position of the paraxial image plane [96–98]. Last, ellipsoidal microlenses can be fabricated by state-of-the-art micro-technology using binary lithography and reflow of photoresist [133]. This is the reason why ellipsoidal microlens arrays are applied in most of the MAOs of Chapters 4 and 5. The apex height (sag) h_L of a spherical lens is described by

$$h_L = R - \sqrt{R^2 - r_a^2} \ , \tag{3.36}$$

using the radius of curvature R and the aperture radius r_a. The same equation is used to describe the sag of ellipsoidal lenses in the tangential (index 't') and sagittal (index 's') planes where R_t and R_s denote the related radii of curvature and a_t and a_s the semi-axes of the elliptical aperture in the respective plane: $R \rightarrow R_{t,s}$ and $r_a \rightarrow a_{t,s}$. The spherical lens is a special case of the ellipsoidal, and thus the radius of curvature in the tangential

or sagittal plane can be determined by transforming Eq. (3.36) to [96, 133]

$$R_{t,s} = \frac{h_L}{2} + \frac{a_{t,s}^2}{2h_L} \ . \tag{3.37}$$

The sizes of the semi-major and semi-minor axis are calculated from the radii of curvature as the latter are being optimized during the design process

$$a_{t,s} = \sqrt{2h_L \cdot R_{t,s} - h_L^2} \ . \tag{3.38}$$

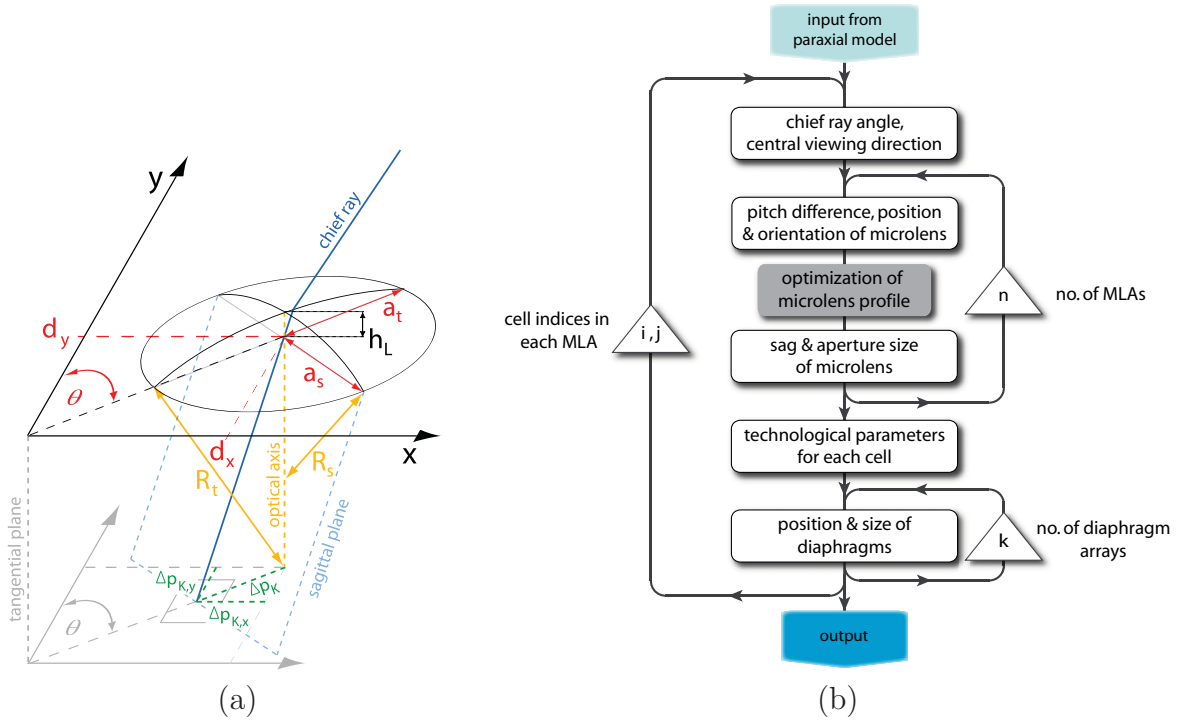As a result of the unsymmetric element, the orientation angle θ of the elliptical base (Fig.

Figure 3.17: (a) Parameters of an ellipsoidal microlens. (b) Schematic macro structure for the semi-automated numerical optical design. The control variables are i, j for the individual optical channels with $i, j \in [0; (K_{x,y} - 1)/2]$.

3.17a) is a new degree of freedom which follows directly from the lens position with respect to the center of the array

$$\theta = \arcsin\left(\frac{i}{\sqrt{i^2 + j^2}}\right) \ . \tag{3.39}$$

The projection of the pitch difference on the main axes of the array yields

$$\begin{aligned} \Delta p_{K,x} &= \Delta p_K \cdot \sin\left(\theta\right), \\ \Delta p_{K,y} &= \Delta p_K \cdot \cos\left(\theta\right) \end{aligned} \tag{3.40}$$

and the center position of each microlens (d_x, d_y) in the plane of the MLA is derived by

$$\begin{aligned} d_x &= i \cdot p_K + \Delta p_{K,x}, \\ d_y &= j \cdot p_K + \Delta p_{K,y} \ . \end{aligned} \tag{3.41}$$

If a regular grid of partial images is assumed (p_K constant), the position of each microlens in Eq. (3.41) is a direct result of the sampling scheme of Eq. (3.17) and the relation

between the local pitch difference Δp_K and the chief ray angle ϑ_r of the central field of each optical channel.

3.3.4   Numerical Simulation

Microoptical imaging optics can be adequately modeled by ray-tracing techniques because the refracting microlenses have a diameter in the range of 50 to 500 microns which is at least a hundred times larger than the wavelength of visible light ($\lambda = 500$nm). Hence, it is not necessary to use propagation methods of wave optics (physical optics) such as *finite-difference time-domain (FDTD)* or *angular spectrum of plane waves method.* However, the diffraction at the microlens aperture or other limiting diaphragms has to be considered.

3.3.4.1   System Optimization via Ray-Tracing

The numerical modeling, optimization and simulation form the key parts of the optical design chain. The numerical methods which were used throughout the described work, are sequential and non-sequential ray-tracing techniques. Sequential ray-tracing was used for the optimization, generation of structural data as well as testing of single optical channels and data export. The non-sequential part served for the image simulation of the collectivity of optical channels as well as the analysis of optical crosstalk and stray light.

Due to the interrelationship between the different optical channels of a MAO, it is beneficial to use a semi-automated design technique based on customized macro script files. Hence, parameter changes can be implemented in short time without the need for editing all of the individual channels by hand. Additionally, it is sufficient to model a representative part of the full array, e.g. a quarter of the whole MLA due its symmetry which accelerates most of the simulation tasks.

The simulation starts with a sequential description of the central, on-axis optical channel using the parameters that have been derived from the paraxial and analytical models. The glass substrate, lens materials as well as thicknesses are chosen and the initial axial positions of diaphragm array layers are set. From a first optimization of the center channel, the on-axis radii of curvature R, sags h_L and aperture radii r_a of the MLAs are derived. The optimized setup for the on-axis channel states the starting point for the automated optical design algorithm which is sketched in Fig. 3.17b. The structure data of each microlens in the array is then automatically calculated and optimized channel by channel. During the optimization, the radii of curvature - or in a more general case the coefficients of the polynomial which describes the surface profile - of each microlens are variable to change while a merit function is minimized by a damped least squares algorithm. For each MLA a dataset of the radii of curvature (R_t, R_s) or likewise the set of coefficients for a polynomial surface profile, the center position (d_x, d_y), the orientation angle (θ), the aperture size (a_t, a_s) and the sag (h_L), as well as geometrical parameters for the related mask tool is created for all lenslets. A similar set is generated for each of the diaphragm

arrays. Here, the center position coordinates (c_x^k, c_y^k) of each opening are read out from the point where the centroid of a ray bundle, which originates from the local object field center, 'pierces' the lateral plane of the k'th diaphragm layer. The semiaxes of each opening (b_x^k, b_y^k) are determined by tracing the marginal rays in the related plane whereas the shape of the openings is in general elliptical. The Figure 3.18 illustrates the next steps that follow the optimization of the optical system.
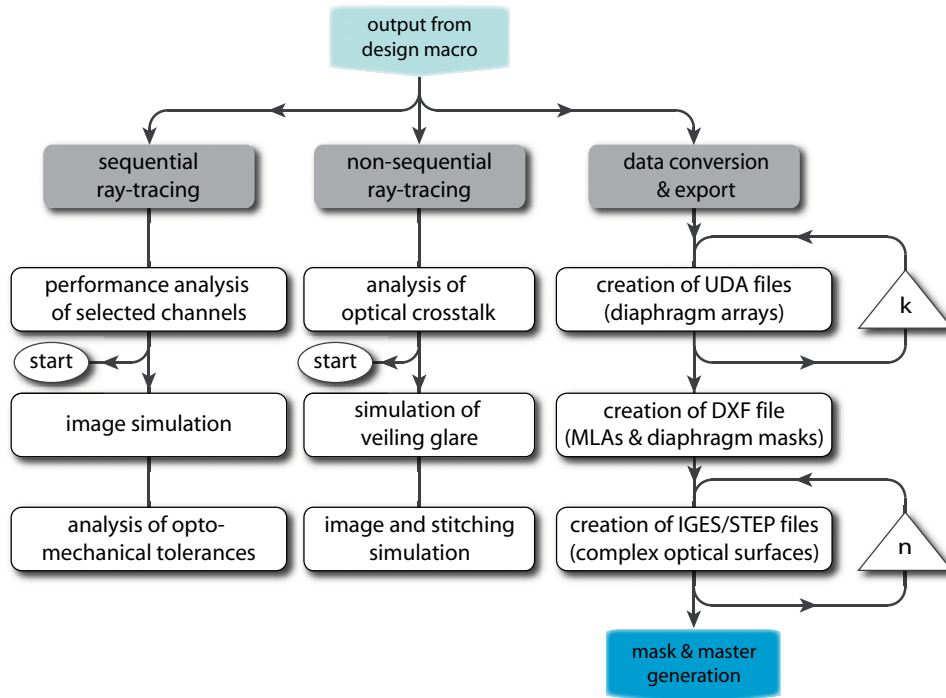

Figure 3.18: Overview of the tasks of numerical optics design subsequent to optimization. The counter k denotes the number of diaphragm arrays and n the number of microlens arrays. If the current system fails to achieve the performance specifications or crosstalk suppression is insufficient, the process has to be repeated from the starting point in Fig. 3.17b using a different optical setup and/or diaphragm positions.

3.3.4.2 Optical Crosstalk Simulation

After the optimized MAO has been transferred into a non-sequential ray-tracing model, the system is analyzed for optical crosstalk. The aim is to avoid light that passes the entrance pupil of a specific channel to hit the partial image plane of another optical channel. Two possible ways for the simulation of crosstalk are shown in Fig. 3.19. On the one hand, rays are traced from an extended object plane towards the full image plane of the optical system (Fig. 3.19a). The size of the radiating object plane is determined by the FOV of the single channel under test and the object distance. Larger angles of incidence are simulated by rotating the object plane around the optical system. In Fig. 3.19b the direction of ray propagation is reversed and the radiating surface is placed in the image plane of the channel under test. It has the size of a single partial image and is therefore much smaller than the radiating surface in case (a). The emitted rays are recorded on a virtual detector plane
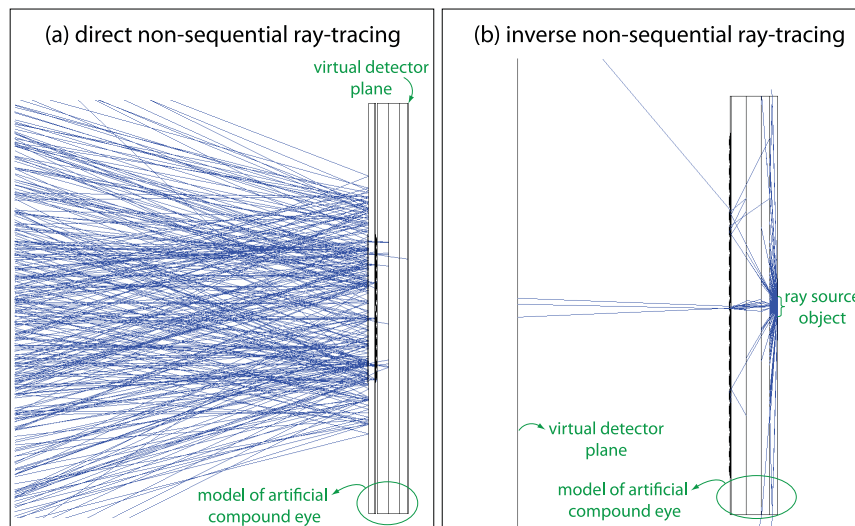
Figure 3.19: Ray-tracing schemes for the simulation of optical crosstalk. (a): Direct tracing of rays from a Lambertian source in object space to a virtual detector placed in the image plane of the artificial compound eye. (b): Inverse tracing of rays from a Lambertian source radiating from the image plane of a single channel of the compound eye into the object space where a large virtual detector captures the incoming rays.

which is large and in close proximity to the front face of the optical system. The second way is preferred over the direct ray-tracing due to its speed because a much smaller radiating surface is used and thus the number of traced rays for the evaluation of crosstalk is smaller by orders of magnitude. The amount of crosstalk is measured by the ratio of integrated irradiance of the ghost projection and that of the direct projection of the source on the virtual detector. The analysis of the veiling glare index in an image which is presented in Appendix F is another simulation tool in order to evaluate optical crosstalk suppression. This technique gives an integral result of stray light and crosstalk on selected parts of the final image.

Appendix E provides an overview of the image simulation method using ray-tracing techniques in Zemax™. It also deals with a way to add the effects of diffraction to images that have been generated by geometrical ray-tracing. The representative channels in the array and the simulation tools for the verification of the performance of a MAO design are introduced in Appendix F.

After assessing the optical characteristics, the design process is concluded by a tolerance analysis and an optional thermal analysis. These are necessary to assure that the optical design is manufacturable with present fabrication techniques and that the operation is possible under application conditions. Due to the complexity and the large number of optical channels it is impractical to use an automated tolerance analysis as common for single aperture optics. Instead, worst offenders are varied manually in order to verify the effect on the system performance.

4 Artificial Compound Eyes with Electronic Stitching of Segments

4.1 Artificial Neural Superposition Eye (ANSE)

A known trade-off of artificial apposition compound eyes is the inverse relationship between resolution and sensitivity [16]. The radiant power hitting a single pixel is increased according to the square of its diameter following Eq. (2.45) whereas the angular resolution is decreased according to the reciprocal of Eq. (3.2), in case that all other parameters are fixed (see Fig. 4.1a). However, when using the redundant sampling of the artificial neural superposition compound eye (ANSE), n_g^2 pixels will record the radiant power that belongs to a common point in object space. In that case, the number of redundant samples is a new degree of freedom in Eq. (2.45) which yields

$$P_{im} = \pi\tau \cdot B_{ob} \cdot \frac{n_g^2 \cdot d^2}{4 \cdot (F/\#)^2} \ .$$

(4.1)

The active area is increased without changing the resolution which is illustrated by the blue curve in Fig. 4.1a.

4.1.1 Increased Information Capacity of APCOs

A demonstration system of the ANSE was simulated and designed, considering the principles of redundant sampling described in Sec. 3.2.2.2. The optical setup is similar to that of an artificial apposition compound eye (APCO): a microlens array integrated on a glass substrate with an aperture array on the front side. The thickness of the substrate is matched to the focal length of the lenslets. The optics module was adapted to a commercially available 2/3 inch CMOS image sensor with a pixel pitch of $p_{px} = 10.6$ µm. The pixel aperture was narrowed down by an additional pinhole array on the back side of the optics chip (Fig. 4.1b) which enabled a higher angular resolution for a short focal length according to Eq. (3.2). In contrast to the APCO, a group of 3x3 pixels is used in each optical channel. The pitch between the central pinholes of each group is a multiple of the sensor pixel pitch. The parameters of the optical system were optimized using sequential ray-tracing.

The interpixel angle $\Delta\phi_{px}$ is fixed by the image sensor pixel pitch [Eq. (3.14)] but the interommatidial angle between adjacent channels $\Delta\phi$ is chosen independently by the difference between the pitch of the microlens array p_L and the pitch of the pinhole group array p_K. According to Tab. 3.2, their ratio has to be an integer number $m_0 > 1$ in order to yield redundant sampling

$$\frac{\Delta\phi_{px}}{\Delta\phi} = m_0 \ .$$

(4.2)

If this condition is fulfilled, $3^2 = 9$ pixels from different channels observe the same point
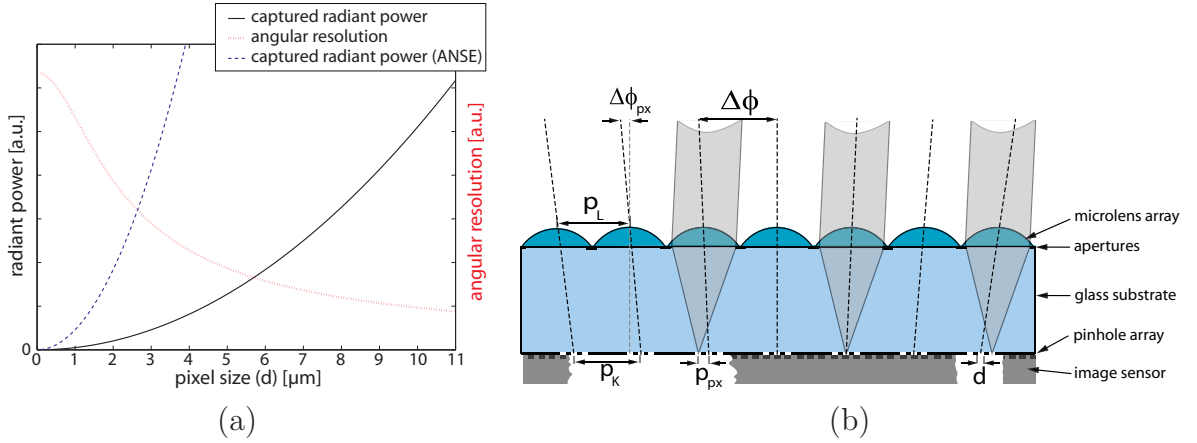
Figure 4.1: (a) Trade-off between angular resolution (red dots) and sensitivity (black line) depending on the pixel size. The sensitivity can be increased for small pixel sizes by redundant sampling (blue dashed line) of the ANSE. (b) Schematic principle of a planar artificial neural superposition eye (ANSE). The number of pixels per channel is n_g^2 with $n_g = 3$ in (a) and (b).

of a distant object. For an optical channel with indices $(k; l)$, there is another pixel which is sampling the same point in all channels $(k \pm m_0; l)$, $(k; l \pm m_0)$ and also in those with $(k \pm m_0; l \pm m_0)$.

Generally, the additional pixels are used to increase the information capacity of the multi aperture optical imaging system when compared to the APCO. In the following prototypes, the additional information is used for an increase of the sensitivity and for color image acquisition without compromising the resolution.

In order to increase the sensitivity, the signals of a group of 9 pixels that are related to the same object point were averaged. This yields an SNR of the average signal that is increased by a factor of $\sqrt{9} = 3$ in a similar manner as the frame averaging described in Sec. 2.2.2.
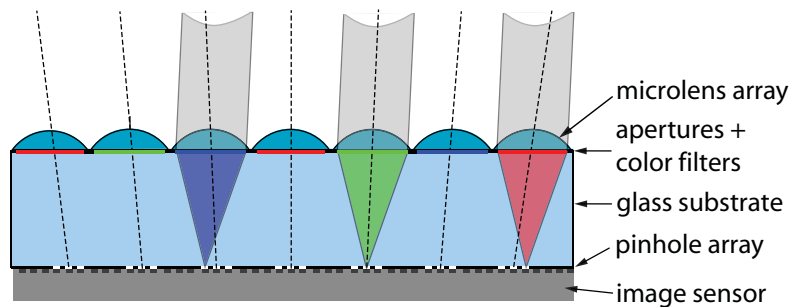
Figure 4.2: Layout of the artificial neural superposition eye (ANSE) with integrated polymer color filters to acquire color images. The case of $n_g = 3$ is shown here. Each point in object space is imaged through a red, green and blue color filter in different channels.

For color imaging, the setup of an artificial neural superposition eye was modified with an additional color filter in the aperture stop of each channel which is shown in Fig. 4.2. Each pixel in the overall color image results from mapping those pixels that share a common viewing direction through a red, green and blue color filter onto the specific location in

the individual color plane. In contrast to conventional color imaging using a Bayer mosaic, there is no interpolation needed for the ANSE approach so that the spatial resolution is conserved as high as in the case of an artificial apposition compound eye.

4.1.2   Fabrication and Integration

The fabrication of artificial compound eyes relies on established processes and equipment of microtechnology [134–136]. Such a system is fabricated by a sequence of process steps which require precise lateral as well as axial alignment throughout the whole process chain (Fig. 4.3). Photolithography is the key implement to achieve the required precision in the micron or even sub-micron range. The highly precise lateral alignment is achieved for many components in parallel using alignment marks on a planar mechanical carrier substrate called *wafer*.
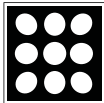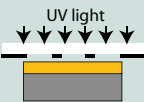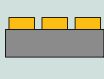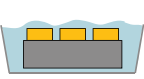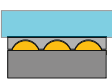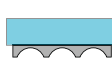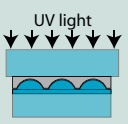
Step	Technology	Result	Accuracy
Mastering by photo lithography	E-beam or Laser lithography	Binary masks (chromium)	$\Delta x, \Delta y \cong \pm 0.2\,\mu m$
	UV-lithography	Binary structures (photoresist)	$\Delta x, \Delta y \cong \pm 1.0\,\mu m$
	Reflow of photoresist	Continuous lens master profiles (photoresist)	$\frac{\Delta R}{R} \cong \pm 2\,\%$ homogeneity > 99 %
Mastering by diamond machining	Diamond turning or milling	Continuous lens master profiles (metal e.g. NiP)	$\Delta x, \Delta y \cong \pm 2.0\,\mu m$ $\Delta R_{PV} \cong \pm 0.25\,\mu m$
Tool creation	Overcasting	UV-transparent replication tool (elastomer)	$\frac{\Delta R}{R} < 1\,\%$
Replication	UV-molding	Microlenses & residual layer (hybrid polymer)	$\frac{\Delta R}{R} < 1\,\%$ $\Delta x, \Delta y \cong \pm 1.0\,\mu m$ $\Delta z \cong \pm 5\,\mu m$

Figure 4.3: Overview of the basic steps for the fabrication of microoptical multi aperture imaging optics. All of the illustrated steps are feasible on wafer level with the indicated accuracy.

A part of the processes of Fig. 4.3 was applied for the fabrication of the prototypes of artificial neural superposition eyes. The set of lithography masks for the different layers

of the ANSE were generated by electron-beam lithography. For the creation of the aperture arrays, a black-matrix polymer resist is spun on a thin glass substrate wafer. The resist is removed at the aperture positions of the arrays and opaque material remains at the intermediate area, after a UV-lithography and development step. A similar process is applied for the color filter arrays. Aperture openings with diameters of a few microns have to be realized by a process chain that includes sputtering metal (such as chromium or titanium), overcoating with photoresist, UV-lithography, development and subsequent etching. The pinhole diaphragm arrays were created on the backside of the glass wafer in that way. For the microlens arrays, a thin resist layer on a carrier substrate is exposed by UV-light through a chromium mask and binary structures (photoresist cylinders) result at the positions of the lenslets after a chemical development step. The subsequent reflow creates smooth surface reliefs for all spherical microlenses in parallel [137]. After that, a negative copy of the MLA master structure is casted in an elastomer for the replication tool. The final MLAs is formed by UV-molding on top of the wafer with the aperture array on the front and the pinhole array on the backside. A UV-polymer is spun on the front side of the substrate wafer. The relief is filled after the stamp has been brought into contact with the liquid polymer layer, and UV light is applied through the transparent stamp in order to cure the polymer [138, 139]. Subsequently, the tool and the replica are separated by demolding.

The color filters can be applied pixel-wise on the backside of the optics module but a channel-wise structure was chosen because it is easier to fabricate due to its larger scale. The filter material was chosen because it can be structured by UV-lithography and filter transmission properties are suitable for color imaging applications (Fig. 4.4).
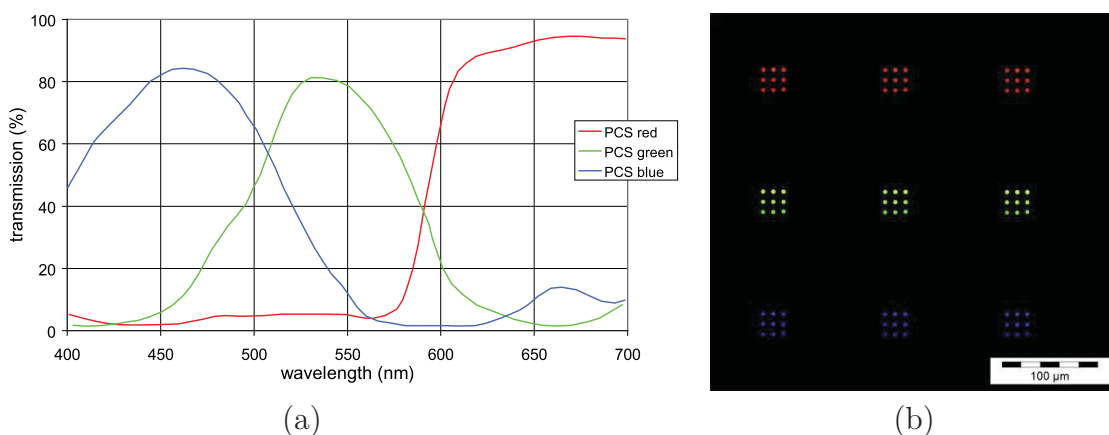
Figure 4.4: (a) Spectral transmission curves of the polymer color filters for a thickness of 1.5 µm (source: Brewer Science Inc.) [140]. (b) Microscopic view on the pinhole group array. The distance between two pinholes of one group and the pinhole diameters are 10.6 µm and 3 µm, respectively [140].

After the fabrication on wafer level, the individual optical modules were diced out from the wafer and were actively aligned and bonded to an optoelectronic image sensor which

is shown in the left part of Fig. 4.5. Alternatively, a temporarily alignment setup was used in order to characterize several objectives with the same image sensor (Fig. 4.5 on the right). The image sensor was positioned on a stage allowing for three axes translation and rotation. A vacuum holder was used in combination with a three axes piezo-electric actuator in order to align the optics module. During the active alignment, the image of an homogeneously illuminated white plane in object space was observed. The homogeneity and brightness of the image determined when the optics was well aligned with respect to the sensor.

| (a) | (b) |
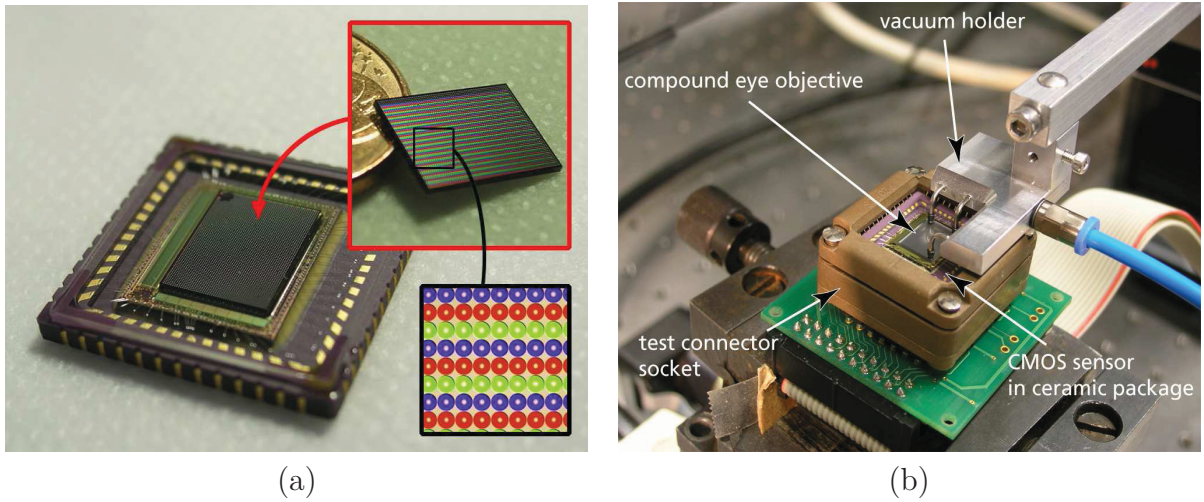
Figure 4.5: (a) ANSE optics module for color imaging (red box) directly attached to CMOS image sensor (type Saentis, ZMD). The microlens array with integrated color filters is shown in the inset (black box) [140]. (b) Lab setup for the alignment, assembly and characterization of the ANSE [140].

The system parameters and alignment tolerances are presented in Tab. 4.1.

Table 4.1: Parameters of selected ANSE prototype systems and tolerances of the alignment on the image sensor.

Property	ANSE color	ANSE SNR
Redundancy m_0	5	5
Microlens diameter [µm]	125	125
F-number	2.5	2.3
System length [µm]	450	400
No. of channels	70 x 53	70 x 53
No. of image pixels	52 x 43	60 x 43
Effective FOV	23°x21°	24°x21°
Footprint size [mm^2]	8.9 x 6.7	
Pinhole diameter [µm]	3	
Lateral tolerance [µm]	±3	
Axial tolerance [µm]	±10	
Horizontal rotation	±0.04°	

4.1.3   Demonstration of Increased Sensitivity and Color Imaging

The rearrangement and averaging of the gray values of pixels with a common viewing direction was implemented in a software read-out interface using a Matlab™ script. The dark signal non-uniformity (DSNU) was corrected by the subtraction of a dark frame and the fixed-pattern-noise (FPN) was reduced using a single flat-field correction (FFC) (see Appendix B). Thus, the individual pixel values of each frame were multiplied by correction factors which had been calculated from a series of frames under homogeneous illumination for a fixed integration time T_{int}.

On the left of Fig. 4.6, captured test images are qualitatively compared in case that the camera is used with and without redundant sampling.
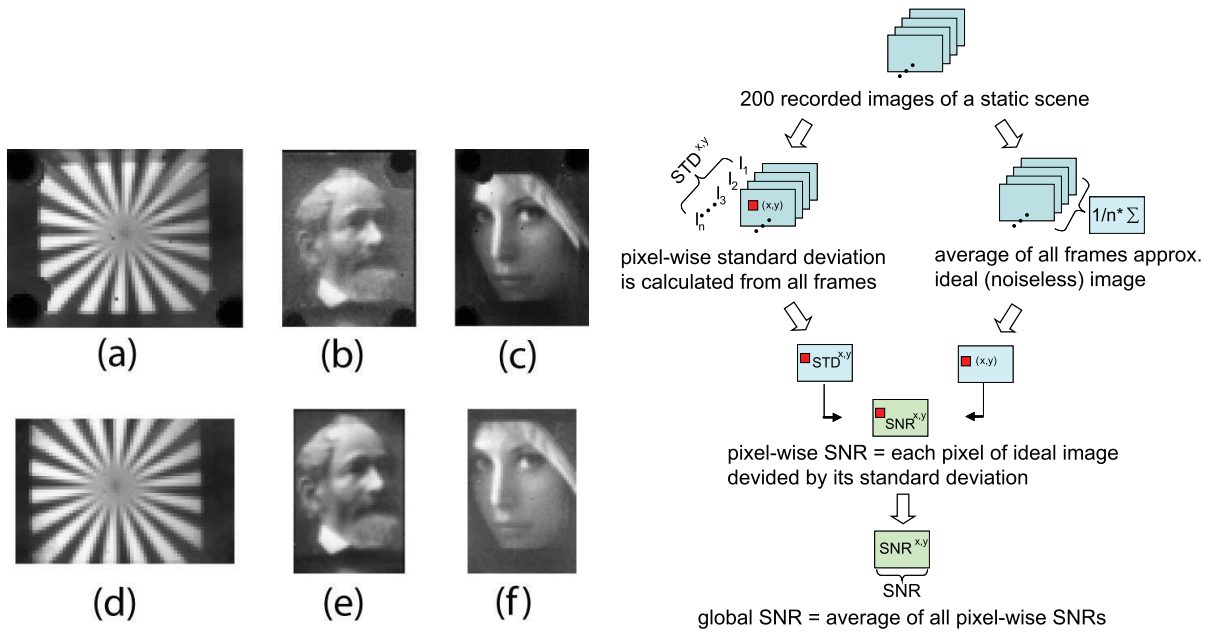
Figure 4.6: **Left:** Captured test images: Siemens radial star target (left), an image of Carl Zeiss (middle) and "Image Processing Lena" (right). (a),(b) and (c): Images from artificial apposition compound eye (APCO) with each image pixel recorded from one pixel per channel. The image resolution is 70x53 pixels. (d), (e) and (f): Images from artificial neural superposition compound eye (ANSE) - each image pixel is an average of nine pixels from different channels. The image resolution is 60x43 pixels. The fixed-pattern noise (FPN) has not been subtracted in (b) and (e) [140]. **Right:** Schematic algorithm for calculating the signal-to-noise ratio (SNR) from an image sequence [140].

The number of final image pixels $(N_x; N_y)$ of the ANSE is lower than the number of optical channels $(K_x; K_y)$ which is due to missing partner channels for the superposition at each margin of the microlens array. The number of pixels in the final image of the ANSE is therefore given by:

$$N_x = K_x - 2m_0; \ N_y = K_y - 2m_0 \ . \tag{4.3}$$

This is noticeable in the difference of the dimensions of e.g. Fig. 4.6(b) and 4.6(e).

The benefit of the averaging process was measured from an image sequence by comparing the signal-to-noise ratio (SNR) of the APCO with that of the ANSE. The right side of Fig. 4.6 illustrates the way how to derive such a parameter for a 2D image sequence.

First, a large number of images of the same scene was acquired. The fixed pattern noise was subtracted using a FFC (see Appendix B). The standard deviation of each pixel was calculated with respect to its variation across all frames. Additionally, the ideal (noiseless) image was approximated by averaging over all frames. Subsequently, the SNR was calculated from the ratio of the pixel value in the ideal image and the standard deviation of that pixel. The SNR was then integrated over a region of interest in the image to give the global SNR. The last step is advantageous in order to reduce the influence of a spatially varying illumination on the SNR.

It should be noted that even with the fixed-pattern noise included, the average of pixel values will lead to an increased SNR, but the amount of increase is difficult to predict because the FPN of spatially separated pixels is not uncorrelated Gaussian distributed [69]. Nevertheless, the image displays less FPN because the offset between adjacent pixels in the final image is reduced after the averaging process. An LED with collimation and homogenization optics was used to illuminate a white screen. In this way, variations of the illumination, flickering or surging amplitude and a resulting shift of the average gray value of individual frames in the sequence was prevented. The distance to the screen was adjusted at about 1.3 m in order to fill the FOV of the camera. The measured SNRs for the read-out of one pixel per channel and for the redundant sampling mode are shown in Fig. 4.7a as a function of integration time. The increase of the SNR, which is given by

$$SNR_{\text{increase}} = \frac{SNR_{\text{ANSE}}}{SNR_{\text{APCO}}} \ , \tag{4.4}$$

ranges from 2.7 to 4 which is in good agreement with the predicted factor of 3. The deviation is caused by residual fixed-pattern noise and the spatial inhomogeneity of the illumination.
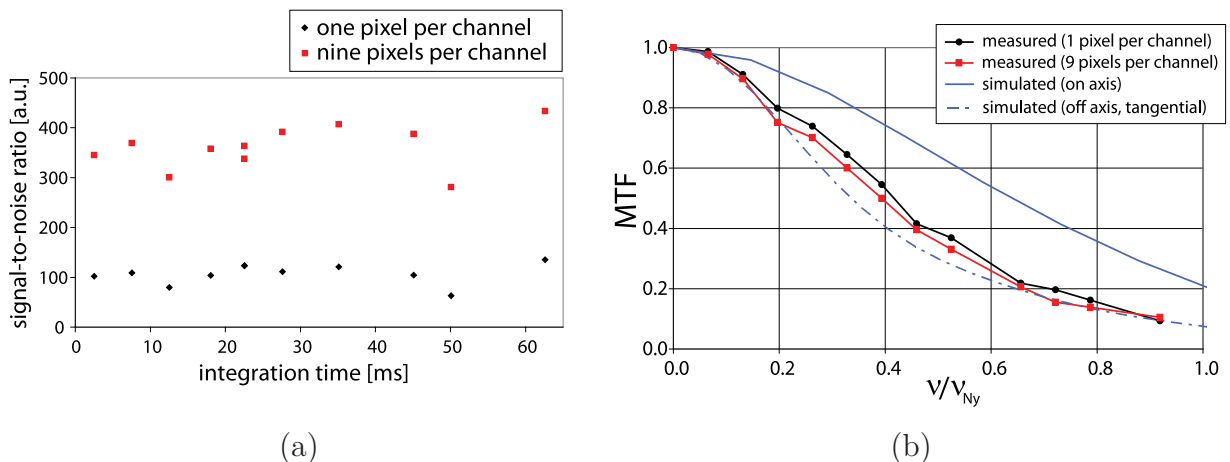
Figure 4.7: (a): The measured signal-to-noise ratio (SNR) as a function of the integration time for the APCO (black diamonds) and the ANSE (red squares) [140]. (b) Measured and simulated MTF (polychromatic, spatial frequency normalized to Nyquist frequency $\nu_{Ny} = 1.28$ cycles/degree) for one pixel per channel (APCO) and nine pixels per channel (ANSE SNR). Both measured curves result from a measurement of an average MTF across all channels which approaches the tangential off-axis simulation rather than the on-axis curve. There is no severe difference between both MTFs [140].

The resolution of the system was measured by imaging bar charts of several spatial frequencies in both modes. The MTF was subsequently determined from the image contrast [73]. A comparison of measured and simulated MTF curves is found in Fig. 4.7b.

The difference between the MTF curve of the APCO and that of the ANSE is less than five percent and thus in the range of the measurement accuracy. It is caused by deviations of the acceptance angles of the individual pixels due to variations of the pinhole diameter and radii of curvature of the lenslets. In other words, each pixel images a field of slightly different size leading to a blur in the post-processed image. Variations of 5% for the pinhole diameter and 1.3% for the radii of curvature were measured by inspection with a microscope and stylus measurements, respectively.

The software read-out was adapted for the color imaging artificial neural superposition eye (ANSE color) by the implementation of a different pixel rearrangement in the color planes. An additional white balancing was carried out together with the FPN correction. Example color images that were captured on the test bench are shown in Fig. 4.8.
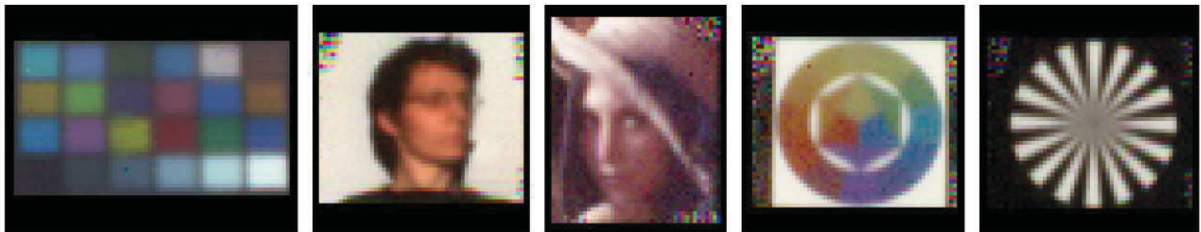
Figure 4.8: Images captured with the color imaging artificial neural superposition eye (ANSE color): From left to right: Macbeth color chart, a self-portrait, "Image Processing Lena", a color mixing circle and a radial star pattern. The left image has a resolution of 70x39 pixels (preliminary prototype), all others are 52x43 pixels. Color artifacts in the corners of the images are caused by the vacuum holders that covered some optical channels during the alignment of the optical module to the sensor. After fixation, the holders can be removed and the artifacts disappear (see left image) [140].

The number of pixels in the final color image is lower than the number of optical channels according to Eq. (4.3) e.g. $N_y = K_y - 2m_0$. The rescaling is limited to one dimension as only three pixels need to be superimposed in order to yield a full color sample for one object point along each column of the array. There is no superposition along the rows.

The modulation transfer function (MTF) of the ANSE color was measured for bar charts of different color (Fig. 4.9). Due to the small FOV, a simple microlens array with spherical lenslets was used, which explains the difference between on- and off-axis MTF curves. The image quality suffers from aberrations like astigmatism and field curvature for the larger angles of incidence.
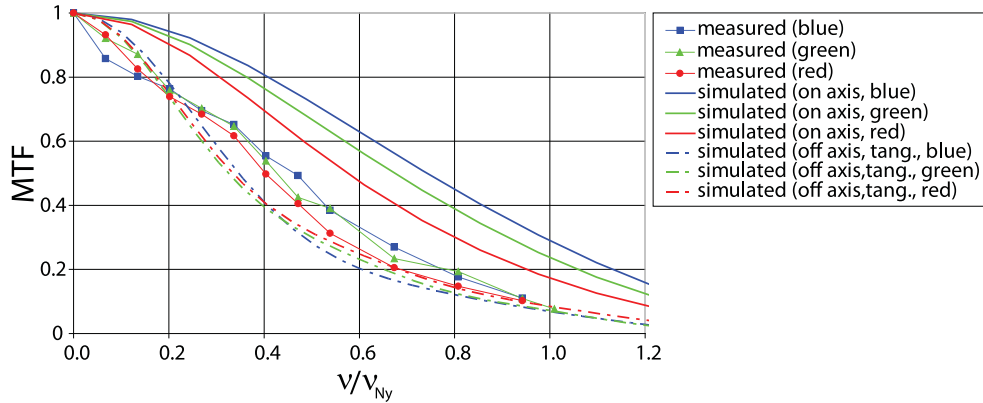
Figure 4.9: Comparison of measured and simulated MTF for the ANSE color (with a Nyquist frequency of $\nu_{Ny} = 1.28$ cycles/degree). The simulations are done for the three wavelengths: $\lambda_1 = 455$ nm for blue, $\lambda_2 = 530$ nm for green and $\lambda_3 = 680$ nm for red. The off-axis simulation was carried out for a field angle of 13.6 degrees tangential [140].

The measured MTF curves lie in between the simulated on and off-axis MTF curves. Several issues are responsible for that. Due to the low number of pixels in the captured images, the determination of the MTF needs a spatial integration over 80% of the image and thus the determined MTF is averaged over that image area. Contrasting to the simulation, the image acquisition for a single color (R, G or B) is not monochromatic due to the spectral distribution of the light source and the transmission curve of the color filter array (Fig. 4.4 left). Hence, the measured single color MTFs are additionally averaged over a certain spectral range.

4.1.4   Contrast Enhancement by Image Deconvolution

Although, the ANSE successfully increases the sensitivity when compared to that of artificial apposition compound eyes, the drawback of a low image resolution remains. With that given optical limitations, image processing can be used to further enhance the image contrast. A Wiener filter was chosen for the processing of an image restoration because it is known to give good results if the degradation by the system is known and it takes into account noise that is introduced in the detection step [60]. Details about the filter can be found in Appendix G. Additionally, after the noise parameter p_n was chosen manually for an example image, the filter can be implemented in real time because it simply requires two Fourier transforms. The results of filtered images are shown on the left side of Fig. 4.10. Both, the images captured with a single pixel per channel (APCO) and the superimposed images of the ANSE SNR prototype were filtered. The image contrast was increased in both cases. However, as the inverse filtering is sensitive to noise [60], the filtered APCO images display strong noise whereas the filtered ANSE images are smooth and less noisy due to the increased SNR. The filter enabled to increase the measured MTF performance up to about 25% for the mid spatial frequencies (see right side of Fig. 4.10).
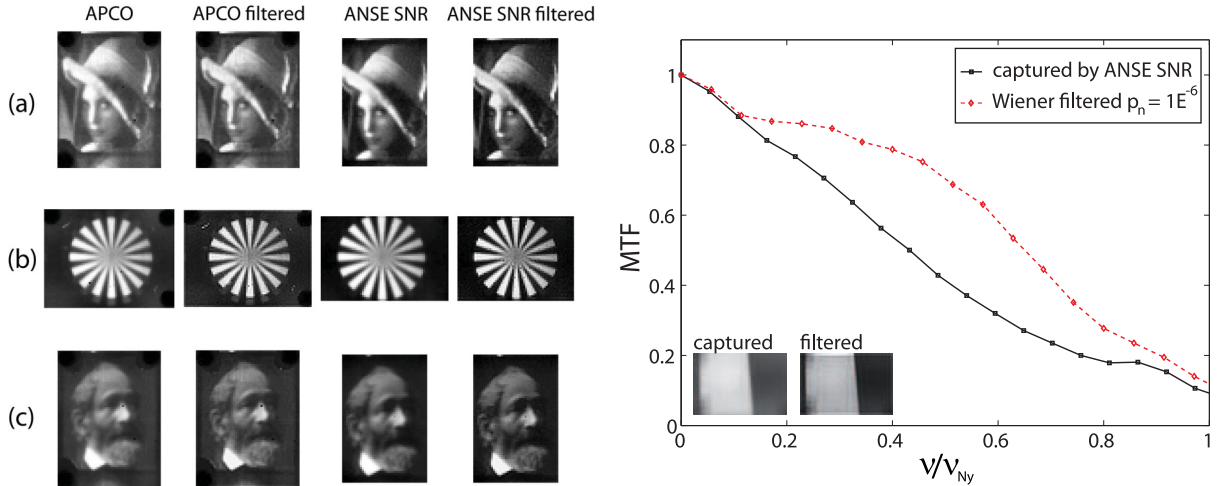
Figure 4.10: **Left:** Experimental images that were originally captured and deconvolved using a Wiener filter (filtered). Left pairs were captured without (APCO) and the right pairs with artificial neural superposition (ANSE). Rows (a), (b) and (c) show different motifs which were processed in the same way. **Right:** MTF curves measured for a captured image of a slanted edge (black line) and the same image after deconvolution with a Wiener filter (red, dashed line).

4.2   Electronic Cluster Eye (eCLEY)

The APCO offered the shortest total track length by applying a single pixel per optical channel (which means a minimum possible number of pixels per channel). On the other hand, a single aperture imaging system combines all pixels in a single optical channel (which is the maximum number of pixels per channel) with a comparably large total track length. The gap in between those extremes is filled by the multi aperture imaging systems which use electronic stitching of segments. Here, a partial image of a certain number of pixels is captured in each channel. The partial images are then flipped and stitched together by means of software processing which lead to the name - *electronic cluster eye* (abbreviated *eCLEY*). The increased sampling which is introduced by the braided FOVs of adjacent optical channels is advantageous for achieving a short total track length compared to a single aperture optical imaging system (see Sec. 3.2.4). In the practical realization, a braiding factor of $k = 2$ was chosen so that the effective pitch difference is

$$\Delta p_{eff} = \frac{p_{px}}{2} \quad \text{and} \quad \Delta p_K = \frac{n_g p_{px}}{2} \; . \tag{4.5}$$

Thus, the sampling in object space is effectively doubled and the total track length can be reduced to about a half of that of comparable single aperture optics. The substitution of Eq. (3.16) into Eq. (3.15) yields the non-linear dependance of the focal length of the eCLEY on the total number of pixels (e.g. N_x along the x-dimension) of the final image. This is illustrated in Fig. 4.11. The higher the output image resolution, the stronger the focal length has to be increased in order to achieve a sufficient angular sampling resolution for a given FOV.
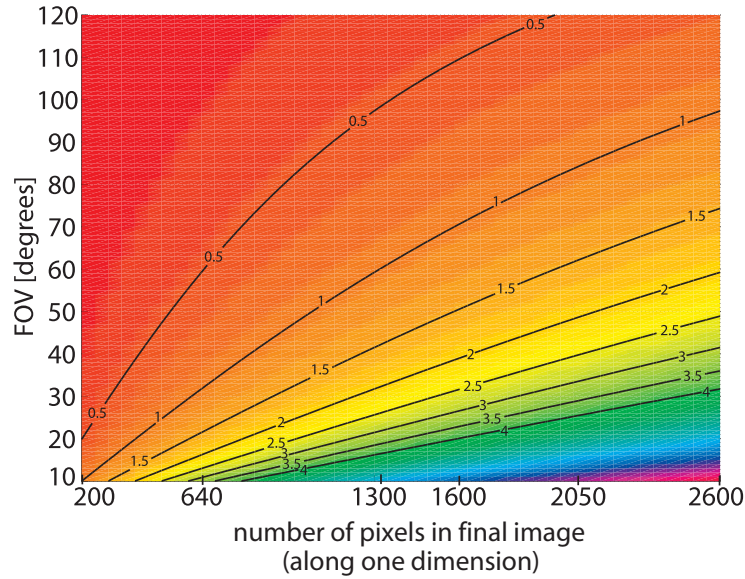
Figure 4.11: Effective focal length of the eCLEY as a function of the number of resolvable pixels in the image (along one dimension) and the size of the field of view (FOV). Each contour line displays a constant focal length of the indicated value in [mm]. The following parameters were used: $F/\# = 2.8$, wavelength $\lambda = 0.55$ µm, pixel pitch $p_{px} = 1.75$ µm and braiding factor $k = 2$.

For current demonstrations, commercially available image sensors had to be used so that a pixel array of larger resolution was needed for a certain resolution of the eCLEY. In that case, the scaling behavior of the required image sensor format and the linear fill factor Γ can be derived as a function of the eCLEY's image resolution and the number of pixels per channel from the trade-off which is shown in Fig. 4.12.
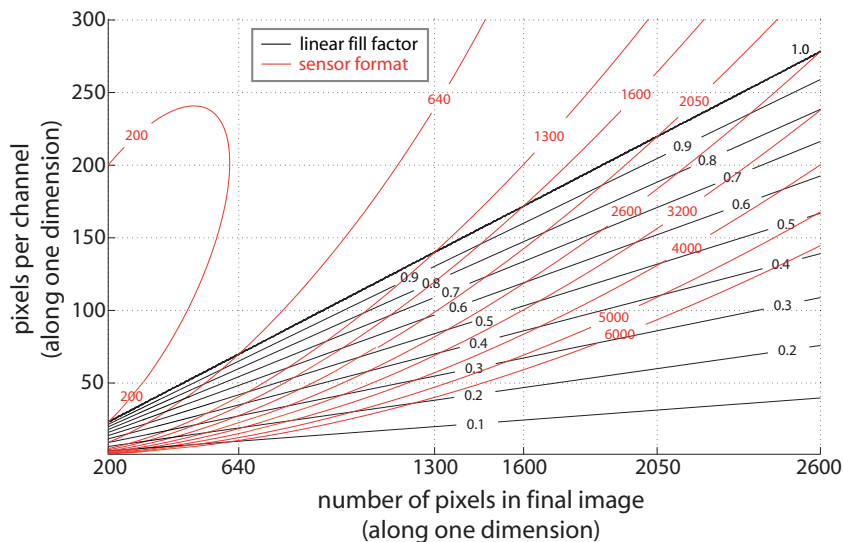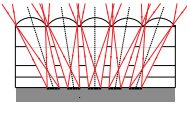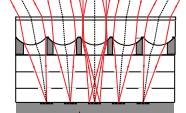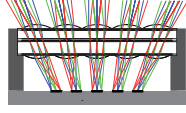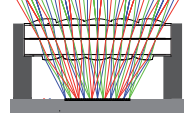
Figure 4.12: Lateral scaling behavior of the eCLEY when using commercial image sensors. The linear fill factor Γ (black lines) as well as the sensor format size in pixels along one dimension (red lines) are shown as functions of the final image resolution (x axis) and the number of pixels per channel (y axis). The bold black line marks the case of a maximum fill factor of $\Gamma = 1$. The system parameters are: FOV of 70°, $F/\# = 2.8$, wavelength $\lambda = 0.55$ µm, pixel pitch $p_{px} = 1.75$ µm and $k = 2$. The labels on the x axis relate to standard image formats, in ascending order: 200P, VGA, 1.3MP, 2MP, 3MP and 5MP.

The number of pixels per optical channel is a linear function of the total image pixel number for a constant fill factor. The same applies to the number of optical channels itself according to Eq. (3.8). However, as the focal length is increasing in a non-linear fashion with growing total pixel number (Fig. 4.11) and it is coupled to the diameter of a lenslet via the f-number, each channel consumes a non-linearly increasing amount of footprint area on the chip. Thus, the image sensor format scales non-linearly with the image resolution of the eCLEY. In other words, Fig. 4.12 indicates that the eCLEY principle becomes uneconomic for very high image resolutions because the advantage of achieving a short total track length has to be paid by an increased consumption of lateral space on the sensor chip which is dominating the costs of the camera. However, by decreasing the pixel pitch it becomes possible to achieve a certain MP resolution with the principle of electronic cluster eyes while still making economic use of image sensor area.

4.2.1   Optical Design for Thin Wafer-Level Camera Optics

Starting with the analytical relationships of Sec. 3.2, an optical design study was executed in order to explore the possible solution space. Four different configurations were selected for the optimization and simulation using ray-tracing methods. The Table 4.2 lists their basic properties. Two of the described optical designs have been realized, namely the

Table 4.2: Investigated optical designs for eCLEYs of different complexity and resolution.

Demonstrator	eCLEY 200p	eCLEY VGA	eCLEY 1MP	eCLEY 720p
Diagonal FOV [°]	65	70	64	70
F-number	2.4	3.7	2.8	2.8
Image resolution [pixels]	200 x 200	660 x 500	1200 x 840	1440 x 864
No. of channels	23 x 23	17 x 13	13 x 9	15 x 9
No. of pixels/channel	9 x 9	39 x 39	93 x 93	96 x 96
Pixel pitch [µm]	3.2	3.2	2.2	2.2
Total track length [mm]	0.47	1.42	1.67	1.92
Footprint size [mm^2]	3.5 x 3.5	6.8 x 5.2	11.5 x 8.0	8.0 x 4.9
Lenslet diameter* [mm]	0.131	0.375	0.840	0.514
FOV per channel [°]	5.3	7.8	9.0	9.2
2D optical fill factor [%]	5	14	8	31
Layout				
Microlenses/channel	1	1	3	2
Microlens shape	toroidal	toroidal	toroidal	free-form, polynomial

*Value for the center microlens of the front microlens array.

eCLEY 200p and the eCLEY VGA. In terms of image resolution, the eCLEY 200p is the counterpart of former APCO but with the advantage of a three times smaller lateral footprint size (Fig. 4.13a). Due to the larger number of pixels per channel, the information capacity of the counterpart is 200% higher than that of the APCO and the 2D optical fill factor of an eCLEY is generally up to two orders of magnitude higher (compare 0.34 % from Tab. 3.1 to values of Tab. 4.2). The eCLEY VGA was designed with the specifications of a wide angle camera module for VGA resolution (640x480 pixels). In contrast to placing the aperture stop at the lens (like in the eCLEY 200p), a new degree of freedom is necessary for achieving the higher image resolution. Thus, the stop was moved to a position in front of the lens where the coma for an off-axis field is nearly completely corrected ($t \neq 0$ in Eq. A.3 in Appendix A). A tuning ('chirp') of the tangential and sagittal radii of curvature of each microlens according to its individual viewing direction was carried out in order to compensate for astigmatism and field curvature for the central viewing directions of all channels [96, 98]. A material with high refractive index (Exfine CO160, $n = 1.633$ at $\lambda = 588$nm) was used for the lenslets in order to minimize residual field curvature across the limited field inside each channel. Additionally, the reversed microlens array causes a higher telecentricity because ray bundles are refracted at the substrate front face before hitting the individual microlens and the substrate acts as a cover glass (Fig. 4.13b). Details about the simulated resolution as a function of field angle can be found in Appendix H.
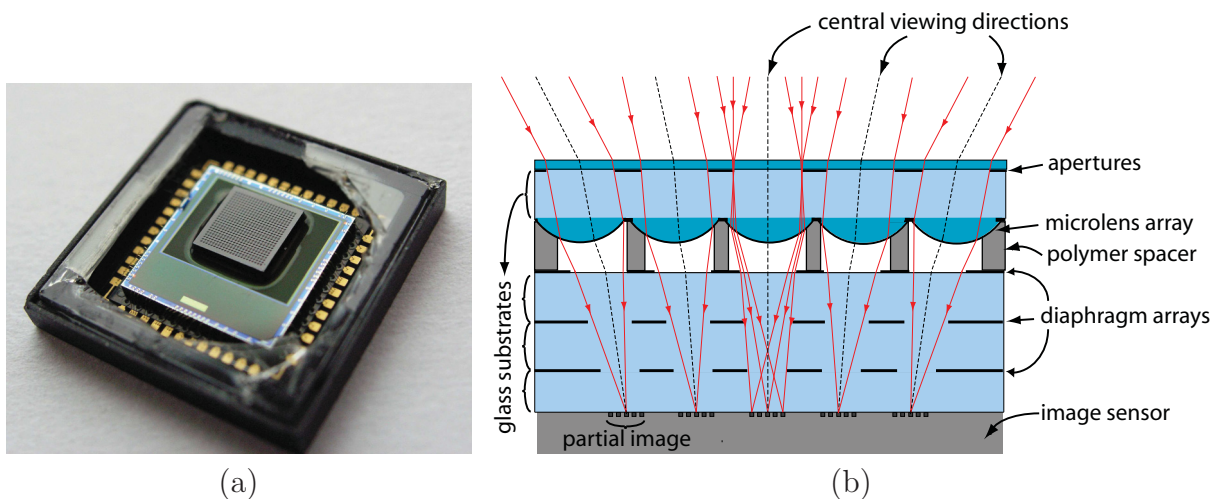
Figure 4.13: (a) Photograph of the eCLEY 200p optics chip attached to a CMOS image sensor. (b) Schematic cross section of the optical layout of the eCLEY VGA demonstrator. The optical module consists of two components: the microlens array with aperture array and a spacer stack containing the diaphragm arrays. Both are fused by molded polymer spacers.

Besides the simulation of the optics MTF, spot diagrams and distortion, a non-sequential ray-tracing model was created to optimize the suppression of optical crosstalk. A fill factor $\Gamma \leq 0.4$ was chosen as a starting point. The axial position and the size of the openings of three additional diaphragm arrays were optimized for a sufficient suppression of crosstalk. An additional aperture array on the front side of the MLA substrate absorbs light which would otherwise hit the intermediate space between lenses and, thus, would cause stray light. The simulation methods have been described in Sec. 3.3.4.2. Some results of the

ghost analysis of the final setup are shown in Fig. 4.14. An analysis of the simulated final image yields a moderate veiling glare index of 3.3%.

(a)   (b)
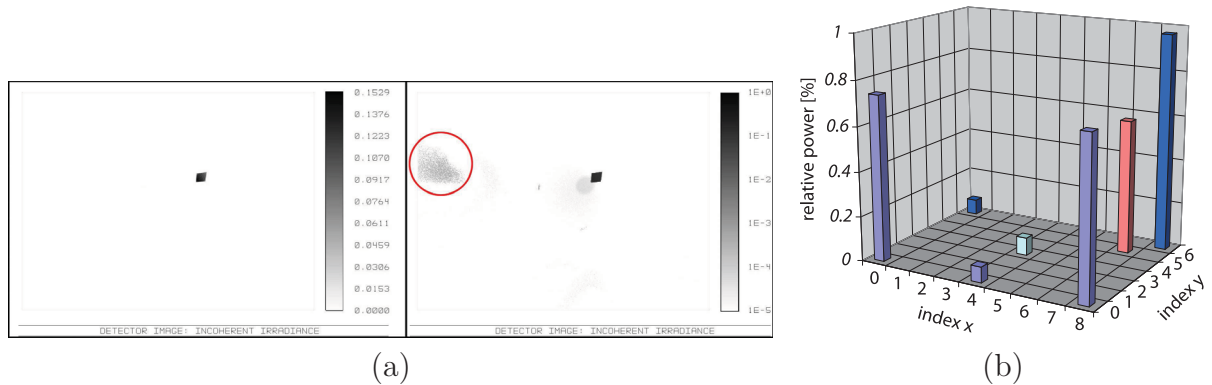
Figure 4.14: (a) Crosstalk analysis simulation using a reversed ray-tracing of 50 million rays starting from the image plane of the maximum diagonal channel into a random direction. The ghost is not visible for a linear intensity scale (left) but for a logarithmic scale (right). Inverse grayscale is used for display. (b) Summary of several crosstalk simulations for different channels (indices on x and y axes). The radiant power of the ghost is measured relative to the power of the intended image. Due to the symmetry, only a quarter of the full array was used with index (0,0) being the center channel. The strongest ghost reaches a maximum of about 1 % of the radiant power of the intended image.

The non-sequential model was also used for testing the image stitching and distortion correction algorithm from simulated images (Fig. 4.15).

(a)   (b)
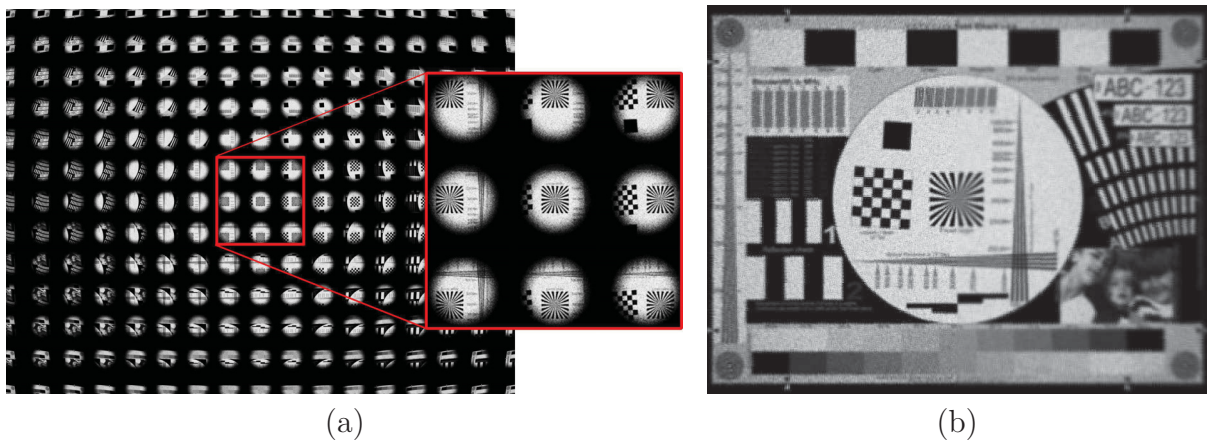
Figure 4.15: Simulated images of the eCLEY using a non-sequential ray-tracing method and a two-dimensional representation with Lambertian illumination for the target object. (a) The simulated image of a CCTV test chart as captured from the image sensor. The inset shows a magnified section. (b) The final image after applying the stitching algorithm. The right half of the image includes the simulation of diffraction blur. The final image resolution is 660x500 pixels. About 12 billion rays were traced to obtain the result.

4.2.2   Fabrication of eCLEY with VGA resolution

The fabrication of master structures and replication tools was carried out with photolithography and reflow according to the description in Fig. 4.3. However, the two main components of the system were processed separately: The MLA wafer which makes up the front part of the stack and the spacer wafer which is a laminate of three glass substrates. The

diaphragm arrays were structured on both sides of a first glass wafer with UV-lithography using a black-matrix polymer resist (PSK 2000, Brewer Science). A second unstructured wafer was bonded after coating the structured wafer with a thin adhesive layer and another diaphragm array is structured on the plain side. Subsequently, the lamination was repeated for a third glass wafer forming a spacer wafer with a total thickness of 1.1 mm. Meanwhile, the MLAs and polymer spacers of 20 µm height were molded in two steps on a second pre-processed glass wafer. Finally, the microlens wafer was integrated upside down with the glass spacer substrates on wafer level. The shallow polymer spacers on top of the MLAs cause the necessary air gap between the two components. Such a chain of vertical integration of binary and continuous microstructures has been demonstrated for the first time on wafer level. The resulting optics wafer stack was diced (see Fig. 4.16a) and single optics chips were aligned to the 3MP image sensors (Micron MT9T001, Fig. 4.16b).

(a)   (b)
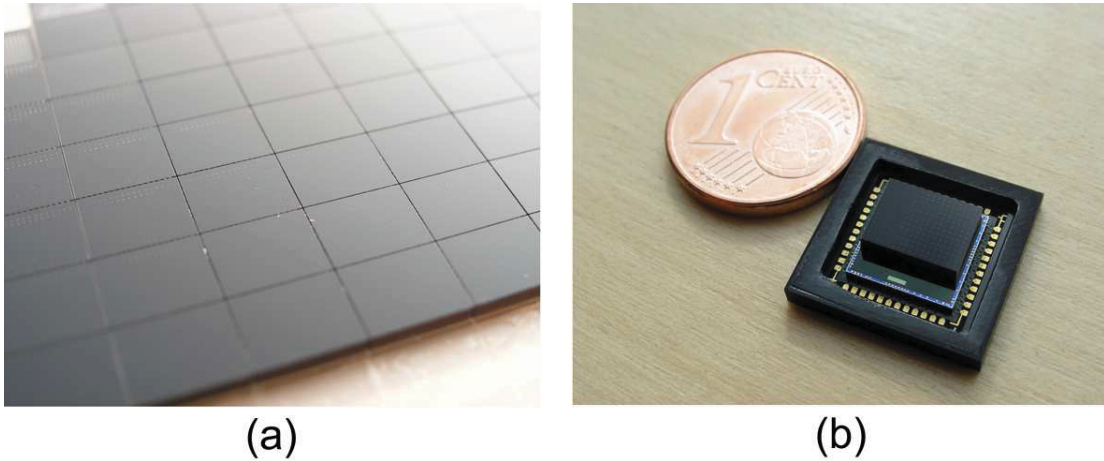
Figure 4.16: (a): Diced wafer with several optics modules of the eCLEY VGA [141]. (b): Size comparison between the eCLEY VGA assembled on an image sensor array and one-cent coin [141].

4.2.3   Software Distortion Correction and Image Stitching

As discussed in paragraph 2.2.1.1, distortion is proportional to the third power of the field coordinate h [Eq. (2.13)]. However, the center of each channel of the eCLEY is directed at a chosen field point h_i and it varies only by a small amount Δh within the field of view of a single channel, so that the aberration term of distortion of the i'th channel is

$$\delta_{distortion}^i = \frac{R}{n} \cdot a_{311} \cdot (h_i + \Delta h)^3 = \frac{R}{n} \cdot a_{311} \cdot (h_i^3 + 3h_i^2 \Delta h + 3h_i \Delta h^2 + \Delta h^3) \ . \qquad (4.6)$$

A section along one main axis of the MLA is assumed, for simplicity. The distortion of the i'th optical channel is split into a sum of four contributions: A constant offset of the partial image position ($\propto h_i^3$), a linear ($\propto h_i^2 \Delta h$), a quadratic ($\propto h_i \Delta h^2$) and a cubic distortion ($\propto \Delta h^3$) [142]. The offset of the partial image is corrected by the channel-dependent pitch difference between the partial image and the microlens in the optical design because h_i is constant for each individual channel. Additionally, for off-axis channels the condition $\Delta h << h_i$ is fulfilled and the linear term ($\propto \Delta h$) in Eq. (4.6) is the dominating part of

the distortion of the individual channel.

Partial image distortion has to be corrected in order to yield a good stitching of image details from the braided sampling of the scene by the eCLEY. A bilinear spatial transformation is used for the software distortion correction because for the above reason it is a good approximation and it is simple and fast.

$$\widetilde{x} = c_1 x + c_2 y + c_3 xy + c_4 \tag{4.7}$$

$$\widetilde{y} = c_5 x + c_6 y + c_7 xy + c_8 \tag{4.8}$$

The variables x, y and $\widetilde{x}, \widetilde{y}$ denote the undistorted and distorted coordinates, respectively. The coefficients c_i of the transform can be calculated from solving the equation system for four different reference points. Once the coefficients are known, the inverse transform is able to create an undistorted image from the distorted input image. In practice, the eight coefficients are tabularized for each optical channel. Furthermore, an interpolation step is necessary after the spatial transform because the equidistant pixel grid of the captured image is transformed into a non-equidistant grid. The exactness of the correction depends on the accuracy of the model in relation to the physical distortion and the method of interpolation. If the calculation is carried out for each color plane individually, the correction of lateral chromatic aberration is feasible by the same procedure as it is linearly dependent on the field coordinate h (Tab. A.1 in Appendix A).
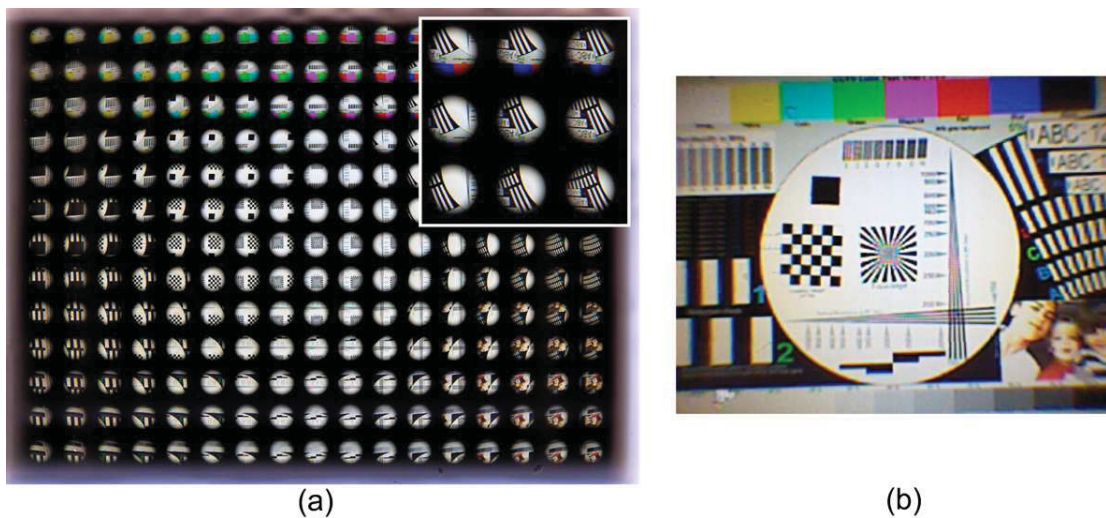
Figure 4.17: Image of a CCTV test chart which was captured with the prototype of the eCLEY VGA. (a): Image as it is recorded by the image sensor with a full resolution of 2050x1540 pixels. The inset shows a magnified section of the 17x13 partial images [141]. (b): Final image (660x500 pixels) after distortion correction and image stitching [141].

The initial image processing pipeline contained: (1) Bayer-demosaicing and color correction done by the sensor read-out software, (2) extraction of the partial images from the full image matrix (Fig. 4.17a), (3) channel-wise bilinear correction of distortion, (4) channel-wise linear interpolation of undistorted partial image pixels on regular sampling grid and (5) mapping of the undistorted pixels of each partial image into the final image matrix including horizontal and vertical flipping as well as braiding. The last step uses the deterministic

algorithm of increased (braided) sampling in order to resemble the original neighborhood of each pixel in object space. A result example is shown in Fig. 4.17b.

4.2.4   Experimental Characterization of eCLEY VGA

The processing time for the distortion correction, interpolation and image stitching was measured to be 20 ms (Intel CoreDuo machine 2.66 GHz) which makes it feasible for real-time capture and display. Processing and capturing frames can be interlaced so that frame rates of > 30 fps are possible on standard hardware.

Some defects like edge displacements ('zipper artifacts') and color aliasing were found when examining the image quality (see star in the center of Fig. 4.17b). However, they are very difficult to quantify. They arise from irregular sampling over the object field which is due to a combination of distortion correction and parallax between adjacent channels [143]. Recent enhancements of the distortion and parallax correction algorithm lead to an improved stitching without zipper artifacts and the possibility for software focusing without moving parts [143, 144].

The suppression of optical crosstalk was tested using a collimated HeNe-LASER source in front of the eCLEY prototype which was mounted on a goniometer in order to change the angle of incidence for the illumination. The first ghost images appeared for large integration times so that a suppression factor between the ghost image and the signal of about 1:20,000 was determined. The difference between the measured value and the simulation results from the fact that the simulated light source in the image plane emitted rays into the half space whereas the real image sensor pixels have a finite angular sensitivity. Thus the simulation is a worst case scenario. Additionally, the eCLEY was used for image capture outside on a bright sunny day (see left of Fig. 4.18) which is one of the most challenging scenarios for stray light and crosstalk and it is close to practical use.
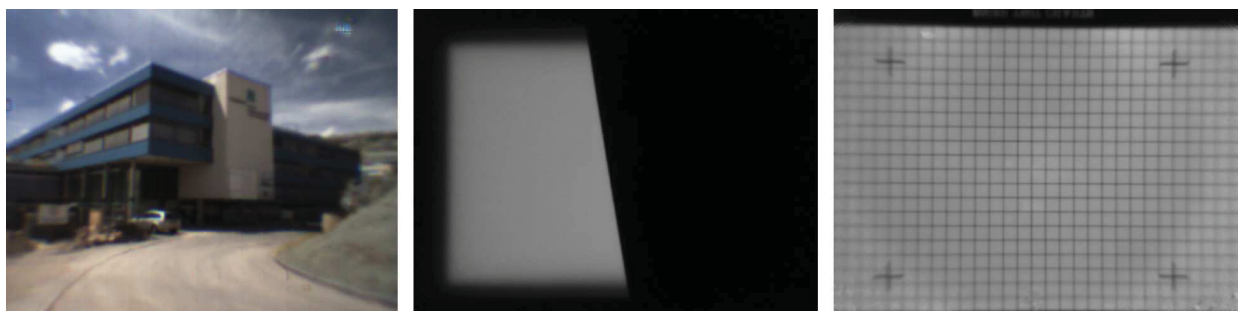
Figure 4.18: Images captured with eCLEY VGA prototype. **Left:** Snapshot of the Fraunhofer Institute IOF in Jena [141]. **Middle:** Slanted edge chart as used for the MTF measurements. **Right:** Image of a regular grid for measuring distortion.

MTF performance

The modulation transfer function of the eCLEY VGA was measured using a slanted edge target (according to ISO 12233) [145]. The results for two field positions are shown in Fig. 4.19. The simulated MTF curves (shown as red solid line) were derived from ray-tracing

software for a single object field coordinate using a calculation method which accounts for diffraction. In order to measure solely the optics MTF (illustrated by black squares), the optical module was placed in the center of a rotation table and the partial image plane of a selected channel was relayed on a CCD camera chip by a 40x microscope objective. Hence, the partial image of the edge object that was created by a single optical channel of the eCLEY was captured with high magnification. The third MTF curve (blue triangles) was measured in the final image of the assembled prototype with the optics mounted to the CMOS image sensor. It includes the influence of the whole image processing chain.

The Nyquist frequency of the system is 312.5 cycles/mm because the effective pixel pitch in the final image is half of the sensor pixel pitch (3.2 µm) due to the braiding factor $k = 2$. The measured single channel optics MTF resembles the simulated MTF well. There is a systematic offset of less than 10 % which is caused by fabrication tolerances and residual defocus due to an incorrect spacer thickness. A significant reduction of the total MTF (by up to 30 %) is caused during the image acquisition by the image sensor. The reason is the aperture MTF of the image sensor pixels as well as a further reduction of spatial resolution due to pixel crosstalk and effects of the Bayer CFA (Fig. 4.20a).
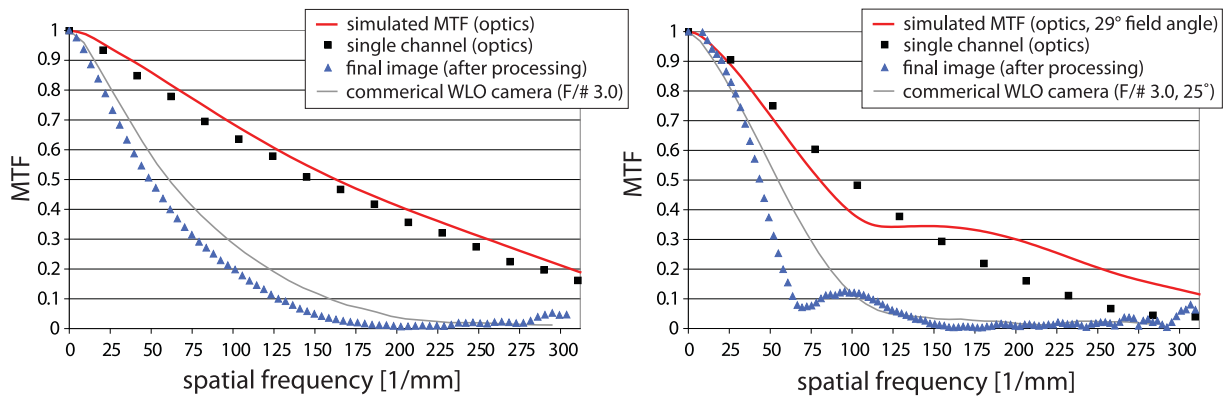
Figure 4.19: **Left:** Comparison between different polychromatic on-axis MTF curves for the eCLEY VGA [141]. **Right:** The same for an off-axis field with an angle of incidence of 29°. Solid red line: Simulated optics MTF for the specific angle of incidence. Black squares: MTF of the optics measured without image sensor. Blue triangles: MTF measured in the final image of the fully assembled prototype (optics and image sensor) including image post-processing. Thin solid gray line: MTF measured from a commercial camera module [146] using the same method. The object distance was 25 cm for all measurements.

It has to be noted that the optical fill factor of the image sensor pixel is not exactly known and thus its influence on the MTF is uncertain. The MTF performance is further decreased by about 10-15 % due to the partial image distortion correction and stitching algorithm (Fig. 4.20a). Although the fabricated optics module has the ability to transfer spatial frequencies higher than the system Nyquist frequency, the MTF of the final image vanishes at about the image sensor Nyquist frequency of 156 cycles/mm in Fig. 4.19. The number of resolvable image points is calculated from the measured MTF according to Appendix I. Another MTF curve (gray line) was added in Fig. 4.19 for comparison with a commercial single aperture WLO camera module with VGA resolution and a total track length of 2.2 mm (OmniVision OVM7690 CameraCube™ [146]). It yields a 10 % advance at mid spatial

frequencies over the MTF of the final (braided) image of the eCLEY VGA. However, the images of the WLO camera contain more noise due to the small pixel size of 1.75 µm.

Distortion and relative illumination

The distortion was measured in an image of a regular grid (see Fig. 4.20b) which has knots at the points where the optical axes of the individual channels meet the object plane at a given object distance. The correction of interchannel distortion was verified by measuring the image coordinates of the knots in the unprocessed image from the image sensor. An average distance of 111 pixels was measured which equals the pitch of the partial images $p_K = 355.2$ µm. Thus, there is no interchannel distortion within the accuracy of the measurement.
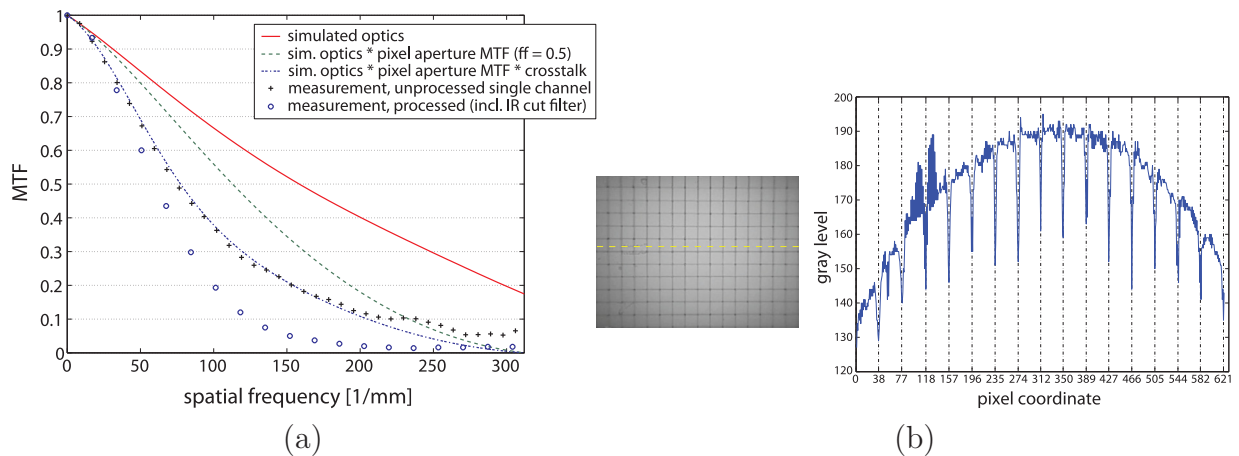
Figure 4.20: (a) Measured influence of software image stitching on MTF. All curves show the polychromatic MTF in the center of the field for about 50 cm object distance. The measured MTF in a single channel (black crosses, prior to post-processing) can be reproduced by a simulation that considers the pixel aperture MTF (green line, at a fill factor of 0.5) and pixel crosstalk (blue line). The MTF in the final image (blue circles) is decreased due to the image stitching post-processing. (b) Measurement of distortion from a line scan through the grayscale image of a regular grid. The scan path is indicated by the dashed line. The measured center of each grid line is marked by a tick label on the pixel coordinate axis [141].

Additionally, the distance of each pair of grid lines was measured across the FOV in the final braided image for determining residual distortion of the partial images (Fig. 4.20b). A mean distance between adjacent lines of 38.87 pixels was measured and compared to the designed value (39 pixels) which gives a deviation of 0.3 %. There was no monotonic distribution of distortion found accross the final image. Thus, the image of the eCLEY VGA is nearly free of distortion. However, insufficiencies of the software correction are difficult to quantify from the final images of the eCLEY because displaced image details (zipper artifacts) might also be caused by irregular sampling due to parallax or residual misalignment between the optics module and the image sensor.

The relative illumination in image space was also analyzed from Fig. 4.20b. The irradiance in the image decreases to about 69 % accross a horizontal scan which corresponds to a full field angle of about 50°. This is in good agreement with the simulation. An overview of the measured parameters of the eCLEY VGA demonstrator is given in Tab. 4.3.

Table 4.3: Summary of simulated and measured system parameters of the eCLEY VGA. *Values denote minimum and maximum data of the chirped MLA. **Simulation and measured data from red curve and black squares in Fig. 4.19a, respectively. ***Simulation data from green curve and measured from blue circles in Fig. 4.20a. The system Nyquist frequency is $\nu_{Ny} = 312.5$ cycles/mm due to the increased sampling with a braiding factor of $k = 2$.

Parameter	Simulation	Experiment
Diagonal field of view [°]	70	70.1 ± 0.35
Radius of curvature* [µm]	492-531	493-533
RMS surface deviation [nm]	-	55
Irradiance difference between 0° and 25° field angle [%]	14.5	19.4
Optics MTF**, on-axis, at $\nu_{Ny}/4 = 78$ cycles/mm [%]	75	71
Optics MTF**, on-axis, at $\nu_{Ny}/2 = 156$ cycles/mm [%]	51	48
Capture MTF***, on-axis, at $\nu_{Ny}/4 = 78$ cycles/mm [%]	66.5	38
Capture MTF***, on-axis, at $\nu_{Ny}/2 = 156$ cycles/mm [%]	32	5
Spatial resolution limit (capture MTF=10 %) [1/mm]	233	125
Number of resolvable image points	660x500	530x406
Average image distortion [%]	-	0.3

4.2.5 Improvements of the eCLEY

The degrees of freedom in the optical design of a single channel have to be increased in order to create eCLEY optics of higher resolution and lower f-number. For example, a triplet design with three microlens arrays was investigated for the eCLEY 1MP. The quasi-symmetrical arrangement with respect to the aperture stop corrects most of the coma, distortion and lateral color aberrations. However, the limitation to chirped arrays of spherical microlenses leads to a laterally enlarged system with low optical fill factor due to the large diameters of the individual lenslets (see Tab. 4.2). The correction of spherical aberrations and field curvature in each channel is also limited, especially for off-axis field coordinates, when using spherical lenslets at low f-numbers (e.g. 2.8). Another step of complexity takes advantage of the fact that only a segment of each lenslet is needed to focus the respective part of the FOV. The 2D fill factor is increased by about a factor of four if the lens segments are cut and packed close to each other (Fig. 4.21a). This leads to a complex surface structure with steep slopes between off-axis lens segments which cannot be mastered by reflow of photoresist. Hence, a point-wise mastering technology has to be used so that the lens surfaces may have arbitrary profiles in order to yield good aberration correction. This complex microstructure is further called *refractive free-form array (RFFA)*. The eCLEY 720p was designed including two RFFA components which is one optical surface less in comparison to the eCLEY 1MP but with the advantage of an improved fill factor (from 8 % to 31 %) and increased resolution (Fig. 4.21b). The surface profile of the individual lenslets (z) was described using a polynomial in the local

(a)   (b)
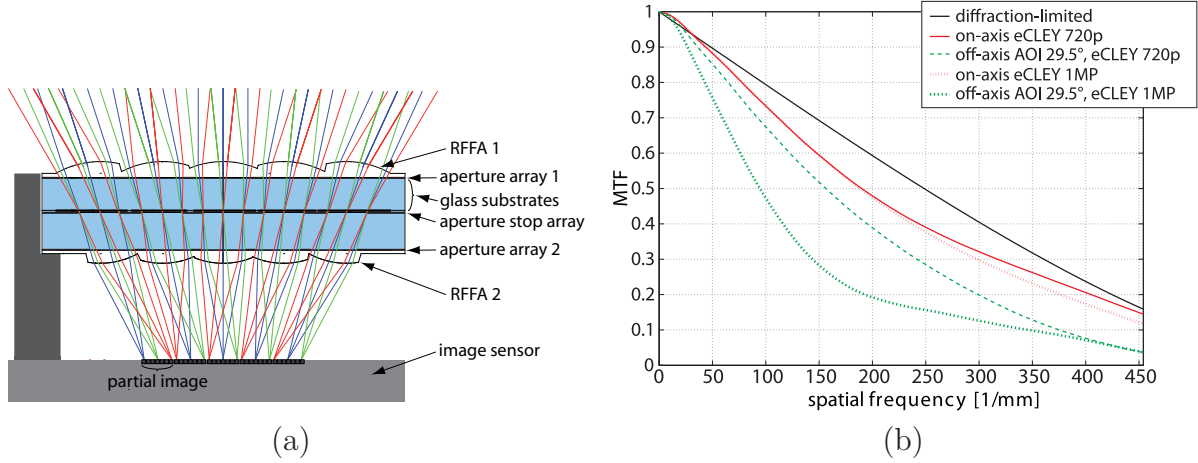
Figure 4.21: (a) Schematic section of the eCLEY 720p which consists of a stack of two glass substrates with refractive free-form arrays (RFFA) on either side. (b) Simulated polychromatic MTF curves of the eCLEY 720p for different field positions. When compared to the curves of the eCLEY 1MP, the RFFAs demonstrate much better off-axis MTF values (e.g. 20 % increase at 200 cycles/mm). The angle of incidence (AOI) for both off-axis fields is 29.5°.

coordinates of the aperture plane x,y:

$$z = \frac{c_v(x^2 + y^2)}{1 + \sqrt{1 - (1 + k_c)c_v^2(x^2 + y^2)}} + \sum_{i=1}^{N} C_i \cdot P_i(x, y) \qquad (4.9)$$

where c_v is the curvature, k_c is the conic constant and C_i are the polynomial coefficients whereas P_i are the N polynomial terms. A number of 25 polynomial terms was applied for the eCLEY 720p ranging from the 2nd to the 6th order in x,y. The optimization of the surface profile of each channel as well as the simulation and image analysis were carried out by ray-tracing according to the methods that have been described in Sec. 3.3.4. The optimized RFFAs were exported into a CAD file format (Fig. 4.22 right) in order to fabricate a master mold by ultra-precision diamond machining. The left part of Fig. 4.22 demonstrates a result of the image simulation for the current optical design.
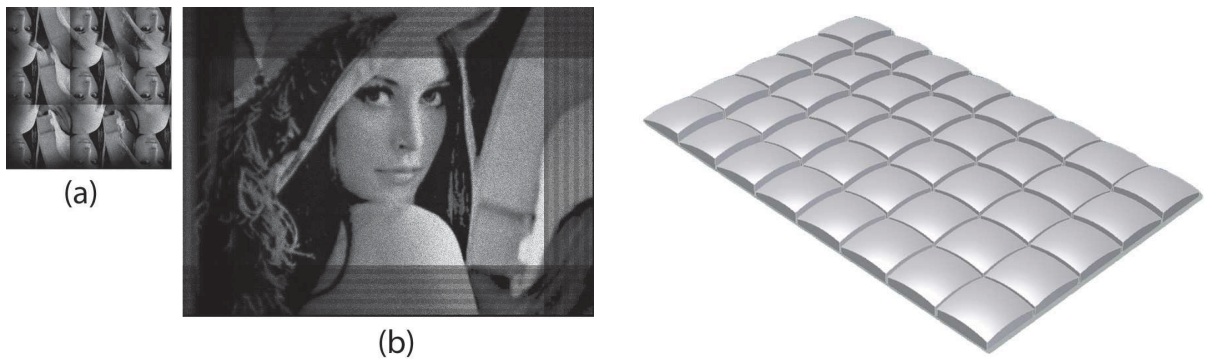
Figure 4.22: **Left:** Image simulation for an eCLEY with RFFA elements: (a) About 3x3 channels of the full array of partial images after tracing one billion rays. (b) Simulated final image after software stitching. Only a quarter of the full array was simulated in order to reduce the tracing time. The image size is 740x560 pixels. **Right:** Layout rendering of the front RFFA of eCLEY 720p. Only a quarter of the array is shown.

Unfortunately, the amount of optical cross talk is increased by the large aperture size of

the lenslets and the enhanced fill factor of pixel groups in the image plane. An additional glass substrate with two diaphragm layers was added near the image plane in the current optical design for the suppression of crosstalk. The non-sequential simulations yielded a strongest ghost of 9 % of the useful signal intensity and a veiling glare index of 6.9 %. Thus, future work is going to investigate the fabrication of vertical separation walls e.g. by two-photon lithography in order to provide a sufficient suppression of cross talk for systems with RFFAs.

4.3   Summary of Electronic Stitching of Segments

The electronic stitching of segments enables the highest degree of freedom for multi aperture imaging systems as it strives for a fusion of optics, opto-electronics and image processing. The artificial neural superposition eyes (ANSE) enabled color imaging and an increase of the signal-to-noise ratio by a factor of three compared to APCOs by applying a redundant sampling in the FOV. They belong to the thinnest artificial compound eyes with a thickness of less than 450 µm but suffer from low image resolution of 60x43 pixels and small information capacity (Fig. 5.22 in Sec. 5.4). Nevertheless, such a setup is suitable for applications of ultra-thin sensors with unlimited depth of field. In contrast, the electronic cluster eye (eCLEY) uses a large number of pixels within each optical channel to capture different parts of the FOV and achieves a fill factor that is higher by an order of magnitude. The object space sampling is increased by a sub-pixel overlap of the FOVs of adjacent optical channels which yields half the total track length of a comparable single aperture optical system of equal pixel pitch. In case of the eCLEY VGA, a short total track length of 1.4 mm was realized with a footprint size of 6.8 mm x 5.2 mm. The different partial images are stitched by means of software post-processing to form a total image of the full FOV with a size of 70°. The stitching algorithm includes the correction of the distortion and lateral chromatic aberrations of each individual channel in real-time. The residual distortion was below 1%. A maximum resolution of 125 cycles/mm was achieved at a moderate f-number ($F/\# = 3.7$). The eCLEY approach yields highest information capacity at smallest thickness when compared to the other demonstrated solutions (see Fig. 5.22). However, an extended lateral sensor format is the price for this advantage. The principle would benefit from a customized image sensor layout with small groups of densely packed photodiodes and gaps in between which are filled with components that are commonly placed at the periphery of a conventional imager. The overall chip size would increase by only 5..10 % for a cluster eye image sensor with high functionality compared to one with the same functionality made for single aperture optics [147]. However, even if such a customized imager is available, the MLA pitch has to be decreased which would cause a lens overlap in case of ellipsoidal lenslets. Thus, the future tasks will deal with the technological realization of refractive free-form arrays which, according to the simulation, enable eCLEYs of MP resolution at low f-numbers. These ultra-thin wafer-level camera optics yield a benefit for applications in consumer, automotive and machine vision.

5 Artificial Compound Eyes with Optical Stitching of Segments

5.1 Optical Cluster Eye (oCLEY)

The optical cluster eye captures a wide FOV on a conventional densely packed image area. It belongs to the class of multi aperture optics which apply optical image stitching and thus overcome a major drawback of the principle of electronic stitching of segments, namely the need for a customized image sensor of larger active area. First prototypes of such a system have already been demonstrated [17, 72]. However, the existing solutions did not yet achieve a satisfying image stitching and focusing performance [17]. The following work is seen as an enhancement of this state of the art.

5.1.1 Design of an Array of Micro-Telescopes on Smallest Format

One of the main problems of a prior oCLEY setup was that with increasing angle of incidence the chief ray angle in image space increased and the tolerance for the axial position of the overall image plane became extremely small in order to achieve a good optical stitching of adjacent partial images [17]. Hence, a fourth microlens array (MLA 3) has been integrated in the present optical design in order to deflect large angles in image space towards normal incidence and create an imaging setup that is more telecentric in image space (Fig. 5.1). Additionally, the distribution of the lenslets was changed from rectangular to hexagonal in order to increase the optical fill factor. Thus the diameter of the partial images was reduced by a factor of $\sqrt{2/3}$.
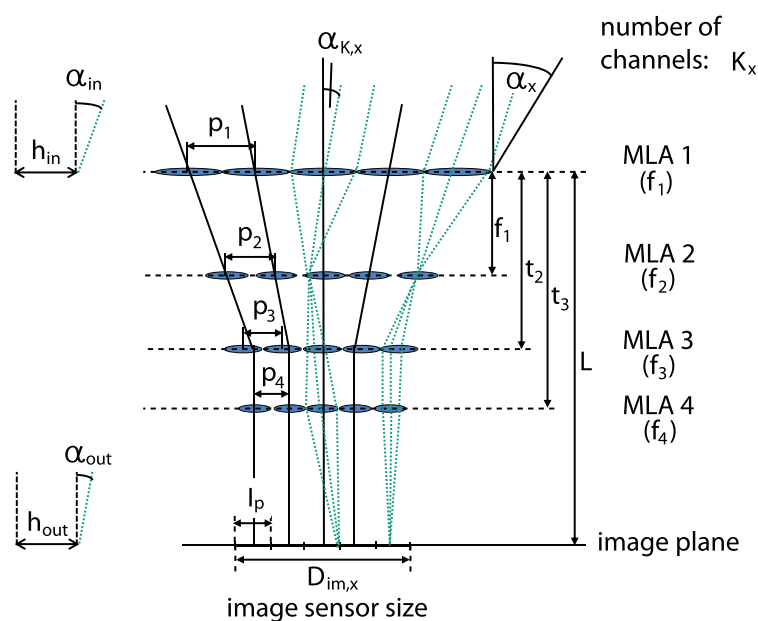
Figure 5.1: Schematic overview of the parameter denotation of the oCLEY (adapted from [148]).

The figure 5.1 illustrates the effect of the different system components. The first microlens array (MLA 1) creates a focused intermediate image of the related segment of the FOV. The second MLA 2 acts as field lens array in order to prevent vignetting at the third MLA. In this way it also suppresses optical crosstalk. The intermediate image is re-imaged on the final image plane by the third and fourth microlens arrays (MLA 3 and MLA 4) whereas MLA 3 mainly acts to reduce the angle of incidence on the image plane. After the magnified relay imaging of the intermediate images, the true sided partial images stitch together on the image sensor. The principle resembles an array of focused Kepler micro-telescopes with titled optical axes.

A paraxial matrix method was used to describe the relationship of the basic parameters and to find a starting point for the numerical simulation [148, 149]. The system transfer matrix $\widetilde{M}$ is constructed by applying the elementary matrices of Eq. (3.28) sequentially for all system components.

$$\widetilde{M} = M_{P,4} \cdot \underbrace{M_{D,4}^{-1} M_{L,4} M_{D,4}}_{\text{MLA 4}} \cdot M_{P,3} \cdot \underbrace{M_{D,3}^{-1} M_{L,3} M_{D,3}}_{\text{MLA 3}} \cdot$$
$$M_{P,2} \cdot \underbrace{M_{D,2}^{-1} M_{L,2} M_{D,2}}_{\text{MLA 2}} \cdot M_{P,1} \cdot \underbrace{M_{D,1}^{-1} M_{L,1} M_{D,1}}_{\text{MLA 1}} \tag{5.1}$$

The propagation distances are $d_1 = f_1$, $d_2 = t_2 - f_1$, $d_3 = t_3 - t_2$ and $d_4 = L - t_3$. The matrix multiplications in Eq. (5.1) yield the individual elements of the transfer matrix of Eq. (3.27). The unknown parameters of $\widetilde{M}$ are found by solving the equation system (3.27) in a similar way as described in [73]. A number of 14 different side conditions are needed as there are 18 unknown parameters (f_1, f_2, f_3, f_4, p_1, p_2, p_3, p_4, t_2, t_3, L, $F/\#$, α_x, $\alpha_{K,x}$, $D_{im,x}$, I_P, K_x, T) and only a subset of four (L, $F/\#$, α_x, $D_{im,x}$) is given as input from the application. One important example is the condition for the decentration of the lenslets in MLA 3 which is chosen in a way that the chief ray subtends the normal of the image plane under a small angle. This is expressed by:

$$\alpha_{out} \left(h_{in} = 0; \; \alpha_{in} = 2i \cdot \alpha_{K,x} \right) = M_{22} \cdot 2i \cdot \alpha_{K,x} + M_{23} \overset{!}{=} 2i \cdot \alpha_{K,x} \cdot (1 - T) \; . \tag{5.2}$$

The telecentricity coefficient $T = 1 - \alpha_{out}/\alpha_{in}$ which is between 0 and 1 is used to control the amount of deflection for the chief ray of the i'th channel ($2i \cdot \alpha_{K,x}$). A value $T = 1$ defines normal incidence on the image plane whereas $T = 0$ means no deflection. Even with all side conditions at hand, four parameters - the telecentricity coefficient (T), the half FOV of a single channel ($\alpha_{K,x}$), the distance between MLA 1 and MLA 3 (t_2) and that between MLA 1 and MLA 4 (t_3) - has to be chosen by an iterative technique while limiting the numerical apertures of the MLAs [148].

An important trade-off for the f-number of oCLEYs was derived in Fig. 5.2a by successive use of the model for different given values of the total track length. A low f-number is achieved only for a large total track length, as long as the numerical aperture (NA) of the single MLAs is limited below 0.3 for technological reasons. For example, a total track length of 5 mm (in air) is needed for $F/\# = 3$, which is a common value for small cameras.
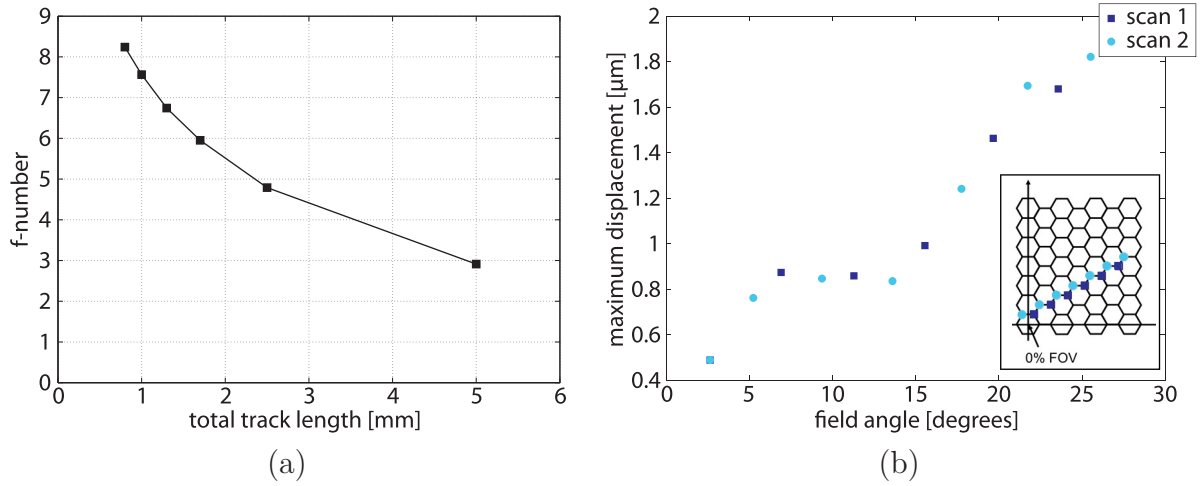
Figure 5.2: (a) F-number as a function of total track length derived from several simulated oCLEY systems using the paraxial matrix method for a maximum lens $NA = 0.3$ (all propagations in air). (b) Displacement of point image position at the intersection of adjacent channels for two different positions across the field of the final oCLEY design (adapted from [149]).

After a suitable parameter set had been derived, an optical design was created for a prototype system using ray-tracing techniques and the paraxial elements were replaced by real lenslets on glass substrates. The different system components were optimized and the performance was analyzed. The quality of the optical image stitching was verified by a simulation of the image spot centroid position for selected points in the FOV that correspond to image positions at the intersection of adjacent partial images (Fig. 5.2b). The displacement of image points that should perfectly overlap, increases towards larger field angles due to distortion. The maximum deviation is about 1.8 µm which is less than one pixel ($p_{px} = 2.25$ µm).

The Figure 5.3a gives an overview of the layout and parameters of the oCLEY prototype.
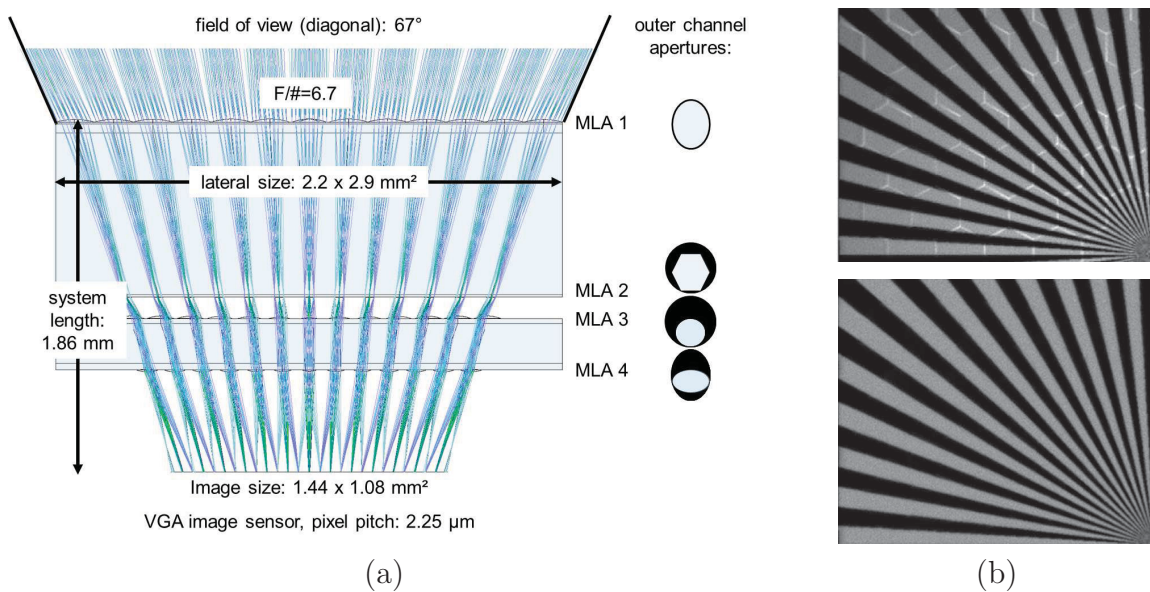
Figure 5.3: (a) Overview of the final optical design of the oCLEY demonstrator with VGA resolution [148]. (b) Simulated image of a Siemens star without (top) and with (bottom) flat-field correction [149]. A quarter of the full array was used to speed up the simulation. The central channel is in the lower right corner.

The telecentricity of the optical design could not be chosen higher than $T = 0.17$ due to the limitation of the numerical apertures of the microlenses below 0.3. Hence, an angle of incidence of 20.8° on the image plane resulted for a field angle of 25°. Image simulations were made using the ray-tracing software Zemax™ in order to verify the image quality (Fig. 5.3b) and to determine the resolution at the intersections of partial images. Further simulation results are included in Fig. 5.6 and Tab. 5.2.

5.1.2   Prototype Fabrication

The fabrication of the oCLEY relies on the same microoptics technologies which have been introduced in Sec. 4.1.2. The MLA master wafers and aperture arrays were structured by photolithography and the lenslets by reflow of photoresist due to the small size and low sag. The aperture array of the front MLA 1 was etched in black chromium in order to yield good absorption of light in the intermediate space between lenslets (see Fig. 5.4a&b). For the first time, black chromium was chosen instead of black-matrix polymer due to the fine structure which had to be created in between lenses of high fill factor and due to the reduced back reflection. The hexagonal openings of the field aperture in the intermediate image plane were etched in titanium (Fig. 5.4c). They define the final shape of the partial images. The MLA 1 and 2 as well as MLA 3 and 4 were sequentially molded on both sides of the respective glass wafers with integrated aperture arrays in UV-polymer (OrmoComp, Micro Resist Tech.). Finally, the wafers were diced and the two components of the oCLEY were assembled on die-level (Fig. 5.4d) using alignment marks which were integrated in the aperture layers.

(a)   (b)   (c)   (d)
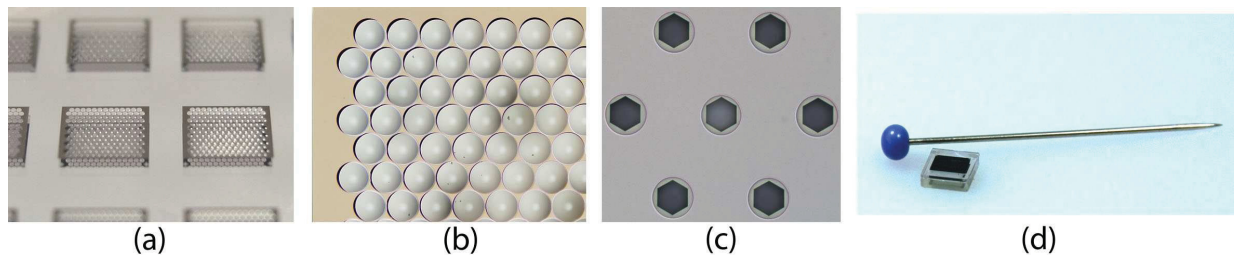
Figure 5.4: (a) Close-up of a part of the full wafer. (b) Double-sided microlens array. (c) Field microlens array with hexagonal field aperture. (d) Comparison of the optical module to a pin. Adopted from [149].

The basic parameters of the fabricated oCLEY are listed in Tab. 5.1.

5.1.3   Characterization of oCLEY

The oCLEY module was actively aligned in front of an image sensor of the design pixel pitch but with larger active area (model Aptina MT9M032). The read out images were cropped to the target resolution of 640x480 pixels. A flat-field correction has been applied to the captured images because the irradiance in the image decreases considerably towards the image edges (Fig. 5.5a). Thus, the low irradiance at the image margin has to be

Table 5.1: Parameters of the oCLEY demonstration system. For chirped arrays, the minimum and maximum values are specified.

Parameter	Value			
Effective focal length [mm]	1.39			
F-number	6.7			
Total track length [mm]	1.86			
Lateral dimensions [mm^2]	2.2×2.9			
Image size [mm^2]	1.08×1.44			
	MLA 1	MLA 2	MLA 3	MLA 4
Radius of curvature [µm]	$315 - 417$	145	185	$122 - 248$
Sag [µm]	$12.3 - 16.5$	$3.7 - 4.4$	$5.5 - 16.2$	$6.6 - 11.1$

increased by a factor of four which increases noise and causes low contrast in that part of the images. The color filter array on the CMOS image sensor enabled the acquisition of images in full color as shown in Fig. 5.5b.

| (a) | (b) |
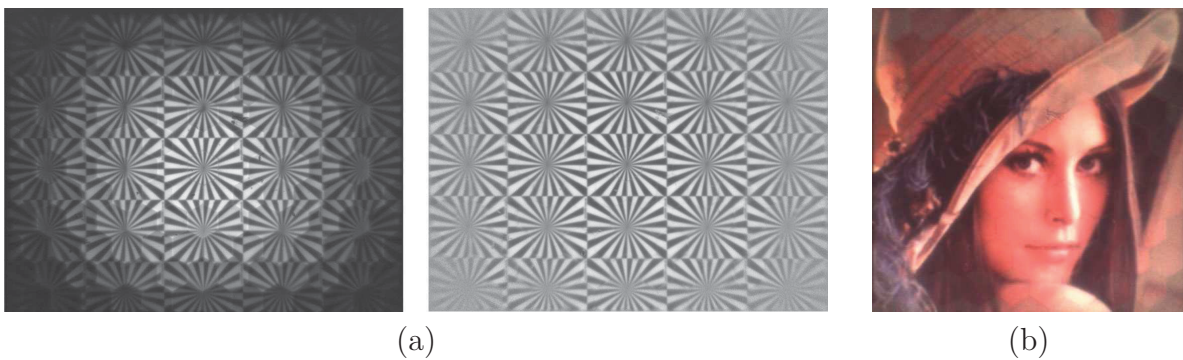
Figure 5.5: (a) Image of an array of Siemens star targets captured with the oCLEY (left) and with applied flat-field correction (FFC, right) [148]. (b) Captured image of 'Lena' with FFC (cropped) [148].

The MTF was measured according to ISO 12233 with a slanted edge in different field positions. The results for an on-axis position and 70 % of the FOV (corresponding to a field angle of 23°) are shown in Fig. 5.6a in comparison to the simulated curves. The maximum difference between the simulated optics MTF and the measured MTF (optics & contribution of sensor pixel) is about 15 %. For instance, the simulated MTF value is 73 % and the measurement yields 60 % at 55.5 cycles/mm (quarter Nyquist frequency). At the off-axis position, it is 61 % in the theoretical and 45 % in the experimental curve. The highest spatial frequency that can be transmitted by the oCLEY demonstrator is 155 cycles/mm (MTF = 10 %, on-axis). The discrepance between measurement and simulation is partly due to the unknown pixel fill factor. The correct pixel aperture MTF could not be derived as the fill factor is not communicated by the image sensor supplier. Furthermore, it is caused by fabrication tolerances of the axial thickness of the components and the radii of curvature of MLA 1.
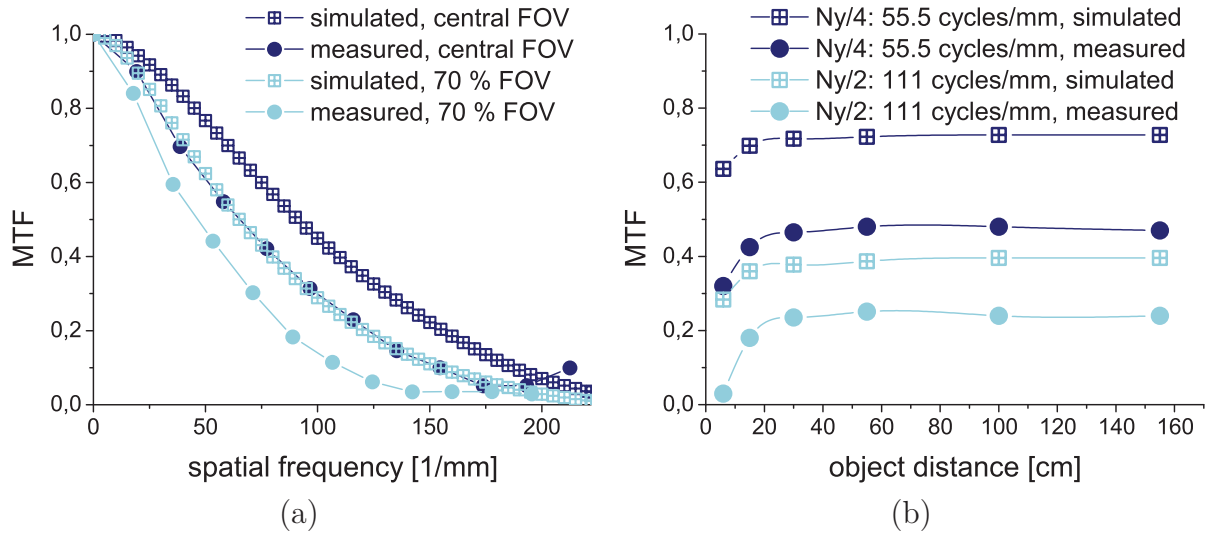
Figure 5.6: (a) Simulated and measured polychromatic MTF of the oCLEY [148]. The Nyquist frequency of the system is 222 cycles/mm (pixel pitch 2.25 µm). (b) Simulated and measured MTF as a function of object distance for half (111 cycles/mm) and for quarter (55.5 cycles/mm) of the Nyquist frequency [148].

The resolution was also characterized as a function of object distance (Fig. 5.6b). The MTF performance saturates for object distances larger than 40 cm which fits to the fact that the optical design was optimized for infinite object distance.

For the experimental verification of the partial image stitching, first the gradient of an edge image (Fig. 5.7a) was calculated perpendicular to the edge on either side of the intersection between adjacent partial images. Subsequently, the positions of the extrema of the gradient were located. Finally, the positions of the extrema which are found on both sides of the intersection between adjacent partial images were compared. The maximum offset was 0.2 pixels in the center and 0.4 pixels at 70 % of the FOV. Hence, the optical image stitching is achieved with sub-pixel accuracy.
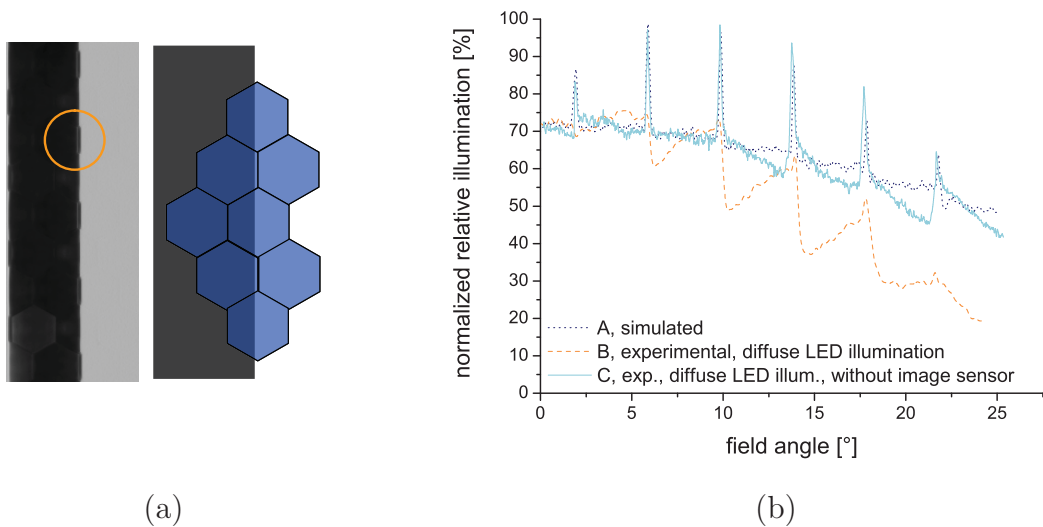
Figure 5.7: (a) Image of edge displacement due to insufficient optical image stitching. The right side illustrates the position of the edge relative to the channel grid. (b) Comparison of simulated and measured relative illumination. The strong peaks originate from the slight overlap of adjacent partial images [148].

The prototype suffered from considerable shading (see left image of Fig. 5.5a) which was analyzed by measuring the relative illumination across the image plane for a homogeneously white test chart. The strong difference between the simulated curve (A) in Fig. 5.7b and the curve (B) measured with the oCLEY mounted on the image sensor is caused by a fill factor enhancing MLA which is integrated on the sensor pixels. Its geometry is adapted to a common distribution of the chief ray angle in the exit pupil of single aperture lenses but it does not match the ray angle distribution of the oCLEY. Thus, a third curve (C) was derived from relaying the image plane of the optical module on a CCD image sensor by using a microscope objective (NA=0.4). Without the influence of the image sensor, the relative illumination curve (C) agrees well with the simulated curve (A). A comparison between the simulated and measured properties of the oCLEY is found in Tab. 5.2.

Table 5.2: Summary of different simulated and experimentally measured parameters of the oCLEY.

Parameter	Simulation	Experiment
Diagonal field of view [°]	66.6	66.5 ± 0.3
MTF, center of field, at $\nu_{Ny}/4 = 56$ cycles/mm [%]	73	60
Spatial resolution limit [cycles/mm]	183	155
Number of resolvable image points	640x480	446x335
Irradiance difference between 0° and 25° field angle [%]	25	
Measured with image sensor		52
Measured in relay image		29
Offset between partial images at 0 % FOV [µm]	0.2	0.2
Offset between partial images at 70 % FOV [µm]	0.4	0.4
Partial image distortion at 82 % FOV [%]	5.1	5.3 ± 0.2

5.2   Ultra-Thin Array Microscope

A special type of optical cluster eye is created when the optical axes of all channels are parallel and thus, there is no pitch difference between the different microlens arrays. Such a setup can only yield optical image stitching if the magnification is unity and its numerical aperture is indirectly proportional to the object distance which makes it a perfect candidate for close-up imaging [108–110]. Prior work on a such a multi aperture setup implemented on an image sensor concluded that the magnification is purely digital and the smallest resolvable object feature is given by the resolution of the lenslets and the sensor pixel size [150]. The result is a microoptical imaging system that can be used similar to a microscope with low magnification. It can be scaled arbitrarily in the lateral dimension to capture larger object fields without scaling its axial length. For that reasons, it was termed *ultra-thin array microscope.*

5.2.1   High Resolution Imaging of Large Object Fields

The first implementation of a microoptical array microscope suffered from strong optical crosstalk because a setup of three MLAs without any aperture arrays was applied [150]. The spatial cut-off frequency of the system was limited to 50 cycles/mm due to the fact that all lenslet arrays had the same optical parameters which limited the degree of freedom. In the following, aperture arrays were integrated and a setup of higher complexity was chosen in order to suppress crosstalk and to increase the spatial resolution. In order to achieve this, a highly symmetric setup of eight lenses per optical channel is proposed (Fig. 5.8).
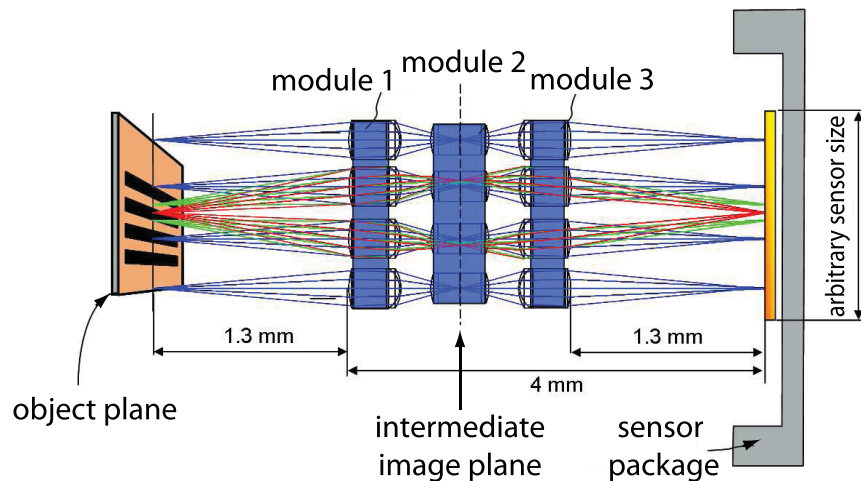
Figure 5.8: Schematic layout section of the working principle of the ultra-thin array microscope.

The first lens group (module 1) with a pitch of 300 µm creates an intermediate image with a de-magnification of 1:4 of the respective part of the object in each channel. A reversed group of the same parameters (module 3) relays the intermediate image onto the final image plane. Hence, each erect partial image has unity magnification which is essential for the optical stitching on the sensor. The size and overlap of adjacent partial images is controlled by the field diaphragm array which is situated in the center of axial symmetry. The field lens arrays (both sides of module 2) are used to control vignetting and to suppress crosstalk. Aperture arrays are integrated under each microlens array for the blocking of stray light. Aspherical surfaces and an achromatic lenslet were designed for the front component to yield highest possible numerical aperture (NA) for a given complexity in order to increase the spatial resolution (Fig. 5.9). The aspherical lenslets correct for spherical aberrations and the pair of achromatic lenses correct color aberrations and provide an additional degree of freedom without adding another substrate. The effort of the numerical optimization is reduced to 10 variables (four radii of curvature, four thicknesses and two conic values) due to the symmetry with respect to the intermediate image plane. Furthermore, it is sufficient to consider a simulation setup for a single channel because the properties of all channels are the same. The size of each partial image and the relative illumination are controlled via side conditions in the merit function as both are important for the optical image stitching. The parameters of each channel were optimized to yield a constant resolution of 5 µm (or
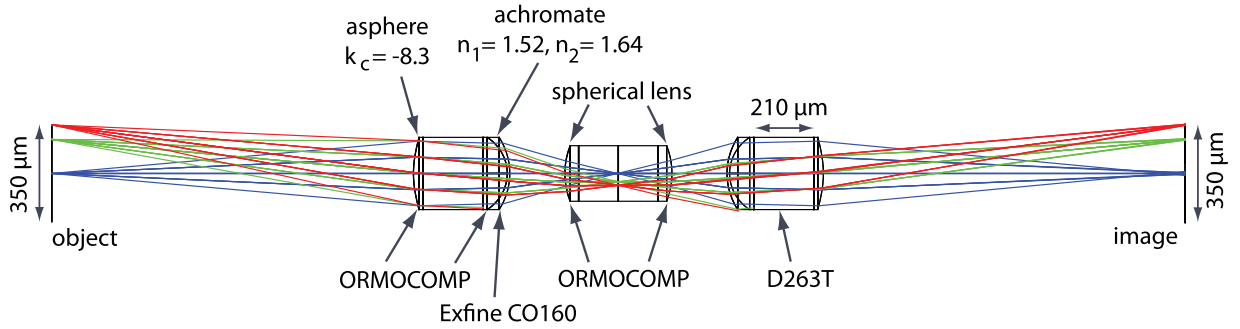
Figure 5.9: Layout sketch of the optical design of a single channel of the ultra-thin array microscope [151].

200 cycles/mm) across the whole object field (Fig. 5.10 left). Using a hexagonally shaped field diaphragm array in a hexagonal distribution leads to the highest fill factor for the optical stitching of the partial images so that there are no gaps between adjacent partial images and the residual shading due to vignetting is only about 11 %. This was verified from image simulations through multiple optical channels (Fig. 5.10 right).

(a)   (b)
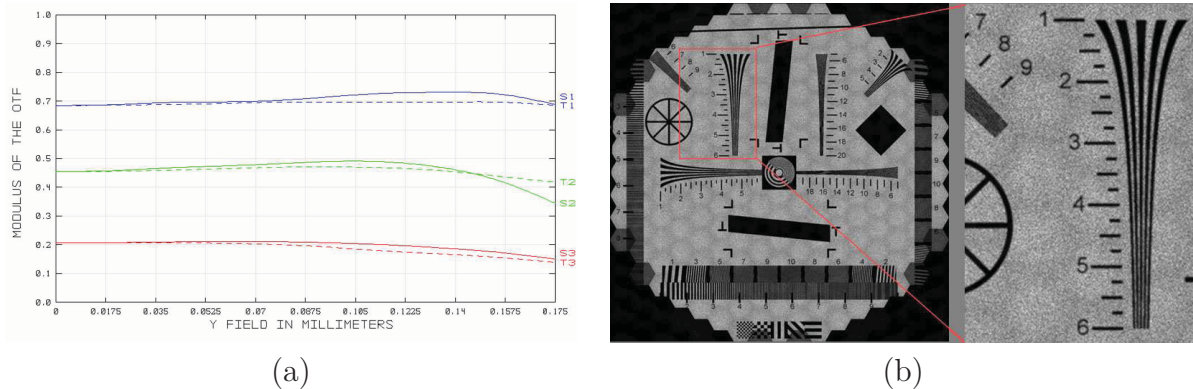
Figure 5.10: (a) Simulation of polychromatic MTF over radial field coordinate in a single channel for three spatial frequencies (50 cycles/mm blue, 100 cycles/mm green, 200 cycles/mm red). Wavelength range spans from 486 nm to 656 nm. Tangential MTFs are shown as dashed lines, sagittal MTFs as solid lines [151]. (b) Polychromatic image simulation through multiple channels of the ultra-thin microscope. The shown image and the corresponding object sizes is 4x4 mm^2. Wavelength range is the same as on the left, although the result is shown in grayscale. The right part shows a magnified region [151].

5.2.2   Fabrication of a System with Adaptable Lateral Format

Beyond the standard microoptical fabrication methods (Sec. 4.1.2) which were used also for the optics of the ultra-thin array microscope, a step forward was taken by the integration of molded aspherical and achromatic lenslet arrays on either side of module 1. The mastering for the first MLA is similar to that for spherical lenslets using lithography and reflow of photoresist, except for an additional reactive ion etching (RIE) step in order to create convex aspherical masters from spherical resist microlenses. The currently used aspherical profile is at the limits of this non-proportional etching transfer technique. A molding tool for aspherical lenslets results after overcasting. A cemented achromatic microlens array is created on the opposite side of the module by UV-molding the second lens on top of the firstly molded microlens array with a different polymer material. The material of the

first lenslet array is OrmoComp (Micro Resist Tech., refractive index $n_1 = 1.521$ and Abbe number $V_1 = 52.0$ at $\lambda = 588$ nm) that of the second is Exfine CO160 (ChemOptics Inc., $n_2 = 1.634$ $V_2 = 26.2$ at $\lambda = 588$ nm). As the fabrication of the optics modules was carried out for multiple chips in parallel on wafer level, two chips from the same wafer were used for the identical modules 1 and 3. The whole 4 inch wafer area was filled with microstructures (Fig. 5.11 left) so that modules of arbitrary lateral size could be diced out.
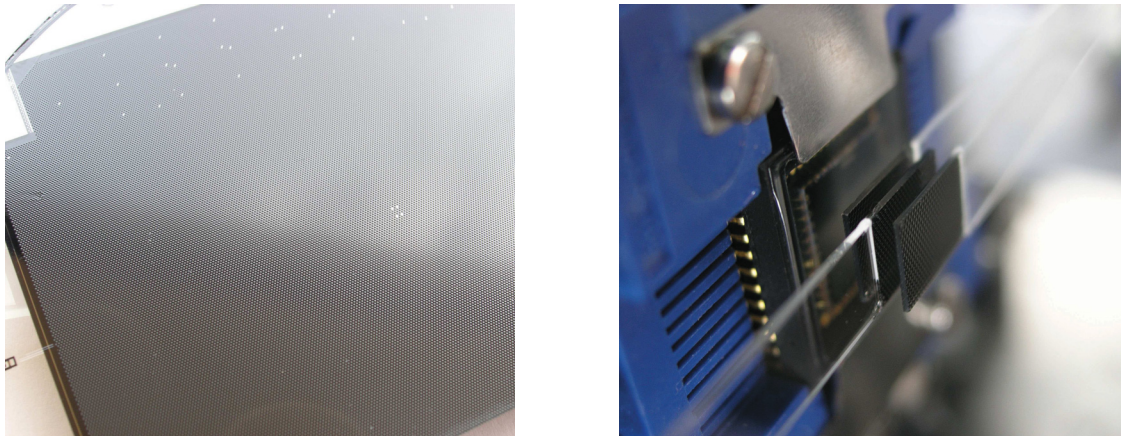
Figure 5.11: **Left:** Photo of the four inch wafer carrying the microlenses for the module 1 and 3. **Right:** Close-up of the test demonstrator on a small image sensor. The three MLAs were temporarily fixed to thin glass stripes so that each can be moved individually in six axes using precision alignment stages.

The parameters of the fabricated microlens arrays for the prototype systems are listed in Tab. J.1 of Appendix J. The first test assembly of the modules 1, 2 and 3 was done actively on die-level in front of a small 1/2 inch format image sensor (Micron MT9T001, Fig. 5.11 right). The basic parameters of that prototype are the same as for the large format demonstrator in Tab. 5.3 except to its lateral dimensions.

The assembly of the demonstration system on a full format image sensor was done using glass spacers to set up the correct air gap thickness between the modules. Module alignment in lateral x,y dimensions was aided by alignment marks on each chip. The module stack was axially joined using adhesive with spacer beads and the glass spacers were removed after that. The complete optical stack was then integrated into a mechanical holder frame (left in Fig. 5.12) which was fixed on the package of the image sensor. The alignment between the holder frame with mounted optics and the CCD image sensor was carried out in an active manner, by optimizing the image quality of a presented test target while adjusting the z-distance and angles of rotation and tilt between the two parts. Subsequently, the two parts were fixed in place with adhesive. The microoptics and image sensor assembly was integrated in a modified commercial camera (Prosilica GE4900) which provides the read-out electronics and interface to a PC (Fig. 5.12 right). The basic system parameters are found in Tab. 5.3.

(a)   (b)
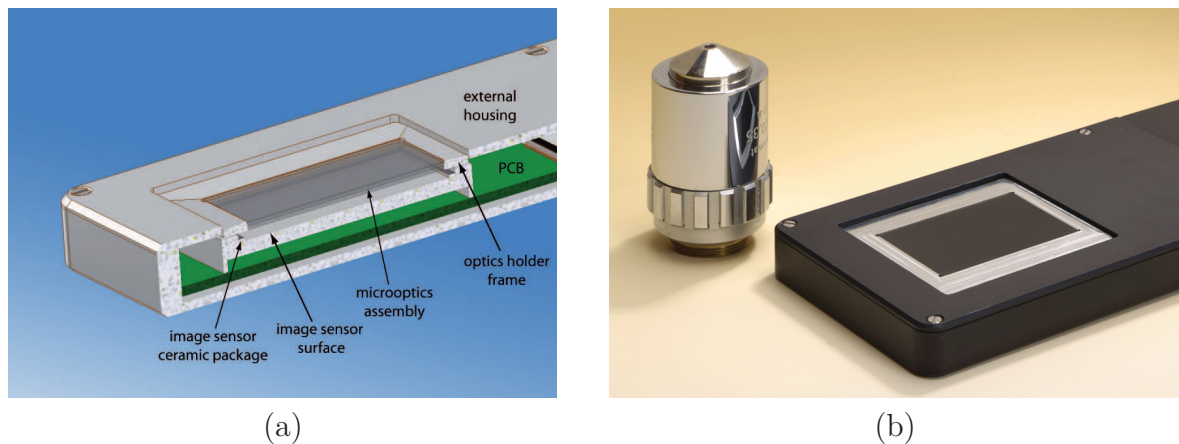
Figure 5.12: (a) Section of the opto-mechanical assembly concept of the optics modules on the CCD image sensor (3D model) [151]. (b) Photograph of the prototype's head in comparison to a conventional microscope objective lens [151].

5.2.3   Experimental Characterization

The current setup is limited to the inspection of semi-transparent objects due to the small object distance of 1.3 mm, so that the object illumination has to be carried out from the backside of the object plane. An LED backlight with diffuser plate was used in the described experiments. The hexagonal illumination pattern which appears in the captured images (see Fig. 5.13 left) is caused by a inhomogeneous intensity on the image plane in zones where adjacent partial images overlap. Its visibility depends on the scene illumination. The difference of brightness between center and edge of a partial image was measured to be 14.5 % for a Lambertian illumination. However, for a fixed illumination the pattern can be filtered by means of image processing similar to a flat-field correction (Fig. 5.13 right).
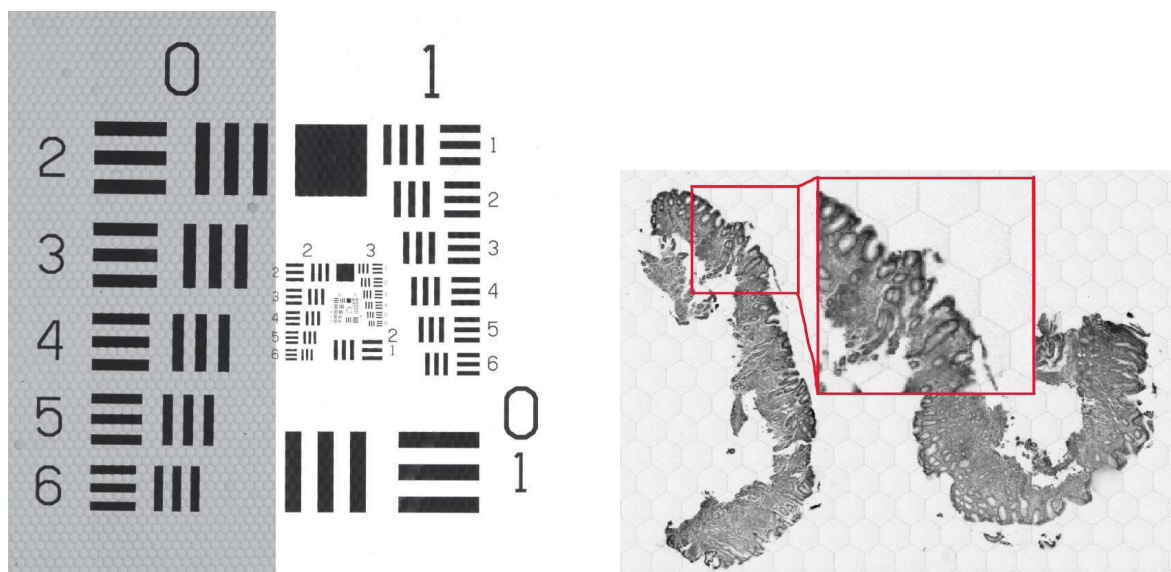
Figure 5.13: **Left:** Image of USAF 1951 test pattern as captured by the ultra-thin array microscope. The image shows a part of the full field with a size of 17.6 mm x 17.6 mm. The right side of the image was post-processed by a software flat-field correction (FFC) [151]. **Right:** Example image of an organic histological section with FFC. Each hexagon relates to one partial image with a diameter of 350 µm. The red square inset shows a 2x magnified region. Specimen by courtesy of the Institute for Pathology Basel.

Images of different test targets such as a high-precision USAF 1951 test pattern or a histological section (Fig. 5.13) were captured in order to characterize the image resolution. A strong phasing effect is found between group 5 element 5 and group 6 element 1 in the image of the USAF pattern which correspond to 50.8 LP/mm and 64 LP/mm, respectively. This is in good agreement with the expected Nyquist frequency of the image sensor which is 67.6 cycles/mm at a pixel pitch of 7.4 µm. The residual hexagonal background pattern is due to a difference of the illumination during calibration and that while capturing the specimen.

Images with slanted edge features were acquired at different field positions in order to analyze the MTF in more detail using an approach similar to ISO 12233 [145]. The results are shown in Fig. 5.14. The pixel aperture of the image sensor (Kodak KAI-16000) is rectangular which yields different sections of the aperture MTF along the horizontal and vertical direction in the pixel array. The related MTFs are shown by the red (vertical section) and the orange (horizontal section) curves. They are composed of the pixel aperture MTF and the simulated optics MTF in the center of an optical channel. The measured data is shown for horizontal sections because the edge was vertically orientated during the measurements. For the MTF measurements in a single channel (denoted by 'sc'), there is a variation of maximum 10% which is likely to result from residual tilt between the object plane or the image sensor plane and the microlens arrays. A bow in one or more modules has the same effect. Additionally, a difference was found between the MTF measured in a single channel at a specific object field position and the MTF measured across several channels (denoted by 'mc' in Fig. 5.14) centered at the same field position. This variation is caused by insufficient image stitching at the interfaces between adjacent partial images. In the case that the image or object distance is out of tolerance, sharp images are created by the individual channels but the magnification is not unity, causing image details to be displaced and not matched at the intersection of adjacent partial images. A limit ($\widehat{H} = 0.1$) of about 115 cycles/mm was measured for the resolution in a single partial image in the center of the object field. The resolution limit is decreased to about 83 cycles/mm (which corresponds to 12 µm structures or 4200 dpi) for an ensemble of several optical channels.

Furthermore, the quality of the optical image stitching was determined by locating the position of contrast edges with different orientation to the pixel matrix. A maximum deviation of the edge position on both sides of the intersection of adjacent partial images of 1 pixel was measured in the center of the field which increased to about 1.8 pixels at the edge of the field. The table 5.3 presents a summary of the measured system parameters in comparison to the simulation.
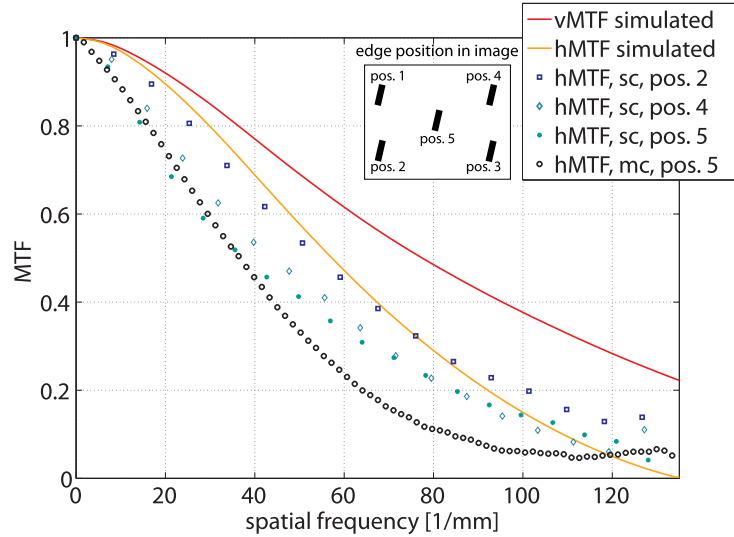
Figure 5.14: Experimental MTF curves measured in a single channel ('sc') and over multiple channels ('mc') for different positions in the image field (see legend). For comparison, sections of the simulated single channel, polychromatic MTF were added, which include the effect of a rectangular image sensor pixel. Along the horizontal direction (prefix 'h'), the pixel aperture is nearly equal to the pixel pitch ($p_{px} = 7.4$ µm) whereas it is about half the size ($d = 3.7$ µm) in the vertical direction (prefix 'v') [151].

Table 5.3: Summary of simulated and measured parameters for the ultra-thin array microscope. The * denotes values from horizontal and vertical sections of the MTF.

Parameter	Simulation	Experiment
Numerical aperture	0.1	
Object field size [mm²]	36.1×24.0	
Object-to-image distance [mm]	5.3	
Sensor pixel pitch [µm]	7.4	
Sensor resolution [pixels]	4872×3248 (16 MP)	
MTF, center of field, at $\nu_{Ny}/4 = 17$ cycles/mm [%]	92 - 94*	80
MTF, center of field, at $\nu_{Ny}/2 = 34$ cycles/mm [%]	76 - 82*	54
Spatial resolution limit [cycles/mm]	108 - 176*	83
Brightness difference center to edge of partial image [%]	11	14.5
Offset between partial images at center field [pixels]	0.03	1

5.3 Microoptical Gabor Superlens (µoGSL)

The optical stitching of segments enables a new degree of freedom by making the partial images of adjacent optical channels overlap. The light sensitivity of the multi aperture optical system is improved depending on the number of channels which contribute to a common image point. The effective entrance pupil size is increased compared to that of the single channel which places the principle of the Gabor Superlens close to the natural archetype - the superposition compound eye of nocturnal insects.

5.3.1 Approach for an Ultra-Compact Objective with High Sensitivity

Compared to the state of the art [21, 103, 104, 152], the current work represents the first realization of a miniaturized Gabor Superlens which is fabricated by microoptical technology. The basic setup is transferred to two microlens arrays which are separated by the sum of their focal lengths and a third array (MLA 2 in Fig. 5.15) has been added acting as a field lens array in order to maximize the light throughput under large angles of incidence.
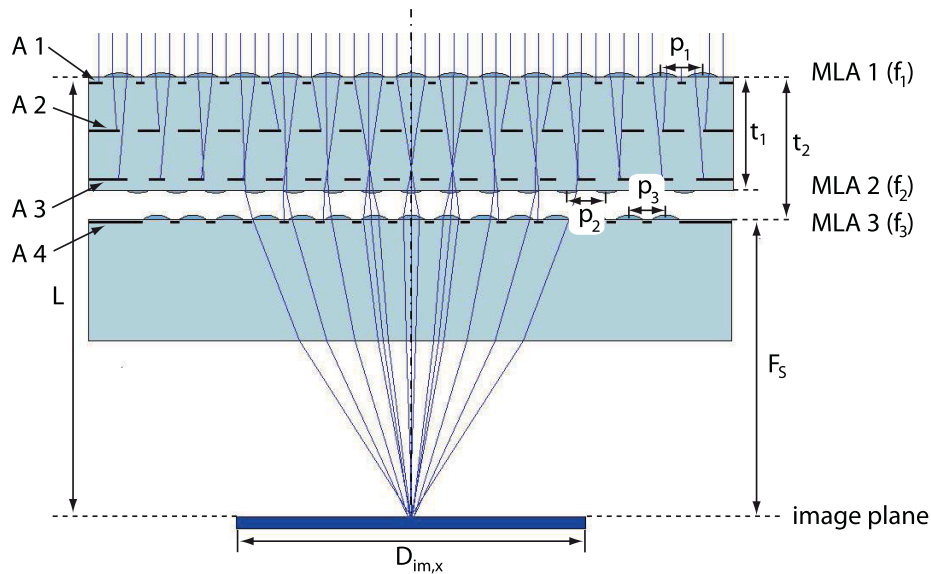
Figure 5.15: Layout sketch of the microoptical Gabor Superlens (µoGSL). Image was modified from [153].

A general lens equation for the Gabor Superlens (GSL) was derived using the thin lens approximation without field MLA [154]:

$$s_i = \frac{p_1 f_3}{(p_1 - p_3) + p_3 f_1/s} \ .$$

(5.3)

It relates the image distance s_i to the object distance s and the main parameters (focal lengths and pitches) of the GSL which are denoted in Fig. 5.15. For a large object distance $s \to \infty$, the known equation for the back focal length F_S of the GSL is derived (see Eq. (3.6) with index 2 changed to 3).

A paraxial system of equations was set up from the system transfer matrix according to Eq. (3.27) in order to find start parameters for the numerical simulation. The paraxial transfer matrix $\widetilde{M}$ is composed of the matrices of the contributing MLAs:

$$\widetilde{M} = M_{P,3} \cdot \underbrace{M_{D,3}^{-1} M_{L,3} M_{D,3}}_{\text{MLA 3}} \cdot M_{P,2} \cdot \underbrace{M_{D,2}^{-1} M_{L,2} M_{D,2}}_{\text{MLA 2}} \cdot M_{P,1} \cdot \underbrace{M_{D,1}^{-1} M_{L,1} M_{D,1}}_{\text{MLA 1}} \qquad (5.4)$$

The total number of unknown parameters is 14 (f_1, f_2, f_3, p_1, p_2, p_3, t_1, t_2, F_S, L, $F/\#$, α_x, $D_{im,x}$, K_x), whereas $t_1 = f_1$, when infinite object distance and imaging in air are assumed. The number of channels of one GSL is given by $K_x = p_1/(p_1 - p_3)$ [21]. Five parameters were given as input specifications (L, F_S, $F/\#$, α_x, $D_{im,x}$) so that seven independent conditions were used to solve the equation system for all unknown values.

One example is the 'focusing condition' which states that all rays emitted from the same object point have to superpose in a common point on the image plane at h_{out} regardless of their input ray height h_{in}:

$$h_{out} = M_{11} \cdot h_{in} + M_{12} \cdot \alpha_{in} + M_{13} \longrightarrow h_{out} \neq f(h_{in}) \longrightarrow M_{11} \overset{!}{=} 0 \qquad (5.5)$$

This yields the following expression for the back focal length [153]

$$F_S = \frac{(f_1 - t_2)f_3}{f_1 + f_3 - t_2} \ . \qquad (5.6)$$

Other side conditions can be found in [154].

With the geometrical parameters at hand, the optical properties of the µoGSL were studied in ray-tracing simulations. The sensitivity of the system is set in relation to the number of channels that contribute to one image point. This number is directly proportional to the diameter of the individual field stops so that the sensitivity is increased by enlarging the field stop. On the other hand, the spot size grows with larger field diaphragm and, consequently, the resolution decreases, because rays contributing from outer channels are increasingly aberrated. In conclusion, the more channels superpose, the higher the sensitivity but the lower the spatial resolution of a µoGSL which is shown in Fig. 5.16.

The resolution was simulated by determining the image contrast for different line pairs per millimeter from image simulations (Fig. 5.17). The simulated contrast at quarter Nyquist frequency (28 LP/mm) is 58 % (see Fig. 5.21). The image contrast at half Nyquist frequency (57 LP/mm) could not be improved beyond 15 % at the present number of superimposed partial images.
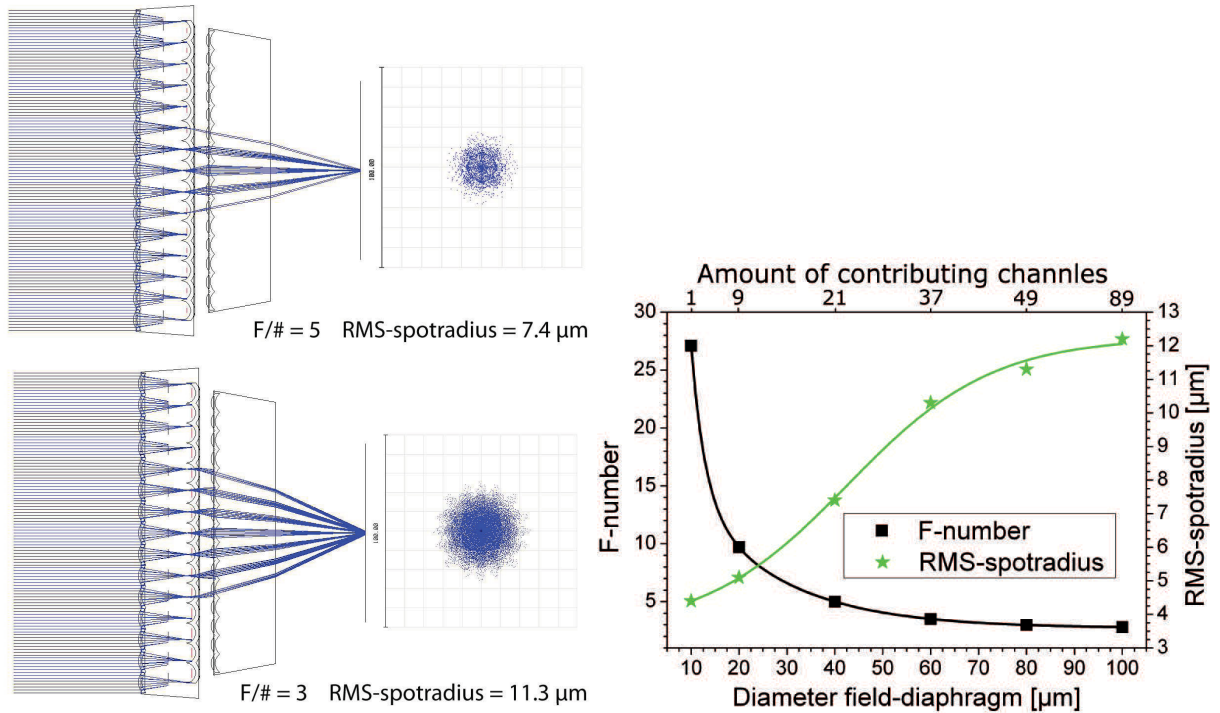
Figure 5.16: **Left:** Top: Ray-tracing simulation layout plot and simulated RMS spot size for a size of the field diaphragm that yields $F/\# = 5$. Bottom: The same for a size that gives $F/\# = 3$. The number of contributing optical channels increased by about a factor of two. The RMS spot size increased by about 50 %. **Right:** Trade-off between f-number of the µoGSL and the spatial resolution represented by the RMS spot size both as a function of the field stop diameter [153].
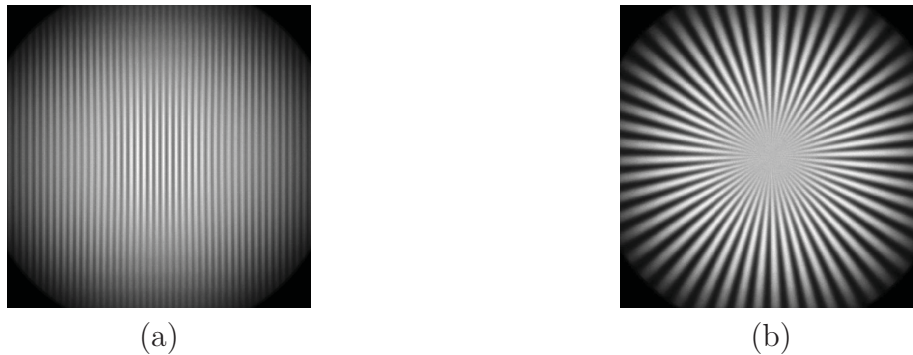
Figure 5.17: (a) Image simulation for 50 line pairs (corresponding to 33 LP/mm in the image plane) using an image analysis tool of Zemax™ [154]. (b) Image simulation of a Siemens spoke with 50 arms. In both images a FOV of 28° x 28° is shown and a sensor of 340x340 pixels with 4.4 µm pitch was modeled [154].

5.3.2   Demonstration of a Prototype System

A demonstration system was fabricated using microoptical fabrication techniques according to Fig. 4.3 with the parameters that are listed in Tab. 5.4.

Single optical modules were diced from the two component wafers and the integration was carried out on chip-level. The two components of the µoGSL were mounted on individual cantilevers in order to separately align them to a CCD image sensor (Fig. 5.18 left). Additionally, a passive alignment with spacers, marks and fixation through UV-glue was applied (Fig. 5.18 right).

Table 5.4: Parameters of the µoGSL components of Fig. 5.15 [154].

	MLA			Aperture			
	1	2	3	A 1	A 2	A 3	A 4
Radius of curvature [µm]	145	127	98				
Pitch [µm]	191	179	167	191	185	179	167
Diameter [µm]	-	-	-	150	80	100	120
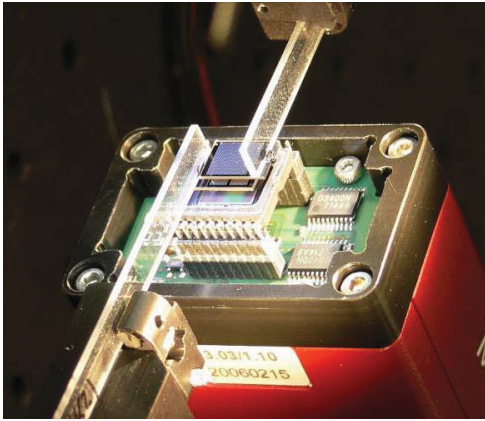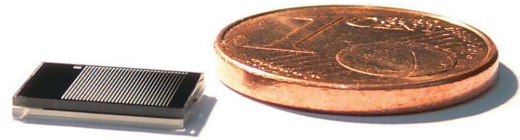
(a)   (b)

Figure 5.18: (a) The two components of the optical module were separately aligned to a CCD camera [153]. (b) Size comparison of a fully assembled microoptical Gabor Superlens. Each assembly contains an array of 2x2 µoGSLs [153].

Due to the optical stitching, any conventional image sensor is feasible for recording the image of the µoGSL as long as the pixel array is large enough. Different sensors were used to capture test images during the experimental examinations (Fig. 5.19).
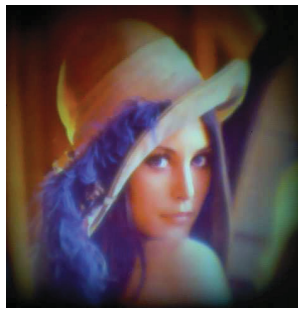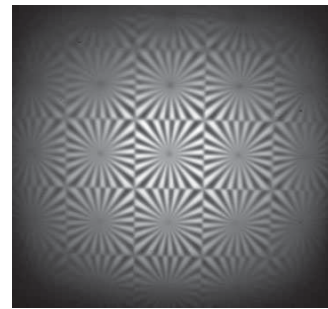
(a)   (b)

Figure 5.19: (a) Image of 'Lena' captured with the µoGSL on an image sensor with color filters and 3.2 µm pixel pitch. Image size is 500 x 500 pixels [153]. (b) Captured image (360 x 360 pixels) of a 5x5 array of Siemens spoke targets on a monochrome image sensor (4.4 µm pixel pitch) [153].

Two experiments were performed for the determination of the f-number of the µoGSL according to ISO 517:2008. The first setup for measuring the effective focal length is illustrated in Fig. 5.20a. A homogeneously illuminated Ronchi ruling (2) [constant-interval bars made of chromium on glass] was projected to infinity by an achromatic lens (3) with known focal length f_{Achr}. An LED panel with diffuser plate was used as light source (1).

The image (5) that is created by the µoGSL (4) is scaled according to the magnification of the system so that the effective focal length f_{GSL} is derived from

$$f_{GSL} = f_{Achr} \frac{h_{img}}{h_{obj}} \; . \tag{5.7}$$

The image height h_{img} was measured from the pixel extension in the image. The pixel pitch and the object height h_{obj} were known.
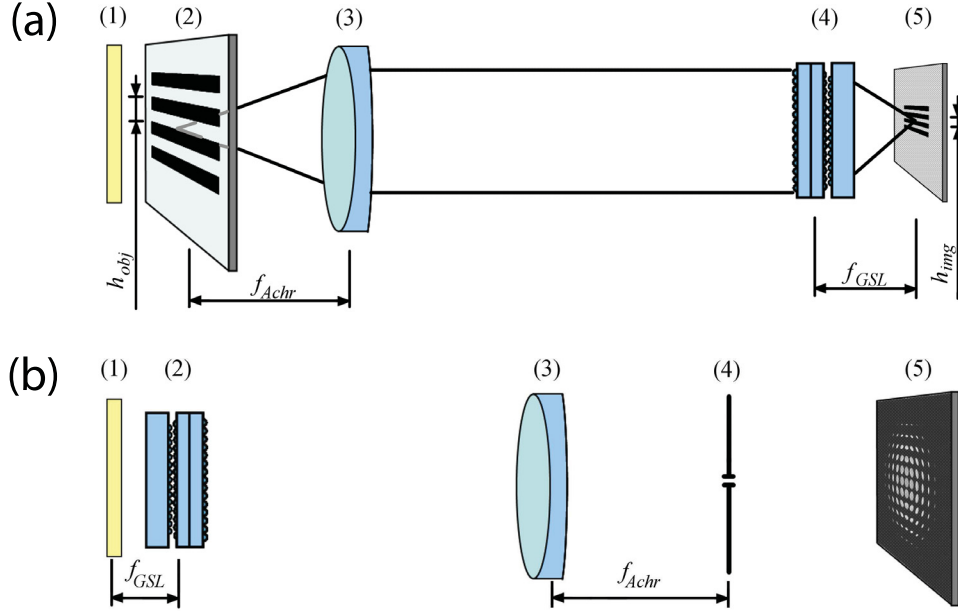
Figure 5.20: (a) Setup for measuring the effective focal length of the µoGSL [153]. (b) Setup for the determination of the effective diameter of the distributed entrance pupil [153].

A second experiment was used to measure the size of the effective entrance pupil (Fig. 5.20b). For that purpose, the light source (1) was positioned in the image plane of the µoGSL (2) and the entrance pupil (index 'enp') was illuminated homogeneously from the backside. An achromatic lens (3), that had been focused to infinity on an iris diaphragm (4), created a sharp image of the distributed entrance pupil (5) when the µoGSL was at the correct axial position. A pinhole (index 'ph') of known diameter was imaged with the same setup in order to retrieve a calibrated size of the entrance pupil from the relations:

$$D_{enp} = \sqrt{A_{enp} \cdot \frac{4}{\pi}} \; ; \quad A_{enp} = A_{ph} \cdot \frac{A_{enp,i}}{A_{ph,i}} \; . \tag{5.8}$$

Here, A_{ph} is the known area of the pinhole and $A_{enp,i}$ and $A_{ph,i}$ are the image areas of the distributed entrance pupil and the pinhole, respectively. An effective focal length of $f_{GSL} = 2.4$ mm and an entrance pupil diameter of $D_{enp} = 864$ µm were measured yielding an f-number of $F/\# = 2.8$ [153].

The resolution of the µoGSL was measured by determining the image contrast of bar charts of several different spatial frequencies. The simulated curves on the left of Fig. 5.21 were derived by the same method using image simulations.
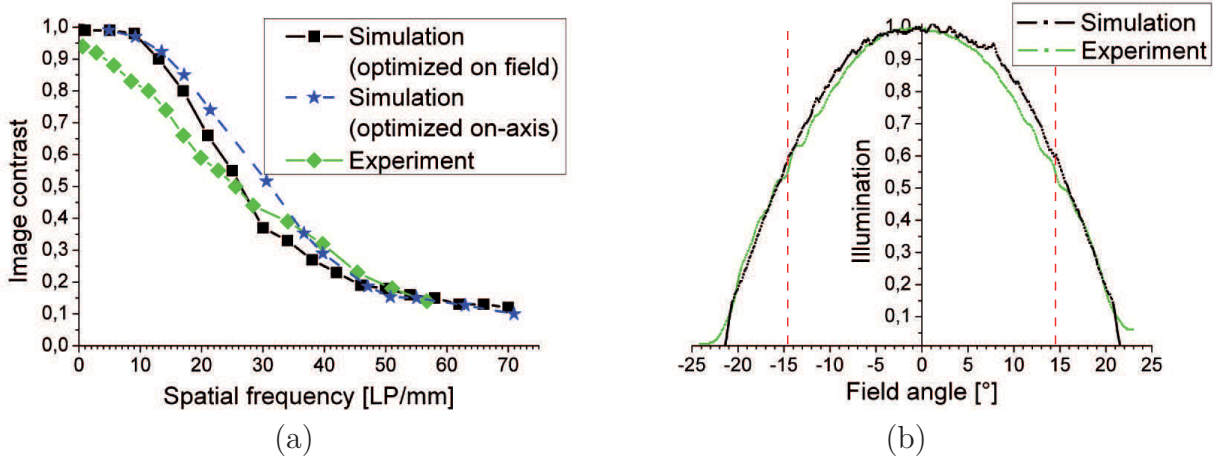
Figure 5.21: (a) Simulated and measured contrast transfer [153]. (b) Comparison of simulated and measured relative illumination in the image plane of the µoGSL. The red lines indicate the usable FOV [153].

At quarter Nyquist frequency or 28 LP/mm the measured contrast is 44 % which is in good agreement with the simulated contrast for a system configuration that was optimized for a high contrast transfer across the whole field. However, a simulated setup that was optimized on-axis achieves 58 % contrast at that spatial frequency. The resolution limit at a residual contrast of 10 % is reached at about 71 LP/mm for all curves.

The relative illumination in the image plane was determined from a normalized scan through the image of a white plane which is shown on the right of Fig. 5.21. The image brightness decreases rapidly at the edge of the FOV which is caused by a decreasing number of channels contributing to each image point for large field angles. The brightness drops to 60 % of the maximum value at 14.5° field angle which creates a total FOV of 29°. The measured data deviates only marginally from the simulated curve.

The essential parameters of the µoGSL demonstrator are summarized in Tab. 5.5.

Table 5.5: Summary of simulated and measured parameters for microoptical Gabor Superlens.

Parameter	Simulation	Experiment
Lateral size of single µoGSL [mm^2]	2.8 x 2.8	
Total track length [mm]	2.0	
Diameter of image circle [mm]	1.6	
Number of channels	15 x 15	
Effective focal length [mm]	2.3	2.4 ± 0.1
Effective entrance pupil diameter [µm]	868	864 ± 38
F-number	2.7	2.8 ± 0.2
Diameter of FOV, circular [°]	28.3	29
Image contrast, on-axis, at 28 LP/mm ($\approx \nu_{Ny}/4$) [%]	58	44
Image contrast, on-axis, at 57 LP/mm ($\approx \nu_{Ny}/2$) [%]	15	15
Spatial resolution limit [LP/mm]	71	70
Number of resolvable image points	257x257	158x158

5.4   Summary of Optical Stitching of Segments

In contrast to the electronic image stitching, a regular image sensor can be used for a multi aperture imaging systems with optical stitching of partial images. For example, the prototype of the optical cluster eye (oCLEY) achieved an information capacity of 446x335 resolvable image points on an extremely small sensor footprint size of 1.44 mm x 1.08 mm which yields a benefit for the chip costs. With a total track length of 1.86 mm the array of micro-objectives with tilted optical axes is shorter than single aperture objectives with comparable resolution and information capacity (Fig. 5.22). Contrasting to prior implementations, a focused image was achieved with optical partial image stitching of sub-pixel accuracy by implementing an additional MLA which tilts the optical axes of the off-axis channels towards normal incidence. The strong change of relative illumination across the image could be improved by applying an image sensor with an adapted fill factor enhancing MLA. However, with an f-number of $F/\# = 6.7$, the sensitivity is 3.3 times lower than for the eCLEY as the ratio of the irradiance in the image plane of two systems 1 and 2 scales according to $E_{im,1}/E_{im,2} = (F/\#_2/F/\#_1)^2$ [after Eq. (2.27)]. The trade-off between $F/\#$ and the system length, which is inherent to the oCLEY principle (see Fig. 5.2a), makes it unlikely to be improved without increasing the system length. Thus, the oCLEY is not able to achieve an f-number lower than 4.5 at a competitive total track length for miniature camera applications. Despite, it yields a compact optical imaging system with large depth of field which can be manufactured on wafer level.
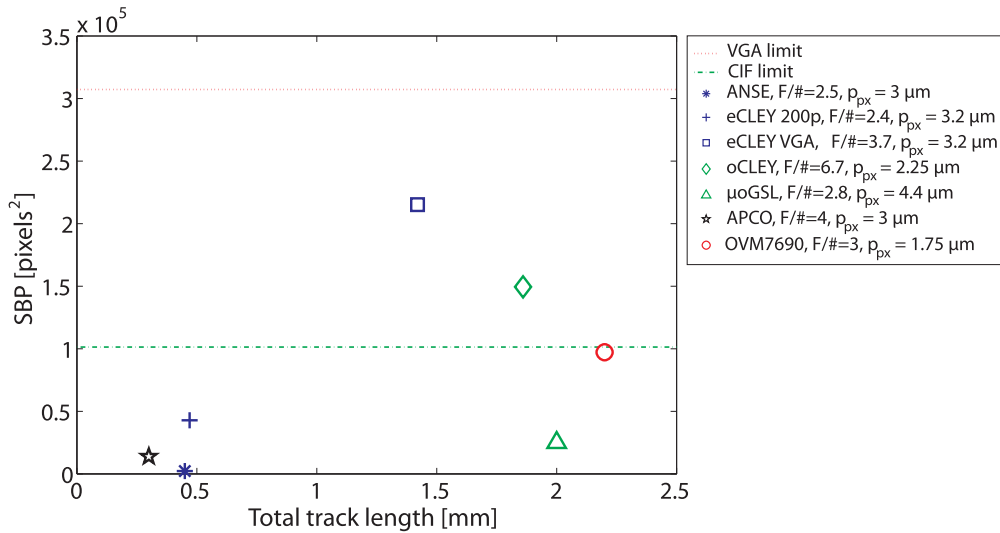
Figure 5.22: Experimentally derived space-bandwidth product (SBP or number of resolvable image points) of several realized MAOs as a function of total track length. The smallest commercially available SAO system OVM7690 [146] is added for comparison.

The overlap of partial images in the microoptical Gabor Superlens (µoGSL) enables the realization of a high sensitivity and thus overcomes the main drawback of the oCLEY. The prototype yielded an f-number of 2.8 at a total track length of 2 mm. This is 5.7 times more sensitive than the oCLEY. However, a large part of the overall FOV is transmitted by each optical channel which causes additional blur across the single partial images due

to off-axis aberrations and leads to a comparably low spatial resolution and, thus, small information capacity (Fig. 5.22). The field of view is limited to about 30° due to vignetting of off-axis rays. But, even this size of the FOV and the small footprint size of 2.8 mm² provide a considerable improvement over former realizations [21]. Future work will have to investigate the extension of the FOV size and the increase of the information capacity.

A multi aperture optical imaging system with unity magnification for close-up imaging was created by the approach of side-by-side optical image stitching with symmetrical MLAs of equal pitch. Such a setup decouples the trade-off between system length and size of the object field. Hence, the captured object field can be enlarged by simply increasing the number of optical channels. A prototype of the ultra-thin array microscope was integrated on a full-format image sensor so that a field size of 36.1 mm x 24.0 mm is captured by a system as short as 4.0 mm in a single exposure. The experimental resolution limit was measured to be 83 cycles/mm (or 12 µm structures) across the object field, taking into account residual imperfections of the partial image stitching. When looking at the simulation results, it is promising that the resolution could be increased up to 200 cycles/mm with a tight control of fabrication tolerances and sophisticated assembly techniques. The integration of a front side illumination and the adaptation of the optical system to image sensors with high frame rates are the key tasks for future work in order to enable the array microscope to enter applications in industrial inspection, quality assessment and biomedical imaging. The numerical aperture could be increased due to a partial image overlap for low-light tasks such as fluorescence imaging.

A detailed list of future tasks for the development of multi aperture optical imaging systems can be found in Appendix K.

6 Conclusions and Outlook

Throughout this thesis, the inspiration from the working principles of natural compound eyes is used for the successful miniaturization of man-made optical imaging systems. Thus, the archetypes of compound eyes were analyzed in order to overcome scaling limits that apply to today's single aperture cameras. There are two main advantages that were adopted for technical solutions in the present work: First, the segmentation of the field of view leading to a reduction of the imaging system's total track length and the adaptation of the optical parameters according to the viewing angle of the specific channel. This yields a simplification of the optical setup and a resolution near the diffraction limit. Second, the equality of scale makes it suitable to apply microoptical fabrication techniques for the creation of objectives on wafer level with relaxed tolerances compared to single aperture systems. The application of processes and equipment from photolithography enables high precision in the range of the visible wavelength for a large number of optical modules in parallel on wafer level. The aligned stacking of wafers is carried out for assembly purposes and an intrinsic housing is achieved for the different microlens arrays.

In the past, the exploitation of the *artificial apposition compound eye (APCO)* led to sub-millimeter thin imaging systems with large field of view [93, 96, 150]. However, the *APCO* is limited to a small spatial resolution (or space-bandwidth product) with a low application potential as it has a small optical fill factor and thus a large consumption of image sensor area which severely increases the system costs.

In this thesis, a novel classification of the different types of artificial compound eyes was introduced which sorts the solutions according to their characteristics of field of view segmentation and sampling. The classes of multi aperture imaging systems with electronic and optical image stitching were investigated by analytical modeling and numerical optical design. Both achieved a larger space-bandwidth product in each individual channel which makes them superior to the *APCO* type. A new semi-automated optical design and optimization technique was developed using sequential ray-tracing which enabled shorter design cycle times and rapid parameter changes. The derivation of a non-sequential simulation tool for optical cross talk was crucial, given the complexity of hundreds of microlenses and diaphragms with varying parameters across the chirped arrays in a single objective. As a result, the different setups of horizontal diaphragm arrays were optimized and, for the first time, a complete cross talk suppression was verified by lab experiments. Demonstration devices were fabricated by using adapted microoptical technologies and new methods of integration and characterization were applied. The experimental characterization included an adoption of measurement techniques for the modulation transfer function (MTF) as well as the determination of distortion, relative sensitivity and other properties of multi aperture imaging systems.

For the electronic image stitching, different extended parts of the overall field of view are captured by individual optical channels. Each optical channel operates separately so that

the partial images are created and recorded individually. Due to the inversion of each partial image, the spatial information is disordered in the image plane. The final image is created by digital image processing using a deterministic correlation between the sampled object points and their corresponding location in the image matrix.

Two different example systems using electronic image stitching have been demonstrated for the first time. The *artificial neural superposition eye (ANSE)* applies a redundant sampling so that pixels from different optical channels observe the same object point. This setup, which is inspired by the *neural superposition eye* of insects, enabled the increase of the signal-to-noise ratio in the image by a factor of three or the capture of first color images with a sub-mm thin artificial compound eye. However, redundant sampling allowed only a small increase of the space-bandwidth product when compared to the *APCO*. The main disadvantages of a low image resolution and a large footprint size remained.

The second type, termed *electronic cluster eye (eCLEY)*, applies an overlap of the fields of view of adjacent optical channels with a defined sub-pixel offset and a reduced focal length. Hence, the scaling limits are overcome and the total track length is decreased by 50% compared to single aperture imaging systems, whereas the object sampling and the space-bandwidth product are maintained.

To date, the demonstrated thickness of 1.4 mm makes the *eCLEY VGA* the thinnest optics module in its class of resolution. The smallest commercially available module has a thickness of 2.2 mm while using even smaller pixels [146]. The necessity of image post-processing led to a paradigm shift for the optical design in the present work. Distortion and lateral chromatic aberrations were left uncorrected in favor of a simplified optical setup and relaxed fabrication tolerances. Subsequent to capture, these errors were corrected by software processing for each partial image in real-time. Thus, the *eCLEY VGA* captured a large field of view with a residual distortion of less than 1%. The mastering of the microlens arrays (MLA) was carried out by photolithography and reflow of photoresist. UV-molding was applied for replication. These microoptical technologies enabled a highly precise fabrication for hundreds of lenslet arrays in parallel on a single wafer which is suitable for a potential production in high volume. However, the optical fill factor of the presented demonstrator was low, due to the mastering of MLAs by melting of photoresist. Consequently, a large megapixel image sensor was applied in order to achieve a VGA resolution which is not competitive for a camera application. But, the study of a customized image sensor and an adapted optical design for refractive free-form arrays proved that the fill factor can be increased from 8% to 31%.

The second investigated class of multi aperture imaging systems creates a seamless image on the sensor even though different parts of the full field of view have been transferred by different optical channels. The optical stitching of segments is enabled by a two-step imaging which resembles an array of focused Keplerian micro-telescopes: A first lens group creates a demagnified, inverted intermediate image which is magnified on the image sensor by a second lens group in each channel. Erect partial images result which is required for the optical image stitching. Hence, the setup becomes more complex and yields a larger

total track length compared to the electronic image stitching.

The optical design, simulation and experimental demonstration of two sampling approaches were investigated. The principle of the *optical cluster eye (oCLEY)* [17] was advanced by implementing 2D arrays with hexagonally distributed lenslets and an additional microlens array in order to achieve a smaller angle of incidence on the image sensor. In result, a focused image was created by optical image stitching with sub-pixel accuracy and, thus, it overcame the trade-off of the predecessor system [17]. The small lateral format size of the *oCLEY* enabled the use of a cheap image sensor. However, the derived trade-off between its total track length and the sensitivity of the system states a handicap for miniature camera applications.

The sampling approach of the *microoptical Gabor Superlens (µoGSL)* provided an increased sensitivity due to the superposition of partial images that were transferred by multiple channels. Although, the demonstration system yielded a sensitivity increase by a factor of six compared to the *oCLEY*, this occurred at the price of a reduced information capacity by about the same factor due to considerable off-axis aberrations that degrade the spot size for large field angles in each channel.

A special system using optical image stitching was formed by an *oCLEY* with parallel optical axes and a close object distance. Although, the so-called *ultra-thin array microscope* is principally limited to 1:1 magnification, it created an image with a resolution of 12 µm over an extended object field of 36 mm x 24 mm. The decisive advantage is that scaling of the field size is achieved by adding more optical channels and adjusting the image sensor size so that a huge information capacity can be achieved with a thin system.

Future work will avoid the trade-off between thickness and sensitivity of the *oCLEY* by the implementation of a partly superposition of few adjacent partial images. Thus, the effective f-number will be decreased without changing the system thickness. The resulting setup will be a hybrid of the *oCLEY* and the *µoGSL*. The integration of refractive free-form arrays into the relay system will enable a higher resolution due to the good correction of off-axis aberrations by free-form profiles. In conclusion, the *eCLEY* and the *ultra-thin array microscope* demonstrated the highest potential for the miniaturization of imaging systems. The assembly techniques of the *array microscope* will be improved in order to exploit diffraction-limited resolution which is feasible with today's microoptics technology. The integration of spectral filters and actuators will be beneficial for applications in medical imaging such as high-throughput screening or point-of-care diagnostics. Future work on the *eCLEY* will be technologically orientated in order to realize refractive free-form arrays which are the key to a high optical fill factor and megapixel resolution. A high-volume production at low costs compatible to microelectronics will be feasible, once the investigated mastering technology is an integral part of the microoptical wafer-level technology chain. Hence, the *eCLEY* offers smallest total track length at a given resolution and low costs which is highly attractive to consumer electronics and automotive applications. It was demonstrated to form a fundamentally new approach to miniaturized vision systems with high resolution which overcomes basic scaling limits of single aperture imaging optics.

Bibliography

[1] M. F. Land and D.-E. Nilsson, *Animal Eyes*, Oxford Animal Biology Series (Oxford University Press, Oxford, 2002).

[2] T. Gustavson, *Camera : A history of photography from Daguerreotype to digital* (Sterling Publishing Co., Inc., New York, 2009).

[3] E. Hecht, *Optik* (Addision-Wesley (Deutschland) GmbH, Bonn [a.o.], 1994), 3rd ed.

[4] W. Vogel, *Glaschemie* (Springer-Verlag, Berlin; Heidelberg; New York, 1992).

[5] S. Bäumer, *Handbook of Plastic Optics* (WILEY-VCH Verlag GmbH, Weinheim, 2005).

[6] J. Bareau and P. P. Clark, "The optics of miniature digital camera modules," in "International Optical Design, Technical Digest (CD)," (OSA, 2006), p. WB3.

[7] S. Mathur, M. Okincha, and M. Walters, "What camera manufacturers want," in "2007 International Image Sensor Workshop," (Ogunquit Maine, 2007).

[8] S. Ogata, J. Ishida, and T. Sasano, "Optical sensor array in an artificial compound eye," Opt. Eng. **33**, 3649–3655 (1994).

[9] J. S. Sanders and C. E. Halford, "Design and analysis of apposition compound eye optical sensors," Opt. Eng. **34**, 222–235 (1995).

[10] K. Hamanaka and H. Koshi, "An artificial compound eye using a microlens array and its application to scale-invariant processing," Opt. Rev. **3**, 264–268 (1996).

[11] K. Hoshino, F. Mura, and I. Shimoyama, "Design and performance of a micro-sized biomorphic compound eye with a scanning retina," IEEE J. Microelectromech. Syst. **9**, 32–37 (2000).

[12] J. Tanida, T. Kumagai, K. Yamada, S. Miyatake, K. Ishida, T. Morimoto, N. Kondou, D. Miyazaki, and Y. Ichioka, "Thin observation module by bound optics (TOMBO): concept and experimental verification," Appl. Opt. **40**, 1806–1813 (2001).

[13] M. Shankar, R. Willett, N. Pitsianis, T. Schulz, R. Gibbons, R. T. Kolste, J. Carriere, C. Chen, D. Prather, and D. Brady, "Thin infrared imaging systems through multichannel sampling," Appl. Opt. **47**, B1–B10 (2008).

[14] G. Druart, N. Guérineau, R. Haidar, S. Thétas, J. Taboury, S. Rommeluère, J. Primot, and M. Fendler, "Demonstration of an infrared microcamera inspired by *Xenos peckii* vision," Appl. Opt. **48**, 3368–3374 (2009).

[15] J. Duparré, P. Dannberg, P. Schreiber, A. Bräuer, and A. Tünnermann, "Artificial apposition compound eye fabricated by micro–optics technology," Appl. Opt. **43**, 4303–4310 (2004).

[16] J. Duparré, P. Dannberg, P. Schreiber, A. Bräuer, and A. Tünnermann, "Thin compound-eye camera," Appl. Opt. **44**, 2949–2956 (2005).

[17] J. Duparré, P. Schreiber, A. Matthes, E. Pshenay-Severin, A. Bräuer, A. Tünnermann, R. Völkel, M. Eisner, and T. Scharf, "Microoptical telescope compound eye," Opt. Exp. **13**, 889–903 (2005).

[18] K.-H. Jeong, J. Kim, and L. P. Lee, "Biologically inspired artificial compound eyes," Science **312**, 557–561 (2006).

[19] J. Duparré and F. Wippermann, "Micro-optical artificial compound eyes," Bioinspir. Biomim. **1**, R1–R16 (2006).

[20] D. Radtke, J. Duparré, U. Zeitner, and A. Tünnermann, "Laser lithographic fabrication and characterization of a spherical artificial compound eye," Opt. Exp. **15**, 3067–3077 (2007).

[21] C. Hembd-Sölner, R. F. Stevens, and M. C. Hutley, "Imaging properties of the Gabor Superlens," J. Opt. A: Pure Appl. Opt. **1**, 94–102 (1999).

[22] N. Wakabayashi and H. Ishibashi, "Optical disk drive apparatus," Pat. US 4,669,073 (1987).

[23] S. Mansfield, W. Studenmund, G. Kino, and K. Osato, "High-numerical-aperture lens system for optical storage," Opt. Lett. **18**, 305–307 (1993).

[24] J. Davis, M. Brosnan, T. Walley, M. Anderson, B. Misek, and A. Norskog, "One chip USB optical mouse sensor solution," Patent Application Publication US 2003/0034959 A1 (2003).

[25] R. A. Natalin and J. Landman, "Where next for the endoscope?" Nature Reviews Urology **6**, 622–628 (2009).

[26] P. Swain, "Wireless capsule endoscopy," Gut **52**, 48–50 (2003).

[27] P. Roulet, P. Konen, and S. Thibault, "Multi-task single lens for automotive vision applications," in "Photonics in the Transportation Industry: Auto to Aerospace II," , vol. **7314**, A. A. Kazemi and B. C. Kress, eds. (SPIE, 2009), p. 731409.

[28] S. Franz, D. Willersinn, and K. Kroschel, "Assessment of image sensor performance with statistical perception performance analysis," in "Intelligent Robots and Computer Vision XXVII: Algorithms and Techniques," , vol. **7539**, D. P. Casasent, E. L. Hall, and J. Röning, eds. (SPIE, 2010), p. 75390I.

[29] A. Schick, F. Forster, and M. Stockmann, "3D measuring in the field of endoscopy," in "Optical Measurement Systems for Industrial Inspection VII," , vol. **8082**, P. H. Lehmann, W. Osten, and K. Gastinger, eds. (SPIE, 2011), p. 808216.

[30] E. E. Anderson and W. L. Wang, "Novel contact image sensor (CIS) module for compact and lightweight full-page scanner applications," in "Cameras, Scanners, and Image Acquisition Systems," , vol. **1901**, H. C. Marz and R. L. Nielsen, eds. (SPIE, 1993), pp. 173–181.

[31] N. Franceschini, J. M. Pichon, and C. Blanes, "From insect vision to robot vision," Phil. Trans. R. Soc. Lond. B **337**, 283–294 (1992).

[32] F. Ruffier, S. Viollet, and N. Franceschini, "OSCAR and OCTAVE: Two bio-inspired visually guided aerial micro-robots," in "Proceedings of ICAR 2003," (ICAR, Coimbra, Portugal, 2003), pp. 726–732.

[33] D. Floreano and J.-C. Zufferey, "Insect vision : A few tricks to regulate flight altitude," Current Biology **20**, R847–R849 (2010).

[34] P. Yager, G. J. Domingo, and J. Gerdes, "Point-of-care diagnostics for global health," Annu. Rev. Biomed. Eng. **10**, 107–144 (2008).

[35] D. Trivedi, C. D. Rahn, W. M. Kier, and I. D. Walker, "Soft robotics: Biological inspiration, state of the art, and future research," Applied Bionics and Biomechanics **5**, 99–117 (2008).

[36] Y. Ma, S. Soatto, J. Kosecká, and S. S. Sastry, *An invitation to 3-D vision*, Interdisciplinary Applied Mathematics, Vol. 26 (Springer, 2004), 1st ed.

[37] B. Javidi and F. Okano, *Three-dimensional television, video and display technology* (Springer-Verlag New York, Inc., Secaucus, NJ, USA, 2002).

[38] J. S. Jang and B. Javidi, "Two–step integral imaging for orthoscopic three–dimensional imaging with improved viewing resolution," Opt. Eng. **41**, 2568–2571 (2002).

[39] E. H. Adelson and J. Y. A. Wang, "Single lens stereo with a plenoptic camera," IEEE Transactions on Pattern Analysis and Machine Intelligence **14**, 99–106 (1992).

[40] R. Ng, "Fourier slice photography," in "SIGGRAPH '05 ACM SIGGRAPH 2005 Papers," , M. Gross, ed. (ACM, New York, NY, USA, 2005), pp. 735 – 744.

[41] U. Perwass, "Digital imaging system for synthesizing an image using data recorded with a plenoptic camera," European Patent Application EP 2 244 484 A1 (2010).

[42] Vista Point Technologies, Inc., "http://www.vptech.com/solutions/," (2010).

[43] R. Fischer and B. Tadic-Galeb, *Optical System Design* (McGraw-Hill, New York, 2000).

[44] M. J. Kidger, *Fundamental Optical Design* (SPIE - The International Society of Optical Engineering, Bellingham, Washington, 2002).

[45] R. Kingslake, *Optical System Design* (Academic Press, New York, 1983).

[46] R. Kingslake, *A History of the Photographic Lens* (Academic Press, San Diego, California, 1989).

[47] M. Born and E. Wolf, *Principles of Optics* (Cambridge University Press, Cambridge [u.a.], 1999), 7th ed.

[48] H. Naumann and G. Schröder, *Bauelemente der Optik - Taschenbuch der technischen Optik* (Hanser, München, 1992), 6th ed.

[49] W. J. Smith, *Modern Opitcal Engineering : The Design of Optical Systems*, Optical and Electro-Optical Engineering Series (McGraw-Hill, New York, 1990), 2nd ed.

[50] M. Rossi, "Wafer-Level Optics for miniature cameras," in "SPIE Photonics Europe - Optics, Photonics and Digital Technologies for Multimedia Applications," (SPIE, Brussels, Belgium, 2010).

[51] E. Wolterink and K. Demeyer, "WaferOptics mass volume production and reliability," in "Micro-Optics 2010," , vol. **7716**, H. Thienpont, P. V. Daele, J. Mohr, and H. Zappe, eds. (SPIE, Brussels, Belgium, 2010), p. 771614.

[52] J. W. Goodman, *Introduction to Fourier Optics* (The McGraw-Hill Companies, Inc., New York, 1996), 2nd ed.

[53] V. N. Mahajan, *Aberration Theory Made Simple* (SPIE Optical Engineering Press, Bellingham, 1991).

[54] A. W. Lohmann, "Scaling laws for lens systems," Appl. Opt. **28**, 4996–4998 (1989).

[55] W. T. Welford, *Aberrations of optical systems* (Inst. of Physics Publ., Bristol, UK, 1986).

[56] H. Haferkorn, *Optik* (Wiley-VCH Verlag, Weinheim, 2003), 4th ed.

[57] Microelectronics Technology Devision, *Application Note DS 00-001 - Solid State Image Sensors Terminology*, Eastman Kodak Company, New York, Rochester (1994).

[58] Kodak Image Sensor Solutions, *Application Note - Kodak Image Sensors - Rev. 2.0 MTD/PS-0218*, Eastman Kodak Company (2008).

[59] R. Lukac, *Single-Sensor imaging: methods and applications for digital cameras* (CRC Press, Taylor & Francis Group, 2009), chap. 4 - R. Palum, "Anti-aliasing filters,", pp. 105 –134.

[60] R. C. Gonzalez and R. E. Woods, *Digital Image Processing* (Prentice Hall, Upper Saddle River, New Jersey, 2002), 2nd ed.

[61] B. E. Bayer, "Color imaging array," Pat. US 3,971,065 (1976).

[62] Kodak Image Sensor Solutions, *Device Performance Specification - Kodak KAI-16000 Image Sensor - Rev. 4.0 MTD/PS-1027*, Eastman Kodak Company (2009).

[63] J. Adams, K. Parulski, and K. Spaulding, "Color processing in digital cameras," IEEE Micro **18**, 20–30 (1998).

[64] R. F. Lyon and P. M. Hubel, "Eyeing the camera: into the next century," in "Proc. IS&T/TSID 10th Color Imaging Conf.", (IS&T/TSID, Scottsdale, AZ, USA, 2002), pp. 349–355.

[65] Kodak Image Sensor Solutions, *Application Note - Conversion of Light (Photons) to Electronic Charge - Rev. 2.1 MTD/PS-0217*, Eastman Kodak Company (2009).

[66] H. Schaumburg, *Sensoren*, Werkstoffe und Bauelemente der Elektrotechnik 3 (B. G. Teubner, Stuttgart, 1992).

[67] Kodak Image Sensor Solutions, *Application Note - CCD Image Sensor Noise Sources - Rev. 2.1 MTD/PS-0233*, Eastman Kodak Company (2005).

[68] H. Tian, B. Fowler, and A. E. Gamal, "Analysis of temporal noise in CMOS photodiode active pixel sensor," IEEE J. Solid-State Circuits **36**, 92–101 (2001).

[69] A. E. Gamal, B. Fowler, H. Min, and X. Liu, "Modeling and estimation of FPN components in CMOS image sensors," in "Solid State Sensor Arrays: Development and Applications II," , vol. **3301**, M. M. Blouke, ed. (SPIE, 1998), pp. 168–177.

[70] I. N. Bronstein, K. A. Semendjajew, G. Musiol, and H. Mühlig, *Handbook of Mathemtics* (Verlag Harri Deutsch, Frankfurt am Main, 2001), 5th ed.

[71] E. Dowski and W. Cathey, "Extended depth of field through wave-front coding," Appl. Opt. **34**, 1859–1866 (1995).

[72] R. Völkel, M. Eisner, and K. J. Weible, "Miniaturized imaging systems," Microelectron. Eng. **67-68**, 461–472 (2003).

[73] J. Duparré, "Microoptical artificial compound eyes," Ph.D. thesis, Friedrich-Schiller-Universität Jena (2005).

[74] T. Chen, P. Catrysse, A. E. Gamal, and B. Wandell, "How small should pixel size be?" in "Sensors and Camera Systems for Scientific, Industrial, and Digital Photography Applications," , vol. **3965**, M. M. Blouke, N. Sampat, G. M. Williams, and T. Yeh, eds. (SPIE, San Jose, CA, USA, 2000), pp. 451–459.

[75] R. Hardie, "Functional organization of the fly retina," Progress in Sensory Physiology **5**, 1–79 (1985).

[76] J. Thorson, "Small-signal analysis of a visual reflex in the locust," Kybernetik **3**, 41–66 (1966).

[77] G. A. Horridge, "The compound eye of insects," Sci. Am. **237**, 108–120 (1977).

[78] K. Nakayama, "Biological image motion processing: a review," Vision Res. **25**, 625–660 (1985).

[79] M. F. Land, "Variations in Structure and Design of Compound Eyes," in "Facets of Vision," , D. Stavenga and R. C. Hardie, eds. (Springer, 1989), chap. 5, pp. 90–111.

[80] J. S. Sanders, ed., *Selected Papers on Natural and Artificial Compound Eye Sensors*, SPIE Milestone Series (SPIE Optical Engineering Press, Bellingham, 1996), 122nd ed.

[81] A. W. Snyder, D. G. Stavenga, and S. B. Laughlin, "Spatial Information Capacity of Compound Eyes," J. Comp. Physiol. A **116**, 183–207 (1977).

[82] K. G. Goetz, "Die optischen Übertragungseigenschaften der Komplexaugen von Drosophila," Kybernetik **2**, 215–221 (1965).

[83] M. F. Land, "Compound eyes: old and new optical mechanisms," Nature **287**, 681–686 (1980).

[84] G. A. Horridge, "The separation of visual axes in apposition compound eyes," Phil. Trans. R. Soc. Lond. B **285**, 1–59 (1978).

[85] A. W. Snyder, "Acuity of compound eyes: Physical limitations and design," J. Comp. Physiol. A **116**, 161–182 (1977).

[86] A. W. Snyder, "Physics of vision in compound eyes," in "Handbook of sensory physiology," (Springer, 1977), pp. 225–313.

[87] H. B. Barlow, "The size of ommatidia in apposition eyes," J. Exp. Biol. **29**, 667–674 (1952).

[88] K. Kirschfeld, "The resolution of lens and compound eyes," Neural Principles in Vision pp. 354–370 (1976).

[89] J. Kim, K.-H. Jeong, and L. P. Lee, "Artificial ommatidia by self-aligned microlenses and waveguides," Opt. Lett. **30**, 5–7 (2005).

[90] K. Jeong, J. Kim, and L. P. Lee, "Polymeric synthesis of biomimetic artificial compound eyes," in "Proc. of the 13th Int. Conf. on Solid-State Sensors, Actuators and Microsystems (Transducers 05)," (2005), pp. 1110–1114.

[91] K. Hoshino, F. Mura, and I. Shimoyama, "A one–chip scanning retina with an integrated micromechanical scanning actuator," J. of Microelectromech. Syst. **10**, 492–497 (2001).

[92] D. Pätz, S. Leopold, F. Knöbber, S. Sinzinger, M. Hoffmann, and O. Ambacher, "Tunable compound eye cameras," in "Micro-Optics 2010," , vol. **7716**, H. Thienpont, P. V. Daele, J. Mohr, and H. Zappe, eds. (SPIE, Brussels, Belgium, 2010), p. 77160K.

[93] A. Brückner, J. Duparré, P. Dannberg, A. Bräuer, and C. Hoffmann, "Ultra-compact vision system for automotive applications," in "Proc. 4th EOS Topical Meeting on Advanced Imaging Techniques," (Jena, Germany, 2009), pp. 166–167.

[94] A. Brückner, J. Duparré, A. Bräuer, and A. Tünnermann, "Artificial compound eye applying hyperacuity," Opt. Exp. **14**, 12076–12084 (2006).

[95] A. Brückner, J. Duparré, A. Bräuer, and A. Tünnermann, "Position detection with hyperacuity using artificial compound eyes," in "Proc. of SPIE - Sensors, Cameras, and Systems for Scientific/Industrial Applications VIII," , vol. **6501**, M. M. Blouke, ed. (IS&T / SPIE, 2007), p. 65010D.

[96] J. Duparré, F. Wippermann, P. Dannberg, and A. Reimann, "Chirped arrays of refractive ellipsoidal microlenses for aberration correction under oblique incidence," Opt. Exp. **13**, 10539–10551 (2005).

[97] F. Wippermann, J. Duparré, P. Schreiber, and P. Dannberg, "Design and fabrication of a chirped array of refractive ellipsoidal micro-lenses for an apposition eye camera objective," in "Optical Design and Engineering II,", vol. **5962**, L. Mazuray and R. Wartmann, eds. (SPIE, 2005), p. 59622C.

[98] F. Wippermann, "Chirped refractive microlens arrays," Ph.D. thesis, Technische Universität Ilmenau (2008).

[99] K. Kirschfeld and N. Franceschini, "Optical characteristics of ommatidia in the complex eye of Musca," Kybernetik **5**, 47–52 (1968).

[100] P. McIntyre and S. Caveney, "Graded index optics are matched to optical geometry in the superposition eyes of scarab beetles," Phil. Trans. R. Soc. Lond. B **311**, 237–269 (1985).

[101] M. F. Land, F. Burton, and V. Meyer-Rochow, "The Optical Geometry of Euphausiid Eyes," J. Comp. Physiol. A **130**, 49–62 (1979).

[102] R. Navarro and N. Franceschini, "On image quality of microlens arrays in diurnal superposition eyes," Pure Appl. Opt. **7**, 69–78 (1998).

[103] D. Gabor, "Improvements in or relating to optical systems composed of lenticules," Pat. UK 541,753 (1940).

[104] M. Hutley, R. F. Stevens, and C. Hembd, "Imaging properties of the *Gabor Superlens*," in "Digest of Top. Meet. on Microlens Arrays at NPL, Teddington,", vol. **13**, M. C. Hutley, ed. (EOS, 1997), pp. 101–104.

[105] M. Toyama and M. Takami, "Luminous intensity of a gradient-index lens array," Appl. Opt. **21**, 1013–1016 (1982).

[106] M. Kawazu and Y. Ogura, "Application of gradient-index fiber arrays to copying machines," Appl. Opt. **19**, 1105–1112 (1980).

[107] N. F. Borrelli, R. H. Bellman, J. A. Durbin, and W. Lama, "Imaging and radiometric properties of microlens arrays," Appl. Opt. **30**, 3633–3642 (1991).

[108] V. Shaoulov and J. P. Rolland, "Design and assessment of microlenslet-array relay optics," Appl. Opt. **42**, 6838–6845 (2003).

[109] R. H. Anderson, "Close-up imaging of documents and displays with lens arrays," Appl. Opt. **18**, 477–484 (1979).

[110] R. Völkel, H. P. Herzig, P. Nussbaum, and R. Dändliker, "Microlens array imaging system for photolithography," Opt. Eng. **35**, 3323–3330 (1996).

[111] R. Völkel, H. P. Herzig, P. Nussbaum, P. Blattner, R. Dändliker, E. Cullmann, and W. B. Hugle, "New lithographic techniques using microlens arrays," in "MLAs, EOS Top. Meet.",, vol. **13**, M. C. Hutley, ed. (EOS, Teddington, UK, 1997), pp. 105–109.

[112] E. Buschbeck, B. Ehmer, and R. Hoy, "Chunk versus point sampling: Visual imaging in a small insect," Science **286**, 1178–1179 (1999).

[113] G. Horváth, E. Clarkson, and W. Pix, "Survey of modern counterparts of schizochroal trilobite eyes: structural and functional similarities and differences," Historical Biology **12**, 229–263 (1997).

[114] W. Pix, J. M. Zanker, and J. Zeil, "The optomotor response and spatial resolution of the visual system in male *Xenos vesparum* (Strepsiptera)," The Journal of Experimental Biology **203**, 3397–3409 (2000).

[115] E. K. Buschbeck, "The compound lens eye of strepsiptera: morphological development of larvae and pupae," Arthropod Structure and Development **34**, 315–326 (2005).

[116] M. C. Hutley, R. Hunt, R. F. Stevens, and P. Savander, "The moiré magnifier," Pure Appl. Opt. **3**, 133–142 (1994).

[117] H. Kamal, R. Völkel, and J. Alda, "Properties of moiré magnifiers," Opt. Eng. **37**, 3007–3014 (1998).

[118] G. Druart, N. Guérineau, R. Haïdar, E. Lambert, M. Tauvy, S. Thétas, S. Rommeluère, J. Primot, and J. Deschamps, "MULTICAM: a miniature cryogenic camera for infrared detection," in "Micro-Optics 2008,", vol. **6992**, H. Thienpont, P. Van Daele, J. Mohr, and M. R. Taghizadeh, eds. (SPIE, 2008), p. 69920G.

[119] S. Farsiu, D. Robinson, M. Elad, and P. Milanfar, "Advances and challenges in Super-Resolution," International Journal of Imaging Systems and Technology **14**, 47–57 (2004).

[120] K. Yamada, J. Tanida, W. Yu, S. Miyatake, K. Ishida, D. Miyazaki, and Y. Ichioka, "Fabrication of diffractive microlens array for opto–electronic hybrid information system," in "Proc. of Diffractive Optics' 99," (EOS, 1999), pp. 52–53.

[121] J. Tanida, R. Shogenji, Y. Kitamura, K. Yamada, M. Miyamoto, and S. Miyatake, "Color imaging with an intergrated compound imaging system," Opt. Exp. **11**, 2109–2117 (2003).

[122] R. Shogenji, Y. Kitamura, K. Yamada, S. Miyatake, and J. Tanida, "Multispectral imaging using compact compound optics," Opt. Exp. **12**, 1643–1655 (2004).

[123] R. Horisaki, S. Irie, Y. Nakao, Y. Ogura, T. Toyoda, Y. Masaki, and J. Tanida, "3D information acquisition using a compound imaging system," in "Optics and Photonics for Information Processing," , vol. **6695**, A. A. Awwal, K. M. Iftekharuddin, and B. Javidi, eds. (SPIE, 2007), p. 66950F.

[124] J. Tanida, Y. Kitamura, K. Yamada, S. Miyatake, M. Miyamoto, T. Morimoto, Y. Masaki, N. Kondou, D. Miyazaki, and Y. Ichioka, "Compact image capturing system based on compound imaging and digital reconstruction," in "Micro– and Nano–optics for optical interconnection and information processing," , vol. **4455**, M. R. Taghizadeh, H. Thienpont, and G. E. Jabbour, eds. (SPIE, 2001), pp. 34–41.

[125] F. de la Barrière, G. Druart, N. Guérineau, and J. Taboury, "Design strategies to simplify and miniaturize imaging systems," Appl. Opt. **50**, 943–951 (2011).

[126] Y. Kitamura, R. Shogenji, K. Yamada, S. Miyatake, M. Miyamoto, T. Morimoto, Y. Masaki, N. Kondou, D. Miyazaki, J. Tanida, and Y. Ichioka, "Reconstruction of a high–resolution image on a compound–eye image–capturing system," Appl. Opt. **43**, 1719–1727 (2004).

[127] K. Nitta, R. Shogenji, S. Miyatake, and J. Tanida, "Image reconstruction for thin observation module by bound optics by using the iterative backprojection method," Appl. Opt. **45**, 2893–2900 (2006).

[128] F. L. Pedrotti and S. J. Pedrotti, *Introduction to optics* (Prentice–Hall, 1993), 2nd ed.

[129] A. E. Siegmann, *Lasers* (University Science Books, Mill Valey, 1986).

[130] N. Lindlein and H. P. Herzig, "Design and modeling of a miniature system containing micro-optics," in "Gradient Index, Miniature, and Diffractive Optical Systems II," , vol. **4437**, T. J. Suleski, ed. (SPIE, 2001), pp. 1–13.

[131] N. Lindlein, "Simulation of micro-optical systems including microlens arrays," J. Opt. A: Pure Appl. Opt. **4**, 1–9 (2002).

[132] A. Gullstrand, "Beitrag zur Theorie des Astigmatismus," Skand. Arch. Physiol. **2**, 269–359 (1889).

[133] N. Lindlein, S. Haselbeck, and J. Schwider, "Simplified theory for ellipsoidal melted microlenses," in "Digest of Top. Meet. on Microlens Arrays at NPL, Teddington," , vol. **5**, M. C. Hutley, ed. (EOS, 1995), pp. 7–10.

[134] Z. D. Popovich, R. A. Sprague, and G. A. N. Conell, "Technique for monolithic fabrication of microlens arrays," Appl. Opt. **27**, 1281–1284 (1988).

[135] H. P. Herzig, *Micro–Optics: Elements, systems and applications* (Taylor & Francis, 1997).

[136] S. Sinzinger and J. Jahns, *Microoptics* (Wiley–VCH, Weinheim, 1999).

[137] D. Daly, R. F. Stevens, M. C. Hutley, and N. Davies, "The manufacture of microlenses by melting photoresist," J. Meas. Sci. Technol. **1**, 759–766 (1990).

[138] P. Dannberg, G. Mann, L. Wagner, and A. Bräuer, "Polymer UV-molding for micro-optical systems and O/E- integration," in "Micromachining for Micro–Optics," , vol. **4179**, S. H. Lee and E. G. Johnson, eds. (SPIE, 2000), pp. 137–145.

[139] R. Houbertz, G. Domann, C. Cronauer, A. Schmitt, H. Martin, J.-U. Park, L. Fröhlich, R. Buestrich, M. Popall, U. Streppel, P. Dannberg, C. Wächter, and A. Bräuer, "Inorganic-Organic Hybrid Materials for Application in Optical Devices," Thin Solid Films **442**, 194–200 (2003).

[140] A. Brückner, J. Duparré, P. Dannberg, A. Bräuer, and A. Tünnermann, "Artificial neural superposition eye," Opt. Exp. **15**, 11922–11933 (2007).

[141] A. Brückner, J. Duparré, R. Leitel, P. Dannberg, A. Bräuer, and A. Tünnermann, "Thin wafer-level camera lenses inspired by insect compound eyes," Opt. Exp. **18**, 24379–24394 (2010).

[142] D. J. Brady and N. Hagen, "Multiscale lens design," Opt. Exp. **17**, 10659–10674 (2009).

[143] A. Oberdörster, A. Brückner, F. C. Wippermann, and A. Bräuer, "Correcting distortion and braiding of micro-images from multi-aperture imaging systems," in "Sensors, Cameras, and Systems for Industrial, Scientific, and Consumer Applications XII," , vol. **7875**, R. Widenhorn and V. Nguyen, eds. (SPIE, San Francisco, CA, USA, 2010), p. 78750B.

[144] A. Oberdörster, A. Brückner, F. Wippermann, A. Bräuer, and H. P. Lensch, "Digital focusing and re-focusing with thin multi-aperture cameras," in "submitted to SPIE Conference on Electronic Imaging, Digital Photography VIII, EI116 (2012)," (2012).

[145] P. D. Burns and D. Williams, "Practical MTF metrology for digital cameras and scanners," Tutorial notes, Eastman Kodak Company, San José, CA, USA (2004).

[146] OmniVision, *OVM7690 640x480 CameraCube™ device, product brief*, 1st ed. (2010).

[147] T. Schweiger and H. Neubauer, "Scaling of cluster eye type image sensors," (2011). Feasibility study.

[148] J. Meyer, A. Brückner, R. Leitel, P. Dannberg, A. Bräuer, and A. Tünnermann, "Optical Cluster Eye fabricated on wafer-level," Opt. Exp. **19**, 17506–17519 (2011).

[149] J. Meyer, "Entwicklung eines hochauflösenden Multiapertur-Abbildungssystems," Diplomarbeit, Friedrich-Schiller-Universität Jena (2010).

[150] J. Duparré, D. Radtke, A. Brückner, and A. Bräuer, "Latest developments in micro-optical artificial compound eyes: a promising approach for next generation ultracompact machine vision," in "Machine Vision Applications in Industrial Inspection XV," , vol. **6503**, F. Meriaudeau and K. S. Niel, eds. (SPIE, 2007), p. 65030I.

[151] A. Brückner, J. Duparré, F. Wippermann, R. Leitel, P. Dannberg, and A. Bräuer, "Ultra-compact close-up microoptical imaging system," in "Current Developments in Lens Design and Optical Engineering XI; and Advances in Thin Film Coatings VI," , vol. **7786**, R. B. Johnson, V. N. Mahajan, and S. Thibault, eds. (SPIE, 2010), p. 77860A.

[152] M. Hutley and R. F. Stevens, "The formation of integral images by afocal pairs of lens arrays (*Superlenses*)," in "Digest of Short Meet. on Microlens Arrays at NPL, Teddington," , vol. **30**, M. C. Hutley, ed. (IOP, 1991), pp. 147–154.

[153] K. Stollberg, A. Brückner, J. Duparré, P. Dannberg, A. Bräuer, and A. Tünnermann, "The Gabor Superlens as an alternative wafer-level camera approach inspired by superposition compound eyes of nocturnal insects," Opt. Exp. **17**, 15747–15759 (2009).

[154] K. Stollberg, "Gabor-Superlinse - Miniaturisierte Abbildungsoptik nach dem Vorbild natürlicher Superpositionsaugen," Diplomarbeit, Friedrich-Schiller-Universität Jena (2009).

[155] J. Adams, "Design of practical color filter array interpolation algorithms for digital cameras," in "Real-Time Imaging II," , vol. **3028**, D. Sinha, ed. (SPIE, San Jose, CA, USA, 1997), pp. 117–125.

[156] R. Keys, "Cubic convolution interpolation for digital image processing," IEEE Transactions on Signal Processing, Acoustics, Speech, and Signal Processing **29**, 1153 – 1160 (1981).

[157] F. Hirigoyen, A. Crocherie, P. Boulenc, J. Vaillant, C. Tavernier, and D. Hérault, "Finite-difference time domain based electro-optical methodologies to improve CMOS image sensor pixels performances," in "Optics, Photonics, and Digital Technologies for Multimedia Applications," , vol. **7723**, P. Schelkens, T. Ebrahimi, G. Cristóbal, F. Truchetet, and P. Saarikko, eds. (SPIE, Brussels, Belgium, 2010), p. 772318.

[158] E. W. Jin, "Image quality quantification in camera phone applications," in "IEEE International Conference on Acoustics, Speech and Signal Processing, 2008. ICASSP 2008," (IEEE, Las Vegas, NV, USA, 2008), pp. 5336 – 5339.

[159] C. D. Carey, D. P. Godwin, P. C. H. Poon, D. J. Daly, D. R. Selviah, and J. E. Midwinter, "Astigmatism in ellipsoidal and spherical photoresist microlenses used at oblique incidence," in "Digest of Top. Meet. on Microlens Arrays at NPL, Teddington," , vol. **2**, M. C. Hutley, ed. (EOS, 1993), pp. 65–68.

Appendix

A   Scaling of Primary Aberrations

The following table lists the primary wavefront and transverse ray aberrations together with their common names.

Table A.1: List of primary wavefront and transverse ray aberrations as well as first order chromatic aberrations and their variation with the object field coordinate h [53, 55]. The term (r_n, Θ) defines the cylindrical pupil coordinates with $0 \leq r_n \leq r_{ExP}$ and $0 \leq \Theta \leq 2\pi$. The identifier r_{ExP} denotes the radius of the exit pupil.

Name of aberration	Wavefront aberration	Transverse ray aberration
Spherical	$a_{040} \cdot r_n^4$	$\frac{4R}{n\cos(\Theta)} \cdot a_{040} \cdot r_n^3$
Coma	$a_{131} \cdot h \; r_n^3 \cos(\Theta)$	$\frac{3R}{n} \cdot a_{131} \cdot h \; r_n^2$
Astigmatism	$a_{222} \cdot h^2 r_n^2 \cos^2(\Theta)$	$\frac{2R}{n} \cdot a_{222} \cdot h^2 r_n \cos(\Theta)$
Field curvature	$a_{220} \cdot h^2 r_n^2$	$\frac{2R}{n\cos(\Theta)} \cdot a_{220} \cdot h^2 r_n$
Distortion	$a_{311} \cdot h^3 r_n \cos(\Theta)$	$\frac{R}{n} \cdot a_{311} \cdot h^3$
Axial chromatic defocus	$a_{020} \cdot r_n^2$	$\frac{2R}{n\cos(\Theta)} \cdot a_{020} \cdot r_n$
Lateral chromatic tilt	$a_{111} \cdot h \; r_n \cos(\Theta)$	$\frac{R}{n} \cdot a_{111} \cdot h$

The maximum wavefront aberration results when substituting the radius of the exit pupil r_{ExP} and the maximum field coordinate h_{max} as well as $\Theta = 0°$ into Eq. (2.10) which gives:

$$
\begin{aligned}
W_{max} \left(r_{ExP}; h_{max} \right) = & \\
a_{020} \cdot r_{ExP}^2 + a_{111} \cdot h_{max} \; r_{ExP} + a_{040} \cdot r_{ExP}^4 + a_{131} \cdot h_{max} \; r_{ExP}^3 + & \\
a_{222} \cdot h_{max}^2 r_{ExP}^2 + a_{220} \cdot h_{max}^2 r_{ExP}^2 + a_{311} \cdot h_{max}^3 r_{ExP} + W_{ho} &
\end{aligned}
\tag{A.1}
$$

In order to examine the scaling behavior of the maximum aberrations, the assumption that the optical system consists of a single thin lens with an refractive index n which is surrounded by air is useful for the derivation of simplified expressions for the aberration coefficients in Eq. (A.1) [47]. It is additionally assumed that the object plane is at infinity. The main properties of the thin lens are the optical power $\phi = 1/f$ and the total curvature $c = (1/R_1 - 1/R_2)$ [49] with f and R_i being the focal length and the radius of curvature of the i'th surface, respectively. An additional parameter is the distance between the aperture stop and the lens t. With these parameters, the coefficients of the Seidel aberrations can be expressed as [47]:

$$
a_{040} = -\frac{U}{4}
\tag{A.2}
$$

$$a_{131} = -tU + V \tag{A.3}$$

$$a_{222} = -t^2U + 2tV - \frac{\phi}{2} \tag{A.4}$$

$$a_{220} = -\frac{t^2}{2}U + tV - \frac{n+1}{4n}\phi \tag{A.5}$$

$$a_{311} = -t^3U + 3t^2V - t\frac{3n+1}{2n}\phi \tag{A.6}$$

The terms for a_{020} and a_{111} are left aside for the moment. The identifiers U and V are defined as:

$$U = \frac{\beta}{2} + \frac{n(4n-1)}{8(n-1)^2(n+2)}\phi^3 + \frac{\phi}{2n(n+2)}\left[\frac{n+2}{2}c - (n+1)\phi\right]^2 , \tag{A.7}$$

$$V = \frac{\phi}{2n}\left[\frac{n+1}{2}c - \left(n+\frac{1}{2}\right)\phi\right] . \tag{A.8}$$

The parameter β can be used to model aspherical surface deformations using

$$\beta = (n-1)(b_1c_1^3 - b_2c_2^3) , \tag{A.9}$$

where b_1 and b_2 are the conic constants of the first surface with curvature c_1 and the second with curvature c_2, respectively.

The behavior of the basic properties of the lens during a proportional scaling with the factor M is:

$$\begin{aligned} c &\to \frac{c}{M} \\ \phi &\to \frac{\phi}{M} \\ \beta &\to \frac{\beta}{M^3} \\ t &\to Mt . \end{aligned} \tag{A.10}$$

When looking at Eq. (A.7) and (A.8) it follows that

$$\begin{aligned} U &\to \frac{U}{M^3} \\ V &\to \frac{V}{M^2} , \end{aligned} \tag{A.11}$$

which yields the scaling of the Seidel coefficients a_{ijk} in Eq. (A.2) to (A.6)

$$\begin{aligned} a_{040} &\to \frac{a_{040}}{M^3} \\ a_{131} &\to \frac{a_{131}}{M^2} \\ a_{222} &\to \frac{a_{222}}{M} \\ a_{220} &\to \frac{a_{220}}{M} \\ a_{311} &\to a_{311} . \end{aligned} \tag{A.12}$$

It has been described in Sec. 2.3 that the radius of the exit pupil r_{ExP} will scale linear with M whereas the maximum object field coordinate h_{max} is constant. Finally, the substitution of the dependancy of the Seidel coefficients on M into Eq. (A.1) (neglecting higher orders W_{ho}) yields that each of the maximum aberrations and, thus, the sum of the primary wavefront aberrations scale linearly proportional to M. [54].

The paraxial equations Eq. (2.2) and Eq. (2.1) of Sec. 2.2.1 yield

$$r_{ExP} = \frac{f}{2F/\#} \tag{A.13}$$

and together with the magnification $m = h'_{max}/h_{max}$

$$h_{max} = \frac{h'_{max}}{m} = \frac{f}{m} \cdot \tan(\alpha) \tag{A.14}$$

which are set into Eq. (A.1) resulting in:

$$\begin{aligned} W_{max}\left(f; F/\#; \alpha\right) &= a_{020} \cdot \left(\frac{f^2}{4F/\#^2}\right) + a_{111} \cdot \tan(\alpha) \cdot \left(\frac{f^2}{2mF/\#}\right) + \\ a_{040} \cdot \left(\frac{f^4}{16F/\#^4}\right) &+ a_{131} \cdot \tan(\alpha) \cdot \left(\frac{f^4}{8mF/\#^3}\right) + a_{222} \cdot \tan^2(\alpha) \cdot \left(\frac{f^4}{4m^2F/\#^2}\right) + \\ a_{220} \cdot \tan^2(\alpha) \cdot &\left(\frac{f^4}{4m^2F/\#^2}\right) + a_{311} \cdot \tan^3(\alpha) \cdot \left(\frac{f^4}{2m^3F/\#}\right) + W_{ho} \ . \end{aligned} \tag{A.15}$$

B Basic Examples of Image Processing

Image Interpolation
The interpolation of 2D data fields is a very common task of image processing in a camera system. The demosaicing in color image acquisition with color filter array (CFA) is a prominent example [63]. In case of a Bayer pattern CFA, the values for half of the number of pixels for green and three quarters of all pixels for the red and blue color have to be derived from interpolation in order to yield a full color image. Common interpolation methods are: nearest neighbor replication, bilinear interpolation and bicubic interpolation. The easiest and fastest method is called *nearest neighbor replication*. It fills up each empty pixel in a single color plane by copying the pixel value of the adjacent pixels from the other two color planes. The algorithm may produce different results depending on the direction where the neighbor is taken from because more than one nearest neighbor might exist for the color of interest. This method gives the worst results in terms of resolution of the full color image and strong color artifacts at contrast edges [155]. However, it is often used for previewing due to its advantage in processing speed. The *bilinear interpolation* uses a neighborhood of a number of pixels from each of the two complementary color planes for the calculation of an unknown color pixel value. It processes the mean value of equidistant spaced neighbors in the grid or a weighted sum including pixels of different distances. Both forms are linear calculations. The following equations give an example for a pixel with blue color filter and index $(k; l)$ (unknown red and green values):

$$R_{k;l} = a_1 \cdot R_{k-1;l-1} + a_2 \cdot R_{k-1;l+1} + a_3 \cdot R_{k+1;l+1} + a_4 \cdot R_{k+1;l-1} \tag{B.1}$$

$$G_{k;l} = b_1 \cdot G_{k-1;l} + b_2 \cdot G_{k;l+1} + b_3 \cdot G_{k+1;l} + b_4 \cdot G_{k;l-1} \tag{B.2}$$

The coefficients a_i and b_i can be used as weights for the single contributing pixels. Alternatively, they are the reciprocal of the number of values which are used for the interpolation and thus constant in order to average between the pixels. These interpolations are used to gradually fill up the empty pixel values in each individual color plane. The bilinear interpolation yields much smoother results in still relatively short processing time. However, it compromises the sharpness of edges and blurs contrasting details of the original image. In practice, even more sophisticated methods such as the *bicubic interpolation* or edge sensing and pattern recognition algorithms are used in order to preserve the image details during the interpolation. The general form of a bicubic interpolation can be written as

$$p\left(x, y\right) = \sum_{k=0}^{3} \sum_{l=0}^{3} c_{kl} \cdot x^k y^l \ . \tag{B.3}$$

A linear system of equations has to be solved in order to find the 16 coefficients c_{kl} which have to be known in order to calculate the interpolated function $p(x, y)$. Hence, additional information is needed about the original function as usually only four points are given for the interpolation. A special form of the bicubic interpolation has been implemented as convolution kernel for a fast processing on regular 2D data grids such as images [156].

Shading and Flat-Field Correction

Shading describes the change of image intensity with the coordinate in the image field. In contrast to the fixed-pattern noise (FPN), it describes a smooth change which is usually falling off in a monotone way towards the edges of the image. Both natural vignetting and vignetting at apertures contribute to this effect [49]. The net effect of these contributions is described by the relative illumination curve from Sec. 2.2.1.2. However, the decrease of sensitivity and increase of crosstalk in sensor pixels for large angles of incidence have a significant contribution to shading [6].

At first, the dark signal non-uniformity (DSNU) is corrected by subtracting from each acquired frame an average of a number of images that have been captured in absence of any light in the scene (dark frames). The image of a homogeneously illuminated object plane W_{cap} would then ideally contain only a single gray value $\hat{M}$. However, for each pixel there is a deviation from the ideal case W_{sys} due to the shading and the photoresponse non-uniformity (PRNU) of the imaging system

$$W_{cap}(k;l) = \hat{M} \cdot W_{sys}(k;l) \ . \tag{B.4}$$

After a calibration image W_{cap} has been captured, the ideal gray value $\hat{M}$ can be approximated by the average gray value in the image using

$$\hat{M} \approx \frac{1}{N_x N_y} \sum_{k=1}^{N_x} \sum_{l=1}^{N_y} [W_{cap}(k;l)] \ . \tag{B.5}$$

The indices $(k;l)$ denote the pixels with maximum values N_x and N_y in the two dimensions of the image. Any other image which is captured with the camera would contain the same deviation caused by shading and PRNU and thus

$$E_{cap}(k;l) = W_{sys}(k;l) \cdot E_{cor}(k;l) \tag{B.6}$$

where E_{cap} and E_{cor} are the captured and the correct images, respectively. The flat-field correction can now be applied to yield the correct image of the scene by

$$E_{cor}(k;l) = M_{FFC}(k;l) \cdot E_{cap}(k;l) \ , \tag{B.7}$$

with a correction matrix that is derived from Eq. (B.4) and (B.6) and given by:

$$M_{FFC}(k;l) = \frac{\hat{M}}{W_{cap}(k;l)} \ . \tag{B.8}$$

Alternatively, the average gray value $\hat{M}$ could be calculated for a smaller part (region of interest) in the image of the flat-field scene W_{cap}. It has to be noted that the proposed correction yields good results only for a specific sensor condition because the DSNU and PRNU may change considerably with integration time and temperature whereas the shading is constant.

C   Minimum Pixel Size

One limit of the scaling of imaging systems is given by the minimum pixel size of an image sensor in order to yield a specific signal-to-noise ratio (SNR). The limiting factor here is the increasing amount of noise when the photosensitive area of a pixel and therefore the number of absorbable photons is decreased. The radiant power P_{im} on a single, squared pixel of an imaging system can be calculated by Eq. (2.45). The incoming radiant power depends on the total energy of the N_{phot} photons hitting the photodiode within a time interval dt which gives

$$P_{im} = \frac{N_{phot} \cdot E_p}{dt} \; . \tag{C.1}$$

As the photons are absorbed, a number of N_{elec} free electrons are generated in the photodiode and a photocurrent I_{pc} of

$$I_{pc} = \frac{N_{elec} \cdot |e|}{dt} \tag{C.2}$$

results. The photocurrent in Amperes per incident radiant power in Watts defines the spectral sensitivity R_λ from Eq. (2.36) by introducing the quantum efficiency η_q which is the number of created electrons per incident photon:

$$\eta_q = \frac{N_{elec}}{N_{phot}} \; . \tag{C.3}$$

In the case that solely photon shot noise is present, the noise in the photocurrent scales with the square root of the number of generated electrons (see Eq. (2.38)) and hence the SNR is equal to the square root of the number of incident photons. A certain number of photons is needed to achieve a certain SNR according to:

$$SNR_{shot} = \frac{N_{phot}}{\sqrt{N_{phot}}} = \sqrt{N_{phot}} \;\; \rightarrow \;\; N_{phot} = SNR_{shot}^2 \; . \tag{C.4}$$

For simplicity, it is assumed that the photodiodes have an ideal quantum efficiency of $\eta_q = 1$. The incident power on one pixel during a finite exposure time T_{int} that is necessary for a certain signal-to-noise ratio SNR may be calculated by:

$$P_{phot} = \frac{SNR^2 \cdot E_p}{T_{int}} \; . \tag{C.5}$$

Setting equal Eq. (4.1) and Eq. (C.5) and solving for d gives the necessary pixel size for given SNR

$$d = 2F/\# \cdot SNR \cdot \sqrt{\frac{E_p}{\pi \tau T_{int} \cdot B_{ob}}} \; . \tag{C.6}$$

The following gives a numerical example for a camera which should yield a SNR of 100 in a typical indoor illumination at daytime. A value for the brightness in such a scene is $0.01 \; cd \cdot cm^{-2}$ which can be found in literature tables [49]. This value has to be converted to radiance by using the maximum of the visual sensitivity curve at a wavelength of 555 nm where the following conversion applies [49]:

$$1 \; cd \;\; \overset{\lambda=555nm}{\longrightarrow} \;\; \frac{1}{680}\frac{W}{sr} \; . \tag{C.7}$$

Hence the radiance in object space is $B_{ob} = 1.47 \cdot 10^{-5} \; W \cdot sr^{-1} \cdot cm^{-2}$. Another simplification is used by setting the transmission of the optical system to $\tau = 1$. The f-number is set to

2.8 and the integration time is 30 ms which gives about 30 frames per second. Substituting all these values into Eq. (C.6) gives a minimum pixel size of 2.85 µm.

Solving Eq. (C.6) for the SNR, reveals its linear dependancy on the pixel size in the case of photon shot noise which is plotted in Fig. C.1.
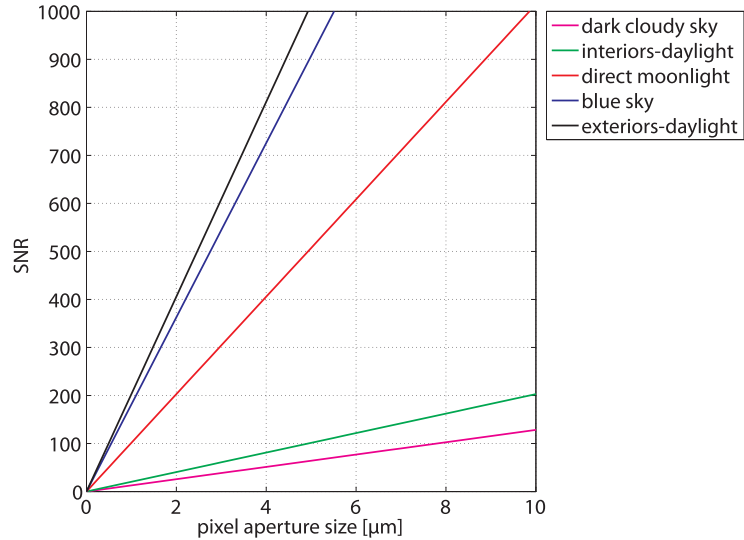
Figure C.1: Scaling of the signal-to-noise ratio of photon shot noise for different illumination scenarios. The following parameters were used: $\lambda = 0.55$ µm, $F/\# = 2.8$, $T_{int} = 0.01$ s. The values of the scene illumination were derived from [49].

In current pixel designs with a size below two microns the pixel sub-structure plays an important role for the opto-electronic sensitivity [157].

D   Assignment of Basic Features to Types of MAO

The following schematic figure gives an overview of the application of the superordinate features of multi aperture optical imaging systems in the specific types of realized systems.

	Multi Aperture Imaging Optics					
	Apposition Type	Electronic Stitching of Segments			Optical Stitching of Segments		Multi Aperture Super-Resolution
Feature of Multi Aperture Architecture	APCO	ANSE	eCLEY	MULTICAM	oCLEY	µoGSL	TOMBO
Spatial Segmentation of FOV		■	■	■	■		
Spectral Segmentation		■	■				■
Overlap of FOVs of different optical channels	■	■	■			■	■

Figure D.1: Overview of the characteristics of multi aperture imaging systems together with the mapping to the individual types. *APCO*: artificial apposition compound eye, *ANSE*: artificial neural superposition compound eye, *eCLEY*: electronic cluster eye, *MULTICAM*: multi aperture imaging system of [14], *oCLEY*: optical cluster eye, *µoGSL*: microoptical Gabor Superlens, *TOMBO*: multi aperture imaging system of [12]. Full tone color = feature fully applies; half tone color = feature may apply.

E Modeling diffraction in Image Simulations

The simulation of the image formation is one of the last steps in the optical design chain (see Fig. 3.18) which can be carried out in the sequential or non-sequential ray-tracing model depending on the complexity of the MAO. In general, a non-sequential method has to be used when the parameters of the individual optical channels differ according to their local position (chirped MLAs). A non-sequential image analysis uses a light source of the size of the object plane which emits collimated light directly on a slide object close to the source and placed in the object distance of the imaging system. The target modulation is defined by applying a grayscale or color content (e.g. a bitmap) to the slide object. A single wavelength is used for the emitted source rays in order to limit the simulation time. The scattering of the slide is modeled by a Lambertian scatter profile but rays are considered only if they have been scattered within the limited cone angle of the optical system seen from the local point on the slide object. This simulation allows a realistic image formation from a fixed object distance including effects such as parallax, crosstalk and stray light. The image stitching can be analyzed and optimized from the result. However, several limitations apply to this simulation: (1) the object scene is purely two-dimensional and planar, (2) sampling effects of the color filter array and the angular sensitivity of image sensor pixels are difficult to include, (3) the simulation duration is high in order to achieve a good signal-to-noise ratio and (4) due to the ray-tracing nature there is no diffraction included in the simulation.

Especially diffraction has to be considered because the aperture size of the microlenses is small enough to yield a spot size near the diffraction limit. In the following, a method is proposed which adds the diffraction effects to images which have been simulated by ray-tracing techniques.

The diffraction-limited PSF of the (i, j)'th microlens is not rotationally symmetric due to the generally elliptical aperture (a_t, a_s) and the different radii of curvature (R_t, R_s) along the tangential and sagittal planes of each individual microlens (Sec. 3.3.3). For simplicity, the PSF is assumed to be rotationally symmetric by using a mean aperture radius of the lens of

$$a_m^{i,j} = \frac{a_t^{i,j} + a_s^{i,j}}{2} \ , \tag{E.1}$$

and a mean radius of curvature of

$$R_m^{i,j} = \frac{R_t^{i,j} + R_s^{i,j}}{2} \ . \tag{E.2}$$

Hence the focal length of the (i, j)'th microlens is approximated by

$$f_m^{i,j} = \frac{R_m^{i,j}}{n_1 - 1} \ , \tag{E.3}$$

and according to Eq. (2.2) the average f-number is calculated by

$$F/\#_m^{i,j} = \frac{f_m^{i,j}}{2 \cdot a_m^{i,j}} \ . \tag{E.4}$$

The calculation of an average f-number according to Eq. (E.4) is valid as long as a single microlens with an aperture stop near the lens is used and aberrations are low. In case of a more complex optical system, a numerical calculation of $F/\#$, e.g. via ray-tracing methods, has to be chosen. The average f-number $F/\#_m^{i,j}$ and the wavelength λ are set

into Eq. (2.4) to yield the approximated diffraction-limited PSF $\left|h_{diff}^{i,j}\right|^2$ of each optical channel. Subsequently, each partial image of the (i,j)'th optical channel is convoluted with the related PSF in order to simulate diffraction in the image from the ray-tracing simulation:

$$E_{diff}^{i,j}(x_k, y_k) = E_{ray}^{i,j}(x_k, y_k) \otimes \left|h_{diff}^{i,j}(x_k, y_k)\right|^2 \ . \tag{E.5}$$

Such an algorithm has been implemented in Matlab™. An upsampling before and down-sampling after the convolution with the related discrete representation of the channel's PSF preserves the smoothness of the resulting image. The total integral over the irradiance of the ray-trace image (E_{ray}) and that of the convoluted image (E_{diff}) is used to verify the energy conservation of the operation:

$$\Delta E = \left| \frac{\sum_{xi} \sum_{yi} (E_{ray} - E_{diff})}{\sum_{xi} \sum_{yi} (E_{ray})} \right| \tag{E.6}$$

It should be controlled that ΔE stays far below one percent.

F   System Quality Assessment

The geometric and RMS spot size from ray-tracing and the MTF are analyzed for representative positions in the image field in order to find quantitative measures for the resolution of the system. The figure F.1 illustrates commonly used representative channels.

- **0 -** on-axis channel with zero degrees field angle
- **1 -** maximum off-axis channel in vertical direction
- **2 -** maximum off-axis channel in horizontal direction
- **3 -** maximum off-axis channel in diagonal direction
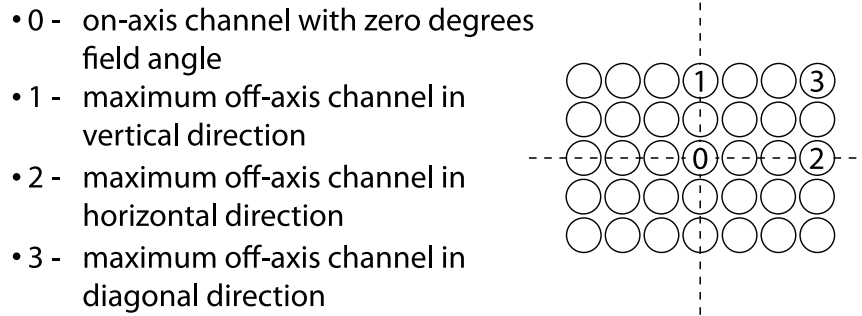
Figure F.1: Representative channels of a microlens array which are used for the simulation.

The MTFs are simulated for a set of wavelengths λ_i so that the performance could either be analyzed for a single wavelength or from an average MTF of different wavelengths

$$\widehat{H}_a = w_1 \widehat{H}(\lambda_1) + w_2 \widehat{H}(\lambda_2) + w_3 \widehat{H}(\lambda_3) \ldots \tag{F.1}$$

where w_i are the weighting factors for the individual wavelengths λ_i. The average MTF ($\widehat{H}_a$) is referred to as *polychromatic MTF*. Except for the on-axis image point, the PSF is unsymmetric and thus the MTF is a not rotationally symmetric function in the 2D spatial frequency domain (see Appendix E). This is accounted for by simulating the tangential and sagittal sections of the 2D MTF. Often, an average of the two sections is then used for comparison. Additionally, the MTF may be further analyzed with respect to its variation across the image field (of a single channel), the variation along the optical axis in image space (*through focus*) and the variation with object distance. Quantitatively, the curves are evaluated at a set of spatial frequencies such as the half and quarter Nyquist frequency. The analysis of MTF can be carried out similar to single aperture imaging optics in case

that the individual optical channels of the multi aperture optical system are uncorrelated. This is fulfilled for some of the MAO using electronic stitching of segments Chap. 4 but not for those that use optical stitching of segments of Chap. 5. The MTF of these multi aperture imaging optics has to be assessed from image simulations, if several individual optical channels contribute to the same image point. Therefore, an image of an edge is simulated that is slanted by a small angle with respect to the pixel grid of the virtual detector. The MTF can be determined from the line spread function in the simulated image according to ISO 12233 [145].

Image simulations are also needed to test the quality of optical or electronic partial image stitching. In case of electronic image stitching, the simulated image (as would be captured on the pixel array) has to be post-processed in order to create the final image of the full FOV. The optical image simulation was processed with the ray-tracing software Zemax™, the simulations results were exported and the image stitching and analysis was carried out by customized algorithms in Matlab™. A quality measure for image stitching is the sub-pixel displacement of different partial images of the same object point.

A special simulation method has been adapted to multi aperture optics in order to quantify the integral effect of optical crosstalk through a large number of optical channels as well as stray light. A test scenario is constructed where an homogeneous Lambertian radiator covers a large amount of the FOV except the FOV segment of the specific channel under test which is left completely dark. An image simulation in non-sequential ray-tracing is performed using a method like described in Sec. 3.3.4.2 with the whole MAO imaging system. Subsequently, the amount of irradiance within the partial image field of the channel under test $E_{dark}^{i,j}$ is measured relative to the irradiance E_{bright} on an equal image area in the illuminated part of the image

$$v_g = \frac{E_{dark}^{i,j}}{E_{bright}} \ . \tag{F.2}$$

As the considered image region is supposed to be dark, the smaller the ratio the lower the amount of diffuse stray light and crosstalk for the considered optical channel. The so-called *veiling glare index (VGI)* origins from ISO 9358 and can be ranked as follows: <1%: good, <3%: moderate, >6%: poor [158].

G   Image Reconstruction Using a Wiener Filter

According to Eq. (2.3) of Sec. 2.2.1 the ideal (geometric) image is degraded by the intensity point spread function of the optical system $|h|^2$ which is at least approximately known from optical design. In practical scenarios, noise has to be additionally considered so that the model can be extended e.g. with an additive noise term $n(x,y)$

$$E_{im}(x,y) = E_{geo}(x,y) \otimes |h(x,y)|^2 + n(x,y) \ . \tag{G.1}$$

This can be expressed as:

$$G_{im}(f_x, f_y) = c_2 \, G_{geo}(f_x, f_y) \cdot H(f_x, f_y) + N(f_x, f_y) \tag{G.2}$$

using the convolution theorem of the Fourier transform [70] with G_{im}, G_{geo} and $N(x,y)$ being the Fourier transforms of E_{im}, E_{geo} and $n(x,y)$, respectively. The factor c_2 is a constant. The Wiener filter is an inverse filter method that takes noise into account and can be used for a fast calculation if the PSF of the system is known [60]. Assuming that the signal and the noise are uncorrelated, the function of the filter to undo the degradation

of the system can be reduced to a minimization problem of the mean square error between the filtered image $\hat{E}_{geo}$ and the ideal image E_{geo} which is expressed in Fourier space as

$$\hat{G}_{geo}(f_x, f_y) = G_{im}(f_x, f_y) \cdot W(f_x, f_y) \ , \tag{G.3}$$

with $\hat{G}_{geo}$ being the frequency spectrum of the filtered image $\hat{E}_{geo}$. The merit function for the minimization is

$$\Phi = \left\| \hat{G}_{geo}(f_x, f_y) - G_{im}(f_x, f_y) \right\|^2 \ . \tag{G.4}$$

The zero of the first derivative of Eq. (G.4) with respect to W leads to the parametric form of the Wiener filter

$$W(f_x, f_y) = \frac{H^*(f_x, f_y)}{|H(f_x, f_y)|^2 + p_n} \tag{G.5}$$

where $p_n = |N(f_x, f_y)|^2 / |G_{geo}(f_x, f_y)|^2$ is an unknown parameter that denotes the normalized power spectrum of the noise [60]. The term H^* and $|H|^2$ are the complex conjugate and the power spectrum of the optical transfer function, respectively. The constant p_n can be derived by manual modification until a pleasing result is obtained or by using an iterative algorithm for the minimization of Eq. (G.4).

H Resolution as a Function of Field Angle for the eCLEY VGA

The demonstration systems of the electronic cluster eye (eCLEY) use ellipsoidal microlenses which can be mastered by photolithography and melting of photoresist [133]. Hence, the degrees of freedom of this technology are exploited by the adaption of the following optical parameters for each channel according to its central viewing angle (or field angle):

- Tangential and sagittal radii of curvature in order to correct for astigmatism for the center viewing angle [96, 97, 159]

- Axial focus position in order meet the image sensor plane and, thus, to compensate for field curvature [96, 97]

- Center position of the microlens in order to correct for interchannel distortion [96, 97]

A quantitative graph of the radii of curvature as a function of field angle is shown in Fig. H.1.

Although, the relationship between the radii of curvature and the field angle could be derived from an analytical relationship such as Gullstrand's equations [132], a numerical optimization of the values by commercial ray-tracing software was chosen instead, as this allows to consider also other off-axis aberrations such as coma, chromatic, and higher order aberrations. The resulting trade-off of the modulation transfer function (MTF) on the field angle is shown in Fig. H.2 for two different spatial frequencies, namely the quarter (78 cycles/mm) and half (156 cycles/mm) of the Nyquist frequency of the eCLEY VGA.
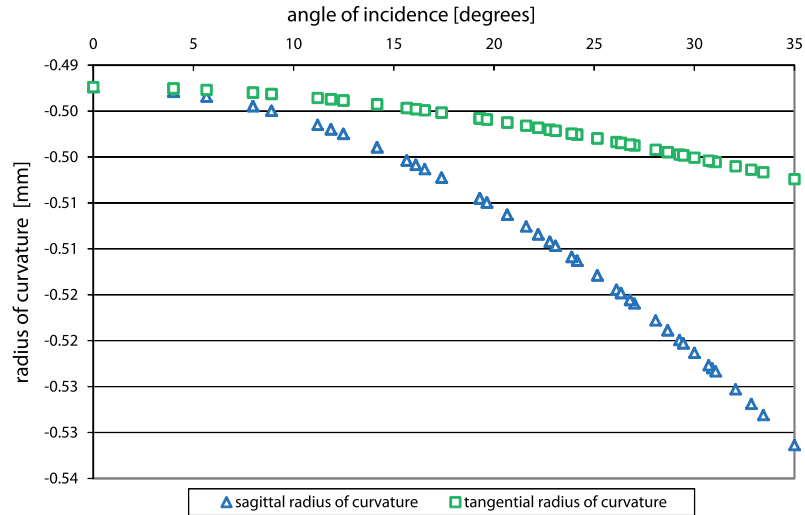
Figure H.1: Tangential and sagittal radii of curvature as a function of field angle for all lenslets of the chirped microlens array of the eCLEY VGA demonstrator.

(a)

(b)
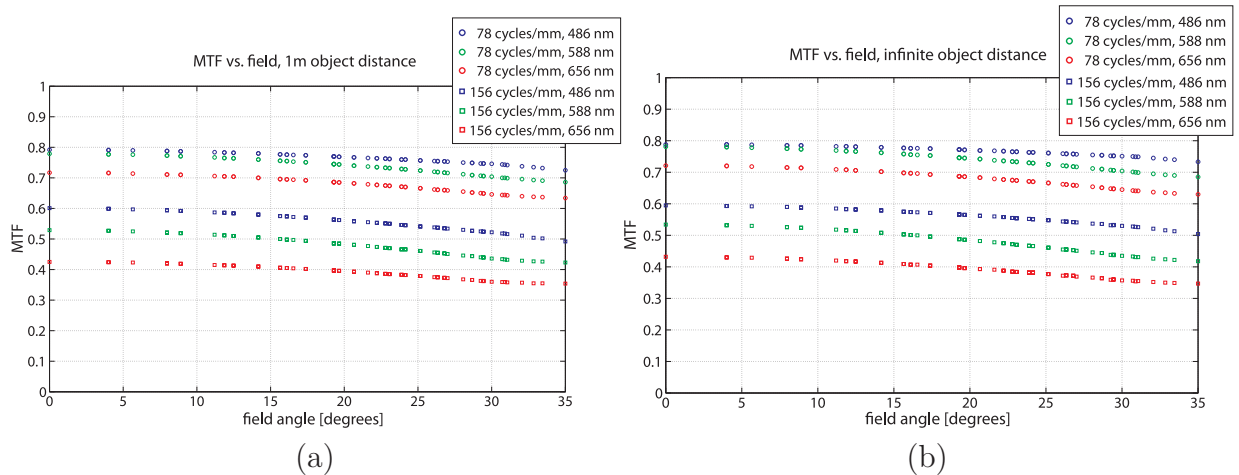
Figure H.2: The simulated modulation transfer function (MTF) as a function of field angle for the eCLEY VGA demonstrator. The two graphs have been calculated for (a) one meter and (b) infinite object distance and both for quarter Nyquist (78 cycles/mm) and half Nyquist (156 cycles/mm) spatial frequencies. The three indicated wavelengths are shown separately as lateral chromatic aberrations are corrected by image processing in the stitching algorithm. Each MTF value was calculated from an average of the tangential and sagittal MTF.

Due to the chirp, a maximum decrease of the MTF over 35° radial field of only 9% results for quarter Nyquist and 11% for half Nyquist frequency, respectively. The maximum deviation between the MTF at a wavelength of 486 nm (blue) and that at 656 nm (red) is 17%. This is due to the dispersion of the lens polymer and spacer glass material because in each channel there is only a single element with optical power which is made of a flint-like material (Exfine CO160 UV-polymer). The occuring lateral chromatic aberrations are corrected by a software transformation and interpolation in the stitching algorithm. The comparison of the MTF curves of different object distances (Fig. H.2a and b) demonstrate a peak difference of 1% which is an indication for a very large depth of field ranging from one meter to infinity.

I   Number of Resolvable Image Points

The number of resolvable image points is closely related to the space-bandwidth product (SBP) or information capacity from Eq. (2.9). In this thesis, it is used for the comparison of the different multi aperture optical imaging systems and their performance relative to state of the art single aperture cameras. In order to derive this figure of merit, the spatial frequency ρ_{co} is identified at which the measured on-axis MTF curve falls below a modulation of 10%. This frequency is considered to be the effective Nyquist frequency of the real spatial information capacity of the system, so that the real bandwidth is twice as large $2 \cdot \rho_{co}$ and thus the size of one resolvable image point is

$$p_{res} = \frac{1}{2 \cdot \rho_{co}} \ . \tag{I.1}$$

The number of resolvable image points N_{res} in the image follow from the related image edge lengths (given by the product of the total number of pixels N_x, N_y and the pixel pitch p_{px})

$$N_{res} = \frac{N_x \cdot p_{px}}{p_{res}} \cdot \frac{N_y \cdot p_{px}}{p_{res}} \ . \tag{I.2}$$

However, the calculation does not consider the amount of image contrast at certain spatial frequencies, or a change of spatial resolution with field coordinate.

J   Parameters of Ultra-Thin Array Microscope Demonstrator

The following Table J.1 lists the geometrical parameters of the different components of the prototype system of an ultra-thin array microscope which has been discussed in Sec. 5.2.2.

Table J.1: Overview of the module parameters of the ultra-thin array microscope [151].

Component	Parameter	Value	Comment
Module 1 - MLA 1	diameter radius of curvature (ROC)	0.260 mm 0.346 mm	aspherical lenslets conic value -8.5
Module 1 - MLA 2	diameter ROC	0.260 mm -0.236 mm	achromatic lenslets spherical outer lens
Module 2 - MLA 3	diameter ROC	0.200 mm 0.271 mm	spherical
Modules 1,2 and 3	microlens and aperture pitch	0.300 mm	along hexagonal axes
Module 1 - module 2	air space thickness	0.200 mm	
Intermediate image plane	diameter of field diaphragm	0.043 mm	hexagonal aperture
Image plane	diameter of partial image circle	0.350 mm	

K   Future Working Tasks for MAO

Future Tasks for Electronic Stitching of Segments

1. The increase of the resolution and the information capacity of the electronic cluster eye (eCLEY) will require additional efforts for the manufacturing of a single array master for the refractive free-form arrays by diamond micro-machining (e.g. milling). Issues such as surface deviations, rounding off at edges as well as surface roughness and tool path traces will have to be investigated when applying this technology. Subsequently, the master wafer is created by a sequentially molding from the initial mold stamp (*step and repeat* process). The final stamp for a replication of multiple free-form arrays on wafer level will be created by overcasting. However, also the UV-replication of such steep structures with large sag will yield further challenges due to shrinkage issues and induced stress.

2. The intended increase of the optical fill factor for future eCLEY systems leads to a higher vulnerability to optical cross talk e.g. in setups using refractive free-form arrays. First simulations obtained only moderate suppression by the current technique using horizontal diaphragm arrays. Alternative 3D structures will have to be

applied for the optical isolation of channels. These can be created by techniques like LASER-, two-photon lithography or by LASER drilling.

3. The combination of the optical working principle of the eCLEY with channel-wise parallelized signal pre-processing on the image sensor chip would allow for features like high-speed imaging, high dynamic range imaging, and fast movement detection with ultra-thin cameras.

4. The application of different spectral filters to each optical channel of an eCLEY system enables to acquire multispectral information with thin artificial compound eyes. Especially, a configuration in which the spectral filters are distributed across the channels like the RGB color filter array of a Bayer-mosaic will enable the acquisition of full color images with standard de-mosaicking techniques as the increased sampling algorithm (braiding) creates a final image with a standard Bayer-mosaic pattern as long as distortion is corrected in each optical channel. This reduces the complexity of the distortion correction and stitching processing making it suitable for the implementation on the hardware of mobile devices.

5. The resolution of the eCLEY can be increased by using a single color filter per optical channel and optimizing the optical properties of each channel according to the spectral bandwidth of the related color filter additional to the chirp according to the central viewing direction in the field of view.

6. An eCLEY with extremely large depth of field in a single image can be obtained due to the short focal length of each optical channel. The partial image of each channel contains focused information from an extended range of object distances but the different information are currently stitched together to match up for only a single working distance. In order to achieve a matching for the whole range of distances, the current parallax compensation method has to be applied with varying parameters according to the relative distance of objects in each patch of the final image. Furthermore, 3D imaging for objects in a distance of less than one meter are to be investigated using an adapted algorithmic solution on current images of the eCLEY VGA.

7. Another task for the enhancement of image post-processing is the investigation of a reconstruction of the stitched image data which is sparsely sampled in several parts depending on the local parallax. It can be developed in order to increase the image quality for still pictures from an eCLEY system as present methods ask for considerable computational load.

8. The integration of active elements into an eCLEY will be of growing importance with increasing image resolution and, thus, decreasing f-number (for shifting the optical diffraction limit towards the ever smaller pixel size) which results in a limited depth of field even for a short focal length. Hence, an integrated axial translation of one or more optical arrays will be able to provide an autofocus function to a thin camera device. However, the optical design and system construction have to be adapted to the integration of actuation because otherwise regions of the partial images would fall on light-insensitive image sensor areas (in the gaps between pixel groups) due to the large angles of incidence for the off-axis optical channels.

9. The integration of a scanning actuation of the objective in the micron-scale relative to the image sensor can be investigated for the increase of image resolution by sequential image acquisition.

Future Tasks for Optical Stitching of Segments

1. The trade-off between total track length and f-number or sensitivity of the optical cluster eye (oCLEY) can be coped with by the implementation of a partly superposition of adjacent partial images. Thus, the effective f-number of a system with short total track length is increased due to the overlap of a few partial images per each image point on the sensor plane. In result, each optical channel will still image only a segment of the full field of view and its optical parameters can be tuned according to the central viewing direction of the group of superimposing channels for one image point. The resulting system is a mixture between the oCLEY and the µoGSL. The trade-off between resolution and sensitivity of the microoptical Gabor Superlens (µoGSL) could be treated by the same method.

2. The principle of the microoptical Gabor Superlens is going to benefit from the development of image sensors on non-planar and especially spherical substrates. The field of view and the resolution of this setup can be largely increased due to the intrinsic curving of the eye and a compensation of field curvature by an adapted bending of the image plane.

3. The examination of the prospects of the artificial counterpart of a reflective superposition compound eye could reveal its benefits in terms of the absence of chromatic aberrations and the extension of the field of view size. However, to date, there is no known fabrication technology for a micro-scale array of edge-deflectors.

4. The integration of a front side illumination into the imaging concept of the array microscope will open up new possible fields of application e.g. in the inspection of opaque objects with high resolution such as printed circuit boards or structured silicon wafers. The challenge is to achieve a homogeneous illumination over the large object area that can be captured by the device in close working distance. Hence, suitable approaches are (1) the integration of organic or inorganic LEDs into the gaps between lenslets on the front side of the imaging system or (2) the side illumination using a transparent back-light.

5. The combination of the ultra-thin array microscope with different spectral filters e.g. with a channel-wise structured filter array will yield the possibility for a wide-field multi-spectral imaging and microscopy.

6. The implementation of a superposition of a few partial images while keeping the unity magnification in each channel of the array microscope enables the increase of the numerical aperture and, thus, the sensitivity of the device. Even the resolution can be increased due to constructive interference caused by the superposition of ray bundles that have an optical path difference from the propagation through different optical channels provided that the wavelength bandwidth is limited and the system is thoroughly built.

7. The combination of the ultra-thin array microscope with spectral multi-bandpass filters, e.g. placed axially behind the last MLA on the image sensor side, enables to

observe fluorescence from backside-illuminated specimen. Even though, the numerical aperture of the setup is limited to $NA \approx 0.1$, the sensitivity will be sufficient as the image brightness is proportional to NA^2/m^2 and the magnification $m = 1$ is used. However, as the NA also limits the spatial resolution, the ultra-thin microscope will be limited to applications which need only coarse overview of fluorescence fields or which apply intensity or counting measurements rather than the analysis of fine structures like cells.

8. The investigation of the integration of micro-actuators into the ultra-thin microscope will have several advantages. Fabrication and assembly tolerances can be compensated by a small axial translation of the position of the individual arrays. The highly precise movement of the whole module stack together with the image senor yields a z-scan movement in order to create high resolution images for a several depths in object space.

9. The implementation of a lateral (x,y)-scan can be used in order to increase the spatial resolution by a sequential image acquisition with sub-pixel displacement or for capturing gaps in the object field in case that a magnifying array microscope is used so that each observed object field is smaller than the diameter of a partial image in one capture.

10. The integration of a pinhole or an array of pinholes in the intermediate image plane of the ultra-thin microscope will create an array of miniaturized confocal microscopes for imaging a surface topology over an extended field with high resolution.

Abbreviations and Symbols

200p	Image resolution format of 200x200 pixels
720p	Image resolution format of 1280x720 pixels
1D	One-dimensional
2D	Two-dimensional
3D	Three-dimensional
ANSE	Artificial neural superposition eye
APCO	Artificial apposition compound eye
CAD	Computer-aided design
CCD	Charge-coupled device
CCTV	Closed circuit television
CD	Compact disc
CFA	Color filter array
CIS	Contact image sensor
CMOS	Complementary metal oxide semiconductor
CRA	Chief ray angle
dpi	Dots per inch
DSNU	Dark signal non-uniformity
DVD	Digital versatile disc
eCLEY	Electronic cluster eye
FDTD	Finite-difference time-domain
FFC	Flat-field correction
FOV	Field of view
FPN	Fixed-pattern noise
FWHM	Full width at half maximum
GRIN	Gradient-index
GSL	Gabor Superlens
HeNe-LASER	Helium Neon LASER
ICT	Information and communication technology
ISO	International organization for standardization
LED	Light-emitting diode
LP	Line pairs
MAO	Multi aperture optical imaging system
MAV	Micro air vehicle
mc	Multi-channel
MLA	Microlens array
MP	Mega pixel
MTF	Modulation transfer function
MULTICAM	Multichannel camera for infrared detection [14]
NA	Numerical aperture
oCLEY	Optical cluster eye
OTF	Optical transfer function
PC	Personal computer
PCB	Printed circuit board
PRNU	Photoresponse non-uniformity
PSF	Point spread function

PV	Peak to valley
RFFA	Refractive free-form array
RGB	Red, green, blue or full color
RIE	Reactive ion etching
RMS	Root mean square
SAO	Single aperture optical imaging system
SBP	Space-bandwidth product
sc	Single-channel
SNR	Signal-to-noise ratio
STD	Standard deviation
TOMBO	Thin observation module by bound optics [12]
TTL	Total track length
USAF 1951	US Air Force resolution test chart
UV	Ultra violet
VGA	Video graphics array
WLO	Wafer-level optics
µoGSL	Microoptical Gabor Superlens
a_{ijk}	Aberration coefficients
a_s	Sagittal semi-diameter of an anamorphic lens
a_t	Tangential semi-diameter of an anamorphic lens
A_{enp}	Area of entrance pupil
$A_{enp,i}$	Area of the image of the entrance pupil
A_i	Area of image
$A_{i,k}$	Output signal of pixel i,k
A_p	Area of image spot
A_{ph}	Area of pinhole opening
$A_{ph,i}$	Area of the image of a pinhole
A_{ps}	Area of a photodiode (active area)
A_{px}	Area of a pixel
$\widehat{A}_{i,k}$	Average output signal of pixel i,k
b_I	Blur diameter in image plane
b_x^k, b_y^k	Semi-diameters in x,y of the openings of the k'th diaphragm array
B_{ob}	Radiance in object plane
c	Speed of light
c_i	Constant, coefficient
C_i	Coefficient of i'th polynomial term of a free-form surface
c_v	Curvature of a lens
c_x^k, c_y^k	Positions in x,y of the openings of the k'th diaphragm array
d	Edge length of a photodiode
d_{Airy}	Airy diameter
d_i	Thickness of i'th layer
d_S	Thickness of substrate
d_x, d_y	Center position of a lens in the Cartesian plane of an array
D	Lens diameter
D_{eff}	Effective diameter of entrance pupil
D_{enp}	Diameter of entrance pupil
D_{im}	Diameter of image circle

$D_{im,x}$	Image width in x dimension
e	Fundamental charge
E_p	Energy of a single photon
E_{geo}	Intensity / irradiance distribution of the geometric image
E_{im}	Intensity distribution in image plane
E_{max}	Maximum intensity in image plane
E_{min}	Minimum intensity in image plane
f	Focal length
f_1, f_2, f_3, f_4	Focal length of microlenses in the array 1,2,3,4
f_{Achr}	Focal length of achromatic lens
f_{eff}	Effective focal length
f_{GSL}	Effective focal length of GSL
f_{mao}	Focal length of MAO
f_{max}	Sampling spatial frequency
f_{sao}	Focal length of SAO
f_x, f_y	Cartesian coordinates in spatial frequency plane
F_s	Back focal length of GSL
$F/\#$	F-number
$F\{\}$	2D Fourier transform
$g(\vartheta)$	Relative illumination function
h	Radial object field coordinate
$|h|^2$	Intensity point spread function
$|h_{diff}|^2$	Diffraction-limited point spread function
h_{im}	Image height
$(h_{in}; \alpha_{in})$	Coordinates of input ray, distance and angle to optical axis
h_L	Lens thickness / sag
h_{max}	Maximum radial field coordinate
h_{obj}	Object height
$(h_{out}; \alpha_{out})$	Coordinates of output ray, distance and angle to optical axis
h_P	Planck's constant
h_x, h_y	Cartesian coordinates in object space
$\hat{h}$	Normalized radial field coordinate
H	Optical transfer function
$\hat{H}$	Modulation transfer function
$\hat{H}_{cap}$	Capture modulation transfer function
$\hat{H}_o$	Optics modulation transfer function
$\hat{H}_{px}$	Pixel aperture MTF
i, j, k	Integer values (indices)
$(i; j)$	Channel position index in the Cartesian plane of an array
I_c	Photocurrent
I_p	Edge length of partial image
J_1	Bessel function of first order (first kind)
k	Braiding factor, integer value larger unity
K	Contrast
k_c	Conic constant
k_i	Integer value
K_x, K_y	Number of optical channels in x,y dimensions of an array
K_{ch}	Number of nonredundant optical channels

K_{im}	Contrast in image plane
K_{ob}	Contrast in object plane
L	Total track length of the optical system
m	Lateral magnification
M	Scaling factor
$\widehat{m}$	Longitudinal magnification
$\widetilde{M}$	Paraxial 3x3 system transfer matrix
m_0	Redundancy, integer value
M_D	Paraxial elementary transfer matrix for a decentration
M_{ij}	Elements of system transfer matrix
M_L	Paraxial elementary transfer matrix for a thin lens
m_{moire}	Moiré-magnification
M_P	Paraxial elementary transfer matrix for a linear propagation
n	Refractive index in space under consideration
N	Number of polynomial terms for a free-form surface
N_e	Number of generated electrons
n_g	Number of pixels along one edge of a squared partial image
n_i	Refractive index of i'th layer
$n_{i,k}$	Temporal noise of pixel i,k
n_x, n_y	Number of pixels along x,y dimensions of a partial image
N_x, N_y	Number of pixels along x,y dimensions of the image
NA	Numerical aperture
$o_{i,k}$	Spatial noise of pixel i,k
p_1, p_2, p_3, p_4	Pitch of microlenses in the array 1,2,3,4
p_K	Pitch of partial images in the image plane
p_L	Pitch of lenses in an array
p_n	Noise parameter for a Wiener filter
p_{px}	Pixel pitch of image sensor
$P_i(x, y)$	i'th polynomial term of free-form surface
P_{in}	Incident radiant power
$\widehat{P}_{px}$	Pixel aperture function
q	Number of frames
R	Radius of curvature of reference sphere or spherical lens
r_a	Radius of clear aperture
r_{ExP}	Radius of exit pupil
R_{EYE}	Radius of curvature of spherical compound eye
r_n	Radial pupil coordinate
R_s	Sagittal radius of curvature of an anamorphic lens
R_t	Tangential radius of curvature of an anamorphic lens
R_λ	Spectral sensitivity
rect	Rect-function
$\hat{r}$	Normalized radial pupil coordinate
s	Object distance
S	Signal
$S_{i,k}$	Signal of pixel i,k
SBP	Space-bandwidth product
SNR	Signal-to-noise ratio
T	Telecentricity coefficient

t_i	Axial distance between first and i'th MLA
T_{int}	Integration time
u, v	Cartesian coordinates in the image plane
V	Abbe number
W	Wavefront aberration
W_{ho}	Wavefront aberration of higher order than the Seidel aberrations
x, y, z	Coordinates in Cartesian space
$(\tilde{x}, \tilde{y})$	Distorted coordinates in image plane
z_{im}	Axial position of image plane
α	Half angle of full diagonal field of view
$\alpha_{K,x}, \alpha_{K,y}$	Half angle of FOV for a single channel in x,y dimension
α_x, α_y	Half angle of full field of view in x,y dimension
β	Half cone angle of entrance pupil
δ_a	Transverse ray aberrations
δ_I	Axial distance of defocus (depth of focus)
δ_I^{diff}	Diffraction-limited depth of focus
δ_o	Depth of field
δ_o^{diff}	Diffraction-limited depth of field
δ_{diff}	Lateral distance of two point images after Sparrow criterion
$\delta_{distortion}$	Transverse ray aberration term of distortion
$\delta_{primary}$	Primary ray aberrations (Seidel aberrations)
Δ_j	Lateral distance of ray intersection with j'th layer
Δh	Decentration
Δp_{GSL}	Pitch difference of lens arrays in GSL
Δp_K	Pitch difference of lenses and partial images
$\Delta p_{K,x}, \Delta p_{K,y}$	Projection of pitch difference on the main axes of the array
ΔR	Tolerance of radius of curvature of a lens
ΔR_{PV}	Peak to valley deviation of the surface profile
Δs_L	Spacing between adjacent lenslets in array
Δt	Time interval
$\Delta x, \Delta y, \Delta z$	Position tolerances in Cartesian space
$\Delta \alpha$	Angular tilt
$\Delta \delta$	Smallest resolvable angle in object space of SAO
$\Delta \phi$	Interommatidial angle of artificial compound eyes
$\Delta \phi_{eff}$	Effective sampling angle (radial)
$\Delta \phi_{eff,x}, \Delta \phi_{eff,y}$	Effective sampling angle in x,y dimension
$\Delta \phi_{nat}$	Interommatidial angle of natural compound eyes
$\Delta \phi_{px}$	Interpixel angle
$\Delta \varphi$	Acceptance angle
$\Delta \varphi_{nat}$	Acceptance angle of natural compound eyes
$\Delta \rho$	Geometrical projection angle of photoreceptor
ϵ_i, ϵ_j	Angle of incidence measured to normal of the i'th or j'th layer
Φ_{IS}	Geometrical fill factor of image sensor
Γ	1D optical fill factor in image plane
Γ^2	2D optical fill factor in image plane
η_q	Quantum efficiency
λ	Wavelength of light
λ_i	Spectral range of light

ν	Angular frequency
ν_{Ny}	Nyquist frequency
ν_{px}	Spatial frequency of the first zero of pixel aperture MTF
ϑ	Angle of incidence
ϑ_r	Central viewing angle of an optical channel
ϑ_x, ϑ_y	Central viewing angle of an optical channel in x,y
θ	Orientation angle of an anamorphic lens in the array
Θ	Orientation angle in pupil plane
ρ	Radial spatial frequency
ρ_0^{diff}	Diffraction-limited cut-off spatial frequency
σ	Standard deviation
σ_{shot}	Shot noise
σ_{tot}	Standard deviation of the sum of noise components
τ	Transmission of optical system
ξ, η, ζ	Cartesian coordinates in (exit) pupil space
∞	Infinity

Acknowledgments

First of all I would like to thank Prof. Andreas Tünnermann for the supervision of my thesis. I appreciate his support throughout this time, the helpful discussions which opened up different viewing directions and his impulses on new ideas of my work.

A very special thanks is dedicated to Dr. Andreas Bräuer for inspiring me to pursue the path of applied research in the field of microoptics. I am grateful for his strong backup and support throughout the years, going far beyond the period of this thesis. He always encouraged me to take the next step and to look on things from a more optimistic perspective. I appreciate having the opportunity to work in the open-minded and friendly atmosphere in his department "Microoptical Systems" at the Fraunhofer Institute for Applied Optics and Precision Engineering (IOF), Jena.

My grateful appreciation goes to Dr. Jacques Duparré who introduced me to the research topic of multi aperture imaging optics. But even long after the first spark ignition, he always motivated me to go on pushing the frontiers. With his groundbreaking prior work he paved the way on which I walk now and without his engagement the whole research group would not be in its current good situation. I also thank him for his personal support, the various helpful advices and especially for sharing his wisdom on optical design.

I owe special thanks to Dr. Frank Wippermann for the uncountable number of fruitful discussions and the motivation which often came accompanied by one of his cheering jokes. Working together with him always meant laughing together with him, which I really enjoyed. I appreciate the tips and tricks of optical design that I received from him as well as the sessions of "How to [being] use[d by] Zemax".

I would like to thank Dr. Peter Dannberg and Dr. Robert Leitel very much for their time, patience and efforts in bringing the ideas of multi aperture imaging systems into "polymer-on-glass" reality. It is due to their excellent competence and Dr. Dannberg's longtime technological skills that these demonstrators worked as good as an optical designer can dream of. I am grateful for the open-minded discussions in order to find a working solution and their readiness to try out new ways for shifting the technological limits.

Another big thanks goes to Bernd Höfer for his highly accurate assembly work, his patience and time as well as his sharing of knowledge and skills.

Special thanks to all my colleagues at the department of "Microooptical Systems" for their support and the friendly atmosphere which made it enjoyable to work together. I would like to particularly thank Wolfgang Buß, Angela Dielforder, Sylke Kleinle, Gilbert Leibeling, Antje Oelschläger, Ralf Rosenberger, Ulrike Syrotek, and Gisela Wagener.

Furthermore, I appreciate the help of Julia Meyer, who worked on the implementation of the optical design and characterization of the optical cluster eye during her Diploma thesis, and Klemens Stollberg, for his contributions to the development and characterization of the microoptical Gabor Superlens during his Diploma thesis.

Zusammenfassung

Die durch die Entwicklung der Mikroelektronik getriebene Verkleinerung digitaler Einzelapertur-Abbildungssysteme erreicht aktuell physikalische als auch technische Limits. Eine fortschreitende Miniaturisierung führt zu einer Verringerung sowohl des Auflösungsvermögens als auch des Signal-Rausch-Verhältnisses. Des Weiteren sind der Skalierung technologische Grenzen gesetzt, da die resultierenden engen fertigungstechnischen Toleranzen eine unakzeptable Kostensteigerung darstellen.

Einen Ausweg zeigen die Prinzipien der kleinsten in der Natur vorkommenden Sehsysteme - die Facettenaugen. Die parallelisierte Anordnung einer großen Anzahl von Abbildungssystemen (Facetten) ermöglicht, trotz der geringen Baugröße, eine große Informationsmenge aus einem ausgedehnten Gesichtsfeld zu übertragen.

Ziel der vorliegenden Arbeit ist es, die vorteilhaften Charakteristika natürlicher Facettenaugen zu analysieren und diese zur Überwindung aktueller Grenzen der Miniaturisierung von digitalen Abbildungssystemen zu adaptieren. Im Gegensatz zu früheren Arbeiten, wird durch die Synergie von Optik, Opto-Elektronik und Bildverarbeitung, mit der Miniaturisierung die Erreichung von Systemparametern (z.B. Auflösungsvermögen, Gesichtsfeld, Füllfaktor) angestrebt, die für industrielle Anwendungen geeignet sind. Dafür wurde eine systematische Einteilung der bereits aus der Literatur bekannten und der neuartigen, erstmals erforschten Prinzipien von Multiapertur-Abbildungssystemen vorgenommen. Das grundlegende Verständnis der Vor- und Nachteile sowie des Skalierungsverhaltens der verschiedenen Ansätze ermöglichte es, die zwei erfolgversprechendsten Systemklassen von Multiapertur-Abbildungssystemen für detaillierte Untersuchungen auszuwählen.

Für die Systemauslegung der Multiapertur-Abbildungsoptiken wurde eine Kombination aus Ansätzen des klassischen Optikdesigns und neuen semi-automatisierten Simulations- und Optimierungsmethoden mittels Ray-Tracing angewandt, um in jedem Einzelkanal ein möglichst hohes Auflösungsvermögen zu erhalten.

Die mit natürlichen Facettenaugen vergleichbare Größe der Optiken ermöglichte die Verwendung mikrooptischer Herstellungsverfahren im Wafermaßstab mit größerem Toleranzbudget. Dabei kamen Prozesse und Maschinen der Photolithographie zum Einsatz, die für eine hochpräzise, parallelisierte Fertigung kompatibel zur Halbleiterfertigung ausgelegt sind. Die erzeugten Prototypensysteme wurden experimentell untersucht und die simulierten Systemparameter konnten mit Hilfe der für die Multiapertur-Anordnungen angepassten Messmethoden bestätigt werden.

Die dargestellten Lösungen demonstrieren grundsätzlich neue Ansätze für den Bereich der hochauflösenden, miniaturisierten Abbildungsoptik, die kleinste Baulängen bei gegebenem Auflösungsvermögen erzielen. Somit sind sie im Stande die Skalierungslimits der Einzelapertur-Abbildungsoptik zu überwinden.

Ehrenwörtliche Erklärung

Ich erkläre hiermit ehrenwörtlich, dass ich die vorliegende Arbeit selbständig, ohne unzulässige Hilfe Dritter und ohne Benutzung anderer als der angegebenen Hilfsmittel und Literatur angefertigt habe. Die aus anderen Quellen direkt oder indirekt übernommenen Daten und Konzepte sind unter Angabe der Quelle gekennzeichnet.

Bei der Auswahl und Auswertung folgenden Materials haben mir die nachstehend aufgeführten Personen in der jeweils beschriebenen Weise entgeltlich/unentgeltlich geholfen:
Dr. Peter Dannberg, Dr. Robert Leitel sowie André Matthes und Techniker des Fraunhofer Institut für Angewandte Optik und Feinmechanik, Jena bei der Erzeugung von mikrooptischen Strukturen gemäß von mir vorgegebenen Parametern.
Weitere Personen waren an der inhaltlich-materiellen Erstellung der vorliegenden Arbeit nicht beteiligt. Insbesondere habe ich hierfür nicht die entgeltliche Hilfe von Vermittlungs- bzw. Beratungsdiensten (Promotionsberater oder andere Personen) in Anspruch genommen. Niemand hat von mir unmittelbar oder mittelbar geldwerte Leistungen für die Arbeiten erhalten, die im Zusammenhang mit dem Inhalt der vorgelegten Dissertation stehen.

Die Arbeit wurde bisher weder im In- noch im Ausland in gleicher oder ähnlicher Form einer anderen Prüfungsbehörde vorgelegt.

Die geltende Promotionsordnung der Physikalisch-Astronomischen Fakultät ist mir bekannt.

Ich versichere ehrenwörtlich, dass ich nach bestem Wissen die reine Wahrheit gesagt und nichts verschwiegen habe.
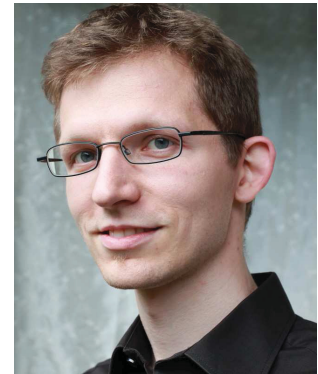
Jena, 08. September 2011

Andreas Brückner

Lebenslauf

Persönliche Daten

Name:	Andreas Brückner
Geburtsdatum:	09. August 1980
Geburtsort:	Magdeburg

Schul- und Hochschulausbildung

1987 - 1991	Polytechnische Oberschule "Maxim-Gorki" in Magdeburg
1991 - 1999	Gymnasium "Otto von Guericke" Magdeburg,
	Abschluss: Abitur
07/1999 - 05/2000	Grundwehrdienst
10/2000 - 07/2006	Grund- und Hauptstudium der Physik an der Friedrich-Schiller-Universität Jena,
	Abschluss: Diplomphysiker
	Thema der Diplomarbeit: "Hochgenaue Positionsbestimmung mit künstlichen Facettenaugenobjektiven"
	(durchgeführt am Fraunhofer-Institut für Angewandte Optik und Feinmechanik IOF, Jena)
01/2004 - 06/2004	Auslandssemester an der Dublin City University, Irland
seit 07/2006	wissenschaftlicher Mitarbeiter am Fraunhofer-Institut für Angewandte Optik und Feinmechanik, Jena

Auszeichnung

2008	Hugo-Geiger-Preis 2008 (1. Platz)

Jena, 08. September 2011

Andreas Brückner

Wissenschaftliche Veröffentlichungen

Referierte Journale

A. Brückner, J. Duparré, A. Bräuer, and A. Tünnermann, "Artificial compound eye applying hyperacuity", Optics Express **14** (25), 12076-12084 (2006).

A. Brückner, J. Duparré, A. Bräuer, and A. Tünnermann, "Analytic modeling of the angular sensitivity function and modulation transfer function of ultrathin multichannel imaging systems", Optics Letters **32** (12), 1758-1760 (2007).

A. Brückner, J. Duparré, P. Dannberg, A. Bräuer, and A. Tünnermann, "Artificial neural superposition eye", Optics Express **15** (19), 11922-11933 (2007).

K. Stollberg, A. Brückner, J. Duparré, P. Dannberg, A. Bräuer, and A. Tünnermann, "The Gabor superlens as an alternative waferlevel camera approach inspired by superposition compound eyes of nocturnal insects", Optics Express **17** (18), 15747-15759 (2009).

K. Stollberg, A. Brückner, J. Duparré, P. Dannberg, A. Bräuer, and A. Tünnermann, "The Gabor superlens as an alternative waferlevel camera approach inspired by superposition compound eyes of nocturnal insects", in "Virtual Journal for Biomedical Optics (VJBO)", G. W. Faris, ed., vol. **4** (10), Oct. 2 2009.

A. Brückner, R. Leitel, P. Dannberg, J. Duparré, A. Bräuer, and A. Tünnermann, "Thin wafer-level camera lenses inspired by insect compound eyes", Optics Express **18** (24), 24379-24394 (2010).

J. Meyer, A. Brückner, R. Leitel, P. Dannberg, A. Bräuer, and A. Tünnermann, "Optical Cluster Eye fabricated on wafer-level," Optics Express **19** (18), 17506-17519 (2011).

Zur Veröffentlichung eingereicht:
A. Brückner, R. Leitel, A. Oberdörster, P. Dannberg, F. Wippermann, A. Bräuer, "Multi aperture optics for wafer-level cameras", Journal of Micro/Nanolithography, MEMS, and MOEMS (JM3), (zur Veröffentlichung angenommen am 24.08.2011, in Überarbeitung).

Konferenzbeiträge

A. Brückner, J. Duparré, P. Schreiber, and A. Tünnermann, "Position detection with hyperacuity using artificial compound eyes", 107. DGaO Tagung, 6.-10.6.2006, Weingarten, Germany, in "DGaO-Proceedings 2006", ISSN 1614-8436.

A. Brückner, J. Duparré, and R. Völkel, "Use and advantage of micro lenses in imaging applications", NEMO-Workshop on Micro-Optics-Benefits for Industry at Photonics Europe 2006, 31.10.2006, Eindhoven, Netherlands.

A. Brückner, J. Duparré, A. Bräuer, and A. Tünnermann, "Position detection with hyperacuity using artificial compound eyes", in "Sensors, Cameras, and Systems for Scientific/Industrial Applications VIII", vol. **6501**, M. M. Blouke, Ed., (IS&T / SPIE, 2007), p. 65010D.

J. Duparré, D. Radtke, A. Brückner, and A. Bräuer, "Latest developments in micro-optical artificial compound eyes: a promising approach for next generation ultracompact machine vision", in "Machine Vision Applications in Industrial Inspection XV", vol. **6503**, F. Meriaudeau and K.S. Niel, eds., (SPIE, 2007), p. 65030I.

A. Bräuer, J. Duparré, P. Dannberg, F. Wippermann, A. Brückner, and S. Voltz, "Ultradünne, künstliche Facettenaugen-Kamera - Synergie zwischen Mikrooptik und Optoelektronik", in "MikroSystemTechnik Kongress 2007", MikroSystemTechnik - Kongress, Dresden, 2007.

A. Brückner, J. Duparré, P. Dannberg, and A. Bräuer, "Compact color vision and increased sensitivity using artificial compound eyes", International Symposium on Flying Insects and Robots, Monte Verità, Ascona, Switzerland, (August 2007).

A. Brückner, J. Duparré, and A. Bräuer, "Advanced artificial compound-eye imaging systems", in "MOEMS and Miniaturized Systems VII", vol. **6887**, D. L. Dickensheets, H. Schenk, eds., (SPIE, 2008), p. 688709.

R. Tudela, A. Brückner, J. Duparré, and A. Bräuer, "An image restoration approach for artificial compound eyes", in "Image Processing: Algorithms and Systems VI", vol. **6812**, J. T. Astola, K. O. Egiazarian, E. R. Dougherty, eds., (SPIE, 2008), p. 68120O.

R. Tudela, A. Brückner, J. Duparré, and A. Bräuer, "Image capture and processing for a microoptical compound-eye sensor", in "Optical and Digital Image Processing", vol. **7000**, P. Schelkens, T. Ebrahimi, G. Cristóbal, F. Truchetet, eds., (SPIE, 2008), p. 700019.

A. Brückner, J. Duparré, and A. Bräuer, "Microoptical system for close-up imaging of extended objects", in "Technical digest of the Fourteenth Microoptics Conference (MOC'08)", H. Thienpont, ed., Brussels, Belgium, Sept. 25.-27., 2008, (Tokyo: The Microoptics Group,

2008), pp. 94-95.

A. Brückner, J. Duparré, P. Dannberg, A. Bräuer, and C. Hoffmann, "Ultra-compact vision system for automotive applications", in "Proceedings 4th EOS Topical Meeting on Advanced Imaging Techniques, Jena, Germany (2009)", pp. 166-167.

J. Duparré, R. Tudela, A. Brückner and A. Bräuer, "Small stereovision system using artificial apposition compound eye objectives", 4th EOS Topical Meeting on Advanced Imaging Techniques, 10.-12.06.2009, Jena, Germany.

A. Brückner, K. Stollberg, J. Duparré, P. Dannberg, and A. Bräuer, "Recent developments in microoptical artificial compound eyes", in "Proceedings 15th Microoptics Conference (MOC'09)", Tokyo, Japan, Oct. 25.-28., 2009, p. C5.

A. Brückner, J. Duparre, P. Dannberg, R. Leitel, and A. Bräuer, "Driving micro-optical imaging systems towards miniature camera applications", in "Micro-Optics 2010", vol. **7716**, H. Thienpont, P. Van Daele, J. Mohr, H. Zappe, eds., (SPIE, 2010), p. 77160J.

R. Leitel, K. Stollberg, A. Brückner, J. Duparré, P. Dannberg, and A. Bräuer, "A wafer-level camera approach based on the Gabor superlens", in "Micro-Optics 2010", vol. **7716**, H. Thienpont, P. Van Daele, J. Mohr, H. Zappe, eds., (SPIE, 2010), p. 77160L.

A. Brückner, J. Duparré, R. Leitel, P. Dannberg, and A. Bräuer, "Ultra-compact close-up microoptical imaging system", in "Current Developments in Lens Design and Optical Engineering XI; and Advances in Thin Film Coatings VI", vol. **7786**, R. B. Johnson, V. N. Mahajan, S. Thibault, eds., (SPIE, 2010), p. 77860A.

A. Brückner, R. Leitel, P. Dannberg, F. Wippermann, and A. Bräuer, "A multi aperture approach to wafer-level camera lenses", in "MOEMS and Miniaturized Systems X", vol. **7930**, H. Schenk, W. Piyawattanametha, eds., (SPIE, 2011), p. 79300B.

J. Meyer, A. Brückner, R. Leitel, P. Dannberg, A. Bräuer, and A. Tünnermann, "Ultra-compact imaging system based on multi aperture architecture", in "MOEMS and Miniaturized Systems X", vol. **7930**, H. Schenk, W. Piyawattanametha, eds., (SPIE, 2011), p. 79300C.

A. Oberdörster, A. Brückner, F. Wippermann, and A. Bräuer, "Correcting distortion and braiding of micro-images from multi-aperture imaging systems", in "Sensors, Cameras, and Systems for Industrial, Scientific, and Consumer Applications XII", vol. **7875**, R. Widen-

horn, V. Nguyen, eds., (SPIE, 2011), p. 78750B.

Zur Veröffentlichung angenommen: A. Brückner, R. Leitel, F. Wippermann, P. Dannberg, A. Oberdörster, and A. Bräuer, "Microoptical multi aperture cameras", 4th EOS Topical Meeting on Optical Microsystems (OµS'11), 26.-28. September 2011, Capri, Italy.

A. Brückner, F. Wippermann, R. Leitel, P. Dannberg, W. Buß, B. Höfer, A. Bräuer, and J. Duparré, "Flachbauendes Mikroskop: Ein mikrooptisches Abbildungssystem für digitale Nahaufnahmen", MikroSystemTechnik Kongress 2011, 10.-12. Oktober 2011, Darmstadt.

A. Oberdörster, A. Brückner, F. Wippermann, A. Bräuer, and H.P.A. Lensch, "Digital focusing and re-focusing with thin multi-aperture cameras", submitted to SPIE Conference on Electronic Imaging, Digital Photography VIII, EI116 (2012).

Zeitschriften / Buchkapitel

A. Brückner, J. Duparré, P. Dannberg, S. Kleinle and, A. Bräuer, "Farbsehen mit künstlichen Facettenaugen - Artificial compound eye for color vision", Annual Report 2006 Fraunhofer Institute for Applied Optics and Precision Engineering, pp. 50-51 (2006).

R. Tudela, A. Brückner, J. Duparré and, A. Bräuer, "Echtzeit-Bildverarbeitung für den ultra-dünnen Bildsensor - Image processing for a thin compound-eye sensor", Annual Report 2007 Fraunhofer Institute for Applied Optics and Precision Engineering, pp. 100-101 (2007).

A. Brückner, J. Duparré, P. Dannberg, F. Wippermann, S. Kleinle, A. Oelschläger, and A. Bräuer, "Ultra-kompakter abbildender Sensor für Anwendungen im Automobil - Ultra-compact vision sensor for automotive applications", Annual Report 2008 Fraunhofer Institute for Applied Optics and Precision Engineering, pp. 100-101 (2008).

A. Brückner, K. Stollberg, J. Duparré, P. Dannberg, S. Kleinle, A. Oelschläger, and A. Bräuer, "Ultrakompaktes Abbildungssystem erhöhter Lichtstärke - Ultra-compact imaging system with increased sensitivity", Annual Report 2009 Fraunhofer Institute for Applied Optics and Precision Engineering, pp. 56-59 (2009).

A. Brückner, P. Dannberg, R. Leitel, A. Oberdörster, F. Wippermann and A. Bräuer, "Ultra-dünne Kamera mit VGA Auflösung - Ultra-thin camera with VGA resolution", Annual Report 2010 Fraunhofer Institute for Applied Optics and Precision Engineering, pp. 59-63 (2010).

A. Brückner, J. Duparré, F. Wippermann, P. Dannberg, and A. Bräuer, "Microoptical Artificial Compound Eyes", in "Flying Insects and Robots", D. Floreano, J.-C. Zufferey, M.V. Srinivasan, C. Ellington, eds., Springer (2010), ISBN: 978-3-540-89392-9.

Patentanmeldungen

T. Egloff, A. Brückner, W. Buss, and P. Schreiber, "Optischer Sensor und Verfahren zur optischen Abstands- und/oder Farbmessung", DE 10 2005 043627 A1, (2005).

J. Duparré, P. Dannberg, A. Brückner, and A. Bräuer, "Bilderfassungssystem und Verfahren zur Herstellung mindestens eines Bilderfassungssystems", DE 10 2006 004 802.4, (2006).

A. Brückner, J. Duparré, and F. Wippermann, "Vorrichtung zur optischen Navigation und dessen Verwendung", DE 10 2009 005 092.2, (2009).

A. Brückner, J. Duparre, F. Wippermann, P. Dannberg, and A. Bräuer, "Vorrichtung, Bildverarbeitungsvorrichtung und Verfahren zur optischen Abbildung", DE 10 2009 049 387.5, (2009).

J. Duparré, A. Brückner, F. Wippermann, and partners "Artificial compound eye and method for fabrication thereof", EP 2306230 A1, (2009).

J. Duparré, A. Brückner, F. Wippermann, R. Leitel, R. Völkel, and A. Bräuer, "Vorrichtung zur optischen Abbildung", DE 10 2009 047 361.0, (2009).

A. Oberdörster, A. Brückner, and F. Wippermann, "Bildaufnahmevorrichtung und Verfahren zum Aufnehmen eines Bildes", DE 10 2010 031 535.4-31, (2010).

A. Oberdörster, A. Brückner, F. Wippermann, H. Neubauer, and T. Schweiger, "Abbildungsvorrichtung und Verfahren für eine Abbildungsvorrichtung", DE 10 2011 081 408.6, (2011).

A. Oberdörster, A. Brückner, F. Wippermann, H. Neubauer, and T. Schweiger, "Bildsensor, Abbildungsvorrichtung und -verfahren für einen Bildsensor", DE 10 2011 081 405.1, (2011).